



**HAL**  
open science

# Turbulent flow manipulation using sliding mode and machine learning control: from the flow over a backward-facing step to a real-world car

Camila Chovet

► **To cite this version:**

Camila Chovet. Turbulent flow manipulation using sliding mode and machine learning control: from the flow over a backward-facing step to a real-world car. Fluid mechanics [physics.class-ph]. Université de Valenciennes et du Hainaut-Cambresis, 2018. English. NNT: 2018VALE0016 . tel-02015823

**HAL Id: tel-02015823**

**<https://theses.hal.science/tel-02015823>**

Submitted on 12 Feb 2019

**HAL** is a multi-disciplinary open access archive for the deposit and dissemination of scientific research documents, whether they are published or not. The documents may come from teaching and research institutions in France or abroad, or from public or private research centers.

L'archive ouverte pluridisciplinaire **HAL**, est destinée au dépôt et à la diffusion de documents scientifiques de niveau recherche, publiés ou non, émanant des établissements d'enseignement et de recherche français ou étrangers, des laboratoires publics ou privés.



Université de Valenciennes et du Hainaut-Cambrésis

École Doctorale Sciences Pour l'Ingénieur (EDSPI-072)

Laboratoire d'Automatique, de Mécanique et d'Informatique Industrielles et Humaines

Lamih

## Thèse

Pour obtenir le grade de

Docteur en Mécanique de l'Université de Valenciennes

Présentée par

Camila CHOVET

# TURBULENT FLOW MANIPULATION USING SLIDING MODE AND MACHINE LEARNING CONTROL: FROM THE FLOW OVER A BACKWARD-FACING STEP TO A REAL-WORLD CAR.

Directeur de thèse: **Laurent KEIRSBULCK**

Co-directeur de thèse: **Jean-Marc FOUCAUT**

Encadrant: **Bernd R. NOACK**

Soutenance le 06/07/2018 devant le Jury composé de :

### Rapporteurs:

J. BORÉE                      Professor, Institut Pprime, France  
L. CATTAFESTA              Professor, Florida State University, USA

### Membres du jury:

S. AUBRUN                    Professor, LHEEA, France (Présidente du jury)  
Q. GALLAS                    Engineer-Doctor, ONERA, France  
B. PODVIN                    CNRS Researcher, LIMSI, France  
L. KEIRSBULCK              Professor, University of Valenciennes, France  
J.-M. FOUCAUT              Professor, Centrale de Lille, France  
B.R. NOACK                  CNRS Research Director, LIMSI, France

### Invitées:

F. HARAMBAT                Engineer-Doctor, PSA Peugeot Citroën, France  
S. DELPRAT                  Professor, University of Valenciennes, France



*“Si mataste al tigre no puedes tenerle miedo al cuero”*

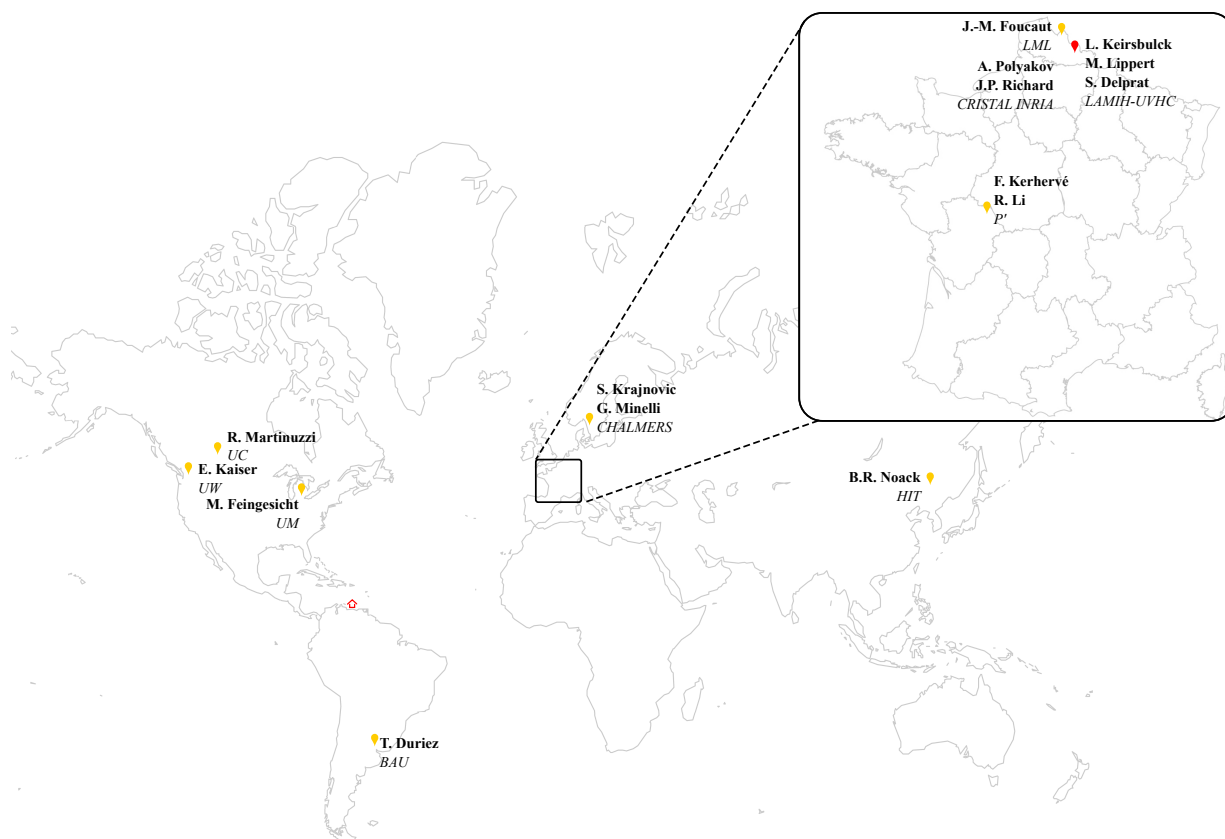
PROVERBIO VENEZOLANO

*“I am among those who think that science has great beauty.”*

MARIE CURIE



# Acknowledgements



Before finishing my thesis I want to take a moment to thank all the people who helped me go through these past few years and motivated me to continue this work.

My first thanks go to my thesis director, Laurent Keirsbulck; the relationship we developed through these years, not only as a director, but also as mentor, has immensely helped me succeed. All the discussion we had led me to create this work. Your knowledge of fluid mechanics and experimental setups was of great importance to develop the configurations I worked on. Our French-English conversations were very useful to improve my technical vocabulary. Your support in each step of the thesis gave me the courage to continue. I will always be thankful for trusting me since we met, especially inviting me to your lab and being part of your team. I never thought this will be such a rewarding experience. Merci beaucoup.

---

I would also like to express my gratitude to my co-director Jean-Marc Foucaut. Your external view of the problematic (as a professor at another university) guided me to improve the results. Your thorough examination of the work gave this thesis meticulous and accurate results.

I thank my advisor Bernd R. Noack. Our extensive conversations on Skype, Hangouts, WeChat or even by phone, guided me to achieve further objectives. Your ultra-careful way of working was of great help to organize all the work created. Your ability to connect international professors and students was key to the success of this work. The knowledge you transmitted me was of great importance in all the aspects of my thesis. I am extremely grateful for giving me the opportunity to work with you and to still continue working with the LAMIH team.

In a more departmental way, I would like to thank all my colleagues/friends at the fluid mechanics' division. Thank you for contributing to an inspiring work environment. Special thanks to Marc Lippert and Sabine Guilain-Houvenaghel; without you, I will still be doing measurements in the micro-blowers and trying to register in my first year. I will always be grateful for your attention and the way you were always willing to help me in any situation. I cannot stop mentioning Anthony and Baptiste that were always there to do measurements with me and explain me how things work. My thesis would not be complete without you.

Many thanks to Prof. Sebastien Delprat, who gave me the opportunity to work on a real car. Also, your ability and knowledge of control and automation were of great support for my thesis. Your codes for dSapce, Matlab, and Python helped me accomplish objectives that were not even in my thesis scope. The automation of several systems was of great use in flow control. We spent really interesting days at the race track with Baptiste trying to accomplish some precise results, I really appreciate you taking the time for this project.

I am grateful for the Sliding Control Team, Prof. Jean-Pierre Richard, Prof. Andrey Polyakov, Maxime Feingesicht, and Prof. Franck Kerhervé. Working in your control approach was really exciting. I want to thank your persistence from day one to help us use your control strategy in LAMIH experimental configuration. The hours spent finding a common ground in automation and mechanics were a great experience to learn a new unexplored topic. I think the results obtained with your collaboration will be promising for future flow control. After all the work we have done together, we deserve a celebration in Venice.

Thank you Prof. Sinisa Krajnović and Guglielmo Minelli for an interesting exchange of knowledge when you came to Valenciennes, I am glad that the work we did in the actuation mechanism assisted you in your problematic. I am looking forward to strong collaborations between both universities.

Last but not least, I am grateful to be part of the MLC community. The information exchange between international personalities was crucial to the success of this work. Special thanks to Eurika Kaiser, Prof. Robert Martinuzzi, and Rishabh Ishar for your understanding of key aspects to improve, not only machine learning control, but also the work we are doing in LAMIH. It was a pleasure working with you and being ready to share your knowledge and experience with us. Moreover, I would like to emphasize all the help given by Ruiying and Diogo. Thanks for raising the bar higher with the creation of outstanding projects. Also, thanks for being there to answer all the questions I had and give me advice to improve my research. I am sorry I spammed your email address.

I thank the rapporteurs Prof. Louis Cattafesta and Prof. Jacque Borée for the time you have given to proofread the manuscript and the advice you have given me. I also thank all the examiners for having accepted to be part of the jury: Prof. Sandrine Aubrun, Eng. Quentin Gallas, Prof. Bérengère Podvin, Prof. Sebastien Delprat, and Eng. Fabien Harbart.

From a more personal point of view, I thank my international friends, the ones in France and the ones around the world, for your direct or indirect support in all the phases of my work. Worth mentioning: Tariq, Marko, Dorian, Sandra, Maria, Blanca, Braulio, Andrés, Romina, Carlos, Maria Corina, Oriana, Mary, to name a few (If I forgot your name I'm really sorry).

I thank my parents, my brother and sister in law for always be there to give me an advice when needed, a getaway to relax or just to tell me that everything is going to be OK. I am extremely happy this time you do not have to travel that far to attend my thesis defence. Also, to my cousin in crime Gabó. Special thanks to my beloved teacher Silvyva, I don not know how to thank you for taking the time to read this thesis from top to bottom. Finally, I thank my partner Artém, who calmly handles my anger and/or stress episodes, and had the courage to read my thesis and correct it. I thank you all for your support.

# Contents

<b>Acknowledgement</b>	<b>i</b>
<b>Introduction</b>	<b>3</b>
<b>1 Background and state of the art</b>	<b>9</b>
1.1 Vehicle problematic	10
1.1.1 Aerodynamic efforts	10
1.1.2 Aerodynamic drag	10
1.1.3 Wake dynamics	11
1.2 Simplified configurations	13
1.2.1 Ahmed body	13
1.2.2 Backward-facing step	16
1.3 Flow control review	18
1.3.1 Passive control	19
1.3.2 Active control	22
1.4 Summary	28
<b>2 Investigation tools, actuation devices and control design</b>	<b>31</b>
2.1 Apparatus	32
2.1.1 General experimental setup and measurement tools	32
2.1.2 Modal and stochastic analysis tools	35
2.2 Actuator characterisation	38
2.2.1 Air-knife	38
2.2.2 Murata micro-blower	42
2.3 Control design	47
2.3.1 Sliding mode control (SMC)	47
2.3.2 Machine learning control (MLC)	52
2.4 Summary	55
<b>3 Backward-facing step</b>	<b>57</b>
3.1 Backward-facing step Experimental setup	58
3.1.1 BFS configuration	58
3.1.2 Sensor placement and actuation mechanism	58
3.2 Baseline flow	59
3.2.1 Flow statistics and dependencies	60
3.2.2 Flow field dynamics	66
3.3 Active flow control	71
3.3.1 Periodic forcing	71
3.3.2 Machine learning control (MLC)	74
3.3.3 Actuation effects on the recirculation area	78
3.3.4 Dynamical control mechanisms	80
3.4 Summary	84
<b>4 Ahmed body</b>	<b>87</b>
4.1 Ahmed body experimental setup	88
4.1.1 Configuration and measurement setup	88
4.1.2 Actuation device	88
4.1.3 Real-time system	90
4.2 Baseline flow	91
4.2.1 Flow statistics	91
4.2.2 Flow field dynamics and POD analysis	93

---

4.3	Open-loop investigation . . . . .	96
4.3.1	Wake modification . . . . .	97
4.3.2	Flow field dynamics and POD analysis . . . . .	101
4.4	Sliding mode control . . . . .	107
4.4.1	Experimental results of SMC application . . . . .	107
4.5	Machine learning control . . . . .	109
4.5.1	Wake modification . . . . .	113
4.5.2	Flow field dynamics and POD analysis . . . . .	115
4.6	Summary . . . . .	117
<b>5</b>	<b>Industrial application-Real vehicle results</b>	<b>121</b>
5.1	Experimental configuration . . . . .	121
5.2	Force estimation . . . . .	123
5.3	First results . . . . .	124
	<b>Conclusion and perspective</b>	<b>127</b>
	<b>Appendix</b>	<b>146</b>
<b>A</b>	<b>Additional investigated configurations</b>	<b>147</b>
<b>B</b>	<b>Metric for attractor overlap (MAO)</b>	<b>149</b>
B.1	Metric for attractor overlap . . . . .	149
B.1.1	Clustering . . . . .	151
B.1.2	Frequency analysis . . . . .	151
B.1.3	Metric of attractor overlap . . . . .	151
<b>C</b>	<b>Notations</b>	<b>153</b>

# Introduction

## The automotive industry commitment

Owning a car has become a priority in day-to-day life. A vehicle provides personal control and autonomy, especially in sparsely populated areas, where it gives the only opportunity for travelling long distances due to a lack of public transport. The sales of motor vehicles (including cars, trucks, and buses) have sky-rocketed, with over 1 billion-units being operated in 2010 (Sousanis, 2011). The amount of transportation vehicles is highly correlated with carbon-dioxide CO<sub>2</sub> emission in the atmosphere, and the strong decrease of oil reserves, to name just a few consequences (Sperling & Gordon, 2004). In fact, the distribution of greenhouse gases emitted shows that transport contributed 24% of the total global emissions (Figure.1). From this third, road vehicles represent more than 70% of the total transport power consumption, being by far the most pollutant ones. Air pollution puts at risk not only the population's health but also the ecosystem sustainability, thus, it needs to be immediately reduced.

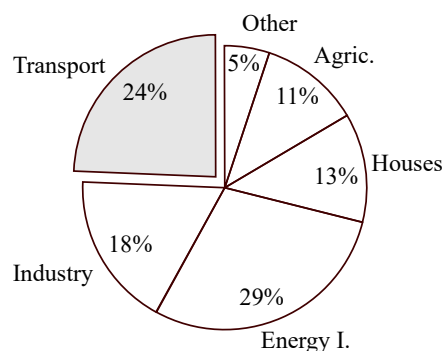


Figure 1 – Greenhouse emissions (Minelli, 2017)

Concurrently, the European Union limited the CO<sub>2</sub> emissions and sanctioned those who over-polluted. The manufacturers must ensure that their new car fleets do not emit more than an average of 95 g(CO<sub>2</sub>)/km by 2020 if they don't want to pay for the exceeded emissions. To achieve these standards, four development areas are identified to improve energy consumption, autonomy and gas emissions: engine performance, reduced friction of the bearings, lightening of the vehicle mass and the aerodynamics. On the WLTP (Worldwide Harmonised Light Vehicle Test Procedure) cycle, aerodynamics contribute a third of the

consumption, for example, for vehicles emitting 100 g CO<sub>2</sub>/km, 3% of aerodynamic gain corresponds to an emission reduction of approximately 1 g CO<sub>2</sub>/km. It is, therefore, one of the preferred ways for manufacturers to achieve their goals. The aerodynamic performance of a vehicle deals with issues from road safety to fuel economy gain. For land vehicles, the aerodynamic efforts become relevant to engine fuel consumption, and therefore, CO<sub>2</sub>, after 70 km/h (Leclerc, 2008). Car manufacturers are consequently urged to develop new technologies that can contribute to significantly diminish the environmental impact of transportation. For these reasons, to reduce the impact, it is essential to control the flow dynamics around a vehicle.

## Thesis scope

In this context, *the present work aims to pre-evaluate flow control parameters to reduce the drag in a real vehicle.*

The originality of this project lies in the use of multidisciplinary knowledge to successfully control the flow. Key aspects, such as actuation mechanisms and flow control algorithms, are widely analysed for different configurations. The range of (conventional) closed-loop control capabilities employed by fluid mechanics is reaching its limit and requires the addition of recent, high-performance control strategies from the automation community.

This thesis proposal aims to concretize an emerging collaboration between LAMIH's mechanical and automation departments around the theme of closed-loop flow control. Flow control is to this day a major challenge in many engineering fields mainly due to vehicle performance caused by flow separation. Some negative consequences are as follows: increase of the drag force, the appearance of violent instabilities often sources of noise (inter-vehicular breakage "cavity in flush flows"), wall vibration leading to premature fatigue or even break (tearing tarpaulins on a railway train). As a result, flow control is a very active field of research. The goal is to modify the flow to reduce and/or eliminate these nuisances at a lower cost. In this context, the goal of the DESIRÉ project "Développement de Stratégies Innovantes de contrôle Réactif d'Écoulements" is to make a significant multidisciplinary contribution to the theme of feedback flow control. Unlike passive control, this type of control, also known as closed-loop control, is normally outside the scope of fluid mechanics research and strongly trespass the automation research. Bringing together these two communities would allow an advance in the field by proposing new and innovative control solutions based on the expertise of automation specialists. This wind tunnel gives the possibility to study very slow flow regimes, where the flow has a long stable recirculation.

Furthermore, in the same context, this thesis is supported by the ELSAT 2020 "ContraTech" regional operation. The ability to communicate with different mechanical and automation laboratories -LAMIH, INRIA, PPRIME- gives the opportunity to test various closed-loop strategies to control an induced flow on different geometrical configurations, representative of real scale transport vehicles. A certain number of international and multidisciplinary collaborations were relevant for the establishment of a real synergy around this problem and allowed the development of new innovative control approaches. This work was the object of different communication levels: at the regional level, this work falls within the framework of the announced themes of the future CNRS Research Federation "Transport and Mobility" as well as those of the CPER ELSAT 2020 project. Strong collaborations with the automation department of LAMIH are currently held. Regionally, the automation laboratory INRIA is working with the LAMIH laboratory to develop innovative control strategies, while a mechanical knowledge exchange is done with LIMSI and PPRIME. At the national level, collaboration were established through communications during the days of the GDR MACS or GDR Automatics and Automotive GT "control of detachment". Finally, at an international level, many collaborations were triggered (Chalmers university) thanks to this project enabling

publications in international conferences and journals.

For a proper decomposition of the topics presented in this thesis, this manuscript is divided into six chapters. An initial literature review is presented to summarize the general concepts to control a flow. From the main industrial application, the forces exerted on a real car are presented. The mean wake and its dynamics are briefly defined targeting the control flow problematic. Once the rear wake of a real vehicle is studied, two simplified configurations are proposed. For a 3-dimensional point of view, a simplified vehicle model, also known as Ahmed body, is examined. This configuration is chosen because it eliminates all the complex structures generated by the windshield, mirrors, etc. Emphasis is placed on the geometry impact on the rear wake. A further simplification is presented for a 2-dimensional configuration. The backward-facing step represents a geometrically simple canonical flow with both a separation and reattachment. Some of the features presented for this configuration are also seen for the Ahmed body and the real car. Once more, the flow dynamics and the mean recirculation region are studied. A brief description of flow control techniques is analysed. The different aspects to control a flow are presented with a priority to active flow control. Here, flow control will be classified depending on the use of external energy to carry out the control. On the one hand, passive devices are introduced as inexpensive solutions to obtain a desired performance with a geometrical change in the model. However, this type of flow control mechanisms is hardly transposable for real industrial control applications. Active flow control is presented as a solution to this problematic. For this approach, an actuator device and sensors are necessary to change the flow around an object. The most common control devices and their location are defined. The control algorithms to drive this actuator are briefly described. Open-loop and closed-loop approaches are introduced depending on if the control action is based on any observation of the flow.

Once the flow control background is proposed, the investigation tools to experimentally characterize and control the flow are presented in the next chapter. The general experimental setup and measurement tools are revised. The experiments are carried out in the closed-loop wind tunnel of LAMIH laboratory, using measurement tools such as pressure sensors, hot-wire (intrusive velocity sensor), and spatial velocity estimation (PIV). The control devices, to drive the actuator mechanisms and sense the sensor signals, are also presented. For post-processing, modal and stochastic analysis tools (proper orthogonal decomposition, and stochastic estimation) are briefly defined. Two different actuation mechanisms are characterized and defined. Air-knives are a type of pulsed jet actuators, able to generate ON-OFF signals (pulsed jet). Air-knives can reach velocities up to 200 km/h; however, they require an external flow source (pressure tank). The air-knife studied has a rounded surface, adjacent to the slit exit, which could be considered as an active boat tail (Coanda effect) for drag reduction. A Murata micro-blower is also studied as an actuator for flow control. Despite being much smaller than other blowing devices, it can reach velocities up to 1 l/min. The most interesting feature of this device is its ability to be driven by any variable DC. Murata micro-blowers energized the boundary layer to directly perturb the vortex structures formed in the shear layer region. The dynamical response for different input conditions (frequency, Duty Cycle, voltage, pressure) is analysed for both actuation devices. The most complex active control approaches are also presented in this chapter. These algorithms are used thanks to the collaborations with the INRIA laboratory, and PPRIME. Sliding mode control is a robust closed-loop approach to track, reach and maintain a predefined set-point regardless of upstream flow perturbations; this approach has on-line adaptivity in changing conditions. Machine learning control is a free model to control non-linear systems. It will be used with genetic programming to learn an effective control law that is judged and optimized with respect to a problem-specific cost/objective function. The main goal is to explore the optimal actuation mechanism. The advantages and drawbacks of each control approach are also presented. A hybrid between MLC and SMC may provide adaptive control exploiting the best non-linear actuation mechanisms. The next two chapters will focus on the characterization and control of two experimental configurations: a backward-facing step and a square-back Ahmed body. These configurations are representative of the mean wake and shear-layer structures related to control of real cars.

A contribution to the study of separating and reattaching flows over a backward-facing step configuration is reported. Simultaneous unsteady wall-pressure and velocity field measurements are made in order to investigate the dynamical aspects of the separated flow field at high Reynolds numbers, of up to 182600. An array of 25 unsteady pressure sensors in the streamwise direction coupled with PIV velocity fields are used to analyse the statistical properties as well as the streamwise time-space characteristics of the separated flow. A comparison with some previous studies is done to highlight the expansion ratio influence and dependency on the main separation flow. Emphasis is placed on the dynamical aspects of turbulent flows at a wide range of Reynolds numbers, specifically in the convective motion of the vortical flow structures. The ability to understand the flow field unsteadiness will lead future investigations to develop active and/or passive flow control techniques in separating and reattaching flows. The unsteady behaviour is investigated under sinusoidal actuation generated by Murata micro-blowers and sensed by pressure probes. Initial measurements are made varying the periodic forcing (Strouhal number) based on the step height,  $St_a$ , from 0.045 to 0.453. Results suggest that an excitation at  $St_a = 0.226$ , associated with the shedding frequency, leads to a decrease of the external reattachment length and an increase of the internal separation length. Machine learning control (MLC) is used to improve performance. MLC optimizes a control law with respect to a cost function and applies genetic programming as a regression technique. The cost function is based on the recirculation length and penalizes actuation. MLC generalizes periodic forcing by a multi-frequency actuation. In addition, a sensor feedback control and a generalized feedback (open- and closed-loop laws) are used to optimize the control. Multi-frequency forcing outperforms, as expected, periodic forcing. The generalized feedback brings a further improvement. Results demonstrate the efficacy of MLC to reduce the recirculation zone in a turbulent flow regime. Given current and past successes, machine learning control will be successfully applied to numerous experimental applications. A further study of both cases, optimal frequency (among the tested) and MLC control laws, is done using modal decomposition techniques; this method separates the dominant spectral contributions. The spectral decomposition showed an increasing peak related to the shedding phenomena. Comparative results highlighted the dynamical flow mechanism involved in actuated flows and underlined that the energetic flow structure interactions are due to a periodic actuation close to the natural flapping and shedding frequencies. This dynamical behaviour is finally confirmed, for the optimal periodic forcing, with a phase averaging of the stochastic flow reconstruction showing convective structures induced by periodic forcing.

Active flow control will be now applied to a square-back Ahmed body at  $Re_H = 9 \times 10^4$ . The goal is to experimentally reduce and further maintain the aerodynamic drag. The flow is manipulated by a slotted jet placed on the top trailing edge, combined with a predefined angle direction, and sensed by a force balance. Base pressure and lift measurements are also obtained in real-time. The interaction between the air jet actuator and the mean near-wake flow are depicted by means of Particle Image Velocimetry. As a benchmark, the non-actuated case will be first analysed. Two open-loop strategies are introduced. Continuous blowing is initially used to directly influence the recirculation area and hence achieve a reduction in the drag. Approximately, a drag reduction of 8% is accomplished making this approach the “optimal case” control strategy. However, because steady blowing mechanisms lead to the highest energy consumption scheme, this strategy will only serve as the first open-loop control reference. The second open-loop strategy involves three periodic forcing frequencies,  $St_a = 0.0765, 0.135$  and  $0.405$ . The influence of these frequencies on the near-wake, and its drag modification, will be further examined. Two closed-loop approaches are also investigated. The first closed-loop separation control experiment on an Ahmed body using a robust, model-based strategy called “sliding mode control” (SMC) is considered. This study also investigates the practical feasibility of this approach which shows a great promise for industrial applications. The proposed sliding mode control (closed-loop strategy) is applied to the same Ahmed body configuration and compared to the open-loop cases. It will be designed on the basis of a simplified input-output model. A second experiment is conducted to show the disturbance rejection of the controller, corroborating the robustness and efficiency of this control approach. SMC is able to reduce and maintain the drag to a desired set-point

regardless of external flow perturbations. These successes are strong indicators that it is applicable to multiple industrial contexts. In addition, machine learning control is applied to this configuration. The goal of machine learning control is to explore and find new feedback mechanisms to optimize drag reduction. The same approaches, multi-frequency forcing, sensor-based and non-autonomous law, are studied. The mean wake and unsteady phenomena, for all the cases, are analysed. A further analysis is performed using modal decomposition techniques. The limitations and difficulties in an experimental setup are discussed for all the actuated cases.

Finally, with the knowledge obtained in the present work, the first experiment in a real car Twingo GT is introduced in the last chapter. The drag force in a real experimental application is estimated through different techniques. The results obtained for this test might be used as a reference to control the flow in more industrial applications or as an “experimental showcase”.

A summary of the main results obtained and a brief conclusion of the work is presented in the last chapter. The future projects and perspectives are also proposed here. An extension of SMC methodology to multi-input bi-linear systems with delays is being developed. Current and future works to improve MLC are also explained. The most interesting parallel works are introduced in the appendix. The collaboration results with Chalmers University are propounded when Murata micro-blowers are used in a simplified truck cabin model. The first results highlight the ability of these micro-blowers to control the flow in different types of configurations. A thesis work in collaboration with ONERA studies the dynamic mechanisms involved in the interaction between a jet and the flow at the vicinity of the wall (boundary layer conditions). A cluster application created by the MLC community is also presented. The metric of attractor overlap MAO is applied to the Ahmed body configuration to facilitate an unsupervised data comparison.



# Background and state of the art

*In the last years, the sales of automobiles (including cars, trucks, and buses) have sky-rocketed. The amount of transportation vehicles is highly correlated with carbon-dioxide  $CO_2$  emission in the atmosphere and the strong decrease of oil reserves. As the resisting force induced by the airflow over a car is the dominant contributor to power consumption at high speeds, an important effort is devoted to reducing this drag force. This first part contextualizes the work previously done. At first, the aerodynamic characteristics of the flow over a real car are presented. Then the flow around a simplified car model, also known as the Ahmed body, is studied. A further geometric simplification is presented as the backward-facing step; its main flow characteristics are also analysed. Finally, a state of the art of flow control is drawn up, with an emphasis on the main control strategies used for different control researches.*

## Contents

---

1.1	Vehicle problematic . . . . .	10
1.1.1	Aerodynamic efforts . . . . .	10
1.1.2	Aerodynamic drag . . . . .	10
1.1.3	Wake dynamics . . . . .	11
1.2	Simplified configurations . . . . .	13
1.2.1	Ahmed body . . . . .	13
1.2.2	Backward-facing step . . . . .	16
1.3	Flow control review . . . . .	18
1.3.1	Passive control . . . . .	19
1.3.2	Active control . . . . .	22
1.4	Summary . . . . .	28

---

## 1.1 Vehicle problematic

### 1.1.1 Aerodynamic efforts

For a vehicle, the shape complexity, limited enclosure and small curvature ratio promote the detachment yielding vortical structure formation near the surface. The formation of these vortex structures is related to a loss of energy and a decrease in the static pressure. Research in the automotive sector is mainly focused on studying the dynamics of detachments and optimizing the distribution of static pressures around the vehicle. First, it is crucial to know the forces exerted by a fluid on the studied vehicle. This result is physically decomposed into a pressure force  $\vec{F}_p$  related to the static pressure on the surface of the geometry and the friction force  $\vec{F}_f$  related to the tensor of the viscous stresses, respectively, normal and tangential to the surface of the geometry (Figure 1.1).

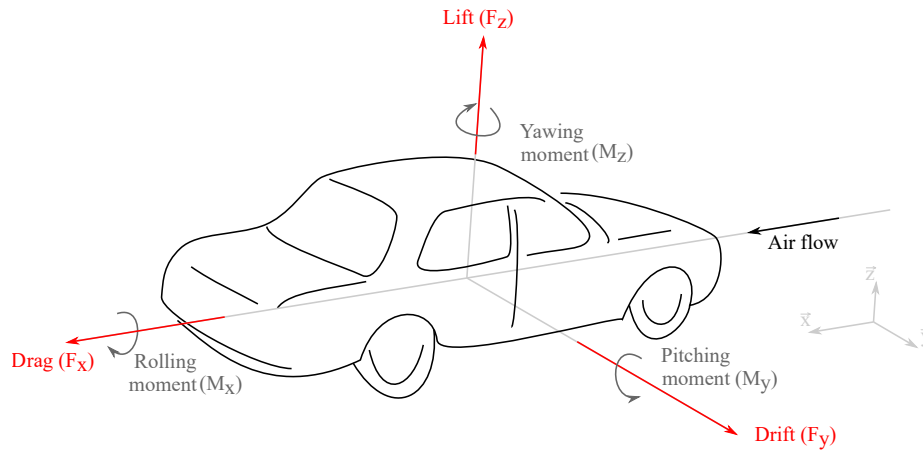


Figure 1.1 – Force and aerodynamic moments linked to a vehicle (Leclerc, 2008)

To overcome vehicle dimensions and vehicle running conditions, aerodynamic efforts are expressed as aerodynamic coefficients by:

$$C_x = \frac{F_x}{1/2\rho U_\infty^2 S_\infty}, \quad C_y = \frac{F_y}{1/2\rho U_\infty^2 S_\infty}, \quad \text{and} \quad C_z = \frac{F_z}{1/2\rho U_\infty^2 S_\infty}, \quad (1.1)$$

where  $\rho$  corresponds to the fluid density,  $U_\infty$  the reference flow velocity and  $S_\infty$  the projected area in the same direction as the exerted force.

The drag force  $F_x$ , hereafter denoted as  $F_D$  ( $C_D$  for the coefficient), is defined as the projection of the resultant of the aerodynamic force on the axis of the main direction of the flow. The lift  $F_z$ , commonly known as  $F_L$ , is used to describe the support of the vehicle related to the aerodynamics. The drift  $F_y$  is generally used to describe the behaviour of the vehicle during an overtaking or a lateral gust of wind. The aerodynamic momentums, presented in Figure 1.1, have a significant impact on the vehicle dynamics; however, they will not be further studied.

### 1.1.2 Aerodynamic drag

A simple approach to understand the drag is to consider it as the resistance to the advancement of a body in a fluid. The drag depends on the velocity; it can slightly vary in certain velocity ranges. To overcome the aerodynamic drag, at 50 km/h, the vehicle needs more than 50 % of the total power; this value reaches 80 % at 130 km/h (Brunton & Noack, 2015). For this reason, car manufacturers are interested in improving the aerodynamic performance of road vehicles.

On a moving vehicle, the distribution of aerodynamic effort (spatial integral of local forces) is very

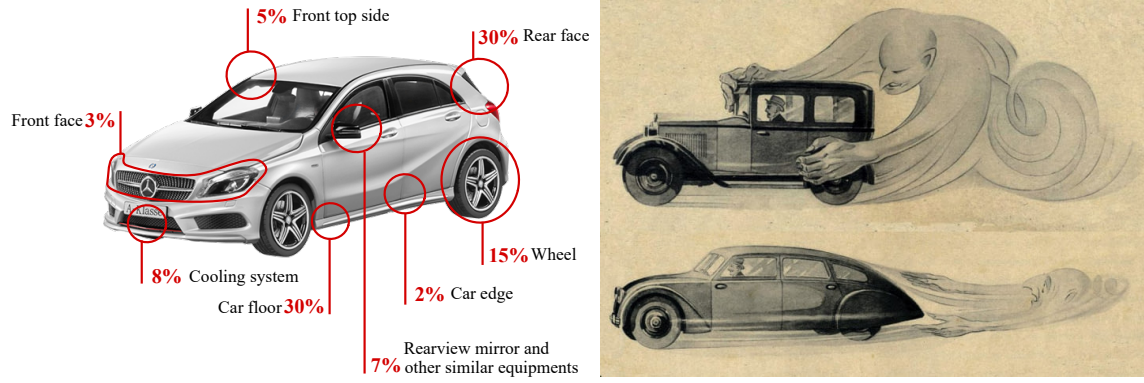


Figure 1.2 – Contribution of each source of aerodynamic creation (Action Moto Magazine, 2007), Design of drag forces applied to different car shapes.

variable along the bodywork. If all these efforts are separated, several forces contribute to the drag (Figure 1.2). The static pressures on the rear of the vehicle represent a total drag gain of around 30 %, equal to the contribution of the underfloor flow. The wheels also cause a significant drag gain, approximately 15 %. The efforts to reduce the drag forces have largely evolved over the years. Car shapes have been strongly optimized in order to decrease the drag (Figure 1.2). However, car manufacturers are still limited to further improve the vehicle structure due to functional aspects such as space for passengers, crash safety and design (Grandemange, 2013). Vehicle shapes are quite standard (Rossitto, 2016) because designers have similar constraint and consequently a similar approach. Aerodynamicists are searching for new ways to reduce drag as well as new alternatives to allow more degrees of liberty in the design. Furthermore, the wall proximity to the vehicle bottom has significant effects on the aerodynamic forces and flow structures (Choi *et al.*, 2014). This distance is called ground clearance. Previous experimental and simulation researchers (Fago *et al.*, 1991; Hucho & Sovran, 1993) have observed noticeable flow variations around a vehicle depending on the type of ground conditions. The drag was reduced 8% when a movable ground was placed instead of a stationary one (Krajnović & Davidson, 2005c).

A more analytical formulation of the aerodynamic drag effort is proposed by Onorato *et al.* (1984). The drag force is decomposed depending on the pressure forces, fluidic rotation, and the induced velocity deficit. From the integral balance of momentum, they have shown analytically and then experimentally the relation between the effects of the wake and the coefficient of aerodynamic drag moving at a velocity  $U_\infty$ ,

$$F_D = \iint_{S_\infty} (P_t^\infty - P_t^{S_\infty}) d\sigma - \frac{\rho U_\infty^2}{2} \iint_{S_\infty} \left( \frac{U_y^2}{U_\infty^2} + \frac{U_z^2}{U_\infty^2} \right) d\sigma + \frac{\rho U_\infty^2}{2} \iint_{S_\infty} \left( 1 - \frac{U_x^2}{U_\infty^2} \right) d\sigma, \quad (1.2)$$

where  $S_\infty$  denotes the surface of the wake downstream of the vehicle,  $(U_x, U_y, U_z)$  the velocity  $\vec{U}$  components,  $P_t^\infty$  and  $P_t^{S_\infty}$  are the upstream pressure and the pressure in the wake  $S_\infty$ .

The first term involves the pressure loss between the front part and the rear part of the vehicle. This difference is strongly related to wake phenomena and is the largest contributor to the aerodynamic drag (up to 80%). The second term takes into account the energy losses associated with the rotation of the fluid in the plane transverse to the main flow (e.g., longitudinal vortices on an Ahmed body with a slant angle (Eulalie, 2014)). This term is of the order of 20% of the drag. The last term represents the energy related to the projected loss of speed on the main flow axis; it becomes weak (or even zero) outside the wake.

### 1.1.3 Wake dynamics

A key phenomenon around ground vehicles, which is not seen in commercial airplanes, ships or submarines, is the massive flow separation. As previously explained, when a car is in motion, the oncoming flow impinges the front part of the car and surrounds it. However, when the flow arrives at the rear part, the abrupt geometry variation forces the flow to separate forming a recirculation region behind the model. This region

is associated with a low pressure and the separated flow is known as the wake. An illustrative example of the wake is presented in Figure 1.2. When the size of the wake is comparable to the body dimensions, the body is referred as a bluff body. All road vehicles and heavy trucks are classified as bluff bodies. They produce a large wake and experience separated flow on large areas of their external surface (Minelli, 2017). This wake significantly affects the aerodynamic forces and moments experienced by the vehicle (Ahmed *et al.*, 1985). The flow at the rear of a vehicle is complex. In the near wall, massive vortices are formed and moreover, these structures are carried further in the wake. To better understand the flow dynamics of transport vehicles, it is important to describe the fundamental characteristics of the rear part of the body. In her Ph.D thesis work, Li (2017) presented a sketch of the wake flow on the vertical symmetric plane of a square-back car in a two-dimensional point (Note that this is a representation and the real structures are highly three-dimensional and more complex, Figure 1.3)

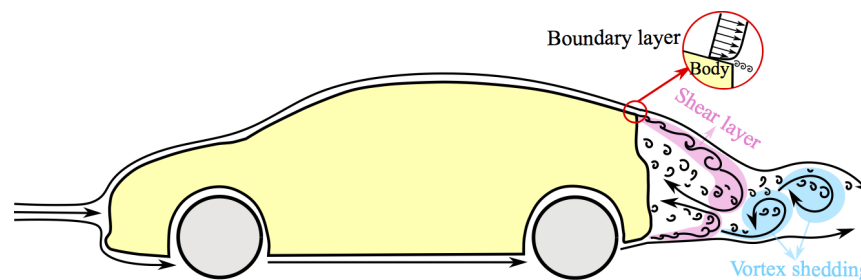


Figure 1.3 – Fundamental wake features behind a square-back car extracted from the PhD. thesis work of (Li, 2017)

In order to characterize the topology of the flow (laminar, transitional or turbulent), a dimensionless value, denoted Reynolds number,  $Re$ , is used. Above a critical value of this number ( $Re > 10^4$ ), the flow topology and dynamics change radically. The Reynolds number is defined as  $Re = \frac{UL}{\nu}$ , where  $U$  is the reference velocity of a flow,  $L$  is its reference length and  $\nu$ , the kinematic viscosity of the fluid under consideration. In aeronautics, turbulent flow is considered harmful because it is responsible for increasing drag and reducing lift and on an automobile, it develops around the vehicle and in its wake. Turbulence disperses and mixes the environment in which it develops (Jacquin & Tabeing, 2006). In highways, car velocity exceeds 70km/h corresponding to Reynolds number in the order of  $10^5$  and based on the car height, this value is in the range of highly turbulent flows.

When a fluid flow encounters an obstacle due to friction on the surface of the obstacle and the viscosity of the flow, the flow velocity is zero on the surface of the obstacle. Above this surface, the flow velocity gradually increases to a certain height where the free-stream flow is found. This zone of velocity gradient is called the boundary layer. The thickness of the boundary layer  $\delta$  is usually defined by the distance to the wall where the velocity  $U$  has reached a certain percentage of the external value, generally 99 %. Furthermore, on a vehicle, several zones may have near-wall flows that are separated at the trailing edge and contribute to the formation of vortex structures. The detachment of the boundary layer yields eddies into the wake. The creation of these vortex structures due to a detachment point (noise amplifier) is known as the shear layer, mixing layer or Kelvin-Helmholtz instability (Drazin & Reid, 2004). The small-scale vortices near the origin gradually grow into larger and larger coherent structures, manifesting the high-dimensional multi-scale vortex dynamics involved in this type of flow (Li, 2017).

When the shear layer is created from opposite edges, it produces a swirling movement that alternates in the wake of the object. This phenomenon is known as von Kármán vortex street (Figure 1.4(a)). A further analysis of the vortex interaction in this configuration was done by Gerrard (1966). As previously mentioned, the shear layer generates a growing vortex on one side (Figure 1.4(bI)). This vortex initially grows in size, until a new vortex is developed on the opposite side, closer to the base. The increase of the second vortex II will cease the formation of vortex I and the latter is released away from the body. These flow dynamics lead to the well-known shedding dynamics presented in Figure 1.3. A simplification of the

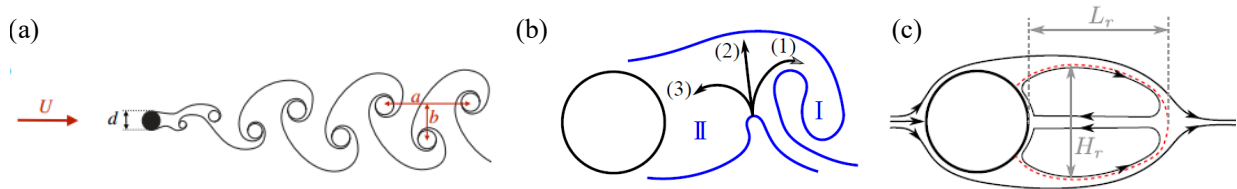


Figure 1.4 – (a) Schematic visualization of the Kármán vortex street (Eulalie, 2014), (b) Interaction of opposing shear layer (Gerrard, 1966), (c) Mean wake of a cylinder, obtained from (Li, 2017), '- -' red dashed line represents the recirculation bubble boundary.  $L_r$  and  $H_r$  are the bubble length and width, respectively.

mean wake of the cylinder is presented in Figure 1.4(c). The sketch presents a recirculation zone, with two bubbles, the upper one rotating clockwise, while the lower one, counter-clockwise. The aspect ratio between the main bubble (recirculation zone) thickness  $H_r$  and the length  $L_r$  will determine the pressure inside this region. Furthermore, the size of the two inner bubbles might vary depending on the model geometry. Note that this configuration is two-dimensional and is predominated by vortex shedding. For a three-dimensional case, the flow interaction come from all the edges creating a more complex wake dynamics. In real vehicles, these highly complex vortex structures are strongly linked to drag performance. The main objective will be to characterize and control them to a desired state, or, ideally, suppress the wake formation at the rear face. This type of practice is called flow control and comprises several different techniques that have different advantages and drawbacks.

## 1.2 Simplified configurations

### 1.2.1 Ahmed body

The drag is mainly associated with the development of vortex structures in the wake of the vehicle. The average topology of the structures that generate the wake evolves according to the vehicle's rear body geometry. The physical phenomena governing the flows around vehicles is highly complex and strongly dependent on the specific geometry of each model. For this reason, the scientific community and industrialists of the automotive world mainly use the Ahmed model. A simplified car geometry is introduced in the work of Ahmed *et al.* (1984). The interest of this simple form is to get rid of vortex structures generated at the levels of bay, windshield or mirrors that are transmitted to the wake, and thus focus on the study of the wake phenomena from massive detachment from the back of the geometry. The simplified three-dimensional model provides a good reference to study the aerodynamics of a vehicle.

#### Geometry impact on the rear wake

In vehicle aerodynamics, many numerical simulations (Krajnović & Davidson, 2003; Minguez *et al.*, 2008; Guilmineau *et al.*, 2011; Östh & Krajnović, 2012) and experiments (Bayraktar *et al.*, 2001; Lienhart & Naguib, 2003; Grandemange *et al.*, 2013b; Zhang *et al.*, 2004; Barros *et al.*, 2016a,b) have been conducted for different simplified car shapes. The comprehension of the flow structures around a model can reproduce similar flow structures presented in real road vehicles. In this section, two well-known vehicles models will be discussed: slanted rear surface and square-back surface. Both cases present a rounded shape at the front.

The study of a variable rear shape is possible thanks to the slanted surfaces (Figure 1.5(a)). Ahmed *et al.* (1984) investigated the effect of the rear slant angle  $\alpha$  on the aerodynamic drag; it is defined as the angle between the slanted rear surface and the upper horizontal surface. For these cases, the flow presents a first separation bubble at the slanted surface, followed by one or two recirculation bubbles at the vertical

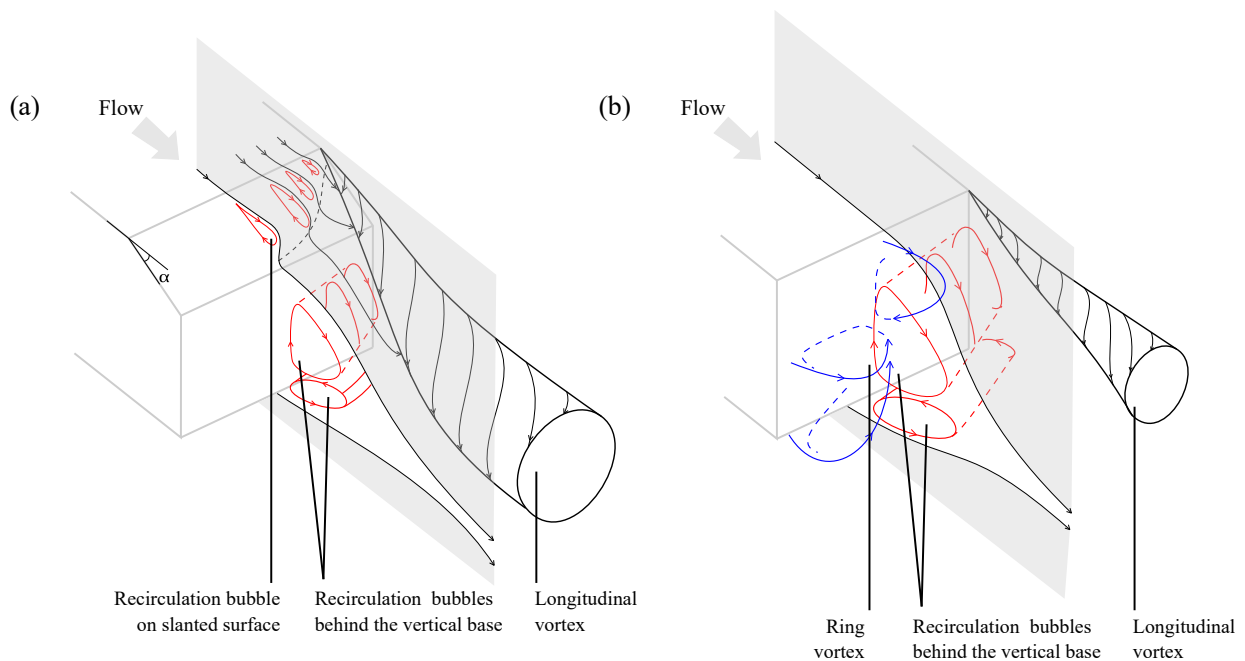


Figure 1.5 – Three-dimensional flow structures in the wake of an Ahmed body. (a) Slanted surface, (b) Square-back, based on the flow characteristics presented by Choi *et al.* (2014) & Krajnović & Davidson (2003)

base. Flow structure generation and its strength will strongly depend on the slant angle. Three different flow topologies are presented for three angle ranges.

For slant angles below 12, the flow will remain attached to the slanted wall and the separation occurs at the vertical surface, similar to a square-back topology (Figure 1.5(b)). In this range, the drag will decrease as the angle increases, reaching a minimum drag value at  $\alpha \approx 12$ . For this case, the wake region is associated with low levels of base pressure and is the major contributor to the aerodynamic drag; it is essentially related to the development of vortical structures at the periphery of the base.

For angle values between  $\alpha \in [12, 30]$ , the flow separates at the top trailing edge but quickly reattaches on the slanted surface, creating a small recirculation bubble (Figure 1.5(a)). The size of this separation bubble will increase when the slant angle increases. Furthermore, the drag will also increase until the angle reaches a value of  $\alpha = 30$ . The wake topology is of a hatchback type.

Slanted angles higher than  $\alpha > 30$  have a similar topology to the ones obtained for angles below twelve and a square-back surface. The overall geometry of the square-back model is similar to that of the Ahmed model with  $\alpha = 0$ , but their detailed dimensions slightly differ. General Motors (Han *et al.*, 1996) presented a square-back rear shape with a blunt trailing edge. For this configuration, the flow is characterized by a massive recirculation bubble on the after-body ('—' red line in Figure 1.5(b)). The separation point is fixed at the blunt trailing edge; it is intrinsically three dimensional, causing a significant drop in the base pressure (Lee & Choi, 2009). For all the cases, two longitudinal vortex structures on the side edges are formed. These structures are highly energetic and cause a significant decrease in pressure values at the geometry surface (Lehuteur & Gilliéron, 2006). Several studies have experimentally seen these coherent structures (Han, 1989; Duell, 1994). A formation of an O-ring structure, also known as toric vortex, is generated at the vertical surface, '—' blue line in Figure 1.5(b). This structure is also presented in Krajnović & Davidson (2003).

Structures related to shear are formed from the points of separation and are characterized by a sharp increase in the values of vorticity related to their creation. As previously explained, the wake region, formed due to a geometry variation, is associated with low levels of base pressure and is the major contributor to the aerodynamic drag, around 70 to 80 %. A more general study of the unsteady dynamics of the flow,

performed on a car wake, is presented by Gilhome (2002). For an Ahmed body, the temporal evolution of the static pressures at the back of the geometry is essentially related to the formation of shear layer structures in the wake of geometry. This non-stationary dynamic is the cause of energy losses which are reflected on the surface by the presence of low values of static pressures. The wake flow development downstream of an Ahmed body, as a function of the slanted angle, appears to be correlated to those obtained in real vehicles (Choi *et al.*, 2014). Nowadays, experimental investigations offer a good knowledge of the structures and wake topology downstream of an Ahmed body (Lienhart *et al.*, 202). For this automotive application, the development of an active control system should focus on controlling instabilities of flow created by the geometry wake topology.

To characterize the different wake dynamics, the non-dimensional Strouhal number will be used,

$$St_H = \frac{fH}{U}, \quad (1.3)$$

where  $H$  is the height of the model. The main frequencies reported in several studies are now presented. Duell & George (1999); Khalighi *et al.* (2001) & Verzicco *et al.* (2002) attained a dominant frequency, obtained from pressure and velocity measurements at the base, for  $St_H = 0.04$ . They suggested that this frequency was related to the recirculation bubble streamwise oscillation, where the upper and lower toric vortex periodically interacted. This phenomenon was first presented by Berger *et al.* (1990) and revealed an oscillation of the recirculation bubble from experimental visualization downstream of a disk. Another frequency peak was found in multiple studies (Khalighi *et al.*, 2012; Grandemange *et al.*, 2013b; Lahaye *et al.*, 2014; Barros *et al.*, 2016a,b) at  $St_H = 0.2$ , and it is related to the vortex shedding formation. Similar results were obtained for two-dimensional flows (Roshko, 1955; Becker *et al.*, 2015; Gerrard, 1966). This peak was better seen in the plane of symmetry. Minguez *et al.* (2008) studied the dominant frequencies over slanted surfaces with  $\alpha = 25$  and found a peak between  $St_H = 0.25 - 0.3$ , which they argued was related to the instability of the shear layer over the slanted surface. Thacker *et al.* (2010) noted the same frequency peak but stated that it may be related to the oscillations of the reattachment position. Duell & George (1999) also observed high-frequency dynamics, at around a dimensionless frequency of  $St_H = 1.15$ . They stated that this frequency was related to the vortical structures roll-up by the shear layer. Barros (2015) obtained the same result at several streamwise locations inside the shear layer. Furthermore, Thacker *et al.* (2010) studied the frequency spectrum downstream of the detachment point of an Ahmed body with  $\alpha = 25$  and identified a high-frequency area at Strouhal value of  $St_H = 1.3$ . A high-frequency was obtained due to the closeness of the sensor location to the mixing layer, between the wake and the reference flow. Although similar dynamics are obtained for previous studies, they also demonstrated the wake sensibility by geometry variations such as cross-sectional geometry and ground clearance.

### Wall effects on the wake flow topology

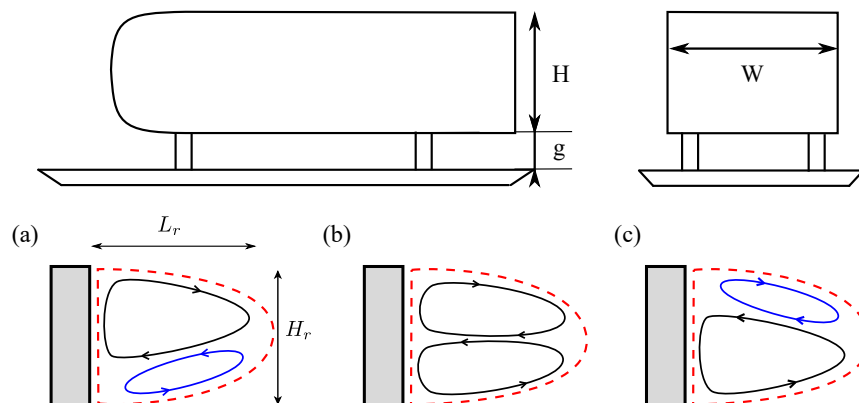


Figure 1.6 – Mean wake topology (a,c) Asymmetric wake (b) Symmetric wake, based on Barros *et al.* (2016b)

The wake motions are strongly affected by wall proximity or ground clearance  $g$ . Grandemange *et al.* (2013a); Podvin *et al.* (2016) and more recently Barros *et al.* (2017) studied the impact of the ground clearance and height/width ratio ( $H/W$ ) on the wake. Barros *et al.* (2017) investigated the underflow perturbation at a given ground clearance. The perturbation was inflicted at the bottom of a square-back Ahmed body (between the model bottom and the ground) with a passive device. An initial wall-normal asymmetric flow topology (Figure 1.6(a)) was obtained for a ground clearance of  $g = 0.05\text{m}$ , with a large clockwise recirculation bubble closer to the top trailing edge and to the vertical surface. This bubble shrinks to a nearly symmetric topology (Figure 1.6(b)) when the ground clearance is decreased by a passive device. If the passive device height is further increased, causing a decrease of the ground clearance, the flow recovers its wall-normal asymmetric topology, but with the larger recirculation bubble closer to the rear wall and floor (Figure 1.6(c)). When the  $H/W$  ratio was changed, Grandemange *et al.* (2013a) noticed that a modification of the ground clearance would break the distribution of the lateral wake. For  $H/W = 1.34$  (Ahmed body geometry), the initial symmetric lateral wake will be perturbed and an asymmetric wake appears. At  $H/W = 1.34$ , the lateral wake remains symmetric, even though the ground clearance is changed. However, a bi-modal behaviour, with an asymmetric topology appears in the wall-normal direction beyond a certain ground clearance value.

These results prove the high sensitivity of the wake when a variation on the Ahmed body configuration is done. The dynamics of the instantaneous flow have different characteristics from the time-average ones. Even though various studies have been carried out in the latter, it is still important to understand the unsteady flow features in car models. The drag generation and its control are strongly linked to the unsteady flow characteristics (Choi *et al.*, 2008). A thorough study of this unsteady phenomenon must be followed. As the flow features are still quite complex for this type of configurations, the study of more simplified geometries might be of great value to understand the most basic flow modification. In the next section, a two-dimensional configuration will be analysed.

### 1.2.2 Backward-facing step

Flows over bluff bodies can yield undesired effects; one of the most important ones is separation of the flow. Fences, ribs, forward-facing-steps, to name a few, present a sharp geometry forming a separation and further reattachment of the flow. This separated and reattaching flows can be found in many practical engineering applications (Bradshaw & Wong, 1972; Ruderich & Fernholz, 1986). According to the linear evolution of perturbations in space and time (Huerre & Rossi, 1998), these unstable flows can be classified in two distinct classes: hydrodynamic oscillators (absolutely unstable) and noise amplifiers (absolutely stable but connectively unstable). In hydrodynamic oscillators, instabilities grow *in situ* and survive for all time. They display an intrinsic dynamic at a well-defined frequency and do not depend on external noise, e.g., flow past a cylinder or cavity flow. For amplifier flows, the basic flow carries growing perturbations away in the downstream direction, and the system eventually returns to its unperturbed state. Noise amplifiers are very sensitive to external perturbations and their characteristics determine the type of structures amplifying the flow (Pier & Huerre, 2001). One of the most common noise amplifier configurations is the backward-facing step. The flow over a backward-facing step BFS represents a geometrically simple canonical flow situation exhibiting both separation and reattachment. This simple configuration exhibits one separation point and one detachment region. The backward-facing step, also known as back-step flow, provides all the complex characteristics of a reattaching/separated flow.

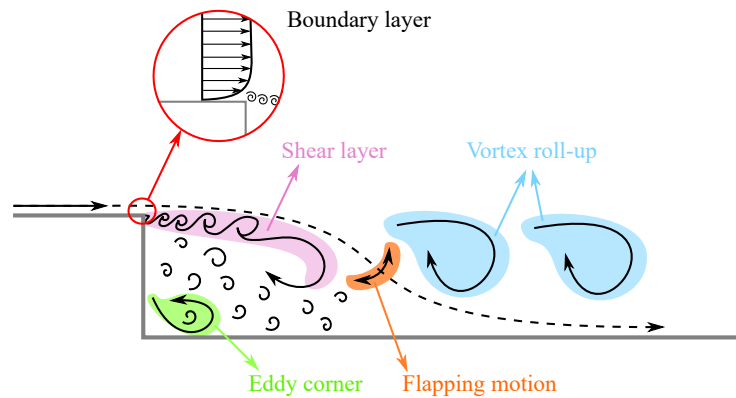


Figure 1.7 – Wake features downstream of a backward-facing step.

## Flow dynamics

To better understand the characteristics of separated/reattaching flows, a first study of the flow dynamics is presented. Figure 1.7 shows a sketch of the main instabilities presented in a backward-facing step. The detachment of the boundary layer generates shear layer structures that will gradually develop, similar to those seen for a square-back Ahmed body. However, the presence of the bottom wall perturbs these vortical structures and breaks them down. Some of the separated vortical structures will move toward the wall, while others will gradually increase and roll-up away from the step. [Kostas \*et al.\* \(2002\)](#) obtained some discrete structures that correspond to classic roll-up caused by the Kelvin-Helmoltz instability; the former structures are also presented in Figure 1.7. These structures grow in size near the reattachment point where the flow becomes strongly three-dimensional. [Troutt \*et al.\* \(1984\)](#); [Furuichi & Kumada \(2002\)](#) & [Furuichi \*et al.\* \(2004\)](#) also analysed these unstable structures suggesting the existence of an organized streamwise motion and that the fluctuations in the reattachment region were related to them. The vertical oscillations of the reattaching shear layer produce a “breathing” motion of the flow, also known as flapping phenomena. The flow separation will create a recirculation region caused by a pressure difference. Due to the fluid viscosity and wall friction, the flow inside the recirculation region will form a secondary vortex at the step corner, known as eddy corner. [Hall \*et al.\* \(2003\)](#) & [Beaudoin \*et al.\* \(2004\)](#) studied the evolution of this vortex and concluded that this structure is highly three-dimensional with a short-living time.

## Mean wake

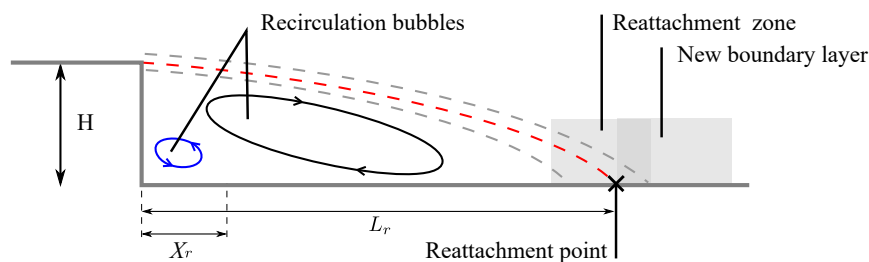


Figure 1.8 – Mean flow downstream of a backward-facing step, adapted from [Sujar \(2014\)](#).

When analysing the mean wake of the BFS, three major regions were observed ([Sujar, 2014](#)). As previously explained, the shear layer structures will impinge the wall and generate a first recirculation region, with a large clockwise bubble, clearly seen in Figure 1.8. A smaller bubble is also formed at the bottom corner and moves counter-clockwise; the distance where these two bubbles meet near the wall is here defined as the internal recirculation length  $X_r$ . The region where the developed shear layer structures impinge is known as the reattachment zone, and the exact “point” is defined as the external recirculation length  $L_r$ . However, the normal-wise oscillation of these structures will strongly move the reattachment region, about one or two steps heights  $H$ , thus  $L_r$  highly varies. The development of a new boundary starts

once the shear layer reaches the wall. The flow adjustment from a reattached flow to a new boundary layer is not an instantaneous process. The new boundary layer hardly reaches a complete equilibrium state. This is due to the organized large-scale structures in the shear layer.

Two independent parameters regarding the backward facing step and its dynamics are summarized in [Sujar \(2014\)](#): inlet flow conditions (boundary layer state and thickness, free stream turbulence) and geometric conditions (Expansion ratio ER and aspect ratio AR).

[Armaly et al. \(1983\)](#) studied the influence of laminar, transitional and turbulent regimes on the flow dynamics. They concluded that a two-dimensional inlet flow upstream of the separation generates a two-dimensional flow separation at the step and at the reattachment point. Conversely, for three-dimensional flows the reattachment is three-dimensional. More recently, they showed that the reattachment point  $L_r$  is sensitive to the inlet conditions, more specifically, the boundary layer thickness  $\delta$  step height  $H$  ratio.

[Ötügen \(1991\)](#) investigated the effect of the expansion ratio. The expansion ratio ER is the ratio between the step height and the height of the experimental facility  $H_0$ ; it is denoted as  $ER = \frac{H_0}{H_0 - H}$ . They concluded that an increase of the expansion ratio will increase the turbulence intensity and that the organized structures are influenced by this geometrical condition. [De Brederode & Bradshaw \(1972\)](#); [Barbee & Ellzey \(1989\)](#) focused on the influence of the aspect ratio on the main flow characteristics. While the expansion ratio compares the height of the system, the aspect ratio is the relation between the height of the step and its width. This parameter is linked to the two-dimensionality of the flow and is defined as  $AR = \frac{W}{H}$ , where  $W$  is the backward-facing step width. An important conclusion was obtained from these studies, an aspect ratio greater than 10 is necessary to obtain primarily two-dimensional flow in the spanwise centre of the model, avoiding the effect of the walls.

The understanding of the flow turbulence is an important problem to achieve flow control. Controlling the flow to a desired state, regardless of the type of configuration, is the main objective of aerodynamic research. Flow control not only minimizes a parameter to a desired value but also improves system performance, geometrical constraints and flow physics knowledge. The following section is devoted to answering an important question: ***How to control the flow?***

### 1.3 Flow control review

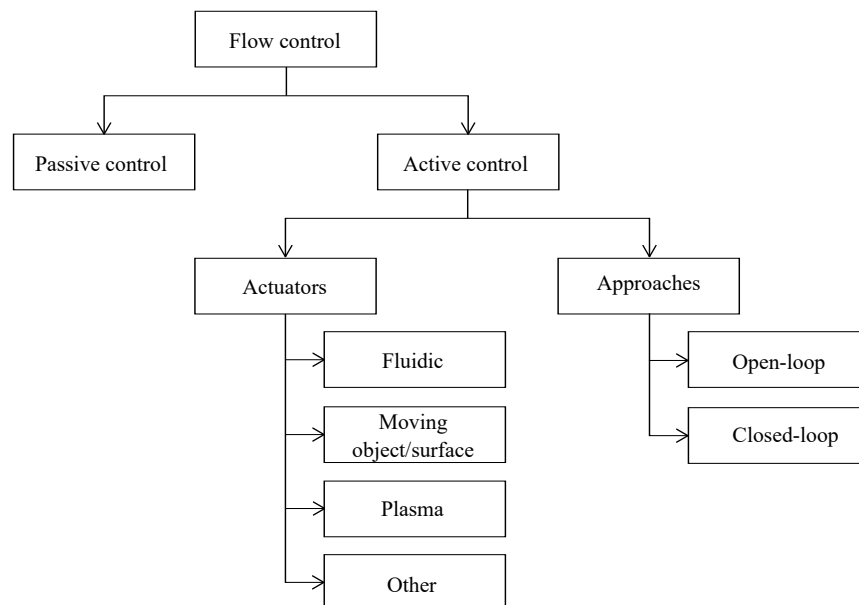


Figure 1.9 – Flow control classification ([Kral, 2000](#); [Cattafesta & Shelpak, 2011](#)).

The objective of this last part is to present the techniques in the field of flow control. The different aspects of control in fluid mechanics are reviewed, with particular emphasis on active control. Flow control has applications in many sectors, such as automobile, aircraft and ship drag, mixing in combustion chambers, and cooling in nuclear power plants. For this reason, it is a multi-disciplinary topic including fluid mechanics, control theory, and computer vision. In a broad sense, flow control includes all the techniques or processes forcing a flow to behave differently than it would have done naturally (Flatt, 1961). Some of the potential benefits of flow control include improved performance and maneuverability, affordability, increased range and payload, environmental compliance drag reduction, lift enhancement, mixing augmentation, heat transfer enhancement, and flow-induced noise suppression (Kral, 2000). This list is not exhaustive, and many applications to specific problems can be identified.

In order to control the flow, Gad-el-Hak (1996) presented three categories: the position where the control technique will be applied, the control characteristics (mean, the instant or a range of dissipative scales) and the energy power used. The latter is the most common one. Following this approach, the classification of flow control methods will be based on energy expenditure and the control loop involved. From Figure 1.9, flow control can be classified into passive or active devices. The main difference between the two is whether to use energy to carry out the control. The border between these two categories can be thin, with methods taking a bit of both, like, for example, the case of passive blowing, which injects energy at a certain point of the wake taken from the energy located elsewhere in the flow.

Passive control does not use external energy; it is usually specific geometric accessories (Hucho & Sovran, 1993). Passive techniques include geometric shaping to manipulate the pressure gradient, the use of fixed mechanical vortex generators for separation control, and placement of longitudinal grooves on a surface to reduce drag (Kral, 2000).

Active control is a solution for changing the flow by adding additional energy. To add this energy and interact with the flow, actuation devices are necessary. Cattafesta & Shelpak (2011) divided these actuators into three major groups: fluidic, moving objects and plasma actuators. Another important topic in active control involves the introduction of steady or unsteady energy inputs without consideration of the state of the flow field. Feedforward open-loop control does not take the state of the flow into consideration, while for feedback closed-loop methods, the power input to the actuator (controller) is continuously adjusted, based on some form of measurement element (sensor).

### 1.3.1 Passive control

Passive control is a simple and inexpensive solution that allows obtaining the desired performance with little geometrical change; it should be attempted before any other complex control approach. The first passive control technique that can be cited is shaping optimization. The optimal shape of a car or of an airplane is searched limiting as much as possible the detachments. However, as previously mentioned, there are heavy constraints to design vehicles. The decisions made are rarely in favour of aerodynamics, and often detrimental detachments cannot be avoided. Solutions based on a wing or spoiler type inserts are then frequently used. However, once again in commercial transportation, these devices are not frequently implemented. The most common passive devices studied for flow control will be discussed here: porous media, vortex generators, and deflectors.

#### Porous media

The control of the drag by porous media works on the principle of velocity variations due to the porous layer compared to those in a surface boundary layer in the fluid domain (Figure 1.10(a)). At the boundary

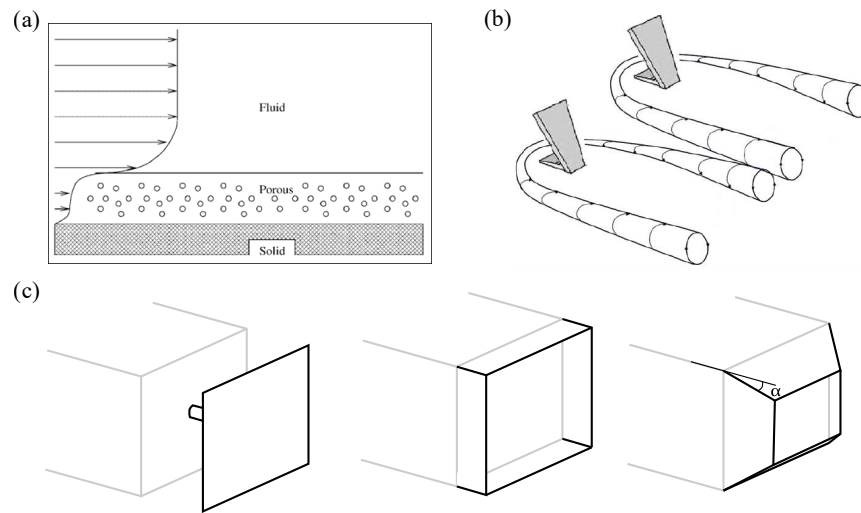


Figure 1.10 – Passive devices. (a) Porous media, (b) Vortex generators, (c) Deflectors (Joseph, 2012; Eulalie, 2014; Choi *et al.*, 2014).

between the porous medium and a fluid, the local flow velocity is not zero. Thus, a porous medium serves as a wall and makes it possible to disturb the establishment of the boundary layer in close proximity, inducing a modification of the resulting downstream flow. Instability phenomena of Kelvin Helmholtz appear and play a role in mixing and disrupting the large structures. In other words, the idea is to “trap” the low-velocity layers of the boundary layer in the thickness of the porous material. Bruneau *et al.* (2010) conducted several studies evaluating the drag gains on an Ahmed body by adding porous media to the walls. DNS-calculation for  $Re_H = 8500$  were conducted in a two-dimensional space for two different porous media configurations. The trailing variations noted were of 22 % for the porous medium located on the pavilion of the body and 25 % for the presence of porous media on the pavilion and the basement. For a simplified backward-facing step configuration, Di Cicca *et al.* (2003) modified the flow topology downstream of a step using a permeable surface, reducing the vorticity and Reynolds shear stress of the shear layer.

### Vortex generators

Vortex generators are intended to disturb the flow in the wall vicinity. These are protrusions of small size -relative to the lengths of the object of study- and arranged in a regularly spaced manner transversely to the incident reference flow. They are attached upstream of the detachment forming a pair of counter-rotating longitudinal vortices allowing momentum transfer. Figure 1.10(b) shows these vortex generators. These devices are based on the interaction between an obstacle and a boundary layer. Aider *et al.* (2010) tested these vortex generators on an Ahmed body. One advantage of this study is the ability to actively control the vortex generators, more specifically, change the inclination angle  $\alpha$ . A strong variation of the wake was obtained decreasing the drag reduction up to -11 %. As an extension of the previous study, vortex generators were mounted on a vehicle already marketed, the PSA Citroën C4. A line of vortex generators was integrated close to the top edge. The wake changes were similar to those found on Ahmed body, and the gains on the drag reduction and lift were 14 % and 100 %, respectively. The use of these small appendages has been widespread in aeronautics for decades (Hoerner , 1965). Their employment in the automotive field is much more recent and is found especially on concept cars: like the Logan Eco2 Concept Renault (Kourta & Gilliéron, 2009), or the PSA C-Airlounge (Aider *et al.*, 2009). Furthermore, they were applied to a production vehicle by Mitsubishi, where they successfully reduced the detachment and drag of the vehicle (Koike *et al.*, 2004).

## Deflectors

As previously discussed, the separation bubble and the pair of counter-rotating longitudinal vortices are the major sources of drag increase. Thus, various ways to weaken or eliminate these flow structures have been examined.

An approach considered for a backward-facing step was to perforate a cavity before the separation with the aim of changing the local inlet turbulent conditions (Isomoto & Honami, 1989). This produced a change in turbulence intensity strongly correlated with the reattachment length.

For Ahmed bodies, a vertical splitter, a plate, is placed on the wake (Figure 1.10(c)Left). Its purpose is to reduce the cross-sectional area of the wake and to increase the pellet pressure by disturbing the wake. Levallois & Gilliéron (2005) showed that the use of a vertical splitter tightens the wake close to approximately 10 % obtaining a drag reduction of 11.6 %. Gilliéron P. (2000) placed a vertical splitter near the wake, behind the Ahmed body, which interrupted the formation of the recirculation bubble and decreased the drag. The main disadvantage of this passive device is its installation on real vehicles due to its size and weight.

A more accessible configuration is done with four downstream extension plates placed around the base perimeter and parallel to the model side surfaces (Figure 1.10(c)Center). This configuration, called base cavity, has been successfully applied in different studies (Duell & George, 1993, 1999; Khalighi *et al.*, 2001, 2012; Evrard *et al.*, 2016). They reported a reduction of the wake unsteadiness and turbulence intensities.

Finally, boat tails present the same cavity but the extension plates are tilted inward with a specific angle, Figure 1.10(c)Right. This configuration deviates the flow reducing the recirculation zone thickness. Khalighi *et al.* (2012) investigated both the base cavity and truncated boat, achieving a higher drag reduction when the plates have inward angles. Gilliéron P. (2000) arranged the plates with a slanted angle of  $\alpha = 15^\circ$  on an Ahmed body and obtain a reduction of the drag of the order of 22 %. The results show that the wake section is reduced and the median longitudinal pressure distribution increases. Aider *et al.* (2010) used similar deflectors; however, they were located in 5 different locations of a  $30^\circ$  slanted Ahmed body (Top, center, bottom, slanted surface side vertical surface side). Different configurations were tested by combining different deflector positions. If all the deflectors were used, the drag coefficient was reduced 25 %. Strong variations on the lift were also obtained for this study (around 100 %). It was shown that the length and slant angle of the boat tail strongly affect drag reduction (Han *et al.*, 1992; Yi, 2007). Nayeri *et al.* (2009) studied the optimal angle on the deflector in a long truck. The optimal angle was achieved at  $12^\circ$  with a drag reduction of 8.5 %. Zühlke (2008) corroborated this result and concluded that higher deflector angles resulted in less interesting drag variations.

Passive control solutions have been also tested on the transport industry. A total gain between 4 and 6 % can be achieved on trucks via aerodynamic appendages (Seifert *et al.*, 2007). Some companies are currently adding passive appendage add-on products and reporting fuel reduction of the order of 3.5 %. The American study program has notably conducted a series of tests on highways and test tracks, where the fuel consumption sensitivity of the vehicles was calculated for different drag control solutions. The goal was to reduce aerodynamic drag by 25 %.

Passive control is, therefore, a solution that can be inexpensive for certain efficiency. In most cases, this is accompanied by a change in the appearance of the object, which is acceptable for vehicles such as trucks, non-commercial vehicles or buses. However, in the automotive industry, design constraints are a critical issue, and some solutions simply cannot be transposed, especially because of the legal standards. To propose drag reduction that does not affect the appearance of the vehicle, it is necessary to move towards the so-called active solutions. Furthermore, active devices have been developed as they can be “turned-OFF” when not needed.

### 1.3.2 Active control

Active control aims to change the flow around the object of study allowing a variation of some key parameters ( aerodynamic drag, recirculation bubble, base pressure, etc.) without altering the stylistic constraints. To achieve active control, two main topics are here discussed: the actuation devices to control the flow (type and position) and the control algorithm to drive them.

There are many types of flow control mechanisms, commonly known as actuators, and they can be categorized depending on various parameters. Cattafesta & Shelpak (2011) classified them based on their function, see Figure 1.9. The first one uses fluid injection or suction. The second one, moving objects are placed inside or on the boundary domain to induce local fluid motion, e.g., ribbon oscillators, vibrating flaps, surface-mounted diaphragms, oscillating wires, rotating surface elements, and morphing surfaces. Another class considered is plasma actuators; it delays the massive separation on the geometry which limits the wake width (Artana *et al.*, 2003; Hyun & Chun, 2003). The most common type is the fluidic actuators. They modify wake flow by local momentum injection. There are several types of injection control. Continuous and pulsed jet actuators that inject a constant flow into the wake. Synthetic jets actuators alternating the suction and blowing phases whose time integral flow is zero. The most usual type of control mechanisms will be here analysed.

Active control may be performed in a predetermined open-loop manner independent of the flow state, e.g., periodic blowing and suction. However, larger gains can be obtained if the actuation takes into consideration some sensor information of the flow state. Most literature on closed-loop flow control falls in one of three categories: stabilization of laminar flow, adaptive control of turbulence, and model-free tuning of control laws. A summary of these categories, based on the work of Brunton & Noack (2015), will also be addressed.

#### Control device and actuation parameters

An important part of flow control studies focuses on the control of the detached bulb presented downstream; this structure generates a large depression area. In the literature, the main control strategy is to decrease the pressure in the immediate vicinity of the edge, due to the acceleration of the fluid as it passes increases the pressure on the rest of the surface. Joseph (2012) presented four types of control actions: control of the detached bulb, control of longitudinal vortices, control of the recirculation region and combination of one or more of these strategies. From this information, the position of the actuator is key for optimal flow control. Sujar (2014) introduced four different positions for the actuators for a backward-facing step, based on previous theoretical studies. Even though the location of the actuators is for two-dimensional models, it can be extended to three-dimensional configurations.

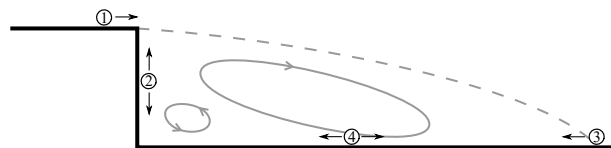


Figure 1.11 – Actuation positions based on theoretical mechanisms presented by Sujar (2014).

Figure 1.11 presents these locations; the first position ① is located upstream the separation region in order to directly interact with the boundary layer and modify the shear layer structures. Another location is at the corner of the vertical wall ② and if possible, it should induce the flow in the cross-stream direction. The idea is to add vortical structures in the shear layer. This two positions can be replicated in Ahmed bodies or even real car configurations. Another actuation placement could be near the reattachment point ③. The goal is to directly modify the reattached flow. However, the reattachment position is never constant making it hard to decide where to exactly place the actuator to have an optimal performance. Finally, the

actuator could be situated in the recirculation region ④, modifying the global effects. Moreover, other studies showed that the closer the actuation is to the detachment region (close to the edge), the more effective it is and requires fewer perturbations to reduce the detachment. For this reason, the most common location is upstream the edge or near it. Nonetheless, other positions might be considered. Once the location of the actuation is decided, one must choose which actuation mechanism will be employed.

Plasma discharge control is the first example of techniques that require energy to operate. Plasma actuators displace the air by ionizing it thanks to high electric voltages (of the order of 10 kV). This displacement of air is called “ionic wind”. In other words, electrodes are placed in the flow, applying current to strip the fluid molecules of some electrons (ionization) creating a plasma, which can then be manipulated by electromagnetic forces. An example of this actuator is presented in Figure 1.12(a). The accelerated charged particles transfer momentum to the surrounding gas adjacent to the surface via collisions with neutral particles (Cattafesta & Shelpak, 2011). Several studies have been done into reviewing plasma actuators and finding possible ways to make them viable for control applications (Kunhardt, 2000; Corke *et al.*, 2007; Moreau, 2007; Duriez *et al.*, 2014; Thomas *et al.*, 2009). The main advantage of this actuator is the creation of a body force near the wall facilitating simulation procedures, and improving the actuation efficiency and effectiveness. Even though this actuation is also easy to mount, it cannot accelerate the fluid enough for practical applications in external aerodynamic air and ground vehicles.

Another approach for active control is the use of moving walls. The idea is to re-accelerate the fluid in the lower layers of the boundary layer by moving the wall. Moving surface actuators can take various forms, but the most common are piezoelectric composite flaps or rotating cylinders. The piezoelectric flap actuator has been successfully used in several applications (Jeon & Blackwelder, 2000; Cattafesta *et al.*, 2001, 1997; Raman & Cain, 2002). Figure 1.12(b) shows an example of this actuation device. The idea is to inject vortical perturbations into the flow; the perturbation can be driven in the spanwise or streamwise direction depending on the geometry and location of the flap end (Joslin & Miller, 2009). A flapping foil was plunged in water ( $Re_H = 12700$ ) downstream of a step by Lai *et al.* (2002). This foil oscillates driven by a sinusoidal signal and this “flapping” motion reduced the reattachment length up to 70 %. Rotating cylinders can be located near the detachment zone, as, for example, in the study of Beaudoin *et al.* (2006). The rotating cylinder implanted at the edge effectively reduced the detachment at the rear of the body. This technique is also studied in aeronautics to eliminate the stall of wing profiles with a high incidence (Modi, 1997). However, these applications are only feasible in more academic approaches.

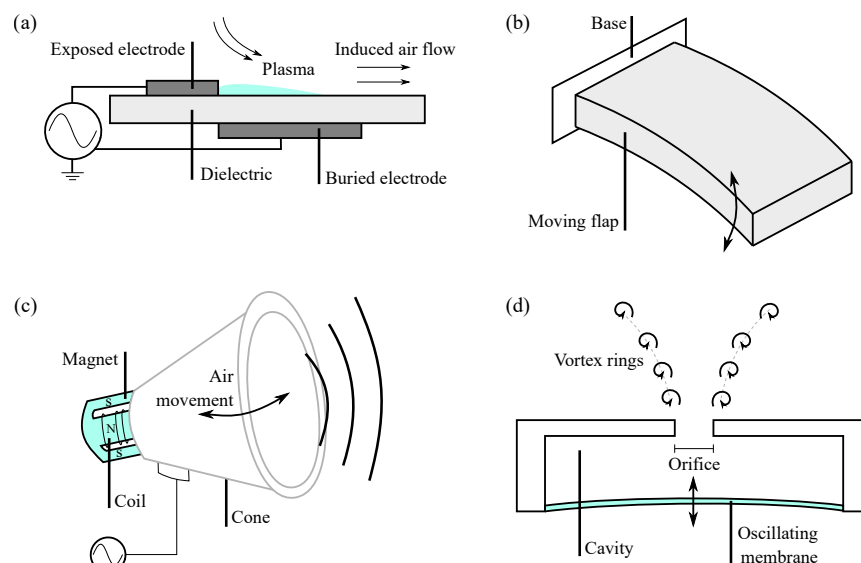


Figure 1.12 – Example of active devices. (a) Plasma actuators, (b) Moving flaps, (c) Loudspeakers, (d) Synthetic jets.

A loudspeaker provides controlled modulation of the air mass flow and directly generates sound waves

(Figure 1.12(c)). [Bhattacharjee et al. \(1986\)](#) mounted a single acoustic speaker above the step, and generated them at frequencies lower than 200 Hz. They managed to reduce the recirculation region up to 10-15 %, showing the increase in turbulence energy profiles for the optimum forced case over the unforced one. [Chun & Sung \(1996\)](#); [Chung et al. \(1999\)](#) attached a similar loudspeaker and perturbed the flow with forced Strouhal in the range of 0 to 5. More recently, [Minelli et al. \(2017\)](#) studied the effect of an embedded loudspeaker on the natural separation of the flow at the front face of a truck cabin model. The optimal actuation frequency was found close to the shear layer separation frequency, which strongly decreased the recirculation region in a forward-facing step configuration.

Synthetic blowing is a special case of pulsed blowing (explained later) with a zero net-mass flow (ZNMF), where the rest phase is replaced by a suction phase. This type of blowing does not require air supply to operate. These actuators are generated by imposing oscillations to a membrane in a cavity under the jet hole ([Milanovic & Zaman, 2005](#)). The oscillations of the membrane generate an oscillating pressure in the cavity, which creates the discharge phase when the pressure in the cavity is higher than the outside pressure, and a suction phase when the pressure in the cavity is lower than the outside pressure ([Gautier, 2014](#)). A schematic of this actuation mechanism is presented in Figure 1.12(d) [Leclerc \(2008\)](#) studied the ability to control the flow of a slanted Ahmed body using synthetic jets; their influence is measured directly on the pressure fields on the base. The gains of  $C_D$  are of the order of 10 %. The main advantage of these devices is their low-power requirements, high bandwidth, and broadband output from DC to several kilo-Hertz ranges. The maximum velocity reaches values lower than 100m/s. Furthermore, for optimal control, ZNMF must be driven near resonance frequencies leading to mechanical failure of the device ([Tesar et al., 2006](#)).

Jet control by continuous or pulsating jet is one of the most studied active techniques. The basic principle is to locally influence the flow by blowing and/or suctioning via wall openings (holes). Unlike synthetic jets devices, continuous or pulsed jets require an external fluid source. The main advantage is that they are physically invisible in design procedures. Control by jets eliminates the shape constraints presented by visible appendages. Its main disadvantage is that it requires elaborated piping and an external pressure system. Two types of jets are generally presented.

The simplest method is continuous blowing. This methodology consists in continuously add momentum, with negligible AC variations. This steady blowing can break up the structures that generate drag or move them away. Another approach is continuous suction; it allows to extract fluid from the wall. The conditions of the boundary layer low-velocity zones can be decreased or even suppressed. This methodology can trigger new vortex structures. Several experimental and numerical studies have been conducted using steady jets ([Compton & Johnston, 1992](#); [Rouméas et al., 2009](#); [Gallas et al., 2016](#)). Even though steady blowing can successfully decrease the desired objective, its energy investment is commonly higher than the energy gain from the reduction.

Pulsed-jets have been imagined to replace continuous jets as they need less energy ([Tilmann et al., 2000](#); [McManus et al., 1994](#)). A pulsed jet is an intermittent continuous blowing, alternating between ON (continuous blowing) or OFF (resting phase). It can be characterized by a square wave with an actuation frequency ( $f_a$ ) and a duty cycle (DC) that indicates the percentage of time that the jet is on in one period of time. Hence, pulsed jets have both a time-averaged or DC component and an unsteady or AC component. As the pulsed-jet is not continuously open, less mass flow rate is needed, so less energy is required. The main benefit of this actuation is the generation of intermittent structures that can be driven at a specific frequency yielding and interacting with the vortex structures generated by the detachment. A significant amount of studies have been conducted using this actuation mechanism ([Glezer et al., 2005](#); [Krentel et al., 2010](#); [Park et al., 2013](#); [Joseph et al., 2013](#); [Barros, 2015](#)). For example, a pulsed jet was used by [Pastoor et al. \(2008\)](#) to control the base pressure of a NACA geometry. The study showed a maximum base pressure variation of -30 % for a specific frequency. In this study, different possibilities of control by modification of the wake were proposed.

The hole diameter of the jet  $d$  is an important parameter because it fixes the jet velocity  $u_{\text{jet}}$ . Higher efficiency is then obtained for smaller hole diameters. Previous studies confirmed that the hole diameter must be at least  $\frac{d}{\delta} = 0.024$ , with  $\delta$  is the boundary layer thickness (Selby *et al.*, 1992; Godard & Stanislas, 2006b). However, in most cases, due to design constraints, the diameters are already predefined or fixed more or less randomly. This parameter will also depend on the amount of jet being applied. When more than one jet is used, an interaction between the jet vortical structures can be triggered. So the distance between two jets  $l_{\text{jet}}$  can promote or kill this vortex synergy (Godard & Stanislas, 2006b). If the distance is too small, strong interactions can occur decreasing the actuation efficiency. On the contrary, a large distance might completely isolate the vortical structures which leads to negligible control. Once again, Selby *et al.* (1992); Godard & Stanislas (2006b) defined an optimal distance of  $\frac{l_{\text{jet}}}{d} \approx 6$ . This distance is also limited by the actuation dimensions and mounting.

The jet can be injected with two different angles. The first one is the angle between the jet axis and the wall, while the second one  $\alpha$  corresponds to the azimuthal angle between the free-stream velocity and the projection of the jets axis on the wall (i.e., in the wall normal direction), for a better explanation see Cuvier (2012). The latter one will be discussed here.

Compton & Johnston (1992) found a higher vorticity on the dominant vortex for angles between  $45^\circ < \alpha < 90^\circ$  applied to a flat plate. These results were corroborated by Khan (1999); Khan & Johnston (2000) and detecting a high turbulent region generation when this angle range was used. For flow separation control, Selby *et al.* (1992); Rouméas *et al.* (2009); Wassen *et al.* (2010); Littlewood & Passmore (2012) vary the jet actuation with respect to the free-stream flow, obtaining similar results to those previously found, with an angle range between  $\alpha \in [45, 90]$ . The effect is similar to that created by a boat tail, so this mechanism can be considered as a variation or active fluidic boat tail.

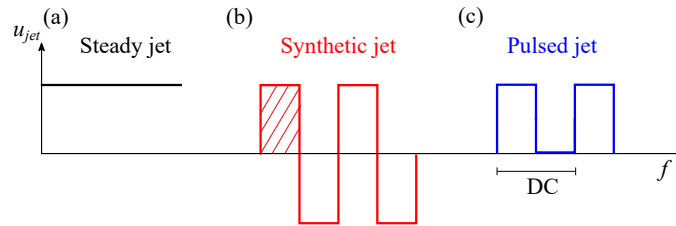


Figure 1.13 – Actuation mechanisms for the calculation of the momentum coefficient  $C_\mu$  (a) Steady blowing, (b) Synthetic jets, (c) Pulsed jets.

The jet velocity ratio  $VR = \frac{u_{\text{jet}}}{U_\infty}$  ( $U_\infty$  is the free stream velocity) is another key parameter for flow control purposes. As previously explained, it is important due to power consumption, but also it was found to govern the strength of the induced vortex (Tilmann *et al.*, 2000; Selby *et al.*, 1992; Khan, 1999). However, due to an extensive amount of actuation parameters, the authors decided to integrate a dimensionless parameter that can quantify the interaction between two flows, defined as the momentum coefficient  $C_\mu$ . This coefficient is defined as the ratio between the momentum injected into the flow and a reference momentum representative of the flow to be tested. (Amitay *et al.*, 2001) presented three different equations to calculate this value depending on the type of actuation, see Figure 1.13. For continuous blowing (Figure 1.13(a)), the momentum coefficient will be obtain directly from the velocity ratio. Synthetic jets have zero-net-mass-flux ZNMF ( $\dot{q} = 0$ ), as seen in Figure 1.13(b). For this case, the momentum coefficient is defined as follows

$$C_\mu = \frac{u_{\text{jet,max}}^2 S_{\text{jet}} DC}{U_\infty^2 S_\infty}, \quad (1.4)$$

where  $u_{\text{jet,max}}$  is the maximum jet velocity, and  $S_{\text{jet}}$  is the total area of the orifice producing the jet.  $S_\infty$  is an area chosen to be representative of the flow to be controlled. Finally, pulsed jets are Non-ZNMF devices (Figure 1.13(c)). Therefore, the momentum coefficient is presented as

$$C_\mu = \frac{\dot{q}}{\dot{q}_\infty} = \frac{u_{\text{jet}} DC}{U_\infty^2 S_\infty}. \quad (1.5)$$

Even though this dimensionless value was set, other parameters must still be defined, such as  $S_\infty$ ,  $u_{jet}$ , etc. The jet velocity can be chosen as the average speed, the effective speed or even another arbitrary speed representative of the jets. Nonetheless, important effects are present, since a certain level of  $C_\mu$  seems necessary to trigger the control action. The control effectiveness increases with an increase of the momentum coefficient until it reaches a point where the separation is completely removed due to the dominance of this momentum injection over the perturbed flow. Leclerc (2008) demonstrated that after a threshold, no further additional effect was perceived, but it also contributes to the degradation of the control performance (McCormick *et al.*, 2000).

Finally, to actively control the flow, the pulsed jet can be driven using different pressure devices, such as fast-acting solenoid valves (Bons *et al.*, 2002), high-speed rotating siren valves (Williams *et al.*, 2007), or the rotating orifice/slots (McManus, 1996). The most common ones are the solenoid valves, used in the studies of Kostas *et al.* (2007, 2009); Shaqarin (2011). This type of valves are limited to a maximum frequency of about 100 Hz at DC = 50 % (Kostas *et al.*, 2007, 2009). This low frequency could be very limiting for real applications.

Control strategies targeting a particular variable may limit the effectiveness of the control. As a result, more and more researches are considering combining control strategies to act on all the flow structures. To get an idea of the potential of a combined control strategy, it is instructive to be interested in the work of Beaudoin & Aider (2008); Bruneau *et al.* (2011); Krentel *et al.* (2010). The latter highlights the importance of the order of initiation of the control actions in the framework of combined strategies. In more real configurations, retractable fins (pseudo-active techniques) can be found on many vehicles like the Volkswagen Group, Audi TT, PSA's C-Sport lounge concept car (Aider *et al.*, 2009), among others. This concept of retractable passive devices is also taken from another study, the C-Airlounge, where a row of vortex generators, implanted at the end of the car, can be deployed or not depending on the speed (Aider *et al.*, 2009). An interesting example is the concept car Gina, developed by BMW. This car is intended to be made of elastic fabric, which can be modified by means of cylinders and other actuators (BMW, 2001). Either way, to implement these strategies, different methods are possible. The next section will attempt to draw up a brief state of the art, focusing on the different strategies for flow control.

## Control algorithms

The first control approach is the open-loop control. As already stated, open-loop means the control action is not based on any observations of the flow. The most common open-loop configurations are based on the optimum continuous blowing, and further variations in the jet velocity  $u_{jet}$ , duty cycle DC and actuation frequency  $f_a$  are applied (Tilmann *et al.*, 2000; Kostas *et al.*, 2007). The duty cycle DC corresponds to the percentage of the time fraction where the jet is active during one period, over the time of a period.

On the other hand, the actuation frequency is the periodic appearance of the excitation and can be characterized by a dimensionless frequency known as Strouhal number, previously defined in Eq.1.3,  $St_a = \frac{f_a H}{U_\infty}$ , where H represents the characteristic length of the studied body.

As detailed by Li (2017), low frequency control ( $St_a < 0.5$ ) can trigger two phenomena: flow instability enhancement due to vortex shedding amplification, or destruction of the shedding structures which attenuates the instability (Berk *et al.*, 2017; Glezer *et al.*, 2005; Barros *et al.*, 2016a; Gao *et al.*, 2016; Pastoor *et al.*, 2008). On the contrary, high-frequency forcing ( $St_a > 0.5$ ) stabilizes the wake (Vukasinovic *et al.*, 2010; Qubain, 2009; Oxlade *et al.*, 2015). Bhattacharjee *et al.* (1986) stated that the most effective Strouhal Number  $St_a$  was between 0.2 and 0.4. They forced the flow (at  $Re_H \approx 10^4$ ) with an acoustic speaker mounted at the step edge and obtained a reattachment length reduction around 15 %. This low-frequency state was corroborated by further studies. Hasan (1992) also achieve a length reduction of 18 % with a slit.

Chun & Sung (1996, 1998) used a loudspeaker and concluded that the most effective frequency actuation at  $Re_H \approx 10^3$  is around  $St_a = 0.27$  giving a length reduction of 35 %. Yoshioka *et al.* (2001a) obtained the minimum reattachment length (with similar conditions as the previous investigation but with a slit actuation) by a perturbation at  $St_a = 0.19$  with a reduction of 30 %. Also, Wengle *et al.* (2001) managed to achieve a reduction around 35 % using a forcing slot by blowing/suction at  $Re_H \approx 10^3$ . Many studies were conducted targeting length reduction; however, most of them were at low Reynolds numbers, and the actuation characteristics (type, position, velocity ratio, etc.) strongly varied from one study to another. Berk *et al.* (2017) analysed a wide range of Strouhal numbers  $St_a \in [0.21, 0.98]$  for a backward-facing step and divided them in three regimes low, medium and high, depending on their influence on the detached flow. The combination of passive devices and periodic actuation has also been developed by numerous studies, such as Chaligné *et al.* (2013); Nayeri *et al.* (2009); Schmidt *et al.* (2015); Barros *et al.* (2016b); Li (2017) Another way to analyse the forcing frequency control is by using a Strouhal number based on the vorticity thickness  $\Lambda$  of the shear layer at the point of separation (denoted  $St_\Lambda$ ). Different authors indicate a constant optimal frequency value at  $St_\Lambda \approx 0.01$ , already demonstrated by Ho & Huerre (1984); Yoshioka *et al.* (2001a,b). The principle of control is then to amplify certain structures mixing between the detached zone and the external flow.

As previously stated, closed-loop control adapts to external operating conditions. However, it needs to acquire the information through one or several sensors in order to develop an optimal control. On the one hand, its ability to monitor some system parameters enables control stability and robustness. On the other hand, its complexity may lead to actuation saturation, damaging the system and creating additional unsteadiness. Control theory deeply studies different strategies to tackle numerous problems. The list of control algorithms is limitless, and for this reason, the most common approaches for flow control will be here listed. The goal is to briefly describe them; for an exhaustive description of the control approaches, please refer to Brunton & Noack (2015). The simplest way to divide closed-loop approaches is based on the need for a model to design the control.

The first approach consists of modelling the flow from a derivation of the Navier–Stokes equations in a high-dimensional non-linear set of ordinary differential equations (white-box model) or empirical data from simulations and/or experiments (gray-box model). This approach requires a full knowledge of the flow and is impractical for industrial applications. Nevertheless, it gives a general idea of the actuator potential (Gautier, 2014)

- Linear modelling: this approach consists in a local linearisation of the Navier-Stokes equations. An extensive literature of linear system control can be found in control theory. Most of the control solutions are done in simulations. This linearisation can be quite complex, increasing computational time; for this reason, reduced order models (ROMs) can be applied. Many authors have used this strategy in simulations and experiments (Liepmann & Nosenchuck, 1982; Bagheri *et al.*, 2009; Roussopoulos, 1993; Rowley *et al.*, 2006; Samimy *et al.*, 2007; Belson *et al.*, 2013). Even though many powerful tools are presented in control theory to obtain the linearisation of the equations, most of the flows studied in real applications are intrinsically non-linear.
- Non-linear modelling: a less common approach, due to higher complexity procedures, is non-linear modelling. In this work, a non-linear approach will be presented, already applied by Luchtenburg (2010) and commonly known as sliding mode control. Without loss of generality, the control law switches from one smooth condition to another. This approach will be further explained in §2.3.1. The advantage of this particular method is its robustness; however, the rapid switch from one condition to another might quickly wear out the actuators.

Model-free approaches, also known as black-box models, are based on input-output data. They are faster to develop but do not understand the flow physics.

- Adaptive control: this approach searches for a control actuation by a slow feedback of a working open-loop control in order to take the system to a desired state. At each instant, the system is fixed through measurements.
  - PID: The proportional integral derivative (PID) continuously calculates an error value as the difference between the desired set-point and a measured variable and applies a correction based on proportional, integral, and derivative terms. This approach was used by [Garwon \*et al.\* \(2003\)](#); [Patnaik & Wei \(2002\)](#) to control separated flows. PID control is also used in conjunction with other non-linear designs to control the spanwise recirculation length downstream a step in [Henning & King \(2007\)](#). This approach was also in other experimental configurations ([Kerstens \*et al.\*, 2011](#); [Zhang \*et al.\*, 2004](#))
  - Extremum seeking: While PID leads the variable to the desired point, extremum-seeking algorithms are used to bring a measured variable to an extremum. This control can be applied to any system with an extremum. [Ariyur & Krstic \(2004\)](#) give a further understanding of this method. The only constraint of this approach is the need of a low-frequency component. [Beaudoin \*et al.\* \(2006\)](#); [Beaudoin & Aider \(2008\)](#) applied this method to a bluff body and the control was able to minimize the drag. Extremum-seeking is harder to implement, and as model-free control, it takes time to adapt to flow conditions.
- MLC: Machine learning, and in particular evolutionary algorithms, can help to achieve the control goal by mimicking the learning process of nature ([Li, 2017](#)). This approach looks for optimal laws with respect to a user-defined cost function. Machine learning control will be also applied in the configuration presented in this work and will be defined in §2.3.2. Nonetheless, successful stories of flow control using this approach are already available ([Li, 2017](#); [Gautier, 2014](#); [Fan \*et al.\*, 2017](#); [Wu \*et al.\*, 2018](#); [Raibaudo \*et al.\*, 2017](#); [Cornejo, 2017](#))

## 1.4 Summary

In this context, *the present work aims to pre-evaluate flow control parameters to reduce the drag in a real vehicle.*

- An information exchange with different experts (from both mechanic and automatic research) is done, on the one hand, to understand the possibilities and the limits of closed-loop commands (from automation to mechanic), and on the other hand, to understand the dominant physical phenomena and their time scales (from mechanic to automation).
- Two different actuation mechanisms (The Murata micro-blower and pulsed jets) are characterized and compared to defined their experimental strength and limitations. Murata micro-blower is able to be driven by any variable **DC**. It energizes the boundary layer to directly perturb the vortex structures formed in the shear layer. The air-knife is a type of pulsed jet actuators, able to generate ON-OFF signals (pulsed jet); it has a rounded surface, adjacent to the slit exit, which could be considered as an active boat tail (Coanda effect) for drag reduction.
- Different open- and closed-loop control strategies are examined, such as continuous blowing, periodic forcing, sliding mode control (SMC) and machine learning control (MLC). Sliding mode control is a robust closed-loop algorithm to track, reach and maintain a predefined set-point; this approach has on-line adaptivity in changing conditions. Machine learning control is a model-free control to learn an effective control law that is judged and optimized with respect to a problem-specific cost/objective function. A hybrid between MLC and SMC may provide adaptive control exploiting the best non-linear actuation mechanisms.

- Finally, all these parameters are brought together and tested in real experimental applications: backward-facing step and square-back Ahmed body. These configurations are representative of the mean wake and shear-layer structures related to control of real cars.

The following chapters will cover the topics bellow. A first chapter is dedicated to present the LAMIH facilities, the measurement techniques, and the mathematical tools. It contains two important topics; it presents the characterisation and comparison of two actuation mechanisms, and it briefly defines the most complex control algorithms: sliding mode control and machine learning control. The next two chapters will discuss the main experimental results obtained from the backward-facing step and the Ahmed body, chapters 3 and 4 respectively. The natural flow will be initially analysed, using post-processing techniques such as proper orthogonal decomposition POD, and linear and quadratic stochastic estimations LSE and QSE. The main actuation mechanisms, including actuator placement and control algorithms, are then studied, and their results are further analysed. The first results in a real car Twingo GT are shortly introduced. The results obtained are summarized in a brief conclusion leading to general perspectives. The most interesting parallel works are also proposed, such as a collaborative thesis with Onera to study the interaction between the actuator and the boundary layer, a post-processing technique -called MAO (Metric for attractor overlap)- to facilitate an unsupervised fluid dynamics data comparison.



# Investigation tools, actuation devices and control design

*Some of the results presented in the chapter, more specifically the Murata micro-blower characterization, are published in [Chovet et al. \(2016\)](#). Three main topics are presented. A detailed description of the facility tools used in the study is presented in §2.1, such as the big wind tunnel, the measurement techniques, and the mathematical tools for post-processing. A further study of the actuator devices (Air-knives and Murata micro-blowers), employed for flow control, is proposed in §2.2. Finally, but not least important, two active flow control strategies will be described in §2.3. A summary of each section will be presented at the end of the chapter.*

## Contents

---

2.1	Apparatus . . . . .	32
2.1.1	General experimental setup and measurement tools . . . . .	32
2.1.2	Modal and stochastic analysis tools . . . . .	35
2.2	Actuator characterisation . . . . .	38
2.2.1	Air-knife . . . . .	38
2.2.2	Murata micro-blower . . . . .	42
2.3	Control design . . . . .	47
2.3.1	Sliding mode control (SMC) . . . . .	47
2.3.2	Machine learning control (MLC) . . . . .	52
2.4	Summary . . . . .	55

---

## 2.1 Apparatus

This section will revise the measurement techniques used in the present work to characterize and control the flow. The experimental wind tunnel facility and the measurement (pressure sensor, hot-wire and velocity) techniques are described in §2.1.1, followed by the control devices in §2.1.1. A further analysis of the numerical tools to reconstruct and predict the flow behaviour is presented in §2.1.1.

### 2.1.1 General experimental setup and measurement tools

#### Closed-loop LAMIH wind tunnel

The experimental tests were carried out in the subsonic wind tunnel of the LAMIH laboratory. The tunnel has a 4.8 m diameter fan that develops a power of 200 kW capable of inducing a flow of 60 m/s in the test section. The produced flow circulates in a closed loop tunnel, passing through the  $5 \times 5 \text{ m}^2$  section return channel. The flow is guided by flaps positioned at the corners of the tunnel; each of the flaps is equipped with a blade grid in order to limit the induced load losses. A 6.25 contraction ratio section leads the flow to the test vein. The test section is 10 m long with a straight area of  $H_0 \times W_0 = 2 \times 2 \text{ m}^2$  and is made of transparent polycarbonate (plexiglass) panels to allow optical visualizations. The wind tunnel is presented in Figure 2.1. Designed for transportation-related applications, the tunnel has a working speed range from 0.5 to 60 m/s. The average turbulence intensity at the inlet of the test section is 0.6 %. The test section is also equipped with a 6-component aerodynamic balance to recover aerodynamic forces.

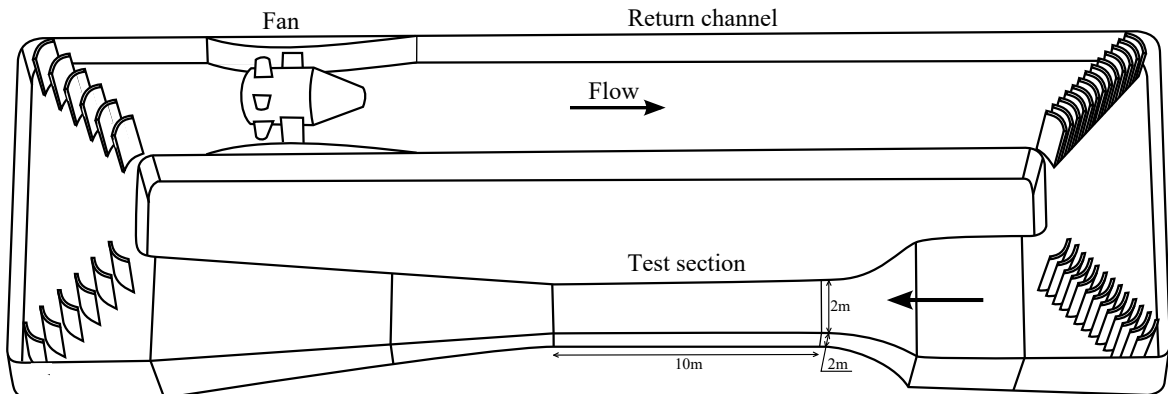


Figure 2.1 – Sketch of the semi-industrial closed-loop wind tunnel at LAMIH.

#### Pressure distribution

Wall-pressure measurements were performed on all the configurations presented in this work. The objective of these measurements is to identify the in-stationary mechanisms that are developed in the shear layer and have a strong influence on the parietal pressure fluctuations. The average pressure is registered at each point using a pressured tap and an electric manometer DP-CALC-5825 manufactured by TSI. For this type of measurement, the integration time was set at 30 seconds. A piezo-resistive Kulite XCQ-062 sensor was also used to obtain unsteady pressure values (see Figure 2.2(a)); this sensor is able to record pressure variations up to 70 kPa. The calibration of the probes was previously done by the manufacturer and it is integrated into the software for a direct acquisition. These acquisition bays have a self-calibration routine using the curves supplied by the sensor manufacturer. The sampling frequency  $f_s$  was set at 10 kHz in order to capture all the physical phenomena involved. An 8 order Bessel type anti-aliasing filter and a cut-off frequency 3 kHz were used to respect the sampling theorem (Jerry, 1977). The acquisition system has an analogue/digital converter for transmitting the acquired signals to a computer for further processing.

In order to attenuate the measurement noise, a third-order Butterworth-type low-pass filter was applied to all the signals after an acquisition. Since the frequencies of the unstable phenomena vary with the Reynolds number, the cut-off frequency was adapted as a function of the external velocity of the flow.

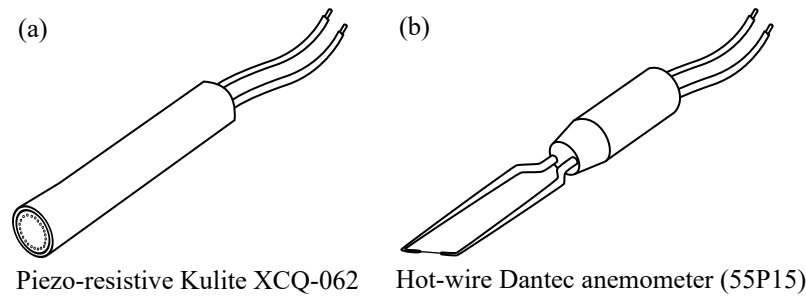


Figure 2.2 – Sensors used for local measurements: (a) Sketch of a piezo-resistive Kulite XCQ-062 sensor, (b) Sketch of a hot-wire Dantec anemometer.

### Intrusive velocity sensor (Hot-wire)

Another common sensor used for aerodynamic analysis, more specifically for local velocity, is the hot-wire anemometer. This classic intrusive technique allows the measurement of the velocity of a fluid at a specific point. The main advantage of this technique is its excellent temporal resolution, which makes it a good choice to study turbulent flows. The main limitations are its fragility and one velocity component measurement; however, there are other hot-wire anemometers that are able to calculate two velocity components. The usual hot-wire anemometer consists of a thin wire about 1 mm long with 1 to 5  $\mu\text{m}$  in diameter stretched between two pins (Figure 2.2(b)). The principle of hot-wire anemometry consists of measuring the power transferred from a Joule-effect thin wire cooled by the passage of the fluid. A previous calibration of the wire must be done in order to obtain the power/velocity ratio. The anemometer used in the present study is a hot-wire Dantec with a wire type 55P15.

### Spatial velocity field estimation

Particle image velocimetry, commonly known as PIV, is a technique of optical diagnosis of aerodynamic fields, the theoretical details of which can be found in Adrian (1991). The method consists in determining the displacement of a cloud of particles between two successive instants. Knowing locally the distance travelled by a group of particles during the time separating the two moments, it is possible to go back to the components of the velocity vector at a given point of space. This method requires the use of tracers sufficiently fine to follow the trajectory of the fluid particles without altering the flow. Olive oil particles, with 1  $\mu\text{m}$  diameter, were generated with a jet atomizer upstream of the stagnation chamber and seeded in the channel. The particle field is then illuminated by a laser sheet that allows it to be detected by a camera, the optical axis of which is perpendicular to the laser plane. The acquisition of the images requires a perfect synchronization between the laser and the cameras. Figure 2.3 shows a schematic diagram of the method. In this work, a two-dimensional and two-component (2D2C) PIV method was used to recover the aerodynamic fields. The PIV system, manufactured by TSI, is composed of a Nd:YAG laser system generating a wavelength of 532 nm with a laser thickness of 0.4 mm. The repetition rate frequency was set to  $\approx 7$  Hz. The laser is furnished with two Cavities (A and B) with a time delay between two laser pulses (Q-Switch) of  $\Delta t = 5 \mu\text{s}$ . The ratio between the thickness of the sheet and the width of the model is less than 1 %, which allows considering the measurement as two-dimensional. The laser plane is normally positioned in the central plane of the model. The time between two successive images, necessary for the determination of the vector fields, was defined taking into account the speed of the external flow. This  $\Delta t$  duration is set at 50, 20 or 10  $\mu\text{s}$  for 10, 20 and 30 m/s, respectively. The laser is used to illuminate olive

oil particles of 1  $\mu\text{m}$  diameter dispersed in the test vein by an atomizer supplied by TSI. The images were captured using two  $2000 \times 2000$  pixels resolution video cameras with an objective of 50 mm.

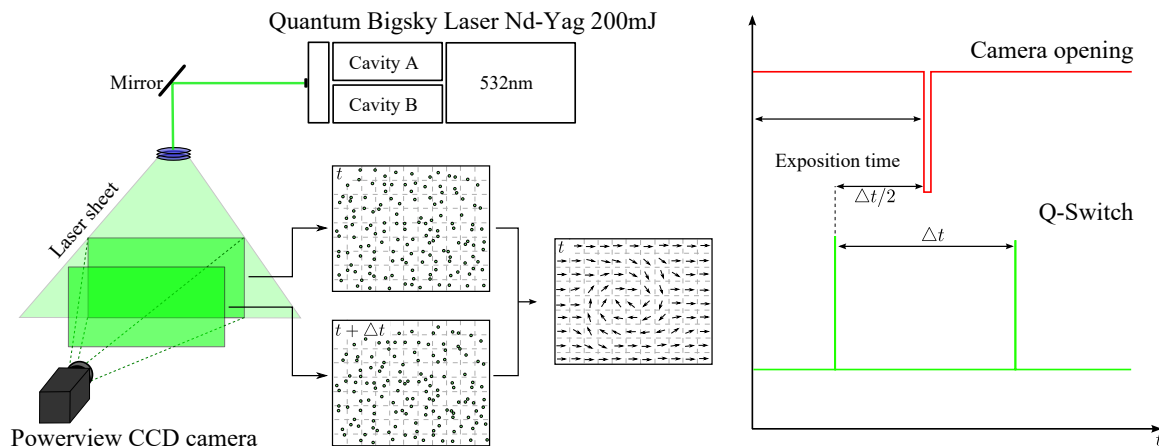


Figure 2.3 – Schematic diagram of measurements by PIV.

The vector fields are reconstructed using a direct correlation algorithm applied to a  $16 \times 16$  pixels interpolation grid. The details of image correlation methods for experimental fluid mechanics can be found in [Kean & Adrian \(1992\)](#). In order to reduce the calculation time, masks are applied to the images in order to correlate only the areas of interest. The sizes and resolutions of the fields obtained after spatial calibration will depend on the configuration studied and will be further reported for each case. For every test, 2000 double-frame pictures are registered to assure the statistical convergence of the velocity fields.

## Control devices

Real-time processing was performed with three different control devices, dSPACE, Arduino, and DEWESoft.

The dSPACE system is a hardware/software platform for electronic control units and mechatronic controls. The hardware system used is a MicroAutoBox that is able to perform fast function prototyping, see [Figure 2.4\(b\)](#). A combination of two software programs was used to enable a real-time communication for closed-loop control. ControlDesk is the dSPACE experiment software for the electronic control unit (ECU) development. It performs all the necessary tasks and gives a single working environment, from the start of experimentation to the end. Real-Time Interface (RTI) is an implementation software, compatible with MatLab, for running models on dSPACE hardware. The main advantage of this platform is its unique combination of high performance, comprehensive automotive I/O, and its extremely compact and robust design ([dSPACE Co., 2002](#)).

Arduino is a single-board micro-controller for building digital devices and interactive objects that can sense and control objects in the physical world ([Arduino Co., 2008](#)). The boards are available commercially in pre-assembled form ([Figure 2.4\(b\)](#)), or as do-it-yourself (DIY) kits. The openness and ease-of-use of the board prompted the use of this micro-controller for flow control application. The board is equipped with sets of digital and analogue input/output (I/O) pins that may be interfaced to various expansion boards (shields) and other circuits, sensors, etc. The boards feature serial communications interfaces, including Universal Serial Bus (USB) on some models, which are also used for loading programs from personal computers. The micro-controllers are typically programmed using a dialect of features from the programming languages C and C++. However, Arduino provides an integrated development environment (IDE) based on the processing language project. The board used in this study is an Arduino MEGA 2560 - Rev3 (with the following dimensions: 11 cm  $\times$  6 cm  $\times$  2 cm).

DEWESoft is a best in class provider of data measurement devices. DEWESoft hardware, called SIRIUS line, measures any kind of signal, anywhere, in any environment with flexibility, precision and ease of

use, shown in Figure 2.4(c). SIRIUS offers endless configuration possibilities: from 4-channel 200 KS/ch distributed USB solutions to high speed 128 channel standalone solutions with internal PC and display. They also provide an intuitive user interface that integrates seamlessly with all hardware, creating an optimal measurement experience for any application. They construct the hardware and software around the outcome of delivering the fastest, most efficient, most intuitive user experience possible (DEWESoft Co., 2000). The device used for this work is of the type STG+.



Figure 2.4 – Control devices. (a) dSPACE MicroAutoBox, (b) Arudino MEGA 250 3V, (c) DEWESoft Hardware system.

## 2.1.2 Modal and stochastic analysis tools

### Proper orthogonal decomposition

Proper orthogonal decomposition POD, also called principal component analysis or *Karhunen-Loeve* analysis, is a data analysis method that identifies the dominant structures of a set of data (Lumley, 1967). POD is a simple way to build basic functions based on their energy content. Presenting an elegant mathematical formalism, this analysis technique proves to be a powerful means of analysing data from numerical simulations or experiments. The POD allows approximating a high-dimensional system to a significantly smaller one built on the basis of optimum eigenfunctions, in the energetic sense. These basic functions enables the spatial identification of the most energetic and recurring phenomena as well as their overall temporal evolutions. It also allows extracting the morphology and the dynamics of these coherent structures from a two-point correlation. The POD modes are obtained by looking for the  $\Phi(\mathbf{x})$  function that has the largest mean squared projection of  $\mathbf{u}(\mathbf{x}, t)$ . This maximization problem leads to the well-known *Fredholm* problem, where the kernel is a two-point correlation tensor  $R_{ij}(\mathbf{x}, \mathbf{x}') = \langle u_i(\mathbf{x}, t) u_j(\mathbf{x}', t) \rangle$ , and where the chevrons are the time average operator. The integral equation has a discrete set of solutions  $\Phi_n(\mathbf{x})$  and  $\lambda_n$  where  $n$  is the decay mode order orthogonal. The eigenfunction is orthonormal, e.g.  $\{\Phi_n(\mathbf{x}), \Phi_p(\mathbf{x})\} = \delta_{np}$ . Then the fluctuating velocity field can be decomposed as follows:

$$u_i(\mathbf{x}, t) = \sum_{n=1}^{n_m} a_n(t) \Phi_n^{(i)}(\mathbf{x}), \quad i = 1, \dots, n_c, \quad (2.1)$$

where  $n_m$  is the total number of modes. The time coefficients  $a_n(t) = \{\mathbf{u}(\mathbf{x}, t), \Phi_n(\mathbf{x})\}$  are not correlated  $\langle a_n a_p \rangle = \lambda_n \delta_{np}$ . For time-resolved PIV measurements, 2000 instantaneous fields are captured, composed of many dependent spatial measurement points. For all the cases, the number of spatial samples is greater than the number of temporal samples. For this reason, the so-called snapshot method (Sirovich, 2007) is used to determine the eigen-modes.

### Stochastic estimation

Stochastic estimation is a means of approximating a conditional average using “unconditional” information. As shown by Naguib *et al.* (2001) & Picard & Delville (2000), the conditional mean of fluctuating velocity  $u_i(\mathbf{x}, t)$  can be formulated using known wall-pressure information (unconditional)  $\mathbf{p}$  to give an estimated velocity  $\tilde{u}_i(\mathbf{x}, t)$ :

$$\tilde{u}_i(\mathbf{x}, t) = \langle u_i(\mathbf{x}, t) | p_j(t) \rangle \quad i = 1, \dots, n_c. \quad (2.2)$$

The conditional mean can be estimated by a Taylor series as indicated by Guezennec (1989):

$$\tilde{u}_i(\mathbf{x}, t) \approx \alpha_{ij}(\mathbf{x}) \cdot p_j(t) + \beta_{ijkl}(\mathbf{x}) p_j(t) \cdot p_k(t) + \dots, \quad (2.3)$$

where the summation over repeated indices is used. When only linear terms are retained, the procedure is known as linear stochastic estimation (Naguib *et al.*, 2001). On the other hand, if the terms of quadratic pressure are preserved, it is called quadratic stochastic estimation (Murray & Ukeiley, 2003).

For the linear stochastic estimation (hereinafter referred as LSE), only the linear coefficients  $\alpha_{ij}$  are retained. These time-independent coefficients are computed by minimizing the mean squared error,

$$e_i(\mathbf{x}) = \langle (\tilde{u}_i(\mathbf{x}, t) - u_i(\mathbf{x}, t))^2 \rangle. \quad (2.4)$$

These equations can be written at the estimation instants PIV using the set of  $m$  values  $u_i(\mathbf{x}, t_k)$ ,

$$e_i(\mathbf{x}) = \frac{1}{m} \sum_{k=1}^m (\alpha_{ij}(\mathbf{x}) p_j(t_k) - u_i(\mathbf{x}, t_k))^2. \quad (2.5)$$

The least squares minimization problem can be written symbolically in matrix form and consists of solving  $\mathbf{c}^{\text{opt}} = \text{argmin}_{\mathbf{c}} (\|\mathbf{Q}\mathbf{c} - \mathbf{f}\|^2)$  with,

$$\mathbf{Q} = \begin{bmatrix} | & & | & & | \\ p_1(t_k) & \dots & p_j(t_k) & \dots & p_{n_s}(t_k) \\ | & & | & & | \end{bmatrix},$$

$$\mathbf{c} = \begin{bmatrix} \alpha_{i|1}(\mathbf{x}) \\ \vdots \\ \alpha_{i|j}(\mathbf{x}) \\ \vdots \\ \alpha_{i|n_s}(\mathbf{x}) \end{bmatrix}, \text{ and}$$

$$\mathbf{f} = \begin{bmatrix} | \\ u_i(\mathbf{x}, t_k) \\ | \end{bmatrix}$$

The ordinary least squares minimization solution of this overdetermined system is  $\mathbf{c} = (\mathbf{Q}^T \mathbf{Q})^{-1} \mathbf{Q}^T \mathbf{f}$ , where  $\mathbf{Q}^T \mathbf{Q}$  is the square matrix of second-order pressure correlations and  $\mathbf{Q}^T \mathbf{f}$  contains spatial coordinates two-point pressure-velocity correlation:

$$\mathbf{Q}^T \mathbf{f} = \begin{bmatrix} \vdots \\ \langle u_i(\mathbf{x}, t) p_j(t) \rangle \\ \vdots \end{bmatrix}, \text{ and}$$

$$\mathbf{Q}^T \mathbf{Q} = \begin{bmatrix} \langle p_1(t) p_1(t) \rangle & \dots & \langle p_1(t) p_{n_s}(t) \rangle \\ \vdots & & \vdots \\ \langle p_{n_s}(t) p_1(t) \rangle & \dots & \langle p_{n_s}(t) p_{n_s}(t) \rangle \end{bmatrix}.$$

It should be noted that since the experimental data considered contains noise, the  $\mathbf{Q}^T \mathbf{Q}$  matrix may be singular. This is why a regularization of Tikhonov is put in place to improve the quality of the estimate. The method is to solve the following new minimization problem,

$$\mathbf{c}_\lambda = \min(\|\mathbf{Q}\mathbf{c} - \mathbf{f}\|^2 + \lambda^2 \|\mathbf{c}\|), \quad (2.6)$$

leading to the following ‘‘regularized’’ solution  $\mathbf{c}_\lambda = (\mathbf{Q}^T \mathbf{Q} + \lambda^2 \mathbf{I})^{-1} \mathbf{Q}^T \mathbf{f}$ . Using the singular value decomposi-

tion of  $\mathbf{Q}^T \mathbf{Q} = \mathbf{U} \mathbf{S} \mathbf{V}^T$ , the regularized solution can be written in a simple way,

$$\mathbf{c}_\lambda = \sum_j \left( \frac{\sigma_j^2}{\sigma_j^2 + \lambda^2} \right) \frac{\mathbf{u}_j^T \mathbf{f}}{\sigma_j} \mathbf{v}_j, \quad (2.7)$$

where  $\mathbf{u}$  are column vectors of the matrix  $\mathbf{U}$  (same for  $\mathbf{v}$ ) and  $\mathbf{S}$  is the matrix diagonal of the singular values  $\sigma_j$  of  $\mathbf{Q}^T \mathbf{Q}$ .

In the case of quadratic stochastic estimation QSE, the linear and quadratic coefficients  $\alpha_{ij}$  and  $\beta_{ijk}$  are preserved. For the sake of brevity, in the following formulation, time dependence will be neglected. The stochastic estimation coefficients are determined by minimizing the mean squared error of the estimate, as previously explained, which requires solving a set of linear equations (Naguib *et al.*, 2001),

$$\begin{aligned} \alpha_{ij} \langle p_j p_q \rangle + \beta_{ijr} \langle p_j p_r p_q \rangle &= \langle u_i p_q \rangle, \\ \alpha_{ij} \langle p_j p_q p_k \rangle + \beta_{ijr} \langle p_j p_r p_q p_k \rangle &= \langle u_i p_q p_k \rangle. \end{aligned} \quad (2.8)$$

This set of equations can also be symbolically written in a matrix form,  $\mathbf{A}[\mathbf{B}] = \mathbf{C}$ , where  $\mathbf{A}$  represents the unknown coefficients,  $[\mathbf{B}]$  is the matrix of pressure correlations and  $\mathbf{C}$  contains the velocity/pressure correlations.

The calculation algorithms for LSE and QSE are implemented using Matlab and the LU factorization is used to solve the matrix system. In this work, the same approach is adopted to obtain an estimate of the time-resolved velocity fields from time-resolved PIV measurements and time-resolved pressure point measurements.

### Application to present work

The proper Orthogonal Decomposition POD estimation approach is used in the present study in order to analyse the dynamical aspect of the flow fields. Taking into account Lumley (1967) proposition, proper orthogonal decomposition was used as an unbiased technique for studying coherent structures in turbulent flows. The inner product  $(\bar{\mathbf{u}}, \bar{\mathbf{v}})$  and the norm  $\|\bar{\mathbf{u}}\| = (\bar{\mathbf{u}}, \bar{\mathbf{u}})^{1/2}$  are considered as:

$$(\bar{\mathbf{u}}, \bar{\mathbf{v}}) = \sum_{i=1}^2 \int_{\Omega} u_i(\bar{\mathbf{x}}) v_i(\bar{\mathbf{x}}) d\bar{\mathbf{x}}, \quad (2.9)$$

where  $u_i(\bar{\mathbf{x}}, t)$  the  $i^{\text{th}}$  component of the fluctuating velocity field  $\bar{\mathbf{u}}(\bar{\mathbf{x}}, t)$  at point  $\mathbf{x}$  of the spatio-temporal domain  $\Omega$ . The POD modes are obtained by searching the function  $\Phi(\bar{\mathbf{x}})$  that has the largest mean square projection of  $\bar{\mathbf{u}}(\bar{\mathbf{x}}, t)$ .

To resolve the entire flow field, linear and quadratic stochastic estimations are first used to estimate velocity information using a conditional averaging scheme applied to the measured locations (Tinney *et al.*, 2008). In general,  $\bar{\mathbf{u}}(\bar{\mathbf{x}}, t)$  indicates the velocity fluctuation, since the mean flow is known and does not need to be estimated. Since the  $n$  temporal POD coefficients,  $a_n(t_s)$ , are obtained through the integration over all space, they contain the global knowledge of the flow field. However, they are also a function of the discrete time step,  $t_s$ , of the measured velocity PIV data, which are generally not time-resolved. To temporally resolve these coefficients, the stochastic estimation techniques have been frequently applied together with the POD (Tinney *et al.*, 2008; Lasagna *et al.*, 2013; Podvin *et al.*, 2018). The MLSE complementary technique allows the estimation of the temporal dependence of the first POD coefficients, providing a temporally resolved low dimensional estimate of the flow state. This technique has also been used in order to define efficient closed-loop feedback control (Pinier *et al.*, 2007). One advantage of the approach is that POD coefficients are scalar quantities which are independent of the spatial location. In the present study, MLSE/MQSE complementary techniques, see (Taylor & Glauser, 2004; Murray & Ukeiley, 2007; Baars & Tinney, 2014), were used to obtain an estimation of the full flow field dynamics from the classical PIV

and the unsteady pressure measurements to investigate the low frequency flapping contributions. The MLSE/MQSE complementary approaches consist of estimating the temporal POD coefficients of velocity fields by a conditional average associated with the  $j$  wall-pressure events denoted by  $p_j(t)$ . This can be written as:

$$\tilde{a}_n(t) = \langle a_n(t_s) | p_j(t) \rangle \quad n = 1, \dots, n_r, \quad (2.10)$$

where the subscript  $n$  denotes the POD mode, from the first to the  $n_r$  mode retained for the low order estimation. The new time-resolved estimated MQSE coefficients can be expressed as a power series expansion truncated at the quadratic terms as follows,

$$\tilde{a}_n(t) = \sum_{j=1}^{n_s} b_{nj} p_j(t) + \sum_{j=1}^{n_s} \sum_{k=1}^{n_s} c_{nj,k} p_j(t) p_k(t), \quad (2.11)$$

where  $p_j(t)$  is the value of the fluctuating pressure probe  $p(\bar{x}_j, t)$  at point  $\bar{x}_j$  of the boundary spatio-temporal domain  $\partial\Omega$ . While in MLSE-POD, it is truncated at the linear term. As an example, the linear term  $b_{nj}$  is obtained by solving the mean square error minimization leading to the linear system of  $n_s$  equations:

$$\sum_{j=1}^{n_s} b_{nj} \langle p_j(t_s) p_k(t_s) \rangle = \langle a_n(t_s) p_k(t_s) \rangle, \quad (2.12)$$

Once the time-resolved estimated MQSE coefficients have been determined, they can then be projected onto the eigenfunctions (obtained from the discretely measured flow field) to reconstruct the following time-resolved estimate of the flow field,

$$\tilde{\mathbf{u}}(\bar{\mathbf{x}}, t) = \sum_{n=1}^{n_r} \tilde{a}_n(t) \Phi^{(n)}(\bar{\mathbf{x}}). \quad (2.13)$$

This estimate of the velocity field was used to estimate power spectra as previously seen in the literature (Tinney *et al.*, 2008).

Stochastic analysis tools will be used to determine the link between wall-pressure fluctuations and aerodynamic field motions. As stated before, the purpose of these methods will be to reconstruct the dynamic behaviour of the velocity field that is strongly correlated with fluctuation fields. These methods require a synchronization of both acquisition systems (velocity fields and instantaneous pressures). To accomplish this, the triggering Q-Switch signal of one of the two cavities of the Nd:YAG laser is recovered on the acquisition bays of the pressure signals with the same sampling frequency as the instantaneous pressures. Since the signals recovered by the arrays are synchronized with the same clock, the data coming from the velocity fields can then be correlated to the pressure signals by recovering the indices corresponding to the peaks on the Q-Switch signal.

## 2.2 Actuator characterisation

In this section, two different actuation devices are compared for flow control: Air-knife and Murata micro-blower. The dynamical performance of both devices, working in pulsed mode, are experimentally investigated to deduce their abilities and limitations. The device design and its dynamical characterization are also addressed.

### 2.2.1 Air-knife

Cattafesta & Shelpak (2011) defined a pulsed jet as an unsteady jet that is ideally either ON or OFF and can be characterized by a square wave with a duty cycle that indicates the percentage of time that the jet is ON. Air-knives are an example of this type of actuator. They were initially used in the manufacturing

industry as devices to contain or remove free-standing materials (liquids or solids) from a surface. However, they have been recently implemented in flow control (Bons *et al.*, 2002; Joseph, 2012).

## Design and principle

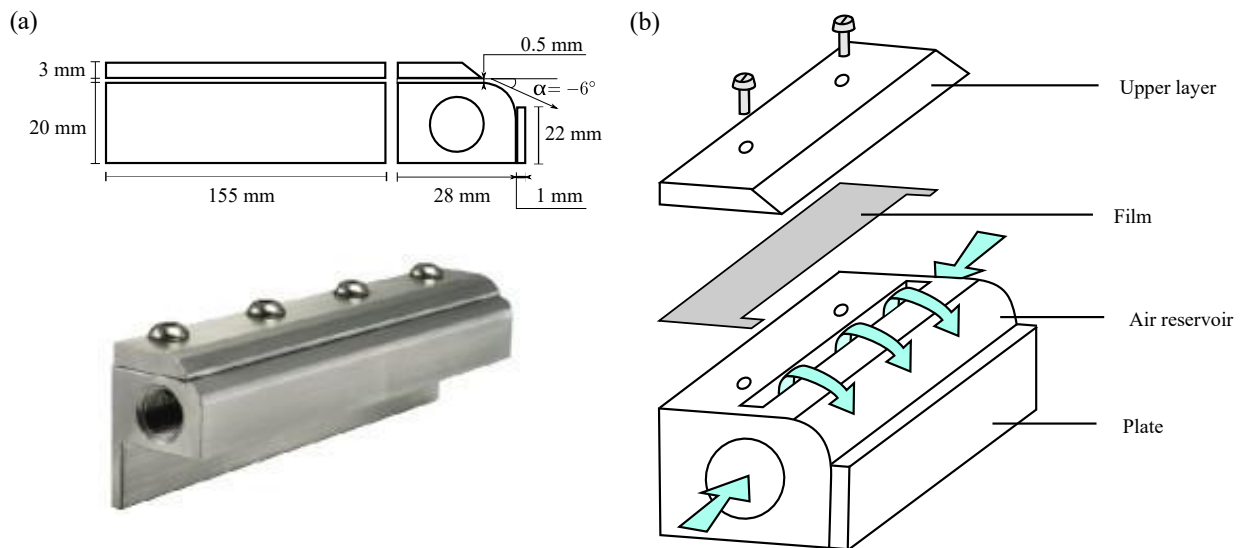


Figure 2.5 – General characteristics of the air-knife. (a) Dimensions, (b) Air slit generation principle.

The actuator is equipped with a slot, commonly called air-knife and consists of a high-intensity uniform sheet of laminar airflow. The air is blasted through the air knife slots via an air compressor, to deliver a predetermined velocity. The slot width is  $d = 0.5$  mm with an actuation length of 155 mm and a total height of 23 mm, see Figure 2.5(a). The air-knife uses a Coanda profile for blowing, where the jet of fluid will follow an adjacent flat or curved surface to entrain fluid from the surroundings (Coanda, 1934); Figure 2.5(b) has a flow representation. This strong effect might negatively affect the flow actuation; for this reason, an additional movable plate is attached to the actuator. The goal of the movable plate is to find the right actuation angle to improve flow control. A similar approach was applied by Eulalie (2014); Barros (2015). To obtain a continuous gap through the whole length, a plastic film is placed between the two metallic layers (Figure 2.5(b)). The air-knife can reach jet velocities up to  $u_{jet} = 200$  km/h. Nonetheless, it requires an external flow source.

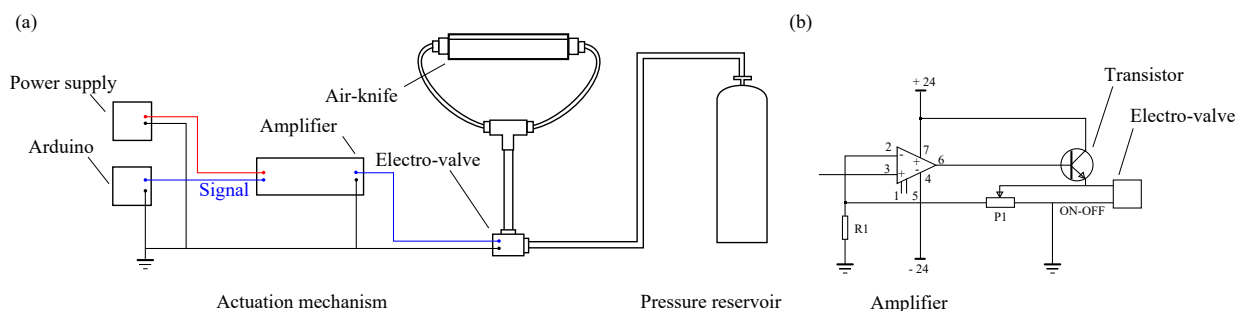


Figure 2.6 – Air-knife generation. (a) Actuation electronics, (b) Electronic circuit of the amplifier.

The pressurized air is supplied by a compressed air reservoir and is driven by a Festo-MH2 solenoid valve that can generate an ON/OFF pulsed jet within an actuation frequency range between  $f_a = 0 - 500$  Hz. The maximum flow rate generated by the solenoid valve is 100 l/min. To operate the solenoid valve, a logical signal is generated by an Arduino waveform generator, magnified from 0-5 V<sub>DC</sub> to 0-24 V<sub>DC</sub> by the amplifier and fed to the solenoid valve (Figure 2.6(a)). The electro-valve is joined to a T connector with a 5 mm radius tube. Two tubes with lengths of 10 cm go out from the junction and are connected to the air-knife entrances on each side of the actuator. The distances between the electro-valve, the connector and the Pulsed jet were calculated to have a minimum pressure loss through the tubes. Figure 2.6(b) shows the

electronic circuit for the system. Hereafter, “pulsed jet actuator” refers to a combination of the pulsed jet actuator and the solenoid valve.

### Dynamical analysis of an air-knife

In order to know the advantages and limitations of this actuation device, the behaviour of the output velocity in response to signal variations (pressure, frequency and duty cycle) is analysed. The single-hot-wire probe (55p15) connected to a STREAMLINE CTA system, previously described in §2.1.1, was employed to survey the velocity distributions at the slot exit of the pulsed jet.

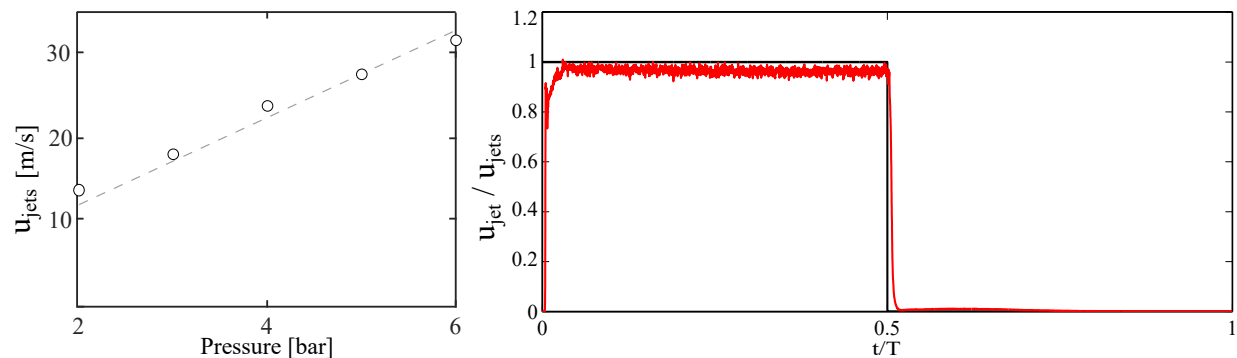


Figure 2.7 – Left: Jet velocity against the supply pressure for continuous jet  $u_{jets}$  ('o' open symbols). Right: Phase average of the jet velocity measured at 1 mm downstream the centreline of the slit exit for an operation cycle for an actuation frequency of 1 Hz. '—' red line denotes the jet velocity  $u_{jet}$ .

To calculate the jet velocity, a hot-wire sensor was located at  $2d$  from the slit exit and  $6d$  down the curved surface; this location was chosen as it is the optimal position to calculate the maximum velocity when the Coanda effect is presented. The continuous jet exit velocity,  $u_{jets}$ , was found to be linearly dependent on the input pressure as shown on the left side of Figure 2.7. The maximum supply pressure of the solenoid valve can reach a pressure value of 8 bars, but the pressure reservoir has a capacity of only 6 bars. For these conditions, the maximum velocity from the slot exit is approximately 30 m/s. Figure 2.7 also shows the jet velocity variation during an operation cycle for an actuation frequency of 1 Hz. When the actuator is activated ( $t = T = 0$ ), a settling time is observed due to the air travel distance from the solenoid valve to the actuator. When the control is turned off, again a brief time-delay is also observed. However, for this specific frequency, a fast actuation response is obtained.

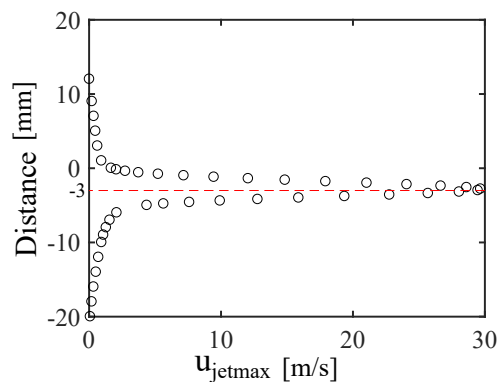


Figure 2.8 – Maximum velocity  $u_{jetmax}$  against variation in the cross-stream distance. Measurements were done to obtain the optimal actuation angle  $\alpha$ .

As previously explained, the actuation angle is critical for an optimal flow control. Following the results of Eulalie (2014), different actuation angles  $\alpha$  were studied:  $+90^\circ$ ,  $+0^\circ$ ,  $-6^\circ$ ,  $-90^\circ$ . The zero angle is defined at the streamwise direction. The angles are obtained moving the plate in the cross-stream direction. The

optimal actuation angle, for this work, is found at  $-6^\circ$ , which agrees well with (Eulalie, 2014) actuation angle range ( $0^\circ < \alpha < -90^\circ$ ). To calculate the correct tilt of the jet, the sensor was moved in the cross-stream direction every millimetre displaying the maximum velocity at that point. Figure 2.8 shows the previously described measurement, with a maximum velocity of 30 m/s at a distance of -3 mm.

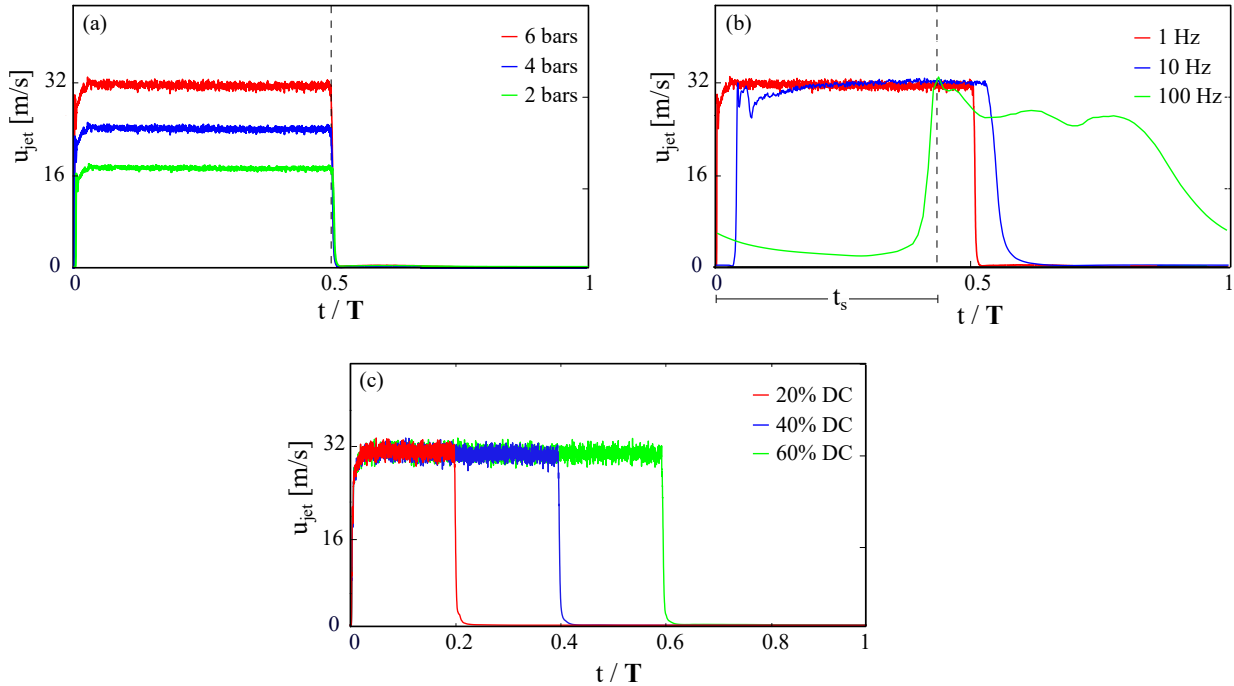


Figure 2.9 – (a) Velocity behaviour for a square signal of  $f_a = 1$  Hz and a duty cycle of 50% and for different supply pressures of '—' red line: 6 bars, '—' blue line: 4 bars and '—' green line: 2 bars, (b) Velocity behaviour for a square signal with a pressure of 6 bars and a duty cycle of 50 % for various frequencies of actuation  $f_a$  '—' red line: 1 Hz, '—' blue line: 10 Hz, and '—' green line: 100 Hz.  $t_s$  denotes settling time, (c) Velocity behaviour for a square signal of  $f_a = 1$  Hz and pressure of 6 bars for various duty cycles of '—' red line: 20 %, '—' blue line: 40 %, and '—' green line: 60 %.

To analyse the transient behaviour and, more generally, the dynamical velocity response of the jet, the square input signal, and the jet velocity is simultaneously acquired. Phase average measurements were calculated in order to reduce signal noises. Different input square signal parameters were varied: pressure, duty cycle and actuation frequency. Figure 2.9(a) indicates the dynamical response for various supply pressures for a square input signal ( $f_a = 1$  Hz, DC of 50 %). Phase-averaged exit-velocity signals were observed with a maximum stability stage reached at different pressure values. A similar response was obtained when a DC variation of 20 %, 40 %, and 60 % is generated; as expected, the flow follows the input signal, Figure 2.9(c). Finally, Figure 2.9(b) highlights a strong actuation frequency effect for three pulsed frequencies: 1 Hz, 10 Hz, and 100 Hz. First, a decrease of the maximum jet velocity with the increase of the frequency can be seen at 100 Hz ('—' green line in Figure 2.9(b)). Second, as previously mentioned, a settling time is observed for all the cases, more predominantly for the highest frequency ('—' blue line). These results indicate that the response of the actuator is strongly affected by the pulsed frequency.

In order to have more details about the frequency phenomena, additional measurements were done for a range of frequencies. The results are shown in Figure 2.10(a). Velocity variations are measured for frequency values between 0.1 Hz and 100 Hz. The ratio between the maximum pulsed jet values  $u_{jet}$  and steady jet velocity  $u_{jet,s}$  was plotted. The velocity stays constant until  $f_a \approx 1$  Hz. After this, it slowly decreases. However, a positive peak at a frequency of 30 Hz is clearly seen, followed by a strong velocity decrease. The velocity behaviour is caused by the actuator settling time, making this parameter a limiting factor to both the frequency top limit and the duty cycle low limit. Settling time proportion to full period grows with frequency, to a point where it is no longer possible to achieve pulsating behaviour and the operation of the pulsed jet transitions to continuous mode (as if it were driven with constant DC). Figure 2.10(b) represents

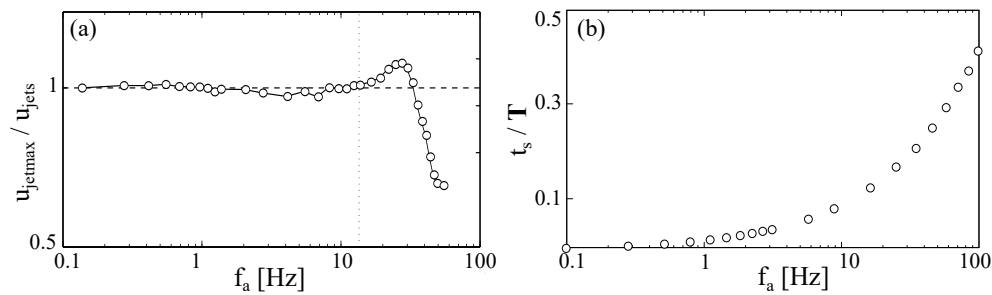


Figure 2.10 – Frequency analysis for the air-knife. (a) Velocity variation for different actuation frequencies (square signal of 50 % and 6 bars). (b) Settling time  $t_s$  as a proportion of full period duration  $\mathbf{T}$  for different input frequencies (square signal duty cycle 50 % and 6bars).  $u_{jetst}$  denotes the jet velocity for steady blowing.

the normalized settling time against the input frequency (constant pressure at 6 bars and 50 % DC); it is clearly visible that  $t_s$  increases exponentially when the frequency increases; when the value reaches 50 % of its total ( $t_s/\mathbf{T} = 0.5$ ), the actuation will not be considered as pulsed jet.

### 2.2.2 Murata micro-blower

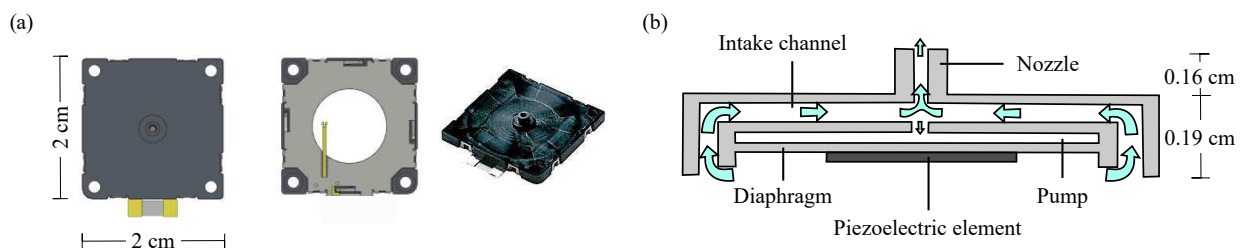


Figure 2.11 – (a) General characteristics of the actuator, (b) Cross-section of the micro-blower.

Micro-blowers are recently being used as flow control devices due to their low energy consumption. A Murata™ micro-blower (Murata Manufacturing Co., 1944) is studied as an actuator device for flow control. This air blower device is designed to function as an air pump using the ultrasonic vibration of ceramics, which can generate high discharge pressures of air from a thin and extremely compact body. In addition to being much smaller than conventional blowing devices, it also features lower power consumption.

#### Design and principle

The operating principle of this micro-blower is completely different from conventional piezoelectric cavity devices. The resulting air jet has an intrinsically non-zero-net-mass-flux, in contrast to the synthetic jet actuator (zero-net-mass-flux) used in numerous studies (Glezer & Amitay, 2002; Seifert *et al.*, 1999). The actuator operates in a double cavity and the diaphragm forces the fluid to flow out from the central and annular nozzles, as shown in Figure 2.11. The nozzle exit diameter  $d$  is 0.86 mm. The inside section of the micro-blower is constructed by attaching a disc-shaped piezoelectric element to a metal diaphragm, which vibrates at approximately 26 kHz. The micro-blower is powered by a driver circuit (also commercially available and shown in Figure 2.13(b) and (d)) that outputs an amplitude modulated square wave, with amplitude proportional to an input voltage of driver circuit. The frequency of the square wave is constant and around 26 kHz, ensuring that the piezoelectric element is driven at resonant frequency regardless of input voltage. The micro-blower is capable of creating 1 l/min of air discharges for a continuous mode.

Figure 2.12 shows the operational principle of the Murata micro-blower phase by phase. The first phase is with a neutral position of the ceramic. Then, the ceramic diaphragm pulls the air from the sides of the

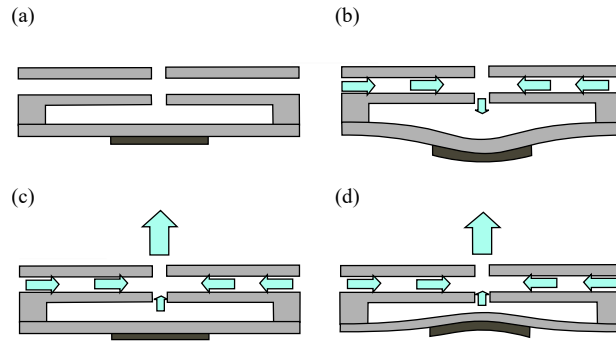


Figure 2.12 – Pulsed jet generation principle: (a) No-load state, (b) Suction state, (c) and (d) Discharge states.

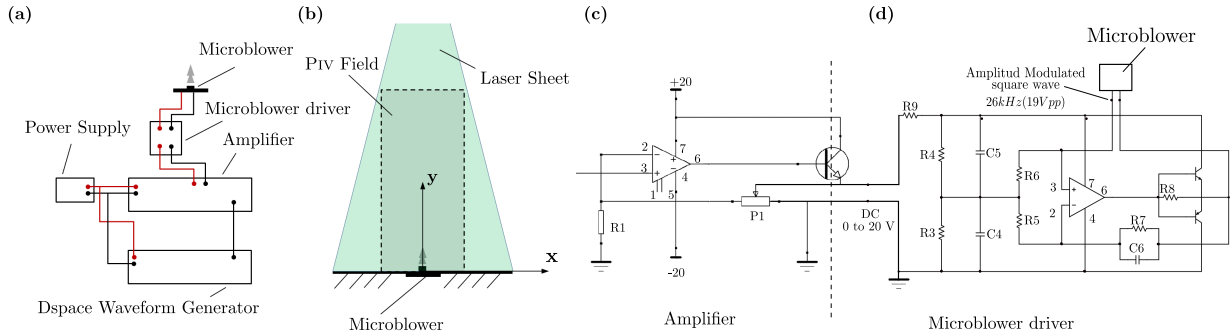


Figure 2.13 – Experimental setup: (a) Micro-blower Electronics and waveform generation, (b) PIV setup and associated reference system, (c) Electronic circuit of the amplifier, (d) Electronic circuit of the micro-blower driver.

micro-blower creating an inlet flow inside the main cavity. The third phase is the expulsion of the flow through the nozzle; here, the small nozzle area contributes to the strong output velocity. Finally, in the last state, the ceramic continues the expulsion of air by Venturi effect. The Murata micro-blower works on the resonance frequency of the piezoelectric element to produce the air discharge and the jet velocity is only driven by the input voltage ( $V_e$ ). This characteristic is not usual in other micro-blowers based on piezoelectric elements. Most of them do not have linear velocity response and they are linked to the resonance frequency of the piezoelectric device. Due to these advantages, this actuator is a great promise for feedback control. It is possible to create continuous and pulsed signals, with square or any other kind of waveform actuation. Figure 2.13(a) shows the electronic setup. A variable DC signal is generated by a dSPACE waveform generator, magnified from 0-1  $V_{DC}$  to 0-20  $V_{DC}$  by the amplifier and fed to the micro-blower driver. Figure 2.13(c) and 2.13(d) present the electronic circuit for the amplifier and the micro-blower driver, respectively. This setup allows a driving actuator with any variable DC (including, but not limited to constant DC, pulsed DC, square wave, etc.) Throughout the study, “Input Voltage” refers to variable DC input to the driver circuit (as opposed to input to the piezoelectric element directly). “Micro-blower” refers to the union of the driver circuit and the piezoelectric element.

### Dynamical analysis of a single micro-blower

As stated before, it is important to know the characteristics of the actuation. This is why, for this actuator, hot-wire and PIV measurements are carried out to characterize the jet. The same hot-wire anemometer is employed to survey the velocity distributions at the nozzle exit of the micro-blower, for different input frequencies, amplitudes, and duty cycles. To obtain the instantaneous velocity time traces, 600000 samples were acquired at a sampling frequency of  $f_s = 2$  kHz. A low-pass filter, set at 1 kHz, was adopted to avoid aliasing phenomena. In order to reduce velocity induced noise and obtain a reasonable statistical accuracy, the ensemble averaging technique was applied.

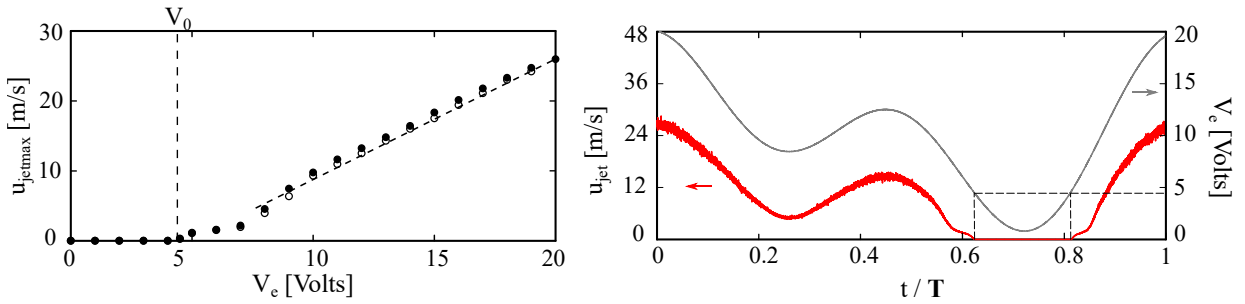


Figure 2.14 – Left: Maximum velocity against the supply voltage for '•' filled circle: continuous jet and for 'o' empty circle: pulsed jet (square signal with  $f_a = 1$  Hz and a duty cycle of 50 %).  $V_0$  denotes the minimum supply voltage needed for the actuator activation. Right: Example of the actuator velocity response for a complex input voltage signal  $V_e = \cos(T) + \cos(2T)$ . '—' grey line denotes the input voltage  $V_e$  and '—' red line denotes  $u_{jet}$ .  $T$  denotes the period of the signals.

To know the behaviour of the velocity flow field of the actuator, PIV measurements were done for continuous and pulsed modes. For the pulsed mode, the phase-locked PIV measurements were also used to observe the behaviour of the jet. Figure 2.13(b) shows the setup used for the PIV measurements with the reference coordinate axes. The measurements were carried out with a TSI system (previously described in §2.1.1). Once the PIV images are captured and digitized, the velocity field was processed using cross-correlation. The interrogation window was fixed to  $32 \times 32$  pixels providing a spatial resolution of approximately  $0.1 \text{ mm} \times 0.1 \text{ mm}$ . The overlap ratio between adjacent interrogation windows was 50 %. For the steady (continuous) jets mode, the mean velocities were computed by ensemble average performed over a set of 1000 instantaneous fields. For the pulsed jet mode (square input signal), the phase-locked PIV measurements were triggered by the electric supply signal of the micro-blower. For a given phase in the blowing cycle, phase-average velocity fields were obtained by averaging 50 instantaneous velocity fields. The beginning (transient part) of the cycle was covered by 20 phases regularly spaced.

Furthermore, the hot-wire sensor was located at  $1.5d$ , with  $d$  the nozzle diameter, from the blower nozzle exit. Both, the continuous jet velocity,  $u_{jets}$ , and pulsed jet velocity,  $u_{jet}$ , linearly increase as the input voltage increases, as shown in Figure 2.14. The maximum supply voltage of the Murata micro-blower can reach almost 30 V, but the recommended supply voltage range is from 5 V to 20 V. For these conditions, the maximum velocity at  $1.5d$  from the blower nozzle exit is approximately 25 m/s. The jet-exit flow is also characterized by an initial voltage shift  $V_0$  (relative to the minimum supply voltage needed for the actuator activation and equal to 4.3 V). After this initial voltage, the exit velocity showed a quite linear behaviour with respect to the input voltage  $V_e$ . However, there is a non-linear behaviour at the exit velocity when the input voltage is lower than 8 V.

As already explained, the most interesting characteristic of the micro-blower is its ability to work with a complex input voltage signal. As an example, Figure 2.14.Right represents the actuator response to a complex input voltage signal  $V_e = \cos(T) + \cos(2T)$ . The response of the micro-jet follows the supplied voltage. However, a small delay can also be observed between the two signals; this behaviour will be analysed in detail afterwards. The global response of the signal was quite linear and showed, as mentioned previously, a deactivation of the micro-blower for a supply voltage lower than  $V_0$ . Non-linear effects are also observed close to the deactivation voltage.

The normalized average velocity fields, for different input voltages, are shown in Figure 2.15. A relatively good symmetry of the velocity fields with respect to the injection plan can be observed. However, a slight jet deviation toward the right is perceptible in Figure 2.15(b), due to residual spanwise flow during the experiment. This deviation does not affect the analysis. Close to the nozzle, there is a bias caused by strong velocity gradients and large particle displacements leading to loss of information. For the three

different input voltages, the micro-blower generates an omnidirectional jet flow normal to the nozzle, with a regular spreading of the surrounding fluid, as classically reported in other steady blowing studies (Bera *et al.*, 2001). The blowing effect of the microjet can be estimated by the penetrating length reached when the normal velocity of the jet is equal to 50 % of the maximum velocity. Then, the penetrating length for the three different supply voltages: 10 V, 15 V, and 20 V, corresponding to the maximum jet velocity of around 10 m/s, 18 m/s, and 25 m/s, are equal to 10d, 30d, and 50d, respectively. The spanwise spreading of the jet at the maximum voltage (20 V) can also reach 20d as shown in Figure 2.15(c) and Figure 2.15(f).

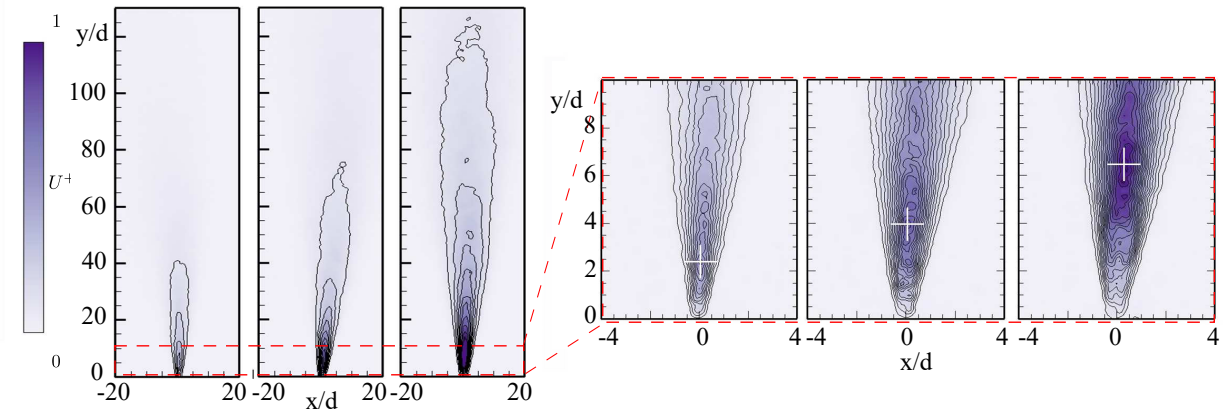


Figure 2.15 – Steady jet mean velocity fields  $U^+$  normalized by the maximum jet velocity, (a)  $V_e=10$  V, (b)  $V_e=15$  V, (c)  $V_e=20$  V. (d), (e) and (f) Closed-up visualizations for the same voltage inputs.

In order to analyse the dynamical velocity response of the jet, the square input signal and the jet velocity were simultaneously acquired. Phase average measurements were calculated in order to reduce signal noises. Different input square signal parameters were varied: amplitude, duty cycle, and actuation frequency. Figure 2.16(a) indicates the dynamical response for various supply voltages (10 V, 15 V and 20 V) for a square input signal ( $f_a=1$  Hz, DC of 50 %). A similar behaviour to that shown in Figure 2.10(a) is obtained. Also, a transient effect can be seen. When a variation of Duty Cycle is studied, an equal conduct is also obtained, as seen in Figure 2.10(c).

Figure 2.16(b) highlights the strong actuation frequency effect for three pulse frequencies: 1 Hz, 10 Hz and 50 Hz. The decrease of the maximum jet velocity with the increase of the frequency can be seen. A delay time and a settling time are observed in '—' blue line, corroborating the strong influence of the frequency on the jet response. Velocity variations were also measured for frequency values between 0.1 Hz and 100 Hz. Similar results are obtained in this case compared to those in the pulsed jet (Figure 2.10(a)). However, no positive peak is seen in this case, just a slow decrease of the velocity. An exponential behaviour is also seen when the settling time is plotted against the actuation frequency.

Two important parameters regarding the effectiveness of the actuators are the strength and position of the ring shape vortices. This vortical structure is associated with strong variations of the jet velocity, inducing shear layers into the flow field (Holman *et al.*, 2005). The velocity variation at the origin of these vortices must be sufficiently strong to generate shear layer when these vortices develop. The transient part of the jet velocity, for a square input signal, will be studied using ensemble-averaged measurements.

The jet behaviour can be divided into three major parts: the brief time period (from  $t=0$  to  $0.2T$ ) when the square input signal is generated, the steady part corresponding to the constant square signal value ( $t>0.2T$  and  $<0.5T$ ) and the transient decreasing signal ( $t>0.5T$ ). Figure 2.18 depicts an ensemble-

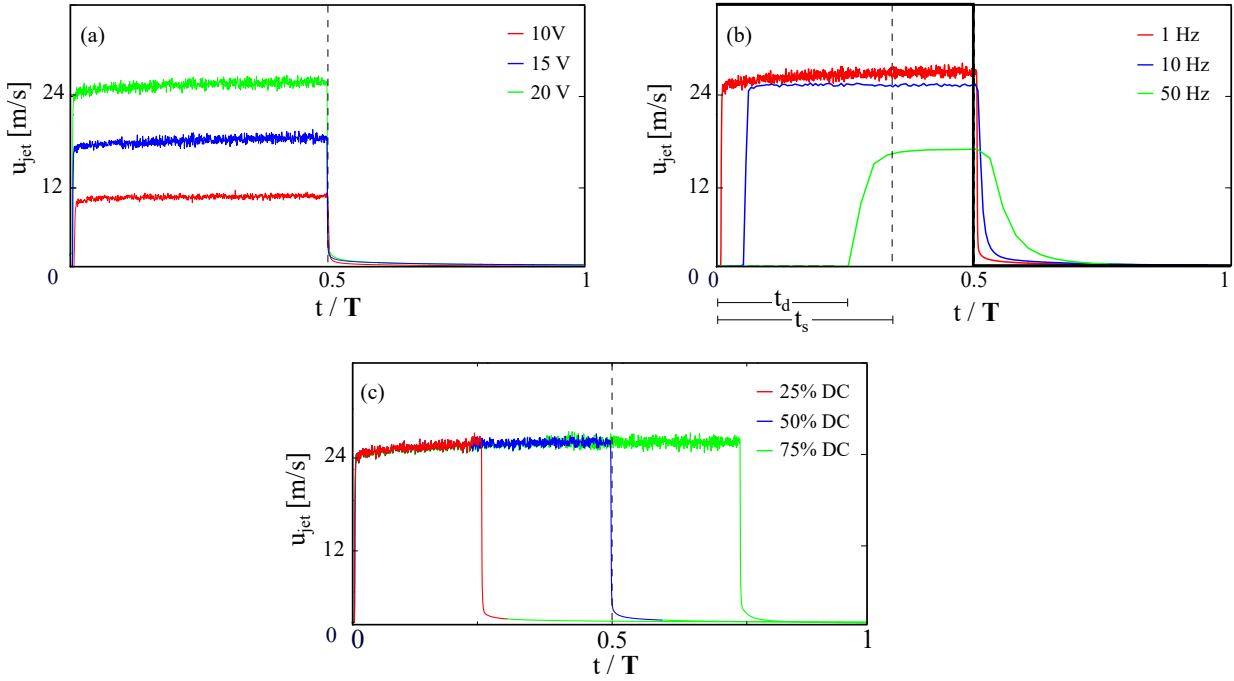


Figure 2.16 – (a) Velocity behaviour for a square signal of  $f_a = 1$  Hz and a duty cycle of 50 % and for different supply voltages  $V_e$  of '—' red line: 10 V, '—' blue line: 15 V, and '—' green line: 20 V. (b) Velocity behaviour for a square signal with a  $V_e = 20$  V and a duty cycle of 50 % for various frequencies of actuation. Continuous line denotes the Phase average for  $f_a$  '—' red line: 1 Hz, '—' blue line: 10 Hz, and '—' green line: 50 Hz.  $t_s$  denotes settling time and  $t_d$  denotes delay time. (c) Velocity behaviour for a square signal of  $f_a$  of 1 Hz and  $V_e = 20$  V for various duty cycles of '—' red line: 25 %, '—' blue line: 50 %, and '—' green line: 75 %.

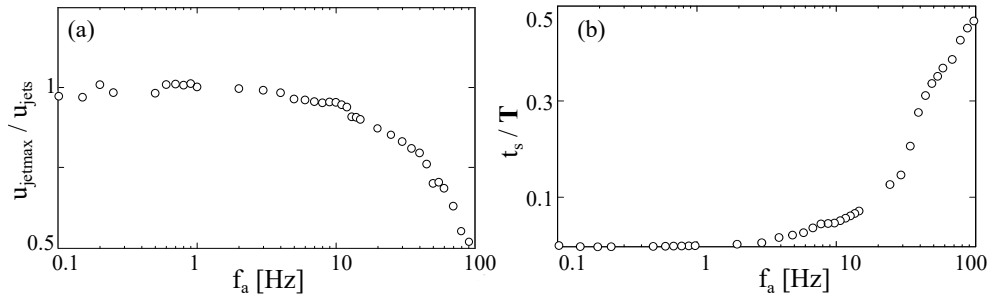


Figure 2.17 – (a) Velocity variation for different actuation frequencies (square signal of 50 % and 20 V). (b) Settling time ( $t_s$ ) as a proportion of full period duration  $T$  for different input frequencies (square signal duty cycle 50% and 20V).

averaged vorticity color plot with overlapping flow vectors near the nozzle. These values were obtained by phase-locked PIV measurements. The images correspond to the increasing transient part of the square input signal ( $t < 0.3T$ ). The sequence of results displayed in Figure 2.18 reveals the presence of a pair of counter-rotating eddies, which develop and move away from the jet nozzle. This pattern was established by the visualization of [Smith & Glezer \(1998\)](#) and also by numerous authors ([Bera \*et al.\*, 2001](#); [Tilmann \*et al.\*, 2003](#); [Tesar & Kordik, 2012](#); [Kostas \*et al.\*, 2007](#)). At the beginning of the cycle in Figure 2.18(a), the fluid is pumped out from the spanwise side of the nozzle and the vortex is formed quickly by viscous effects. During the first transient part of the cycle (Figures 2.18(b) to Figures 2.18(j)), the shear layers, highlighted by the normalized vorticity contour, show in detail the relation between the evolution of the vortices and the shear layer development. Figure 2.18 also shows the phase-averaged trajectories covered by the vortex centres in a step of  $t = 0.005T$  of the phase injection cycle. The average longitudinal convection velocity of the vortices can be deduced and estimated around 0.75-1.25 m/s. The trajectories are clearly linear from the nozzle to the far field and exhibit a spreading angle of  $22^\circ$ .

For both cases, the actuation amplitude can be characterized, as defined by [Amitay \*et al.\* \(2001\)](#), by

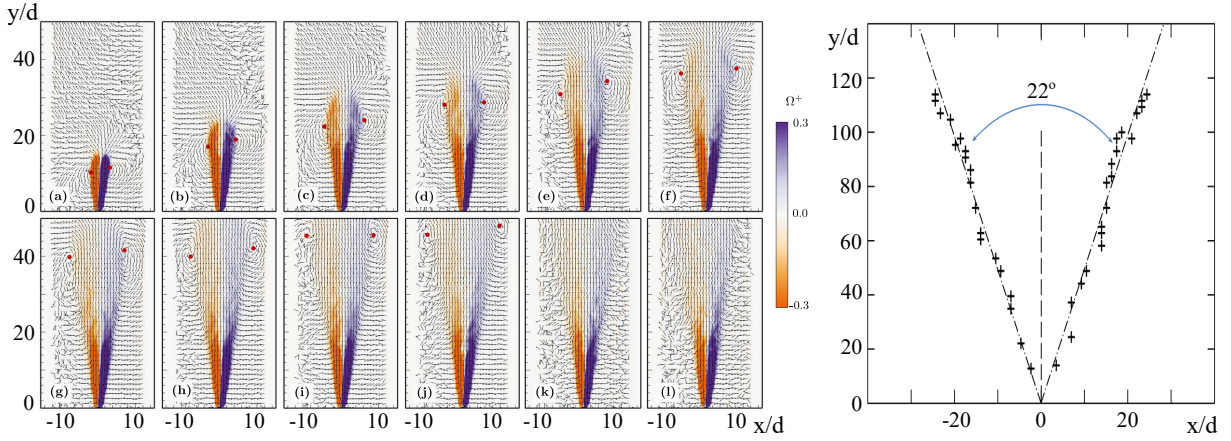


Figure 2.18 – Ensemble-averaged vorticity color plot with vectors superimposed, for a square signal of  $V_e=20$  Volts,  $f_a = 1$  Hz, (a)  $t/\mathbf{T}=0.01$ , (b)  $t/\mathbf{T}=0.02$ , (c)  $t/\mathbf{T}=0.03$ , (d)  $t/\mathbf{T}=0.04$ , (e)  $t/\mathbf{T}=0.05$ , (f)  $t/\mathbf{T}=0.06$ , (g)  $t/\mathbf{T}=0.07$ , (h)  $t/\mathbf{T}=0.08$ , (i)  $t/\mathbf{T}=0.09$ , (j)  $t/\mathbf{T}=0.10$ , (k)  $t/\mathbf{T}=0.20$ , (l)  $t/\mathbf{T}=0.30$ . The clockwise and counter-clockwise flow structures location are identified by the red points. Positions of phase-average vortex centres at each  $t=0.005\mathbf{T}$  of the transient injection cycle.

the momentum coefficient:

$$C_\mu = \frac{S_{\text{jet}} \bar{u}_{\text{jet}}^2}{1/2 S_\infty U_\infty^2} = DC C_{\mu 0}, \quad (2.14)$$

where  $S$  and  $S_{\text{jet}}$  are the slot or nozzle and the cross-sectional area, respectively, and  $\bar{u}_{\text{jet}}$  the mean jet velocity.  $C_{\mu 0}$  refers to the steady blowing momentum coefficient.

## 2.3 Control design

Two different closed-loop control strategies are presented in this section. Sliding mode control SMC proposes a bilinear and delayed model to control turbulent flows. This strategy is thoroughly explained by Feingesicht (2017). Machine learning control MLC presents an optimization of control laws in a high-dimensional space. This approach is fully explored in Duriez *et al.* (2016); Li (2017)

### 2.3.1 Sliding mode control (SMC)

Thanks to a collaboration with the INRIA laboratory, this section will briefly define a robust closed-loop approach refer to as the sliding mode control SMC, developed in the Ph.D thesis of (Feingesicht, 2017). An initial single-input single-output (SISO) black-box model identification is presented using the bilinear model approach presented by Feingesicht *et al.* (2017). For an initial overview of the SMC control process, see Figure 2.19. A desired tracking reference point  $s^*$  is initially set. The plant feeds back the sensor output in real time to the controller  $K$ . An actuation command  $\mathbf{b}$  is computed based on  $\mathbf{s}$  and  $s^*$  and it is finally fed back to the plant. The main goal is to track, reach and maintain a set-point, regardless of the flow perturbations presented upstream.

#### SMC Principle

The problem of a set-point tracking is considered for a control system of the form,

$$\dot{\mathbf{s}}(t) = \mathbf{F} + \mathbf{G}\mathbf{b}, \quad (2.15)$$

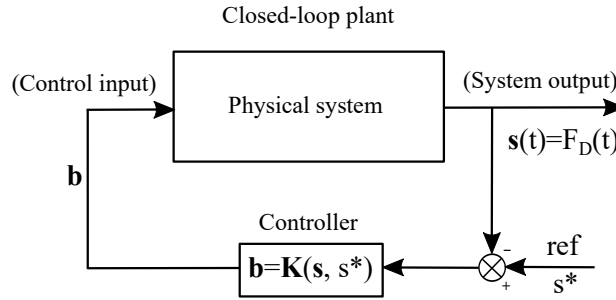


Figure 2.19 – Sketch of the real-time closed-loop control. The plant feeds back the sensor output  $\mathbf{s}$  to the controller  $\mathbf{K}$  with regards to a tracking reference  $s^*$ . The controller computes the actuation command,  $\mathbf{b}$  based on  $\mathbf{s}$  and  $s^*$  and sends it back to the plant.

where  $\mathbf{F}$  and  $\mathbf{G}$  are uncertain functions and  $b(t) \in \{0, 1\}$  is the relay control input. The objective is to determine a control that guarantees  $s(t) \rightarrow s^*$  as  $t \rightarrow +\infty$ , where  $s^*$  is a desired set-point. The control must be also robust with respect to some uncertainties in  $\mathbf{F}$  and  $\mathbf{G}$ . A convenient set-point tracking as well as precise disturbance rejection are desirable qualities. If one can respect the dynamics of the system to lie on a well behaved surface, then the control problem is greatly simplified. Sliding mode control SMC (Utkin, 1991) is based on the design of an adequate “sliding surface” (or “sliding manifold”) defined as,

$$\Sigma = \{(s, t) \mid \sigma(s, t) = 0\}, \quad (2.16)$$

that divides the state space into two parts which correspond to one of the two controls that commute from one to zero when the state crosses the surface in order to maintain the sliding mode  $\sigma(s(t), t) = 0$ . The manifold  $\Sigma$  is defined in such a way that the error  $|s(t) - s^*|$  vanishes to zero when the system state  $s(t)$  is restricted to lie on this surface. The control problem is then reduced to a problem of reaching a phase during which trajectories starting off the manifold  $\Sigma$  move toward it in a finite time, followed by a sliding phase during which the motion is confined to the manifold, and the dynamics of the system are represented by the reduced-order model.

### Introducing example

The sliding mode control principle can be illustrated using a simple example. Let us consider the following system,

$$\dot{s}(t) = -\zeta s(t) + \beta b(t), \quad (2.17)$$

with  $\zeta > 0$ ,  $\beta > 0$ ,  $s(0) \in [0, s_{\max})$ ,  $s_{\max} = \beta/\zeta$  and  $b(t) \in \{0, 1\}$ , that has a bounded positive solution  $0 \leq s(t) < s_{\max}$  for any input signal  $b$ , since,

$$s(t) = e^{-\zeta t} s(0) + \beta \int_0^t e^{-\zeta(t-\tau)} b(\tau) d\tau < s_{\max}. \quad (2.18)$$

Let us consider the simple sliding variable  $\sigma(t) = s(t) - s^*$ , which can be treated as a measure of how far the state  $s(t)$  from the desired set-point  $s^*$  is. The main idea is to monitor the sign of  $\sigma(t)$  in order to decide when it is necessary to switch the control. Let's  $s^* \in (0, s_{\max})$  and

$$b(t) = \begin{cases} 1 & \text{if } \sigma(t) < 0, \\ 0 & \text{if } \sigma(t) > 0. \end{cases} \quad (2.19)$$

In this case, the time derivative of the sliding variable is  $\dot{\sigma}(t) = \dot{s}(t) = -\zeta s(t) + \beta b(t)$  and one has

$$\dot{\sigma}(t) = -\zeta s(t) + \beta > -\zeta s^* + \beta > 0 \text{ if } \sigma(t) < 0, \quad (2.20)$$

and

$$\dot{\sigma}(t) = -\zeta s(t) < -\zeta s^* < 0 \text{ if } \sigma(t) > 0. \quad (2.21)$$

Therefore,  $\dot{\sigma}(t)\sigma(t) < 0$  for  $t > 0$  and  $\sigma(t) \rightarrow 0$  as  $t \rightarrow +\infty$ . Moreover, according to Utkin (1991) the sliding mode on the surface  $\sigma = 0$  arises in a finite time, i.e.,  $t^* > 0$  exists such that  $\sigma(t) = s(t) - s^* = 0$  for  $t > t^*$

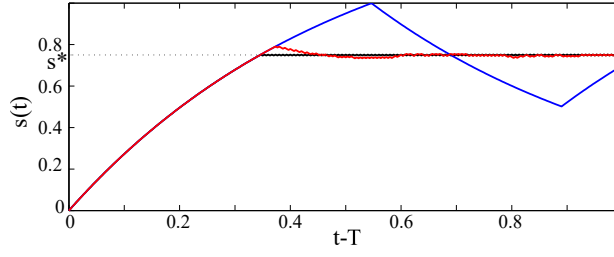


Figure 2.20 – Numerical simulation of the dynamical system for  $\zeta = 2$ ,  $\beta = 3$  and for the set-point  $s^* = -\beta/(2\zeta)$  with a maximum switching frequency  $f_{sw}$  of 300 Hz: '—' black line:  $s(t)$  without input delay, '—' blue line:  $s(t)$  with input delay  $T = 60/f_{sw}$  and without delay compensation, and '—' red line:  $s(t)$  with input delay  $T = 60/f_{sw}$  and with the delay compensation.

(see Figure 2.20).

The conventional sliding mode control methodology was originally developed for delay-free systems. Simulation (see '—' in Figure 2.20) shows the resulting oscillations due to the input delay. This simple example points out the behaviour changes arising in relay-delay systems, and motivates the study of specific SMC design for systems with state and/or input delay (Richard *et al.*, 2001). In order to design the sliding mode control, we need to use some technique for compensating input delay, see e.g., Polyakov (2012); Feingessicht *et al.* (2017) and references therein. Suppose that the system considered above has an input delay:

$$\dot{s}(t) = -\zeta s(t) + \beta b(t - T), \quad (2.22)$$

where  $\zeta > 0$ ,  $\beta > 0$ ,  $h > 0$  and  $b(t) \in \{0, 1\}$ . As the previous one, this system has a bounded positive solution  $0 < s(t) < s_{\max}$  with  $s_{\max} = -\beta/\zeta$  for any input signal  $b$  and any  $s(0) \in [0, s_{\max}]$ . Let us consider the following sliding variable:

$$\sigma(t) = s(t) + \beta \int_{t-T}^t b(\tau) d\tau - \sigma^*, \quad (2.23)$$

where  $\sigma^* = s^*(1 + \zeta T) > 0$  and

$$s^* \in \left( \frac{\beta T}{1 + \zeta T}, \frac{s_{\max}}{1 + \zeta T} \right), \quad (2.24)$$

are selected such that the identity  $\sigma(t) = 0$  for  $t > t^*$  implies  $s(t) \rightarrow s^*$  as  $t \rightarrow +\infty$ . Indeed, since  $\dot{\sigma}(t) = -\zeta s(t) + \beta b(t)$  then the control input  $b$  in the latter equation is not delayed with respect to the sliding variable  $\sigma$ , so the conventional sliding mode design scheme can be utilized (Utkin, 1991):

$$\dot{\sigma}(t) = -\zeta s(t) + \beta > -\zeta \sigma^* + \beta > 0 \quad \text{if } \sigma(t) < 0, \quad (2.25)$$

and

$$\dot{\sigma}(t) = -\zeta s(t) < -\zeta(\sigma^* - \beta T) < 0 \quad \text{if } \sigma(t) > 0. \quad (2.26)$$

Similarly to the previous example it concludes that  $t^* > 0$  exists such that  $\sigma(t) = 0$  for  $t > t^*$  and using equivalent control method (Utkin, 1991), it derives  $\dot{\sigma}(t) = -\zeta s(t) + \beta b_{\text{eq}}(t) = 0$  with  $b_{\text{eq}}(t) \in (0, 1)$  and

$$\sigma(t) = s(t) + \zeta \int_{t-T}^t s(\tau) d\tau - s^*(1 + \zeta T) = 0 \quad \text{for } t > t^*. \quad (2.27)$$

It can be shown that the latter identity implies that  $s(t) \rightarrow s^*$  as  $t \rightarrow +\infty$ .

The simulation of the delayed dynamical system taking into account the input delay is shown in '—' Figure 2.20. Using the presented scheme of sliding surface design, the set-point is reached asymptotically and the oscillations observed previously for the input delay system disappear.

Any mathematical model is just an approximation of reality. The parameters of the model can be found from experimental data with, generally, some errors (due to measurements noise, quantization of digital signals, etc). Therefore, the robustness is the very important issue in the design of model-based controllers.

This work studies robustness of the control system in the sense of input-to-state stability (see [Sontag et al. \(2005\)](#) for more details). In this case, this means that the tracking error of a robust control system must be proportional to a continuous function of disturbance magnitude, which vanishes as the disturbance magnitude tends to zero.

Let the control system be perturbed as follows,

$$\dot{s}(t) = -\zeta s(t) + \beta b(t - T) + \mathbf{P}(t), \quad (2.28)$$

where  $s$ ,  $\zeta$ ,  $\beta$  are as before,  $T \in (0, 1)$  and  $\mathbf{P}(t)$  is a perturbation that does not degrade positivity of the system, i.e.,  $\mathbf{P}(t) \geq 0$  if  $s(t) = 0$ . Let us assume also that the function  $\mathbf{P}$  is bounded,

$$|\mathbf{P}(t)| \leq \kappa < \frac{\zeta\beta(1-T)}{1+\zeta} \quad \text{for } t \geq 0. \quad (2.29)$$

Note that  $\mathbf{P}(t)$  may contain parametric uncertainty of the system, i.e.  $\dot{s}(t) = -(\zeta + \Delta\zeta)s(t) + (\beta + \Delta\beta)b(t - T) = -\zeta s(t) + \beta u(t - T) + \mathbf{P}(t)$ , where  $\mathbf{P}(t) = -\Delta\zeta s(t) + \Delta b(t - T)$  and  $\Delta\zeta$ ,  $\Delta\beta$  describe errors of parameters identification. Repeating the above considerations for

$$s^* \in \left( \frac{\beta > \text{Tau} + \kappa/\zeta}{1 + \zeta h}, \frac{\beta - \kappa}{1 + \zeta h} \right), \quad (2.30)$$

one can derive  $\dot{\sigma}(t) = -\zeta s(t) + \beta b(t) + \mathbf{P}(t)$  leading to,

$$\dot{\sigma}(t) > -\zeta\sigma^* + \beta - \kappa > 0 \quad \text{if } \sigma(t) < 0, \quad (2.31)$$

and

$$\dot{\sigma}(t) < -\zeta(\sigma^* - \beta T) + \kappa < 0 \quad \text{if } \sigma(t) > 0. \quad (2.32)$$

In other words, we again derive  $\sigma(t) = 0$  for  $t > t^*$  and

$$s(t) + \zeta \int_{t-T}^t s(\tau) d\tau - s^*(1 + \zeta h) = \int_{t-T}^t \mathbf{P}(\tau) d\tau \quad \text{for } t > t^*. \quad (2.33)$$

Since  $\mathbf{P}$  is bounded by  $\kappa$  then the latter identity implies  $\|s(t) - s^*\| = O(\kappa T)$  for sufficiently large  $t > t^*$ . This proves the robustness of the proposed SMC.

### SMC for flow control system

An identification procedure of the dynamical system is employed here for flow control application. A black-box SISO modelling approach is considered. Due to the non-linear nature of the governing equations driving the flow dynamics, non-linear models with time-delays are here preferred. The bilinear model proposed by [Feingesicht et al. \(2016, 2017\)](#) is here considered and can be written as,

$$\dot{s}(t) = \zeta_1 s(t - T) - \zeta_2 s(t) + (\beta - \gamma s(t - T) + \gamma s(t - \tau))b(t - T), \quad (2.34)$$

where  $\zeta_1$ ,  $\beta$ ,  $\gamma$ ,  $T$  and  $\tau$  are positive constant parameters to be identified. This type of model proved to be satisfactory in the context of separated flow such as a massively turbulent boundary layer or again a flow over an air-foil ([Feingesicht, 2017](#)). The identification of the model parameters is performed thanks to open-loop control experiments during which the flow response under various forcings is examined. The open-loop forcing experiments consist of successive cycles of actuation and relaxation phases for different values of the control parameters (here frequency  $f_a$  and duty cycle DC). The range of the control parameters over which the flow response is explored must be sufficiently large so that the model can capture the essential changes in the flow due to actuation. In addition, the robustness of the controller to changes in operational conditions can be significantly enhanced if the model identified can properly capture the resulting change in the flow response. The system response is thus first explored thanks to successive periodic forcing and the responses of the defined sensor to the different actuation commands are then concatenated into a single time series. For conciseness, the reader is referred to [Feingesicht et al. \(2017\)](#) for full details of the identification procedure. In the present case, it leads to  $\zeta_1 = 27.37$ ,  $\zeta_2 = 32.70$ ,  $\beta = 1.97$ ,  $\gamma = 1.92$ ,  $\tau = 0.18$  s and  $T = 0.01$  s. The delay  $T$  represents the delay between a change in the input and

a change in the output, usually called the input delay. However, the delay  $\tau$  is a mathematical tool and cannot be directly related to a physical quantity, it is only obtained through identification and can take several different values that lead to a similar accuracy of the model.

The precision of the model has been evaluated by the following FIT index,

$$\text{FIT}[\%] = \left\{ 1 - \frac{\|s_{\text{exp}} - s_{\text{sim}}\|_{L_2}}{\|s_{\text{exp}} - \bar{s}_{\text{exp}}\|_{L_2}} \right\} \times 100\%, \quad (2.35)$$

where  $s_{\text{exp}}$  is the output of the system obtained from the experiment,  $s_{\text{sim}}$  is the output of the identified bilinear model and  $\bar{s}_{\text{exp}}$  denotes the mean value of  $s_{\text{exp}}$ . The obtained FIT index is equal to 59% for the present application. Note that only two time-delays are here retained in the modelling. As detailed in Feingischt *et al.* (2017), a better fit of the plant's response can be obtained if additional terms in Eq.(2.34) are retained. However, this is done at the cost of an increase in the computation time needed to update the controller which is described in the next sections. An example of the model output, obtained for another experimental configuration with hot-film sensors and active air blowers, is presented by Feingischt (2017) and observed in Figure 2.21.

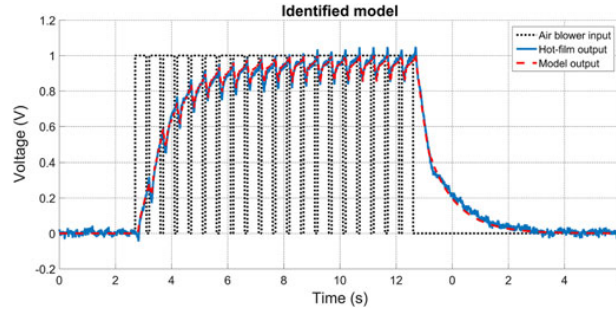


Figure 2.21 – Identified model with state-dependent input delay for a turbulent boundary layer developing along a ramp; subjected to separation due to the presence of a inclined flap with a sharp edge with hot-film sensors and active air blowers. Figure obtained from the PhD. thesis work of (Feingischt, 2017)

Using Proposition 1 of Feingischt *et al.* (2017), we derive that the identified system is positive and its solutions are bounded as

$$0 \leq s(t) < s_{\text{max}} = \frac{\beta}{\zeta_2 - \zeta_1} \quad \text{for } t > 0. \quad (2.36)$$

Let us introduce the following sliding variable

$$\begin{aligned} \sigma(t) = & s(t) - \sigma^* + \gamma \int_{t-\tau+T}^t s(\mu) d\mu \\ & + \int_{t-T}^t (\zeta_1 s(\mu) + (\beta - \gamma s(\mu) + \gamma s(\mu - \tau + T))) b(\mu) d\mu \end{aligned}, \quad (2.37)$$

where  $\sigma^* = s^*(1 + \zeta_2 h + \gamma(\tau - T))$  and  $s^* \in \left(0, \frac{\beta}{\zeta_2 - \zeta_1}\right)$  is a predefined set-point. The time derivative of  $\sigma$  is given by

$$\dot{\sigma}(t) = (\zeta_1 - \zeta_2 + \gamma(1 - b(t)))s(t) + \gamma(b(t) - 1)s(t - \tau + T) + \beta b(t). \quad (2.38)$$

For  $b(t) = 1$   $\dot{\sigma}(t) = (\zeta_1 - \zeta_2)s(t) + \beta > 0$  is obtained, but if  $u(t) = 0$  has  $\dot{\sigma}(t) = (\zeta_1 - \zeta_2 + \gamma)s(t) - \gamma s(t - \tau + T) < 0$ . Hence, it can be shown that  $t^* > 0$  exists such that  $\sigma(t) = \sigma^*$  for all  $t > t^*$ . The system motion on the sliding surface is described by

$$s(t) + \zeta_2 \int_{t-T}^t s(\mu) d\mu + \gamma \int_{t-\tau}^{t-T} s(\mu) d\mu - \sigma^* = 0. \quad (2.39)$$

The latter identity implies that  $s(t) \rightarrow s^*$  as  $t \rightarrow +\infty$ . The reader is referred to Feingischt *et al.* (2017) for more details about the proof of the asymptotic convergence.

## Robustness of control system with respect to perturbations

Let us consider the perturbed model

$$\dot{s}(t) = \zeta_1 s(t - T) - \zeta_2 s(t) + (\beta - \gamma s(t - T) + \gamma s(t - \tau))b(t - T) + \mathbf{P}(t), \quad (2.40)$$

where an admissible perturbation  $\mathbf{P}$  is assumed to be bounded  $|\mathbf{P}(t)| \leq \kappa$  with some constant  $\kappa > 0$  and such that the perturbed system remains positive, i.e  $s(t) \geq 0$  for any  $t \geq 0$  and for any admissible  $p$ . In this case, any solution of the system is also bounded by  $0 \leq s(t) \leq (\beta + \kappa)/(\zeta_2 - \zeta_1)$  for all  $t \geq 0$ .

Let the sliding surface  $\sigma$  be defined as before, but the set-point is selected as follows

$$s^* \in \left( \frac{\kappa}{\zeta_2 - \zeta_1 - \gamma}, \frac{\beta - \kappa}{\zeta_2 - \zeta_1} \right), \quad (2.41)$$

where  $\kappa > 0$  is a sufficiently small number such that the latter interval is non-empty. If  $b(t) = 1$ ,  $\dot{\sigma}(t) = (\zeta_1 - \zeta_2)s(t) + \beta + \mathbf{P}(t) > 0$  for  $s(t) \leq (\beta - \kappa)/(\zeta_2 - \zeta_1)$  is obtained, but if  $u(t) = 0$  one gets  $\dot{\sigma}(t) = (\zeta_1 - \zeta_2 + \gamma)s(t) - \gamma s(t - \tau + T) + \mathbf{P}(t) < 0$  for  $s(t) \geq \kappa/(\zeta_2 - \zeta_1 - \gamma)$ . For sufficiently small  $\kappa$ , it can be guaranteed that the sliding mode on the surface  $\sigma = 0$  arises. The sliding motion equation in the perturbed case has the form

$$s(t) + \zeta_2 \int_{t-T}^t s(\mu) d\mu + \gamma \int_{t-\tau}^{t-T} s(\mu) d\mu - \sigma^* = \int_{t-T}^t p(\mu) d\mu. \quad (2.42)$$

Using some elements of the theory of integral equations one can be shown that  $s(t) \rightarrow s^* + O(T\kappa)$  as  $t \rightarrow +\infty$ , where  $O(\kappa T)$  denotes a function of the order  $T\kappa$ . This implies robustness of the control with respect to bounded perturbations and implies that the tracking error tends to zero as input delay  $T$  or perturbation magnitude  $\kappa$  tends to zero.

### 2.3.2 Machine learning control (MLC)

Machine learning control MLC has recently been proposed as a generic model-free strategy to control non-linear systems (Duriez *et al.*, 2016). Machine learning algorithms will be used to learn an effective control law  $\mathbf{b} = \mathbf{K}(\mathbf{s})$  using the system outputs (sensors  $\mathbf{s}$ ). Following this approach, the control laws are judged and optimized with respect to a problem-specific cost/objective function using genetic programming (Koza *et al.*, 1999).

#### Control problem

Let us consider a control system plant model of the form:

$$\dot{\mathbf{a}}(t) = \mathbf{F}(\mathbf{a}, \mathbf{b}) \quad (2.43)$$

$$\mathbf{s} = \mathbf{G}(\mathbf{a}) \quad (2.44)$$

$$\mathbf{b} = \mathbf{K}(\mathbf{s}) \quad (2.45)$$

where  $\mathbf{a} \in \mathbb{N}^{\mathbf{a}}$  is the system state,  $\mathbf{s} \in \mathbb{N}^{\mathbf{s}}$  an output vector sensing the state,  $\mathbf{b} \in \mathbb{N}^{\mathbf{b}}$  an input vector commanding the actuation, and  $\mathbf{F}$ ,  $\mathbf{G}$  and  $\mathbf{K}$  state-based functions. The objective is to construct the optimal controller  $\mathbf{b} = \mathbf{K}^{\text{opt}}(\mathbf{s})$  to minimize a given cost function  $J$ . Two main difficulties arise from this framework: construct the optimal control and find an adequate cost function for the problem specification. The first obstacle will be further dealt with in depth. Nonetheless, the definition of  $J(\mathbf{a}, \mathbf{b})$  depends on the control goal. To formulate a cost function  $J(\mathbf{a}, \mathbf{b})$  to correctly target the control objective, Duriez *et al.* (2016) presented a simplified cost function that considered separately the effects of the state  $\mathbf{a}$  and the actuation  $\mathbf{b}$ :

$$J(\mathbf{a}, \mathbf{b}) = J_{\mathbf{a}} + \gamma J_{\mathbf{b}} \quad (2.46)$$

where  $J_{\mathbf{a}}$  is the performance measure on the state of the system (in this case the experimental system) and  $J_{\mathbf{b}}$  is a value associated with the cost of actuation. A penalization  $\gamma$  is set to the system.  $\gamma = 0$  ignores actuation cost while large gamma neglects the state.

## Genetic programming

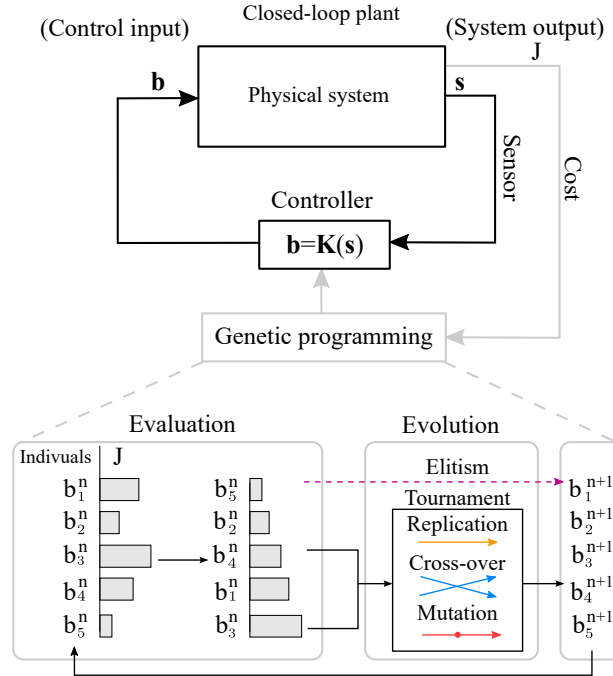


Figure 2.22 – Genetic programming implementation (example for 5 individuals) based on the Ph.D thesis work of Li (2017). In the learning process ('-' light grey line), each individual is evaluated and sorted based on their cost functions  $J_i$ . A new generation of control laws evolves by genetic operators (elitism, replication, mutation and crossover). The process finishes once the stop criterion is met.

Genetic programming GP is an evolutionary algorithm that optimizes both the structure and parameters of an input-output map (Koza, 1992). It is based on the propagation of generations of individuals  $m$  by selection through fitness. GP will be used in MLC in order to find the optimal control law. An initial generation  $n = 1$  of control law candidates  $b_1^1$ , hereafter called individuals, is randomly generated (like in a *Monte-Carlo* method) by combining user-defined functions, constants  $\mathbf{c}$  and sensor signals  $\mathbf{s}$ . Each individual is graded in the experiment yielding a cost value  $J$ . After the whole generation is evaluated, its individuals are sorted in ascending order based on  $J$  ( $J_1^n < J_2^n < \dots < J_{i-1}^n < J_i^n < \dots$ ). A new population  $b_1^2$  is then generated, with genetic operators (elitism, replication, crossover, and mutation), evolving the first generation. Elitism copies a given number of the fittest individuals, ensuring that next generation outperforms the previous one. The rest of the individual(s) are selected by a tournament process: an amount of randomly chosen individuals compete in a tournament and the winner (based on  $J$ ) is selected. Replication copies a statistically selected number of individuals. In crossover, two individuals exchange random sections of their structures. In mutation, individuals replace random portions of their instructions with random new values. After the new generation is filled, the evaluation of this generation can be pursued in the plant. This learning process will continue until some stopping criterion is met and the best individual (lowest  $J$ ) of the final generation is taken as MLC law  $\mathbf{b} = \mathbf{K}^{\text{opt}}(\mathbf{s})$ . This learning process is detailed in Figure 2.22.

In order to construct the control laws, two different representation approaches are employed. A traditional tree-based genetic programming TGP is first presented by Koza *et al.* (1999) and further improved by Duriez *et al.* (2016), and a simplified version called linear genetic programming LGP, presented in Li (2017). TGP and LGP are equivalent in the sense that any LGP-law can be expressed in TGP and vice versa. The difference is the linear versus recursive coding of LGP and TGP, respectively.

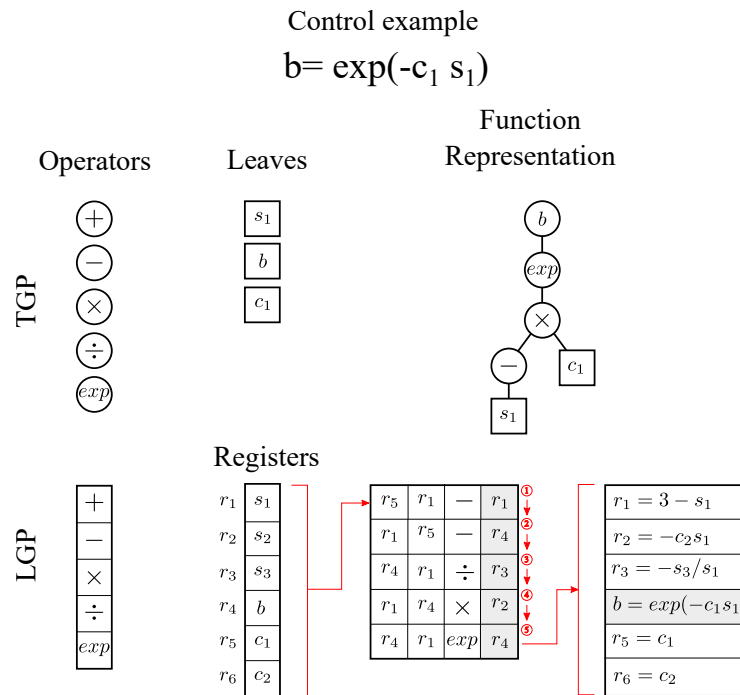


Figure 2.23 – Example of a control law given by  $b = \exp(-c_1 s_1)$  obtain through TGP and LGP. The functions in tree-based genetic programming are represented as a recursive tree, where the actuation signal  $b$  is the root, the leaves (square boxes) are the components of the sensor signals and constants, and the branches/nodes are representations of the elementary operators (+, -,  $\times$ ,  $\div$ , etc.). Linear genetic programming is represented as a function with a sequence of instructions written in lines on a matrix M, the instructions include an operation (column 3) on one or two registers  $r$  (column 1 and/or 2) and assigns the result of the operation to a destination register (column 4).

The main advantages of TGP are the simple interpretation of the expression trees, and their easy synchronization and manipulation in computation using a recursive language. The functions in tree-based genetic programming are represented as a recursive tree (Figure 2.23). The root of the tree is the actuation signal  $b$  and the leaves (square boxes) are the components of the sensor signals and constants. The leaves are connected through branches with nodes, which are representations of the elementary operators (+, -,  $\times$ ,  $\div$ , etc.).

On the other hand, LGP can register multiple contents in a graph-based data flow permitting more compact solutions, and it is applicable to systems with multiple actuators and sensors (multi-input multi-output MIMO). Linear genetic programming is represented as a function with a sequence of instructions, 'o' red circles in Figure 2.23. The term *linear* refers to the linear sequence of instructions (Brameier & Banzhaf, 2007). For simplification purposes, each instruction is written in a line on a matrix M with four columns (see Figure 2.23 as an example). An instruction includes an operation (column 3) on one or two registers  $r$  (column 1 and/or 2) and assigns the result of the operation to a destination register (column 4 in gray in Figure 2.23). The initial registers can be sensor inputs, sensor outputs, and constants. If the operation uses only one register, the second one is discarded. The destination registers are updated after each instruction. Once all the instructions are completed, the final expression of the output register ( $r_4$  in Figure 2.23) will be the representation of the final control law.

GP can also be used to explore open-loop control by including a time-periodic function  $h$  in the input control laws  $b = K(h)$ . This method enables an investigation on multi-frequency control which is hard to obtain if a single frequency approach is used. The creation of control laws based in multi-frequency forcing has a strong influence in turbulent flows, where the turbulent structures are highly related to multiple frequencies. Moreover, a combination of both multi-frequency forcing and sensor feedback control  $b = K(s, h)$ , hereafter called generalized feedback control, permits the selection between an open-loop approach  $b = K(h)$ , a closed-loop control  $b = K(s)$ , or a combination of both  $b = K(s, h)$  depending on which performs better. In the following, the open-loop frequency combination approach is termed as

Parameters	Air knife	Murata micro-blower
Actuator type	Pulsed-jet	Pulsed-jet
External fluid source required	Yes	No
Signal type	square	sin, square, etc.
Actuator area	60 cm <sup>2</sup>	4 cm <sup>2</sup>
Jet diameter	0.5 mm	0.86 mm
Jet area	75 mm <sup>2</sup>	2.32 mm <sup>2</sup>
Max velocity	100 l/min	1 l/min
Optimal frequency range [Hz]	0-500	0-100

Table 2.1 – Summary of the main characteristics for both actuation devices

Multi-frequency forcing and the closed-loop control will be referred as sensor-based feedback control.

## 2.4 Summary

The main mechanisms, actuation devices, control algorithms, etc. used in the experiments are summarized in this section. First, the investigation tools used during the work are defined and explained, i.e., static pressure probes, dynamic pressure probes, hot wire, and PIV. Even though the results obtained are mainly experimental, they require the use of processing methods such as spectral analysis, orthogonal decomposition in eigen-modes and, stochastic methods. This allows to describe the flow topology of the configurations and to better understand the associated physical phenomena.

Furthermore, two actuators are analysed and compared. A thorough dynamical characterization is done for both devices. On the one hand, air-knives are powerful actuators for flow control approaches. The ability to reach high velocities, caused by a narrow slot, make them compelling to control turbulent flows. Furthermore, the incorporation of a Coanda configuration makes this device suitable for industrial applications. However, two main drawbacks are presented for this actuator. The need of an external pressure supply might limit its functionality for industrial flow control. An ON-OFF signal might not be enough to apply innovative control strategies. On the other hand, the micro-blower has the ability to create a linear response when an input signal is assigned. Its extensibility (able to generate different forms of signals) and simplicity (does not need an external source of pressure) create interesting advantages for flow control strategies compared to other actuators. Moreover, its miniature design (less than 5cm<sup>2</sup> area) and low cost enables this actuator to be included in transport vehicles. The main limitation of this device is its low velocity and reduced velocity coverage. To clearly see the difference between each actuator, a summary of the device characteristics is presented in Table 2.1. The knowledge of the actuation strengths and weaknesses might give an insight into the optimal device to control turbulent flows.

In conclusion, the micro-blowers (possibility to use many actuators) have rich dynamics and low authority while the air-knife have a strong authority but with fewer dynamics. The goal is to balance both parameters in a small device. Even though the optimal actuator has not been found, strong efforts are made to create innovative tools to control flows.

Once the actuators are presented, it is crucial to study the control strategies that might drive the actuators. Here, two active control approaches are investigated: sliding mode control (SMC) and machine learning control (MLC). Sliding mode control is a robust closed-loop control technique to reduce and maintain at a desired point a predefined parameter. The goal is to minimize the parameter value and stabilize it regardless of external conditions. The control approach is based on an initial black-box model

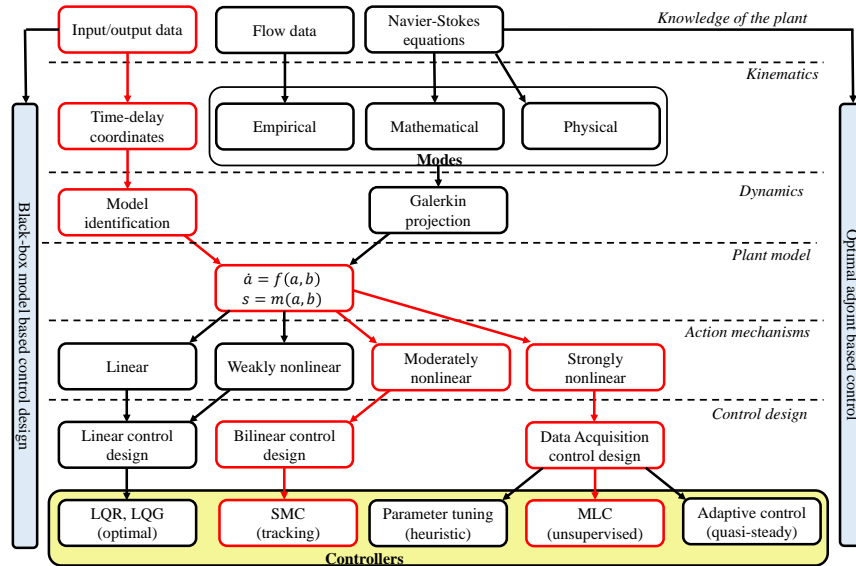


Figure 2.24 – Turbulence control roadmap based on Brunton & Noack (2015) for the both control strategies sliding mode control and machine learning control.

identification presented by Feingesicht (2017). A set of data is used for the model design. In principle, the control idea can be a compilation of open-loop control strategies. However, the actuation frequency has to be carefully selected in real-time depending on the external parameters up- and down-stream of the flow, otherwise, the actuation energy is wasted. The robustness and easy implementation in an experimental set-up makes SMC convenient for industrial applications. If the roadmap presented by Brunton & Noack (2015), Figure 2.24, is followed, this approach could be defined as a gray-box model, where an initial data set is needed to identify the system. The errors obtained in the model identification are attenuated by the control robustness. The model identification leads to a weak non-linear approach, more specifically, a bilinear control-design. The main advantages of this approach are the capability to reduce and keep a specific parameter to a desired value regardless of external flow variation, and high robustness. However, the control approach is not able to optimize the desired problem and doesn't take into account the actuation cost. The rapid switch from one condition to another might wear out the actuators.

Machine learning control is a simple model-free methodology to explore and optimize new feedback control actuation mechanisms. The control logic is chosen to minimize a problem-specific cost/objective function. Genetic programming is used to discover control laws in a high-dimensional search space. Two different representations of the control law are studied: tree-based genetic programming and linear genetic programming. Also three categories of GPC are investigated: an open-loop multi-frequency control  $\mathbf{b} = \mathbf{K}(\mathbf{h})$ , a sensor feedback control  $\mathbf{b} = \mathbf{K}(\mathbf{s})$  and a generalized feedback control  $\mathbf{b} = \mathbf{K}(\mathbf{s}, \mathbf{h})$ , comprising the sensors  $\mathbf{s}$  and the time-periodic functions  $\mathbf{h}$ . Thanks to its model-design independence, this approach can be interpreted as a black-box model. Turbulent flows are strong non-linear systems, making this simple approach attractive in feedback control of turbulent fluid systems. The most important asset of MLC is its efficiency to explore and optimize new control feedback actuation mechanisms in complex control configurations (single-input single-output SISO, single-input multi-output SIMO, multi-input single-output MISO, multi-input multi-output MIMO). This simple tool can be applied to numerous experimental applications. The principal constraint of this approach is its long training time. As seen in this chapter, SMC is a simple control focused on online adaptivity and MLC is a complex control with a single point optimization. A hybrid between SMC and MLC may provide adaptive control exploiting the best non-linear actuation mechanisms. The implementation of different control strategies can lead to revolutionary solutions in flow control.

# Backward-facing step

*Most of the results presented in this chapter are published in [Chovet et al. \(2017a\)](#) and [Chovet et al. \(2018a\)](#). The objective is to experimentally characterize and control the flow of a backward-facing step (BFS); the target will be to modify key parameters, such as internal and external separation lengths and recirculation area. Two control cases will be applied: periodic forcing and machine learning control. The actuators used to accomplish flow control are Murata micro-blowers. The dynamical behaviour of the unforced and actuated flows is further analysed. Throughout a flow reconstruction, using modal decomposition techniques, it will be possible to study the spatial characteristics of the flow downstream of the step.*

## Contents

---

3.1	Backward-facing step Experimental setup . . . . .	58
3.1.1	BFS configuration . . . . .	58
3.1.2	Sensor placement and actuation mechanism . . . . .	58
3.2	Baseline flow . . . . .	59
3.2.1	Flow statistics and dependencies . . . . .	60
3.2.2	Flow field dynamics . . . . .	66
3.3	Active flow control . . . . .	71
3.3.1	Periodic forcing . . . . .	71
3.3.2	Machine learning control (MLC) . . . . .	74
3.3.3	Actuation effects on the recirculation area . . . . .	78
3.3.4	Dynamical control mechanisms . . . . .	80
3.4	Summary . . . . .	84

---

### 3.1 Backward-facing step Experimental setup

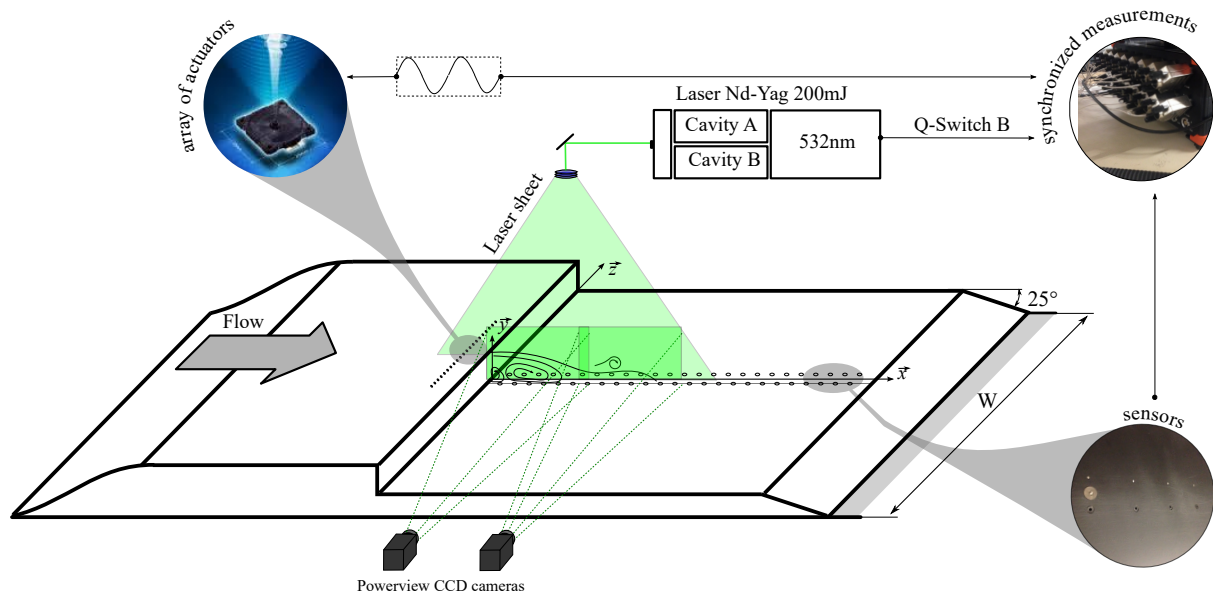


Figure 3.1 – Experimental setup of the backward-facing step. 3-dimensional sketch of the backward-facing step flow and reference system.

#### 3.1.1 BFS configuration

Experiments took place in the optically accessible closed-loop wind tunnel previously described in §2.1.1. The model, a backward-facing step BFS, is mounted in the middle of the test section and exactly fits the spanwise. An initial ramp followed by a regular floor is placed to guide the flow to the BFS. The step height  $H$  is 83 mm, resulting in an expansion ratio  $ER = W/(W - H)$  of 1.04, with  $W$  the wind tunnel height and width. The aspect ratio  $AR = W/H$  (based on the step height and width) is 24, assuring an effectively nominal two-dimensional flow (De Brederode & Bradshaw, 1978). Measurements were performed at various free stream velocities in the range of  $U_\infty = 5.7 - 33.0$  m/s corresponding to a Reynolds number range of  $Re_H = 31500 - 182600$ ; the latter based on the step height and the free stream velocity. The free stream flow velocity was measured by a Pitot tube at  $5H$  downstream of the step edge. The origin of the coordinate system is located at the edge of the step. The  $x$ -axis represents the streamwise flow direction, the  $y$ -axis the normal direction to the flow and the  $z$ -axis the spanwise or cross-stream one. The incoming boundary layer thickness taken at a distance  $H$  upstream of the step edge, and calculated with a pitot tube, is estimated to be equal to  $\delta_{99\%} = 0.7H$ , with a momentum thickness of  $\vartheta = 0.06H$ , calculated following the equation presented by Ma *et al.* (2017). In order to represent the parts above mentioned, a 3-dimensional view is shown in Figure 3.1.

#### 3.1.2 Sensor placement and actuation mechanism

A set of 25 static pressure taps were distributed downstream of the backward-facing step in the streamwise flow direction and  $0.2H$  from the mid-span in the spanwise direction. Probes were placed starting at 25 mm to 1225 mm every 50 mm ( $x_i/H = 0.6$ ) as shown in Figure 4.1(b). In addition, a second set of 25 sub-miniature piezo-resistive Kulite XCQ-062 sensors were also used. Flush-mounted Kulite transducers were placed at the same  $x_i$  location as the static ones but in the mid-span. The 25 sensor array extends up to  $14.75H$ . The velocity flow fields were obtained using a standard two-component TSI particle image

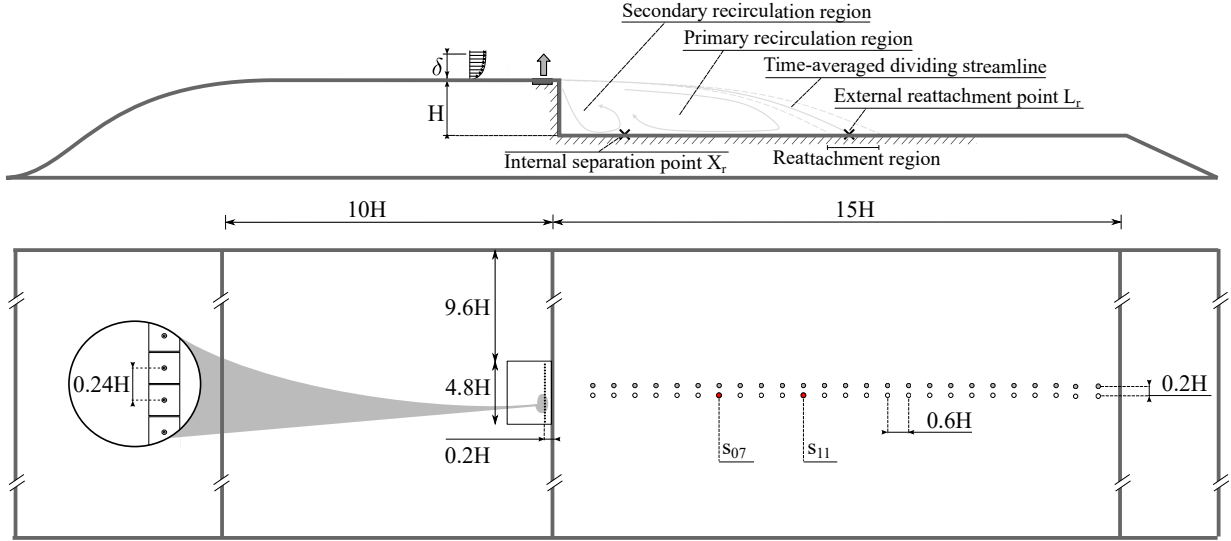


Figure 3.2 – Experimental setup of the backward-facing step. Top and side view of the model, with a focus on the sensor and actuation location.

velocimetry (PIV) system (explained in §2.1.1). The interrogation window size is  $16 \times 16$  pixels with an overlap of 50% and the magnitude ratio is 19.2 pixels/mm leading to a spatial resolution of 4mm. The PIV domain is about  $7.3H \times 1.8H$  on the x-y plane passing through the center of the backward-facing step. For every velocity tested, 2000 double-frame pictures were recorded to assure velocity field statistic convergence. For a dynamical aspect purpose, the unsteady pressure time-histories were recorded simultaneously with the PIV measurements. To achieve the synchronization, the Q-switch signal of the laser B was recorded simultaneously with the 25 pressure transducer signals using a 32-channel A/D converter Dewesoft data acquisition system, at a sampling frequency of 10 kHz and a cut-off filtered at 3 kHz, as shown in Figure 3.1.

The flow was forced through a row of 20 Murata micro-blowers (see §2.2.2). The row was placed on the spanwise center of the test section, covering 20 % of the test section width. This unactuated segment, from the actuation area to the walls, prevents flow interactions between the backward-facing step and the wall corners. Following the configuration presented in literature (Gautier *et al.*, 2015) and the actuator limitations due to design and mounting, the devices were placed upstream of the separation edge at a distance of  $0.2H$ , as shown in Figure 3.2. The distance between two neighbouring micro-blower nozzles is 20 mm ( $l_{jet} = 0.24H$ ). The jet air is introduced in the normal direction, in other words, perpendicularly to the free stream flow. This type of actuation creates a jet cross-flow with unstable dynamics. Mahesh (2013) thoroughly studied this type of flows and stated that they present complex instantaneous behaviour. Upon exiting the orifice, the jet tries to penetrate and expand into the cross-flow and in the process forms strong unsteady structures. The turbulence in this type of cross-flow is highly three-dimensional, anisotropic and in non-equilibrium. The pulsed micro-blowers were quantified using the momentum coefficient,

$$C_{\mu} = \frac{S_{jet} \cdot \frac{1}{T} \int_0^T u_{jet}^2 dt}{1/2 \cdot U_{\infty}^2 \cdot S_{\infty}}, \quad (3.1)$$

where  $S_{jet}$  is the outlet cross-section of the micro-jets and  $S_{\infty}$  is the reference surface of the BFS. In overall, the momentum coefficient had a constant value of 0.4 %. For more realistic images of the BFS model, actuation and sensor placement, please refer to Figure 3.3.

## 3.2 Baseline flow

The main characteristics of the unactuated baseline flow were first investigated and constitute the reference case for the subsequent actuated cases.



Figure 3.3 – Experimental setup of the backward-facing step. Images of the BFS

### 3.2.1 Flow statistics and dependencies

#### Mean flow structure and main parameters

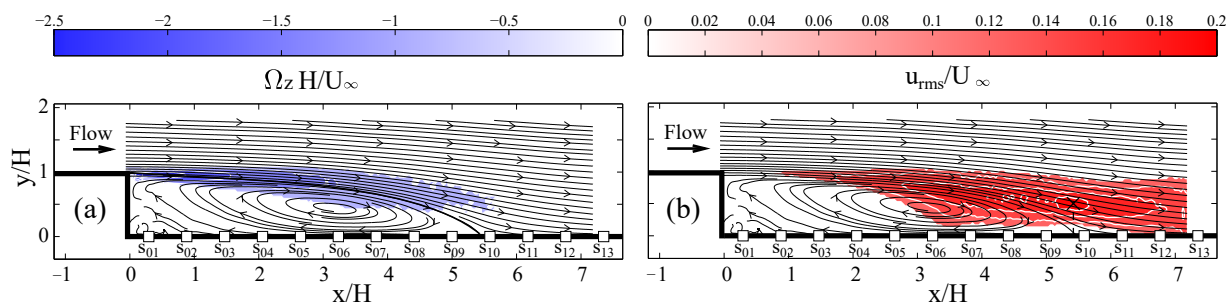


Figure 3.4 – (a) Non-dimensional mean vorticity  $\Omega_z H/U_\infty$  and associate streamlines for  $Re_H = 64200$ . Dark line denotes the streamline originated at the step edge, i.e.,  $x = 0, y = H$ . (b) Contour map of the streamwise rms-velocity ( $u_{rms}/U_\infty$ ) for  $Re_H = 64200$  with associated streamlines. 'x' black cross symbol denotes the maximum rms-velocity location.

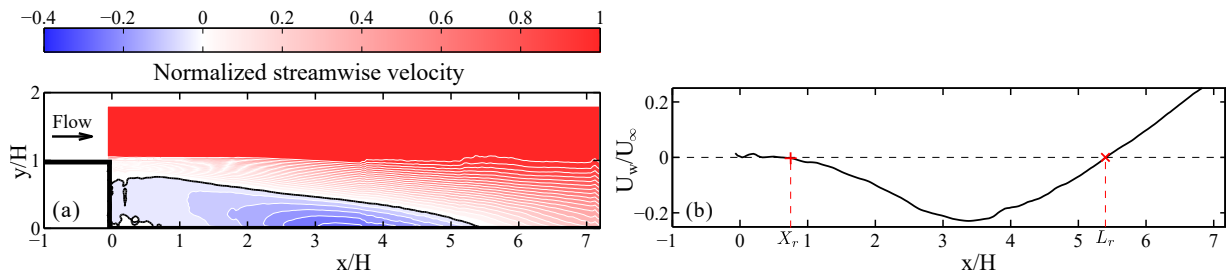
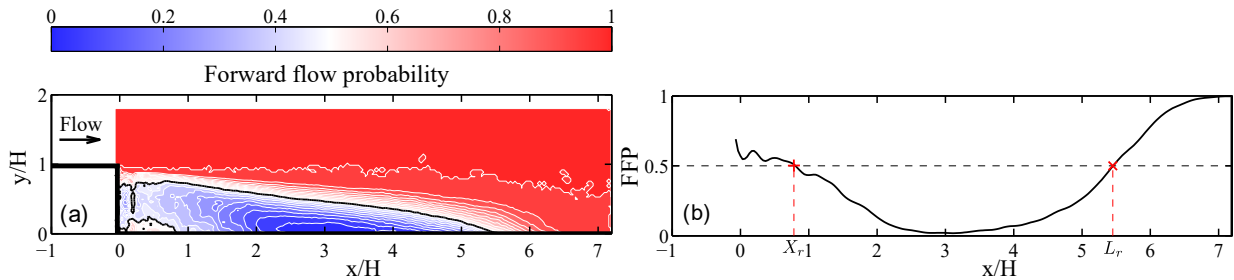
Flow characteristics are investigated for seven Reynolds numbers presented in Table 3.1. For all the cases studied, mean flow fields showed a classic backward-facing step flow topology. As an example, the non-dimensional mean vorticity field in the  $x$ - $y$  plane,  $\Omega_z H/U_\infty$ , with associated streamlines for  $Re_H = 64200$ , is plotted in Figure 3.4(a). The contour map of the mean spanwise vorticity underlines the boundary layer separation at the edge of the step. The formed shear layer is detached from the step, increasing in width throughout the streamwise direction. The transformation of this turbulent boundary layer on the free shear layer produces a separated flow. The shear layer is distributed predominantly around the mean separation streamlines and is globally represented in Figure 3.4(a), as the negative vorticity region. The mean separation streamlines, originated at the step edge, i.e.,  $x=0, y = H$ , and denoted as a dark line in Figure 3.4(a), impacts the surface at the mean external reattachment point. Beneath the shear layer, a primary recirculating region and a secondary recirculation bubble (closer to the step corner and commonly known as eddy corner) are also observed. In addition, the maximum streamwise rms-velocity is presented in Figure 3.4(b). This signature reaches a maximum level near the location where the flow “impinges” on the wall, as described by Farabee & Casarella (2017) and denoted with a 'x' black cross symbol in Figure 3.4(b). This position is strongly linked to the location of the maximum rms pressure coefficient.

On separating and reattaching flows, one of the most important values is the mean external reattachment length  $L_r$ , due to its use as a scaling parameter. Simpson (1996) introduced two different methods to obtain the detachment/reattachment length. Detachment  $D$  is the point where the time-averaged wall shear-stress (or the time-averaged velocity at the vicinity of the wall) is equal to zero. Transitory detachment/reattachment  $TD$  estimates the point where the forward flow probability FFP reaches a value of 50 %. Simpson (1996) states that  $D$  and  $TD$  are at the same  $x$ -location. These two methods are illustrated in Figure 3.5 and Figure 3.6 for  $Re_H = 64200$ . In order to experimentally estimate the mean

$U_\infty$ [m/s]	$Re_H$	$\delta/H$	$X_r/H$	$L_r/H$	Symbols
5.7	31500	0.68	0.87	5.62	□
7.6	42000	0.63	0.83	5.54	○
11.6	64200	0.57	0.76	5.41	◇
16.1	89100	0.53	0.71	5.37	▽
22.3	123400	0.50	0.69	5.32	△
28.0	154900	0.48	0.64	5.30	◁
33.0	182600	0.47	0.62	5.23	▷

Table 3.1 – Mean-flow parameters. Expansion ratio (ER=1.04)

reattachment length  $L_r$ , the first methodology extracts the near-wall velocity profile (Figure 3.5(b)) from the mean normalized streamwise velocity field (Figure 3.5(a)), while the second one extracts the near wall FFP (Figure 3.6(b)) from the FFP field (Figure 3.6(a)). Blue areas correspond to the recirculation region and solid lines represent the zero streamwise velocity and the 50 % FFP values for mean and transitory detachment lengths, respectively. Both cases showed a similar recirculation length around  $L_r \approx 5.3$  corroborating Simpson's statement. Spazzini *et al.* (1999) used the same methodology to calculate this length for lower Reynolds numbers. Another important parameter, normally not taken into account in previous investigations, is the mean external separation location ( $X_r$ ). To deduce the position of this point, both previous approaches were used (see '+' red plus symbols in Figure 3.5(b) and Figure 3.6(b)). Hereafter, results obtained from the TD methodology were used. Table 3.1 summarizes both  $L_r$  and  $X_r$  values, with respective boundary layers (calculated as  $\delta/H = 99 \%U_\infty$ ), for all Reynolds numbers.

Figure 3.5 – (a) Normalized streamwise velocity field, solid line denotes the zero streamwise velocity value, (b) Velocity profile extracted from (a) at  $y/H = 0.07$  for  $Re_H = 64200$ .Figure 3.6 – (a) Forward flow probability field; the solid line denotes the 50% value of the FFP, (b) FFP profile extracted from (a) at  $y/H = 0.07$  for  $Re_H = 64200$ .

### Flow statistics external parameters dependencies

As previously explained, the backward-facing step configuration is a noise amplifier class, thus, it is very sensitive to upstream perturbations. The separated flow structure can be particularly influenced by the inflow conditions. In this framework, planar backward-facing step flow has been the subject of numerous experimental investigations. However, there is a considerable scatter among the values reported in the literature, more specifically for the mean length of the recirculation or the mean- and rms- pressure

Authors	$Re_H$	$\delta/H$	ER	$L_r/H$	Symbols
Chun & Sung (1996)	33000	0.38	1.50	7.80	●
Driver & Seegmiller (1985)	37420	1.50	1.12	6.10±1.00	■
Westphal & Johnston (1984)	42000	0.40	1.67	8.60	▼
Durst & Tropea (1981)	1800-30000	-	1.06-2.05	5.00-11.0	▲
Nadge & Govardhan (2014)	5000-64000	0.18-0.76	1.10-2.50	5.00-8.80	◆
Li & Naguib (2005)	4300-13000	-	1.00	4.33-4.88	+
Heenan & Morrison (1998)	190000	0.21	1.10	5.50	◀
Hudy <i>et al.</i> (2007)	5980-32327	-	1.00	4.28-4.97	▶
Li <i>et al.</i> (2015)	9100	0.12	1.08	5.7	★

Table 3.2 – Mean-flow parameters for various authors

coefficients. The experimental investigations described herein address some of these unsolved discrepancies, in particular, the backward-facing step flow as a function of the Reynolds number and the expanding ratio ER. Durst & Tropea (1981) and more recently Nadge & Govardhan (2014) reported numerous investigations concerning the mean recirculation length dependencies for moderate Reynolds numbers. The authors concluded that both parameters,  $Re_H$  and ER, significantly influence the mean velocity field behind the step. The measurements of Adams & Johnston (1988a,b), at a fixed ER, showed that several parameters, such as the state of the separating boundary layer and the ratio between boundary layer thickness and height, can affect the reattachment length. Nevertheless, the main critical variable was clearly the expanding ratio. Nadge & Govardhan (2014) underlined that for low Reynolds number ( $Re_H \leq 10^4$ ), significant variations of the mean reattachment length can be observed. Once the Reynolds number is sufficiently high, a constant  $L_r$  appears. Figure 3.7 shows a compilation of some of the previous works reported in Table 3.2. Most of these studies refer to moderate Reynolds numbers and only a few of them cover high Reynolds numbers ( $Re_H \geq 10^5$ ). Heenan & Morrison (1998) studied the backward-facing step flow at  $Re_H = 190000$  with an ER = 1.1. The reattachment length at this expansion ratio is slightly lower than the saturation threshold given by Nadge & Govardhan (2014). Present results, reported in Figure 3.7, also showed a decrease of the mean reattachment length when the Reynolds number increases. In other words, for high Reynolds numbers, there is no constant trend as stated by Nadge & Govardhan (2014) but a decrease of the recirculation length due to another parameter. For higher Reynolds numbers, the reattachment length dependency with the Reynolds number disappears making the expanding ratio relevant to modify  $L_r$ .

In the same way, the mean-pressure coefficients found in the literature show strong variations. This coefficient is defined as  $C_p = (P - P_{ref}) / (1/2\rho U_\infty^2)$ , with  $P$  the mean pressure measured along the surface of the model and  $P_{ref}$ , a mean reference pressure measured with a static-pressure tap located upstream of the step edge. Figure 3.8 compares the present mean-pressure coefficients with those obtained from similar previous configurations. For the present results, the mean-pressure distributions show a classic, backward-facing step, pressure profile. Immediately downstream of the step, a positive  $C_p$  peak is clearly seen at  $7H$ . All the amplitudes studied from the mean-pressure coefficients are similar; only small variations close to the separation point can be observed. The present results are in agreement with those obtained by Heenan & Morrison (1998). However, some differences appear when a comparison is made with other references, e.g., data from Driver & Seegmiller (1985) ('●' black filled circle,  $Re_H = 37420$  and ER = 1.12) and Chun & Sung (1996) ('■' black filled square,  $Re_H = 33000$  and ER = 1.5). Figure 3.8 shows these discrepancies in the mean-pressure coefficient graphic due to an expansion ratio effect, corroborating the flow dependency of the latter.

Similar differences also appeared for the rms pressure coefficient. Present and previous rms pressure coefficients, defined as  $C_{p_{rms}} = p_{rms} / (1/2\rho U_\infty^2)$  are shown in Figure 3.8 as a function of  $x/L_r$ . The global

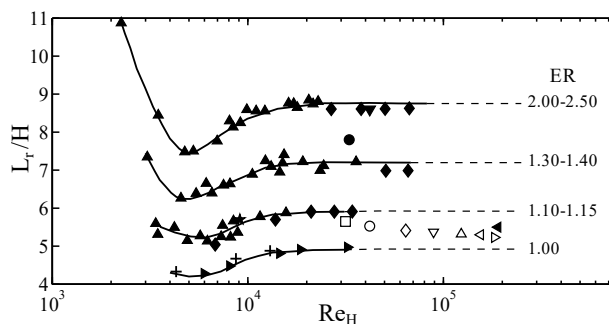


Figure 3.7 – Recirculation lengths against  $Re_H$  for various ER. Authors from Table 3.2 are also reported.

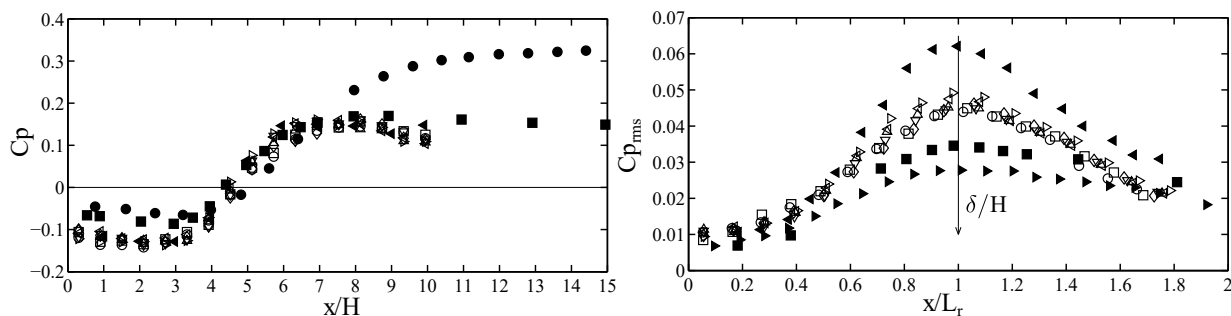


Figure 3.8 – Left: Mean pressure coefficients from present and previous studies. Right: Rms pressure coefficients from present and previous studies for ER between 1.10 and 1.15

behaviour of the rms pressure distribution obtained in the present work is consistent with the findings of [Castro & Castro \(1987\)](#) and [Hudy \*et al.\* \(2007\)](#). A peak in the rms pressure distribution is clearly observed for both past and present studies. Nonetheless, these maximum values are not located at the same  $x/L_r$ . This discrepancy could be related to the variations in the  $\delta/H$  ratio. Nevertheless, for the same ER (approximately  $ER \approx 1 - 1.1$ ) studied, the locations of the peaks are similar and are situated near the reattachment point ( $x/L_r = 1$ ). For higher expanding ratio, these locations were found to be around  $0.8L_r$ . In addition, the location of the maximum rms pressure coefficient is strongly linked to the maximum streamwise rms-velocity, see Figure 3.4. This near-wall interdependence, reattaching shear layer structure and wall rms-pressure in the reattachment region, is due to shear layer structures convecting downstream and producing an increasingly strong wall-pressure signature. This signature reaches a maximum level near the location where the flow “impinges” on the wall, as described by [Farabee & Casarella \(2017\)](#).

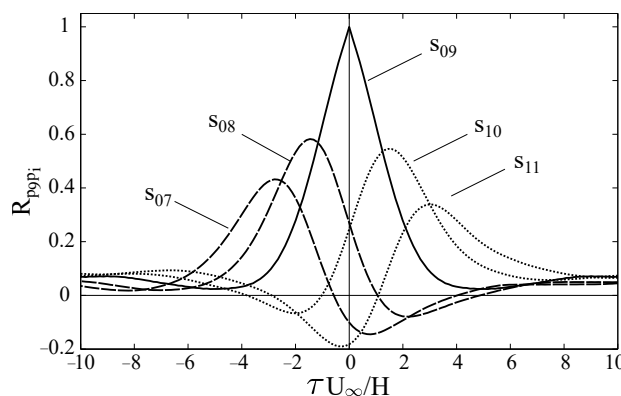


Figure 3.9 – Series of time delay cross-correlation of the wall-pressure fluctuations at a reference point locate near the reattachment length (sensor 9,  $x/L_r = 0.95$ ) for  $Re_H = 64200$ .

### Spatial characteristics in the streamwise direction

To better understand the coherent structure of separated flows and to globally observe the effect of the unsteady flow, the time delay cross-correlation of the wall-pressure fluctuations is calculated in the

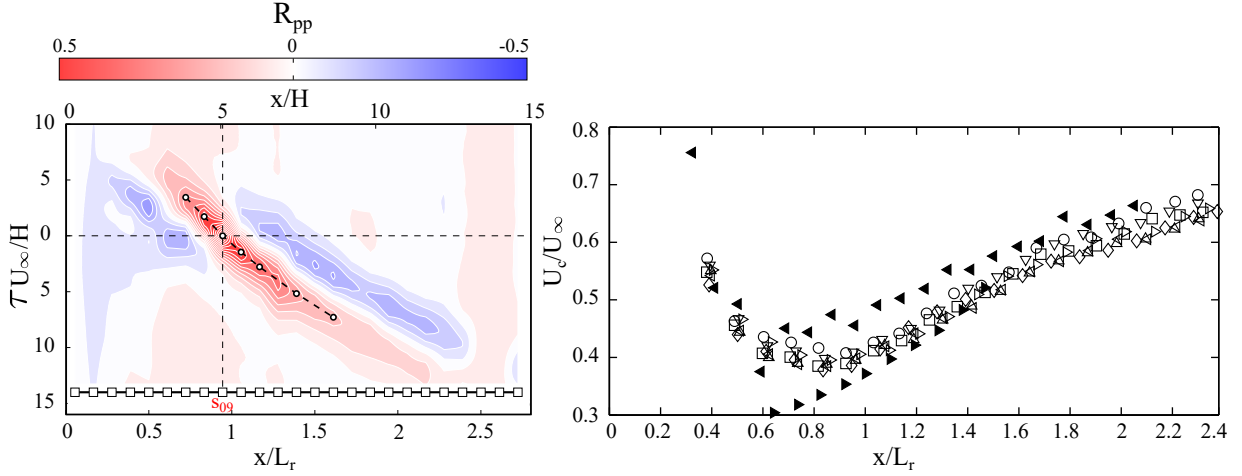


Figure 3.10 – Left: Contour map of the wall-pressure time delay cross correlation for a reference position close to the reattachment point ( $x/L_r = 0.95$ ) for  $Re_H = 64200$ . Right: Convection velocities from wall-pressure measurements for all the Reynolds numbers studied. Results were compared with the data of Heenan & Morrison (1998) & Hudy *et al.* (2007).

streamwise direction and defined as:

$$R_{pp}(x_0, \xi, t + \tau) = \frac{\langle p(x_0, t) \cdot p(x_0 + \xi, t + \tau) \rangle}{p_{rms}(x_0, t) \cdot p_{rms}(x_0 + \xi, t)}, \quad (3.2)$$

where  $x_0$  is the reference position. An example of a series of time delay cross-correlation of the wall-pressure fluctuations is plotted in Figure 3.9 for  $Re_H = 64200$ . The reference point  $x_0$  (sensor  $s_{09}$ ,  $x/L_r = 0.95$ ) is located near the reattachment region. For the sensors upstream of the reference point ('- -' dashed lines, sensors  $s_{07}$  and  $s_{08}$ ), the cross-correlation reaches a positive peak for a negative time delay ( $\tau U_\infty/H < 0$ ), and then drastically decreases arriving to a negative peak for a positive time delay ( $\tau U_\infty/H > 0$ ). The opposite behaviour is observed for the sensors downstream of the reference point ('· ·' pointed line, sensors  $s_{10}$  and  $s_{11}$ ), where the negative peak is seen at the negative time delay and the positive one is reached at the positive time delay. The negative-positive peaks, obtained from cross-correlation, confirm the intermittent motion of the vortices in both (positive and negative) streamwise directions. However, positive cross-correlation peaks are higher than the negative ones which imply that the structures shift more frequently in the positive direction. This behaviour is also known as dual dynamic mode.

To underline the behaviour of the flow structures and especially their velocity propagation (convection), a contour map of all the time delay cross-correlation of the wall-pressure fluctuations is plotted in Figure 3.10.Left. The normalized cross-correlation time delay ( $\tau U_\infty/H$ ) is plotted against the normalized streamwise coordinate where the correlation is obtained ( $x/L_r$ ). The contour bar represents the magnitude of the cross-correlation coefficient ( $R_{pp}$ ). A main positive-peak section (red area) and two negative-peak ones (blue areas) on either side of the main positive-peak section are clearly seen. The main peak is positioned around the time-shifted value, obtained at the largest positive correlation, between the wall-pressure signal, at this  $x$  location, and the reference point (near the reattachment length). 'o' white circles represent the maximum positive correlation for the main peak at each  $x$  location. The relation between these maximum positive correlations can be used to obtain an average of the convection velocities of the flow structures, which are dominant in the generation of surface-pressure fluctuations. This convection velocity, of the dominant wall-pressure generated flow structures, was calculated from the second-order fit ('- -' dashed line in Figure 3.10.Left) of the maximum positive cross-correlation peaks ('o' white circle) following the procedure proposed by Hudy *et al.* (2007). The convection velocities obtained for all the Reynolds numbers, and deduced from wall-pressure space-time correlations, are seen in Figure 3.10.Right. Results show a decrease of the convection velocities from  $U_c/U_\infty \approx 0.6$ , near the step edge, to  $U_c/U_\infty \approx 0.4$ , at  $x = 0.9L_r$ . After this point, values increase almost linearly. For the present case, the convection velocities appear to reach a minimum value near the position where the mean pressure coefficient is equal to zero  $x = 5H$ . A good qualitative agreement with Heenan & Morrison (1998) and Hudy *et al.* (2007) is observed, regardless

of the Reynolds numbers. Nevertheless, the data from Heenan & Morrison (1998) and Hudy *et al.* (2007) seem to reach minimum values lower than those obtained in the present work.

### Time evolution and frequency analysis

The space-time contour plots of instantaneous wall-pressure fluctuations normalized by the rms pressure  $p/p_{\text{rms}}$  are shown in Figure 3.11 for all the pressure sensors. The time-sequence is clearly representative of the full-time history of the instantaneous pressure signal. The downstream convective feature, denoted by a positive slope contour pattern is observed, especially for  $x > L_r$  (over the dashed line) where a downstream evolution of these large-scale vortices can be clearly seen. This behaviour was also reported by Lee & Sung (2001, 2002). The instantaneous negative peaks (blue area) in the wall-pressure fluctuations are associated with the passage of large-scale vortices (Lee & Sung, 2001). On the contrary, the region inside the recirculation bubble ( $x < L_r$  and under the dashed line) shows high-pressure fluctuations, scatter in the pattern, and some upstream motions and a negative slope contour pattern, e.g.,  $\tau U_\infty/H \approx 35$  in Figure 3.11. It is also interesting to observe that the measurements presented here appear to confirm the dual dynamical mode highlighted by the cross-correlation of the wall-pressure fluctuations.

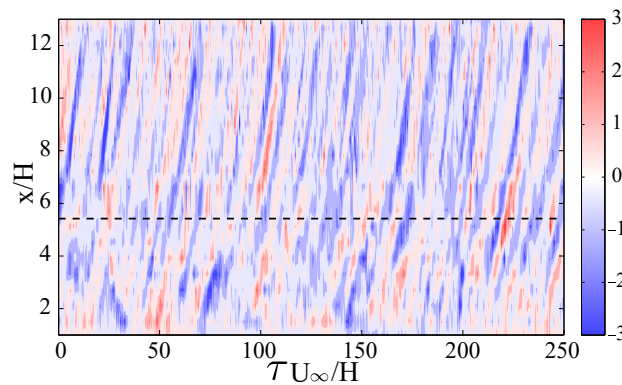


Figure 3.11 – Space-time contour plots of instantaneous wall-pressure fluctuations normalized by the rms pressure  $p/p_{\text{rms}}$  for  $Re_H = 64200$ . '- - -' dashed line denotes the reattachment point.

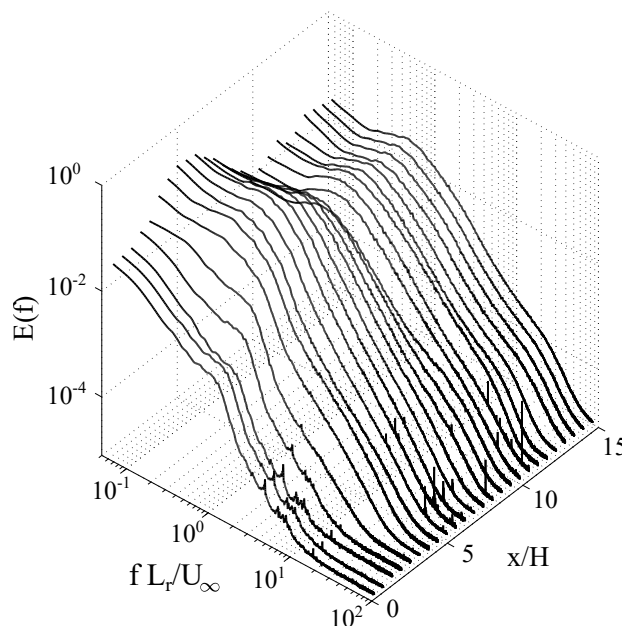


Figure 3.12 – Power spectra of wall-pressure fluctuations for different  $x/h$  locations at  $Re_H = 64200$ .

Figure 3.12 shows a log-log plot of the pressure fluctuation spectra at several  $x/H$  locations downstream the step at  $Re_H = 64200$ . The dynamical behaviours change as a function of the probe position. Four different regions can be identified and showed the global behaviour of the flow downstream the backward-

facing step. The first region, situated downstream of the step edge up to  $x/H \approx 1.5$  ( $x/L_T < 0.3$ ) shows low-pressure fluctuations where the spectra are dominated by both low- and high-frequency fluctuations. The second region represents a transition that occurs from the previous frequency peaks, at  $x/H \approx 1.5$  ( $x/L_T \approx 0.3$ ), to a merged frequency value, at  $x/H \approx 4.5$  ( $x/L_T < 0.8$ ). The third one corresponds to the recirculation region from  $x/H \approx 4.5$  to 6.5, where the pressure fluctuations are strong and high energy levels are clearly visible; this behaviour is consistent with the pressure coefficient results in Figure 3.8. The last region represents the reattached zone where the behaviour approaches a typical turbulent boundary layer spectrum. This global mechanism is also reported for the same configuration but for low Reynolds numbers by Spazzini *et al.* (1999).

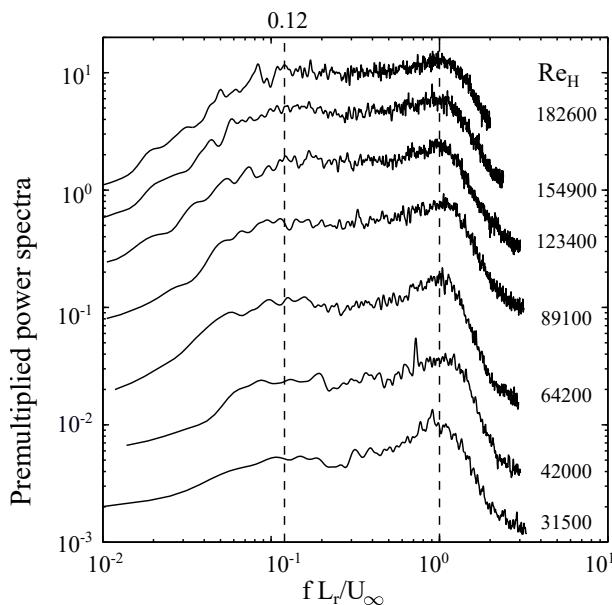


Figure 3.13 – Non-dimensional premultiplied power spectra of fluctuating wall-pressure measured at  $x/H = 1.5$  for the various Reynolds numbers studied. Premultiplied power spectra is define as  $E(f).f/p_{rms}^2$ .

In the literature (Lee & Sung, 2001; Kiya & Sasaki, 1985; Cherry *et al.*, 1984), it is generally accepted, for low Strouhal numbers, that a high frequency corresponds to vortex formation and shedding, while a lower one is related to the flapping motion of the whole flow field. In order to analyse the behaviour of the low frequencies in the flow field and their Reynolds number dependency, premultiplied pressure fluctuation power spectra were evaluated at  $x/H = 1.5$  from the step edge, where the flow is clearly dominated by low frequencies. Several observations have been previously reported for backward-facing step flows at low Reynolds numbers: Li & Naguib (2005) found frequency peaks at 0.1 and 0.65 and Spazzini *et al.* (1999) obtained frequency peaks at 0.08 and 1.0. Peak frequencies of 0.11 and 0.50 were found by Lee & Sung (2001) and of 0.18 and 0.6 by Driver *et al.* (1987). Present results are shown in Figure 3.13 for all Reynolds numbers studied. Two frequency peaks can be observed. A first bump  $fL_T/U_\infty \approx 0.12$  corresponds to a classic well-defined flapping frequency and a higher peak at around  $fL_T/U_\infty = 1$  that could be related to the shedding phenomena.

### 3.2.2 Flow field dynamics

#### Instantaneous flow structures

Once the power spectra reveals the key frequency peaks, it is important to determine which type of vorticity structures are present in the flow. Instantaneous structures play an important role in the dynamics of the flow and are largely responsible for the shear layer growth and momentum transfer across the shear layer. Separated flows are at the origin of strong vortices (Lee & Sung, 2002) and backward-facing flow presents

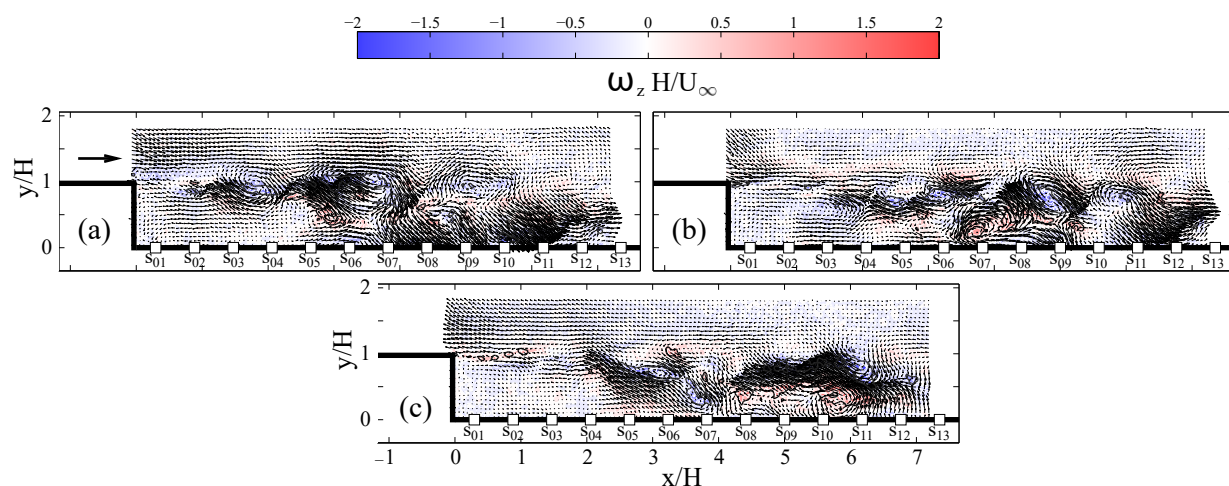


Figure 3.14 – Non-dimensional, fluctuating velocity fields for  $Re_H = 64200$  at various snapshot instant (a) #100, (b) #101, (c) #102. Contour bar indicates the magnitude of the normalized fluctuating vorticity,  $\omega_z H/U_\infty$  illustrating vortical structures in the shear layer. Vorticity levels were plotted as contour plot enhancing the visibility of the dominant features in the flow field.

isolated, spanwise vortical structures in the shear layer. These structures originate from Kelvin–Helmholtz instabilities and grow in size until eventually they roll-up into discrete vortical structures. These vortices can be seen in the fluctuating velocity fields obtained from PIV. Consecutive fluctuating snapshots #100 to #102 are presented in Figures 3.14(a) to Figure 3.14(c), respectively. Some complex interaction phenomena can be qualitatively seen before the reattachment. Following the literature, it is known that at the step edge, the turbulent boundary layer separates and forms a thin shear layer. Due to the Kelvin-Helmholtz instability, the shear layer rolls up to form small vortices with a size equivalent to the thickness of the shear layer. An array of these vortices can be observed close to the separation point, Figure 3.14(c). However, [Hudy et al. \(2007\)](#) proposed a new scenario for flow structure development; they introduced the concept of “wake mode”, in place of the typical “shear layer mode”. Instead of growing inside the shear layer and continuously move downstream, this new concept assumes that flow structures grow in place. The fluctuating velocity PIV in Figure 3.14(a) shows a strong structure transition close to  $x/H = 2$ , corroborating their statement. In the region between the step edge and  $x/H = 2$ , small structures, driven by the shear layer, are observed (e.g., Figure 3.14(c)). However, after  $x/H = 2$ , most of the flow structures show an important spatial correlation leading to large flow structure features as seen in Figures 3.14(a) and (b). Also, for  $x/H > 2$  and more specifically near the mean reattachment point, the flow structures are strongly linked to the wall-pressure footprint as illustrated in Figure 3.15. The normalized streamwise velocity and the pressure correlation coefficient shows, in Figure 3.15(a), a strong elongated positive level as a result of flow structure convection. A negative peak is also observed at approximately  $1.5H$ . This peak underlines the vortical velocity behaviour also seen by the normalized normal velocity and pressure correlation coefficient in Figure 3.15(b). This behaviour is similar for all the other sensors and Reynolds numbers studied. This high degree of correlation allows using stochastic approaches in order to deeply understand the flow dynamics and describe the velocity/vorticity fluctuations.

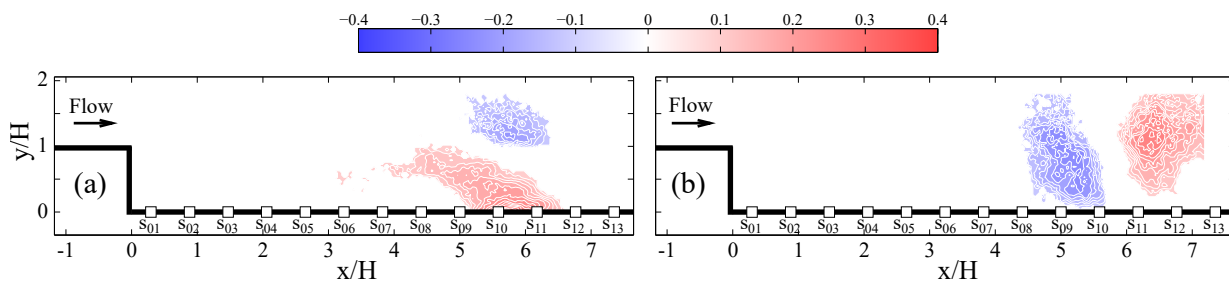


Figure 3.15 – Pressure/velocity correlation coefficient for sensor 10 and  $Re_H = 64200$ , (a) Normalized streamwise velocity and pressure correlation coefficient, (b) Normalized normal velocity and pressure correlation coefficient. Correlation levels between -0.1 and 0.1 were set at zero in order to minimize noise in the contour plots enhancing the visibility of the dominant correlations.

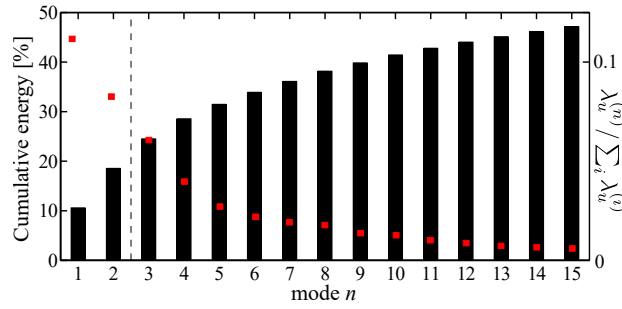


Figure 3.16 – Cumulative energy from the POD decomposition of the velocity fields for  $Re_H = 64200$ . '■' red square symbols denote the normalized mean square energy.

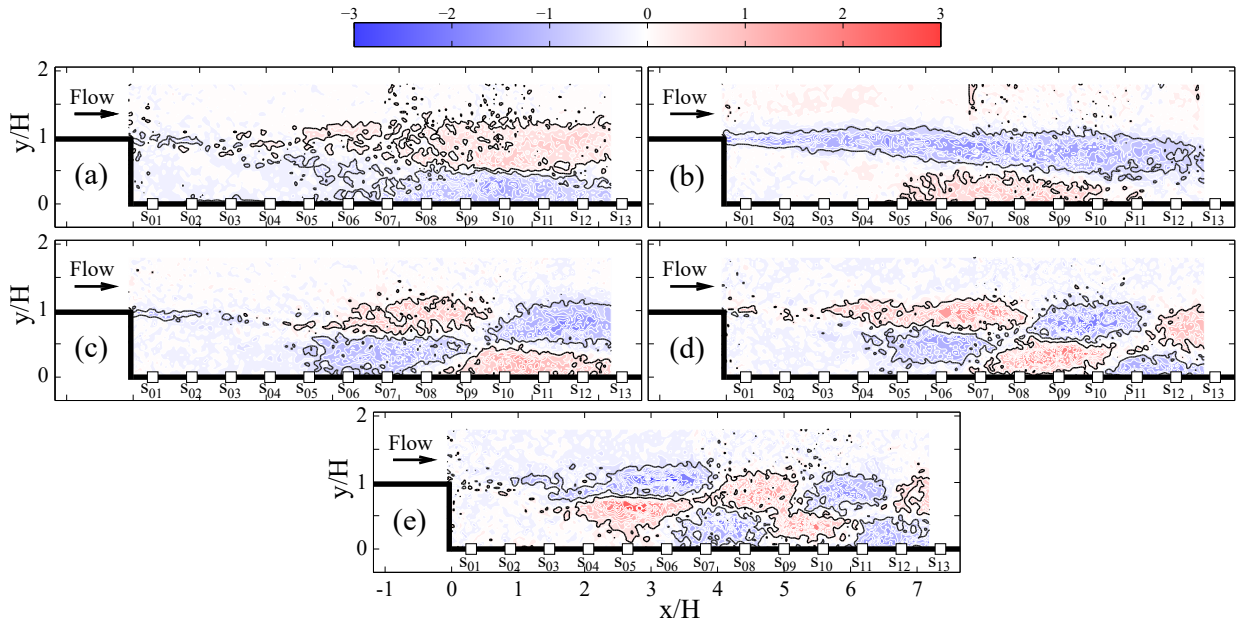


Figure 3.17 – Low-order POD velocity modes: (a) mode 1, (b) mode 2, (c) mode 3, (d) mode 4, (e) mode 5. Contour map shows vorticity calculated from the corresponding POD velocity-base function and normalized with the step height and free stream velocity  $U_\infty$  ( $\omega_z H / U_\infty$ ). Vorticity levels between  $-0.5$  and  $0.5$  were set at zero in order to minimize noise in the contour plots enhancing the visibility of the dominant feature of the modes.

### POD and stochastic results

PIV is able to record two thousand instantaneous two-component velocity fields. The volume of these PIV measurements is sufficient to perform a POD analysis to reveal the statistically dominant structures of the flow. Figure 3.16 shows the cumulative energy of the first fifteen velocity modes with the corresponding normalized mean square energy, defined as  $\lambda_u^{(n)} / \sum_i \lambda_u^{(i)}$ . The energy fraction of the first and second POD modes were found to contain almost 20 % of the total flow energy; the first fifteen modes comprise 50 % and the 200 first modes constitute up to 90 %. Therefore, since the first 200 modes include most of the flow energy, modes up to this value were taken into account. [Ma et al. \(2003\)](#) also indicated that the experimental modes above the fifth were contaminated by noise. Figure 3.17 shows the low-order POD velocity modes (for  $n=1$  to 5) with corresponding vorticity modes. The POD basis functions are non-dimensional and the vorticity calculated from the POD mode  $\omega_z$  is normalized with the step height  $H$  and the free stream velocity  $U_\infty$ . These modes represent the most common events being developed in the fluctuating velocity/vorticity fields. Modes 1 to 5, from the vorticity decomposition shown in Figure 3.17, contribute to approximately 30 % of the total energy. This small energy contribution, compared to the total fluctuating kinetic energy in the flow, suggests a greater diversity of the flow structures. Typical patterns in the POD spatial modes are clearly seen: the two first modes present elongated vorticity regions, while the others show uniformly shaped vortical structures (either positive or negative). The round and regular shape in the streamwise direction and the relatively small degree of elongation might be related to

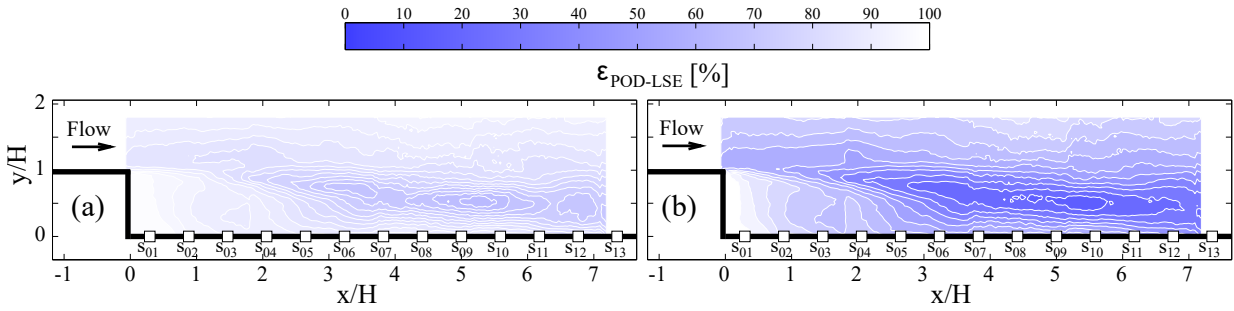


Figure 3.18 – Contour map of the normalized mean-square estimation error  $\epsilon$  from MLSE and MQSE for  $n=200$  POD modes across the whole domain.

a strong organization of vortical structures in space (Kostas *et al.*, 2002).

Whereas the preceding discussion was devoted to the analysis of the instantaneous large-scale vortical structures, based on PIV snapshots, the unsteady aspects of the flapping motion will now be studied. In order to further examine the relation between the flapping motion and the wall-pressure fluctuation in the frequency domain, the previously described MLSE/MQSE complementary techniques are used. In the present case, the conditional average and its approximations via stochastic approach are not able to accurately describe the velocity fluctuations, as mentioned by Murray & Ukeiley (2007). They found out that the MQSE can successfully estimate the structure of the complex cavity flow field using a few wall-pressure measurements. However, previous studies (Tinney *et al.*, 2008; Hudy *et al.*, 2007) suggest that the QSE might be less efficient than the LSE. The selection of the estimation approach will depend on how thorough the large-scale structures will be analysed. To evaluate the accuracy of the two different approximations, MLSE/MQSE, local estimation errors defined as  $\epsilon = \langle (u(t) - \tilde{u}(t))^2 \rangle / \langle u(t)^2 \rangle$  are computed. The parameter  $\epsilon$  describes the fraction of the original variance in  $u(t)$  which has not been recovered by the estimated  $\tilde{u}(t)$ . Furthermore,  $\epsilon$  is bound between  $[0, 1]$ . The estimation accuracy of both, the MLSE/MQSE, complementary approaches is presented in Figure 3.18 by the contour map of the  $\epsilon$  distribution. The quadratic form technique MQSE is chosen as it guarantees a satisfying reconstruction of the whole flow field investigated and strongly highlights the reattachment region, as shown in Figure 3.18(b). To further emphasize the ability of the quadratic complementary technique to reconstruct the flow field, the original PIV and both estimation snapshots of time histories of the five first temporal coefficients, obtained from POD, are shown in Figure 3.19. Even though a short part of the time histories is compared with those estimated, an overall agreement is observed. It can be seen from Figure 3.19 that the quadratic reconstruction MQSE ('—' blue line) fits better to the original PIV ('◇' diamond symbol) than the linear estimation MLSE ('—' red line).

The non-dimensional premultiplied power spectra of the estimated MQSE temporal coefficients for mode 1 to 5 are plotted in Figure 3.20 and compared to the non-dimensional premultiplied power spectra of the fluctuating wall-pressure measured at  $x/H = 1.5$  for  $Re_H = 64200$ . It is clearly seen from the figure that the two first modes exhibit a dominant peak at  $fL_r/U_\infty = 0.12$  corresponding to the flapping frequency. The other modes highlight a transitioning and increasing peak associated with the shedding frequency. The peak variation throughout the frequency range might be due to the fact that the shedding phenomenon is known as a quasi-periodic instability (broadband phenomenon) or as a consequence of experimental data error (commonly exhibited for high energetic modes). This result suggests that the first two modes could be retained if the interest is focused on the low-frequency large-scale dynamics of the recirculation region which, intrinsically, is closely related to the flapping mode, as previously observed by Fadla *et al.* (2016).

The causality relationship between wall-pressure sensors and temporal POD coefficients was investigated. Correlations  $\langle \tilde{a}_i \cdot p_j \rangle$  between the fluctuating wall-pressure  $p_j$  and the temporal POD coefficients (1<sup>st</sup>, 5<sup>th</sup> and 200<sup>th</sup>) are shown in Figure 3.21. A high positive correlation between the wall-pressure and the 1<sup>st</sup> POD mode for  $x/H < 2$  and a strong negative peak around  $x/H \approx 6 - 7$  are observed in Figure 3.21

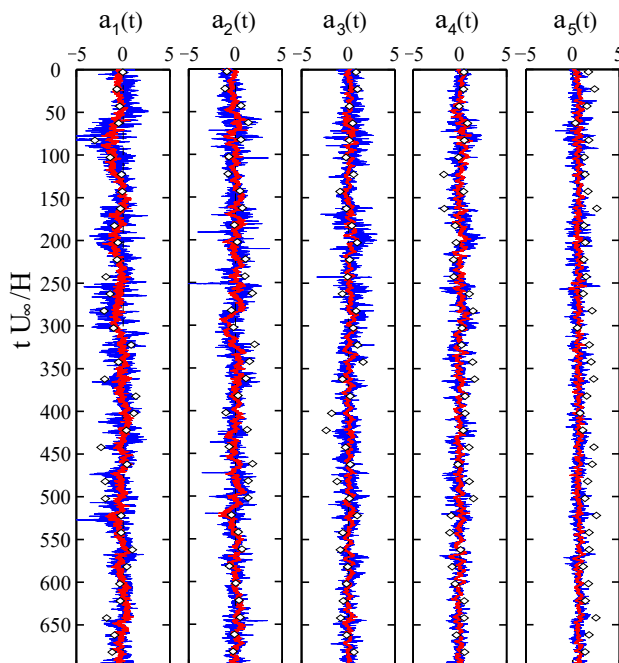


Figure 3.19 – Comparisons between the original ('◇' diamond symbol) and estimated MLSE ('—' red line) and MQSE ('—' blue line) temporal coefficients for the POD mode 1 to 5.

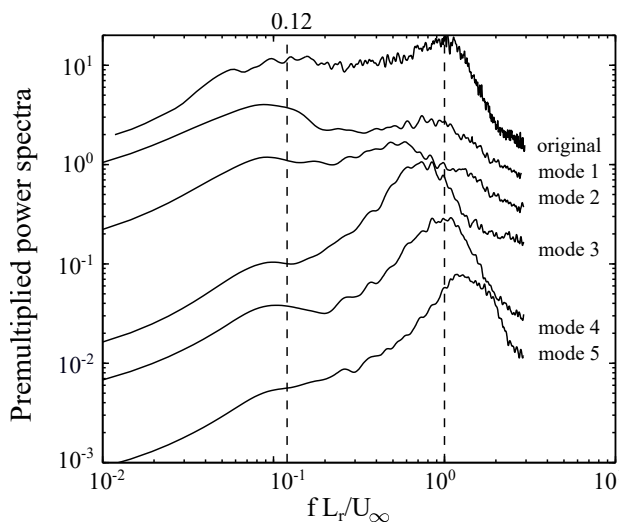


Figure 3.20 – Non-dimensional premultiplied power spectra of the estimated MLSE temporal coefficients for mode 1 to 5 compared to the non-dimensional premultiplied power spectra of the fluctuating wall-pressure measured at  $x/H = 1.5$  for  $Re_H = 64200$ .

('—' black line).

These high peaks highlight that a strong correlation of the flapping phenomena, linked to the 1<sup>st</sup> POD mode, is presented close to the step edge and near the reattachment region, where the shear layer impinges the wall. The introduction of a time delay  $\tau$  in the correlation  $\langle \tilde{a}_i(t + \tau).p_j(t) \rangle$  (not shown here) makes evident a phase opposition of the correlation between the pressure measured inside the recirculation area  $x/H < 5$  and the one measured outside  $x/H > 5$ , positive and negative peaks, respectively. This oscillating behaviour corroborates the breathing motion of the shear layer. Alternating negative and positive peaks, obtained from the correlation between the pressure and the 5<sup>th</sup> POD mode, are clearly seen from  $x/H = 2$  to the end of the domain. This result illustrates the shedding process, associated to POD decomposition, and emphasizes that the modes higher than 2 are sensitive to the dynamics of large-scale structures, as previously observed in the spectral analysis. The correlation between the pressure and the 200<sup>th</sup> POD mode is also plotted to confirm the low correlation level for higher order modes.

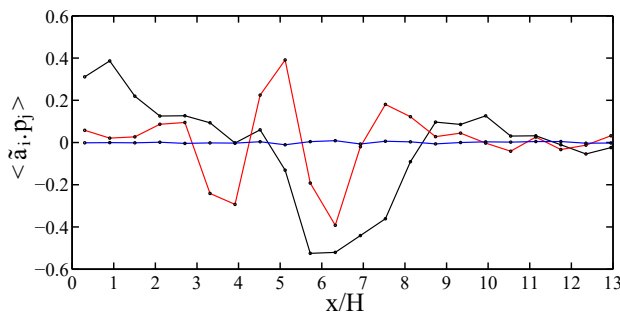


Figure 3.21 – Correlation between the fluctuating wall-pressure,  $p_j$  and the estimated MQSE temporal coefficients for mode 1 ('—' black line), 5 ('—' red line) and 200 ('—' blue line).

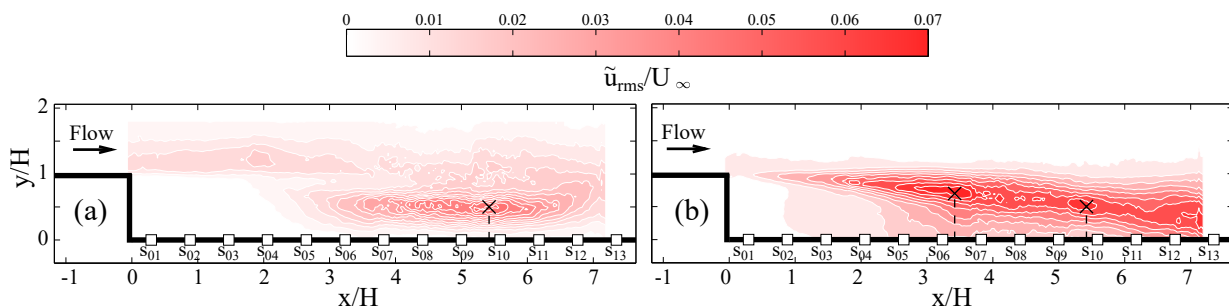


Figure 3.22 – (a) Reconstruction MQSE modes 1 and 2, (b) Reconstruction MQSE modes 3 à 200.

Finally, an estimation of the normalized root-mean-square streamwise velocity  $\tilde{u}_{rms}/U_\infty$  is given for the two first POD modes (Figure 3.22(a)) and for the POD modes between 3 and 200 (Figure 3.22(b)). A strong peak of the first  $\tilde{u}_{rms}/U_\infty$  of the two modes (35% of the total  $u_{rms}/U_\infty$  value) was obtained close to the shear layer impact region, around  $x = L_T$ . The  $\tilde{u}_{rms}/U_\infty$  of the higher modes (3 to 200) exhibits two peaks (contributing to 50% of the global  $\tilde{u}_{rms}/U_\infty$  value); one close to the reattachment zone around  $x = L_T$ , was also obtained in Figure 3.22(a), and a secondary peak located close to the region where the large structure commonly grows in size, i.e.,  $x/H = 3.5$ . This last remark is in agreement with the results of [Hudy et al. \(2007\)](#), stating that there is a particular region, close to the minimum value of the reversal wall-flow velocity, where the structures grow in place instead of a slow continuous formation, as traditionally assumed in the literature.

### 3.3 Active flow control

The unsteady behaviour of a turbulent flow will be now investigated under active flow control actuation. The goal will be to experimentally reduce the recirculation zone. Measurements were performed at a free stream velocity of  $U_\infty = 5.7\text{m/s}$  corresponding to  $Re_H = 30450$  ( $Re_\delta = 22825$ ). As previously described in §3.1.2, the flow is manipulated by a row of micro-blowers (pulsed jets), which are able to generate unsteady jet proportional to any variable  $\mathbf{DC}$ . An initial pulsing jet injection, at a predefined forcing frequency, will be applied to effectively reduce the reattachment point. Furthermore, MLC is used to perform an exploratory research to obtain an innovative control law.

#### 3.3.1 Periodic forcing

To actively control the flow, a first set of experiments were carried out varying the frequency of the periodic actuation. The Strouhal of the local forcing frequency actuation was changed in the range of  $0.045 \leq St_a \leq 0.453$ , based on the actuation frequency  $f_a$  and the step height (see Eq.(3.3)). This range is considered as low-frequency perturbation. Another way to dimensionlessly define the actuation frequency, and to study the reattachment length, is through the momentum thickness. [Chun & Sung \(1998\)](#) stated

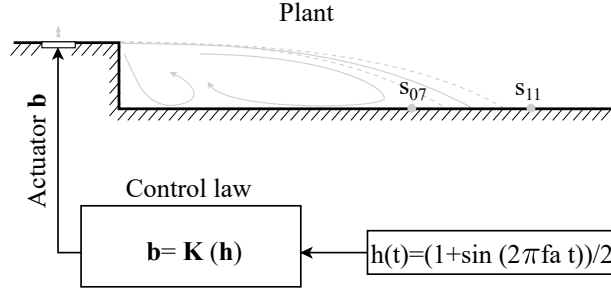


Figure 3.23 – Diagram of periodic forcing architecture

that the reduced reattachment length is closely related to the increased growth rate of the shear layer and the curvature toward the wall. Based on the momentum thickness  $\vartheta = 0.06H$  (calculated following the equation presented by [Ma et al. \(2003, 2017\)](#)), a different version of the forcing frequency can be defined as  $St_{\vartheta} = \frac{f_a \cdot \vartheta}{U_{\infty}}$ . Taking into account this consideration, the range of periodic forcing based on the boundary layer thickness will be between  $0.0029 \leq St_{\vartheta} \leq 0.029$ . For the present work, three different dimensionless frequencies, or Strouhal number, will be used for the characterization of the actuation efficiency, defined as:

$$St_a = \frac{f_a H}{U_{\infty}} \quad (3.3)$$

$$St_H = \frac{f H}{U_{\infty}} \quad (3.4)$$

and

$$St = \frac{f_a L_{r0}}{U_{\infty}}, \quad (3.5)$$

where  $L_{r0}$  is the external separation length, commonly known as the recirculation point of the unactuated flow. Hereafter, the study will be based on the Strouhal number  $St_a$ . The forcing actuation was designed to follow the expression,  $\mathbf{b}^{\diamond}(t) = V_{jet} (1 + \sin(2\pi f_a t))/2$ , where  $V_{jet}$  is the velocity actuation amplitude, set constant to 25m/s (corresponding to 20V), and  $f_a$  the frequency of the actuation which yields a velocity ratio of  $VR = u_{jet}/U_{\infty} = 4.54$ . For a further understanding of the application of the periodic forcing strategy, a diagram of the plant model is displayed in Figure 3.23, defining the input/output parameters of the physical system used for flow control.

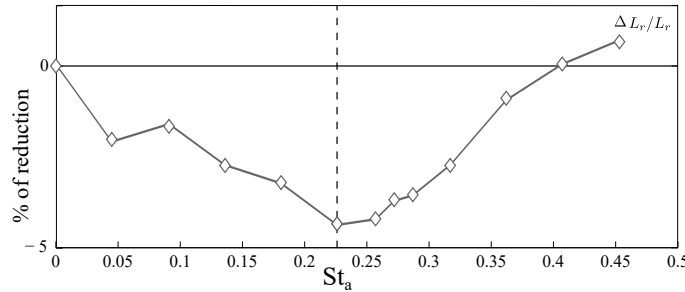


Figure 3.24 – External reattachment length  $L_r$  as a function of the actuation Strouhal number  $St_a$ . Note that no controlled case is reported here as  $St_a = 0$ .

Both the internal and external separation points and the separation area are extracted following the methodology described in §3.2.1 and plotted against the actuation Strouhal Number. Figure 3.24 shows the results of the external separation points  $L_r$  for all the actuated frequencies studied. The external reattachment length and the recirculation area first decreased with increasing  $St_a$  before they reach a minimum at  $St_a = 0.226$  and then increased again; this behaviour was stronger for  $A_r$ . It is worth noting

that for  $St_a = 0.091$ , the  $L_r$  value is slightly higher than those closer to it, giving a non-monotonic change. This might be due to some measurement fluctuation for experimental turbulent flows. In contrast, the internal separation point increases and decreases reaching a peak at the same actuated frequency  $St_a = 0.226$ , denoted with a dashed line. The optimal forcing frequency, among the ones studied, was observed at  $St_a = 0.226$  and could be associated with the shedding phenomena. If the Strouhal number based on the momentum thickness is taken into account, an optimal Strouhal number is obtained of  $St_\theta = 0.014$ , which agrees well with previous investigations (Chun & Sung, 1998; Hasan, 1992; Ma *et al.*, 2017).

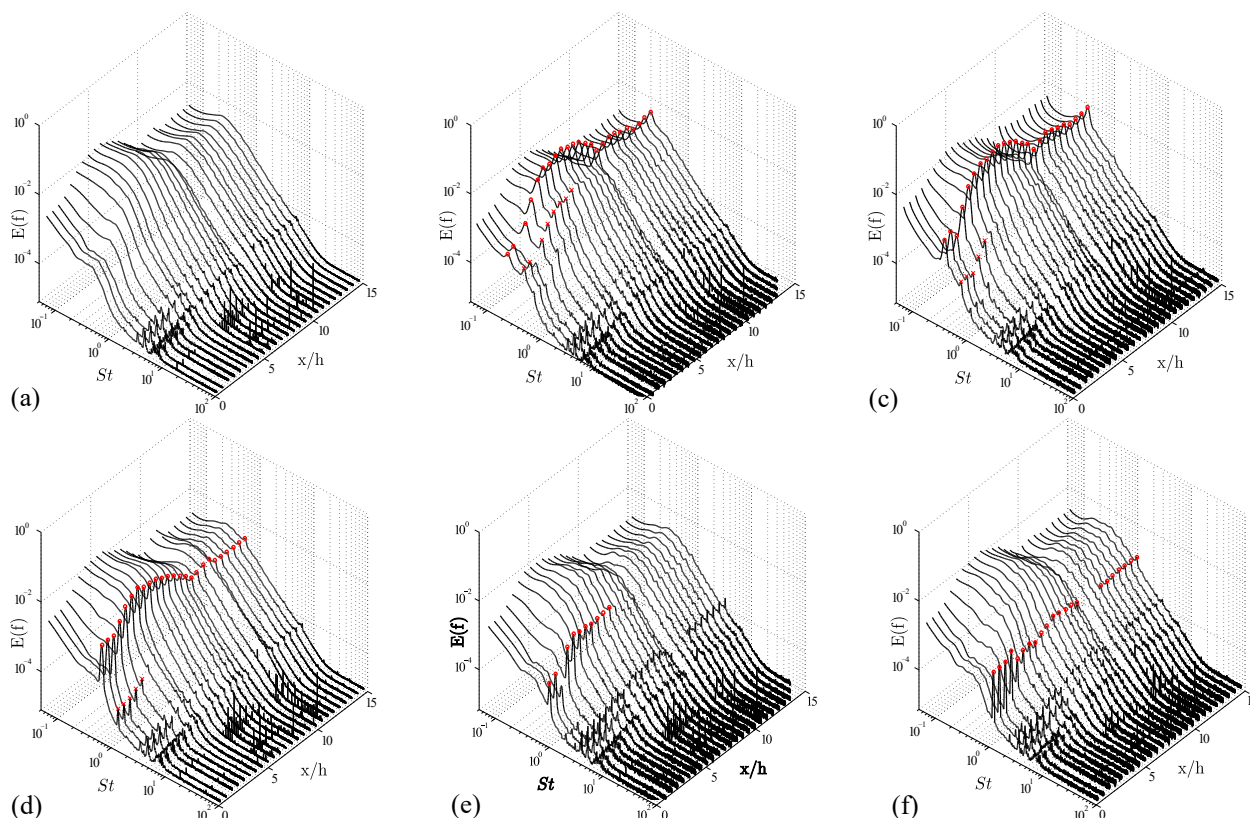


Figure 3.25 – Power spectra of wall-pressure fluctuations for different  $x/H$  locations (a) Unforced, (b)  $St_a = 0.091$ , (c)  $St_a = 0.181$ , (d)  $St_a = 0.226$ , (e)  $St_a = 0.317$ , (f)  $St_a = 0.407$ .

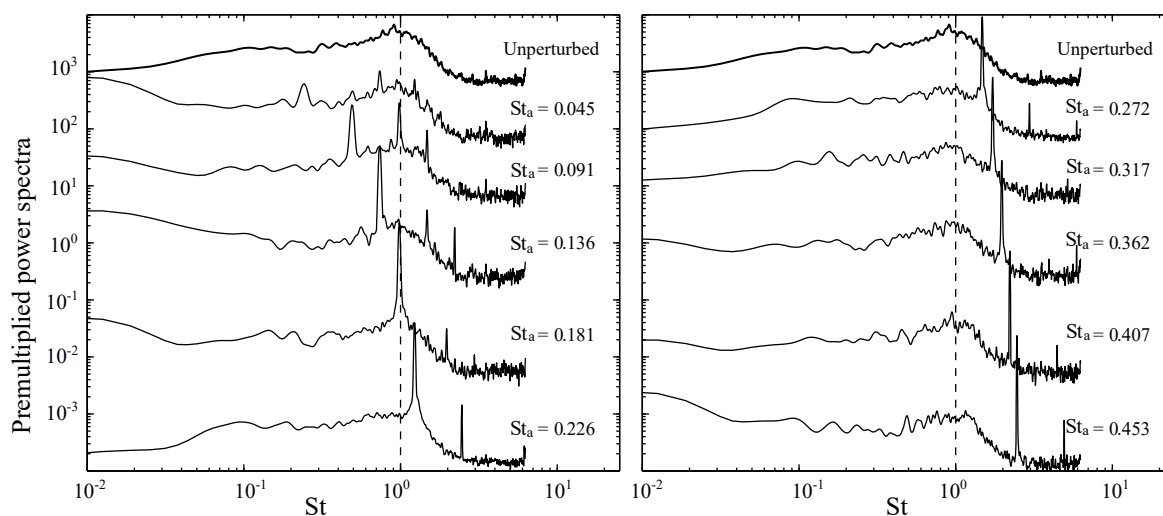


Figure 3.26 – Non-dimensional premultiplied power spectra of fluctuating wall-pressure, defined as  $E(f)f/p_{rms}^2$ , measured at  $x/H = 1.5$  for unforced and forced flows against the Strouhal number.

Spectral analysis may be used to shed light on why a particular perturbation frequency leads to a preferential response of the perturbed baseline flow. Figure 3.25 shows a 3-dimensional-plot of the pressure fluctuation spectra at several  $x/H$  locations downstream the step for unactuated and actuated flows. For all the cases, the dynamical behaviours change as a function of the probe position. Four regions are once again

$f_a$ [Hz]	$St_a$	$\Delta X_r/X_r$ [%]	$\Delta L_r/L_r$ [%]	$\Delta A_r/A_r$ [%]
0	0.000	0.00	0.00	0.00
3	0.045	-31.03	-2.31	3.13
6	0.091	-63.22	-1.78	1.56
9	0.136	22.99	-3.02	-5.21
12	0.181	26.44	-3.56	-4.17
15	0.226	38.39	-4.80	-19.04
18	0.272	25.98	-4.09	-18.75
21	0.317	6.90	-3.02	-8.85
24	0.362	14.48	-1.07	-8.33
27	0.407	11.49	0.00	-4.69
30	0.453	22.99	0.71	-8.85

Table 3.3 – Reduction of the recirculation lengths/area by periodic forcing frequency as flow control strategy.

identified. The first region,  $0 < x/H < 1.5$ , shows both low and high frequencies. A transitory region occurs from  $x/H \approx 1.5$  to  $x/H \approx 4.5$ . The third one corresponds to the recirculation region, where the pressure fluctuations are strong with high energy levels. The last region represents the reattached zone. This global mechanism is also reported for the same configuration by Spazzini *et al.* (1999). For the actuated cases, 'o' red circle symbols represent the harmonic and 'x' red cross symbols the sub-harmonic forcing frequency peaks. The actuation peaks appear in the power spectra after  $St_a > 0.045$  and strongly increase in size as  $St_a$  increases. A high degree of penetration in the  $x/H$  direction was also observed for an actuation (Strouhal numbers) near to the shedding frequency. When the actuation frequency is close to the optimal one ( $St_a = 0.226$ ), the former can be sensed by all the pressure probes, suggesting that these frequencies can perturb the flow in a greater degree. To better understand the flow response to different actuation, the non-dimensional premultiplied power spectra of fluctuating wall-pressure, measured at  $x/H = 1.5$ , is presented in Figure 3.26 for both unforced and forced cases. From the results, two frequency peaks can be observed in the natural case. A first bump at  $St = 0.12$  corresponds to a well-defined flapping frequency (Note that this peak is less visible due to scaling conditions) and a second broadband peak at around  $St = 1$  related to the shedding frequency of the shear layer structures (close to 0.2 if the Strouhal number is based on the step height  $H$ ). These peaks agree well with those obtained in previous investigations (Li *et al.*, 2015). When the flow is forced, additional frequency peaks are observed. The local energy increases due to control actuation. Close to  $St_a = 0.226$ , strong peaks emerged in the spectra.

Hereafter, the study will be based on the optimal Strouhal number  $St_a = 0.226$ . For this frequency,  $X_r$  increases up to 38.4% while  $L_r$  and  $A_r$  decrease to 4.8% and 19.0%, respectively. This optimal forcing is consistent with those obtained in previous experiments (Chun & Sung, 1996; Wengle *et al.*, 2001; Yoshioka *et al.*, 2001a; Bhattacharjee *et al.*, 1986; Li *et al.*, 2015). Results from all the periodic forcing cases are shown in Table 3.3 and corroborate the effectiveness of pulsing jet injection with forcing frequency to reduce the separation length (Nadge & Govardhan, 2014).

### 3.3.2 Machine learning control (MLC)

Machine learning control studies are further carried out to discover new and more effective closed-loop separation control laws. This is possible thanks to the ability of Murata micro-blowers to drive the actuation with any variable DC. As previously explained, the control design is formulated as a regression problem: find the control law which optimizes a given cost function. For this experience, a tree-based genetic

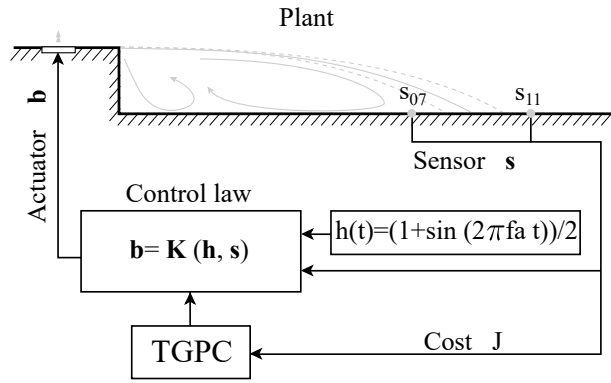


Figure 3.27 – Diagram of machine learning control architecture using tree-based genetic programming

Parameters	Value
Genetic programming approach	Tree-based
Population size	$M = 100$
Generation size	$G = 12$
Tournament size	$N_t = 7$
Elitism	$N_e = 1$
Replication	$P_r = 10\%$
Crossover	$P_c = 60\%$
Mutation	$P_m = 30\%$
Operations	$+, -, \times, \div, \sin, \cos, \tanh, \log_{10}$

Table 3.4 – TGPC parameters.

programming (TGP, Duriez *et al.* (2016)) representation approach will be used. An initial population of 100 control law candidates  $\mathbf{b}_i^1$  is generated. Each individual is graded in the experiment (inner loop) and a cost function  $J_i^1$  is attributed to them. A new population of individuals  $\mathbf{b}_i^2$  is then evolved from the previously evaluated one by genetic operators leading to new cost functions  $J_i^2$ . Without loss of generality, the control laws of the  $n$ -generation are ordered  $J_1^n \leq J_2^n \leq \dots \leq J_{100}^n$ . This learning process will continue until some stopping criterion is met. In the present work, the number of generations was set to 20, which was the minimum amount of generations required to converge toward the best individual and the maximum to search for as many innovative control laws as possible. The optimal control law is the best individual of the last generation. This individual is taken as MLC law. This marks the end of the learning phase. The process previously described is summarized in Figure 3.27. The TGP parameters used for this experiment are listed in Table 3.4. Elitism is set to  $N_e = 1$ , i.e., the best individual of a generation is copied to the next one. The probabilities for replication, crossover, and mutation are 10%, 60% and 30%, respectively. The individuals on which these genetic operations are performed are determined from a tournament selection of size  $N_t = 7$ . Elementary operations comprise  $+, -, \times, \div, \sin, \cos, \tanh$ , and  $\log_{10}$ .

The main goal is to reduce the external separation point ( $L_R$ ), with a cost function  $J = L_R^E + \gamma < b >$  based on an estimated  $L_R^E$  obtained from the unsteady pressure probes. This was achieved using pressure probes ( $s_7$  &  $s_{11}$ ) with an evaluation time for each individual  $T_e = 15s$ . A penalization  $\gamma = 0.1$  was set based on the low energy consumption of the row of micro-blowers. Three different approaches are considered. Multi-frequency control is derived from periodic forcing. In sensor control, the pressure probes are used to generate the control laws. Multi-frequency forcing and sensor feedback are generalized in the generalized feedback law, i.e., a combination of harmonic and sensor inputs is taken.

The use of multiple frequencies in the actuation might expand the search space of the control laws. This approach might be useful to find the optimal open-loop actuation. For the multi-frequency approach,

the control law is a linear combination of a finite amount of harmonic signals and can be written as  $\mathbf{b}^\circ = \mathbf{K}(\mathbf{h})$ , where  $\mathbf{h}(t) = V_{\text{jet}}(1 + \sin(2\pi f_a t))/2$  represents different harmonic functions at the frequency  $f_a$ . The harmonic frequencies are based on the optimal forcing frequencies previously obtained and equal to  $f_a = 14, 15$  and  $16$ , corresponding to Strouhal numbers of  $0.211, 0.226$  and  $0.241$ . The sensor feedback is expressed as  $\mathbf{b}^\times = \mathbf{K}(\mathbf{s})$ , where  $\mathbf{s}$  consists of the pressure sensors  $s_7$  and  $s_{11}$ . The generalized feedback control is performed by combining the multi-frequency harmonics and the sensors, i.e.,  $\mathbf{b}^\otimes = \mathbf{K}(\mathbf{s}, \mathbf{h})$ .

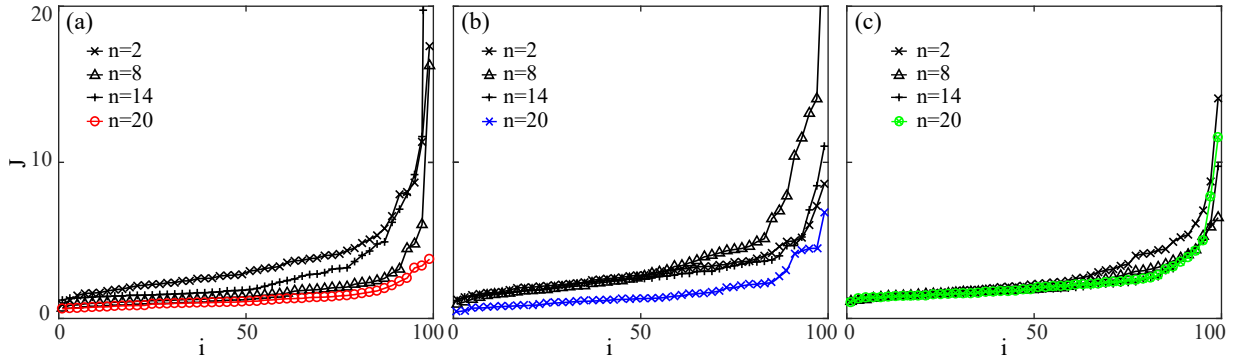


Figure 3.28 – Evolution of the cost function  $J$  versus the individuals  $i$  for 4 generations  $n=5, 10, 15, 20$  for (a) 'o' red circle symbol: multi-frequency forcing, (b) 'x' blue cross symbol: sensor feedback, (c) '⊗' green circled-cross symbol: generalized feedback control.

Figure 3.28 presents the evolution of the cost function  $J$  versus the individuals  $i$  for all the MLC cases. Results for the multi-frequency forcing (Figure 3.28(a)) show a decrease in the cost values as the generation  $n$  increases. The first individuals coincide quickly to the optimal value, while on the last ones, a strong separation between each generation is presented. Twenty generations were necessary to obtain the optimal control law. A similar behaviour is presented for the sensor feedback (Figure 3.28(b)); a decrease of the curve is clearly seen. In this case, the cost values of the last generation are further separated from those of the previous ones, corroborating the necessity of 20 generations to accomplish convergence. The generalized feedback law converges quickly to the optimal cost value (see Figure 3.28(c)). One can assume that 20 generations are not necessary for this control approach; nonetheless, it is preferable to keep this value. Even though the number of input parameters increases (harmonic functions and/or sensor signals), MLC can effectively predict which inputs are pertinent to generate the control functions.

To reduce energy and time consumption, it is important to know the precise sensor to generate the control law. For this reason, the percentage  $\mathbf{P}_s$  of having  $\mathbf{h}$  and/or  $\mathbf{s}$  involved in the individuals is displayed in Figure 3.29 for all the MLC cases. For the multi-frequency case, the proximity of the chosen frequencies ( $f_a = 14, 15$  and  $16$ ) leads to a similar percentage for the three frequencies studied. However, the optimal frequency is chosen more times in the last generation, corroborating the capacity of MLC to find the optimal periodic frequency. For the sensor feedback, similar results are obtained for all the generations. Both pressure  $s_7$  and  $s_{11}$  are strongly used to generate the signals. However,  $s_7$  is slightly higher, probably due to the closeness of this sensor to the recirculation length, i.e., when the recirculation length is reduced, the pressure stamp will increase for the pressure probe 7 and decrease for the probe 11; MLC is able to pick this information and give more importance to  $s_7$  without losing the search for a control law using  $s_{11}$ . The generalized feedback will have to take into consideration the information from both the sensor signals and the harmonic functions. Initially, the first harmonic was greatly used. However, an increase in the second harmonic function ( $f_a = 15\text{Hz}$ ) and the pressure probe  $s_7$  is clearly seen. In the last generation, both sensors are equally chosen. MLC is able to correctly locate the optimal sensor(s) to reproduce a favourable control function; genetic algorithms are capable of generating optimal control laws with the necessary input signals.

Finally, once the evaluation of all the individuals is done, the control functions for the three cases are obtained. For multi-frequency forcing, the optimal control law is based on the three harmonic functions

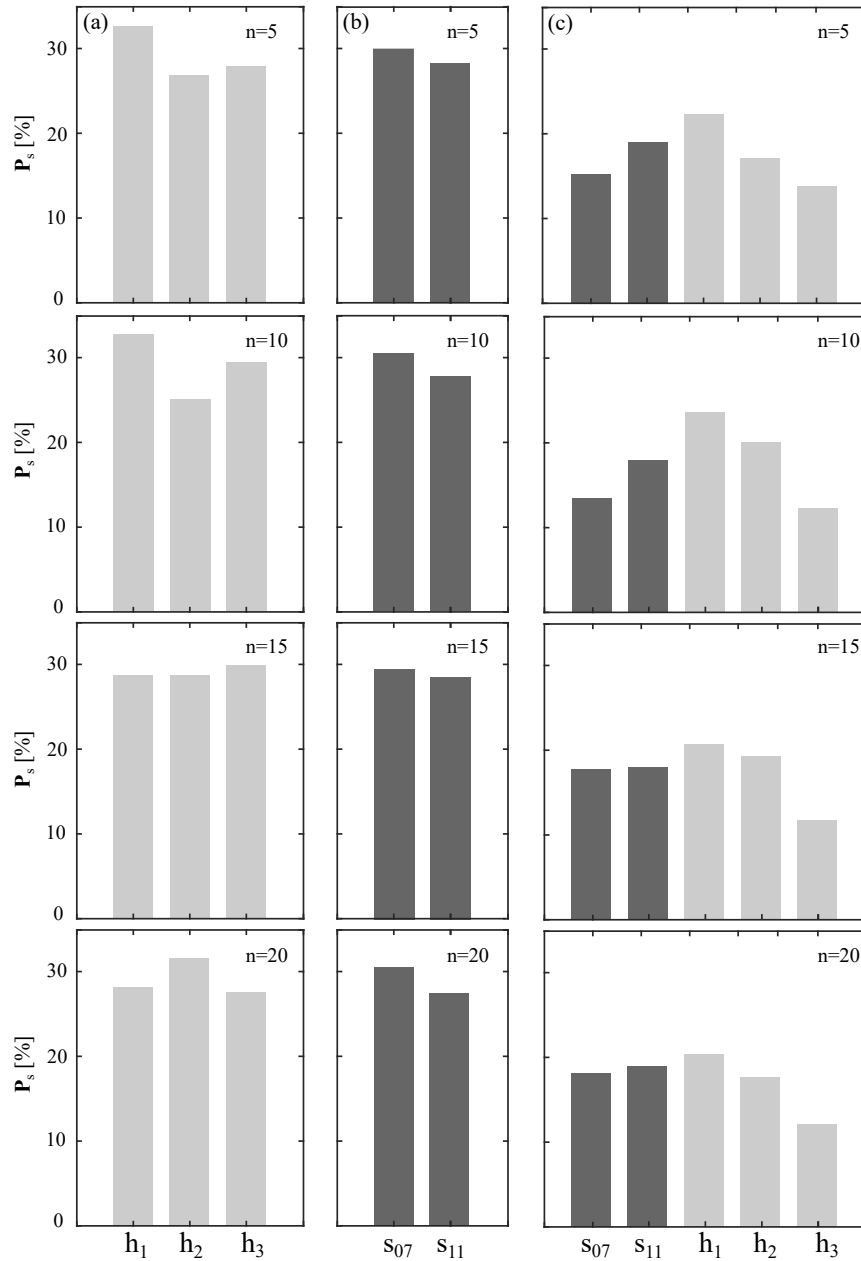


Figure 3.29 – Percentage of having individual h or s in the expression of the individuals, (a) Multi-frequency forcing, (b) Sensor-feedback, (c) Generalized feedback law.

( $f_a = 14, 15$  and  $16$ ) and denoted as:

$$\mathbf{b}^\circ = (\cos((h_1 - (h_3 + ((\cos(\cos(h_1)) + (h_2 + (1.695 + h_1))) \times (\cos(1.343) + (\tanh(h_3) + (2 \times (h_2)))))))) - ((2 \times (h_1)) - \tanh(((h_3 \times (0.6135 + h_2)) + (1.502 + \cos(h_1))) \times (0.2824 - (h_2 \times \tanh(h_2)))))) \times (1.502 + \cos(h_1))).$$

For an easier representation of the obtained control law, please refer to '—' red line in Figure 4.27(a). Even though the three harmonic functions are used, the result control law strongly contains a frequency at 15Hz, ('—' red line in Figure 4.27(b)), equal to the optimal periodic forcing, and two weak frequencies at the other chosen periodic forcing frequencies. Another low-frequency peak is visible at a frequency of  $St_H \approx 0.05$  which generates an intrinsic low frequency in the signal. The other peaks presented, such as sub-harmonics, are probably linked to the noise generated in the final control signal. Hereafter, for easier comprehension, the multi-frequency forcing will be related to the '°' red circle symbol. The sensor feedback, here denoted with '×' blue cross symbol, creates a continuous blowing of  $\mathbf{b}^\times = 1$ . The complete control law contains both sensor signals,

$$\mathbf{b}^\times = \tanh((\tanh(s_7) + \cos(\cos(\cos(\cos(\cos(s_{11}))))))).$$

The generalized feedback case is also based on all the input signals giving:

$$b^{\otimes} = -0.4011 \times s_7(\cos(h_2 + h_2 \times s_7) - h_2) \times (h_2 + \cos(h_1) - \cos(-1.506)) - h_3 \times \tanh(s_7 \times s_{11}) +$$

$$\tanh(\cos(\tanh((\tanh(\tanh(h_1)) + ((h_2 + s_7) \times (2 \times s_{11})))))) + ((\cos(s_{11}) -$$

$$(\cos(\tanh(\cos((0.6697 \times h_3)))) - (h_2 + s_{11}))) - (\cos(h_1) - (h_2 + s_{11}))).$$

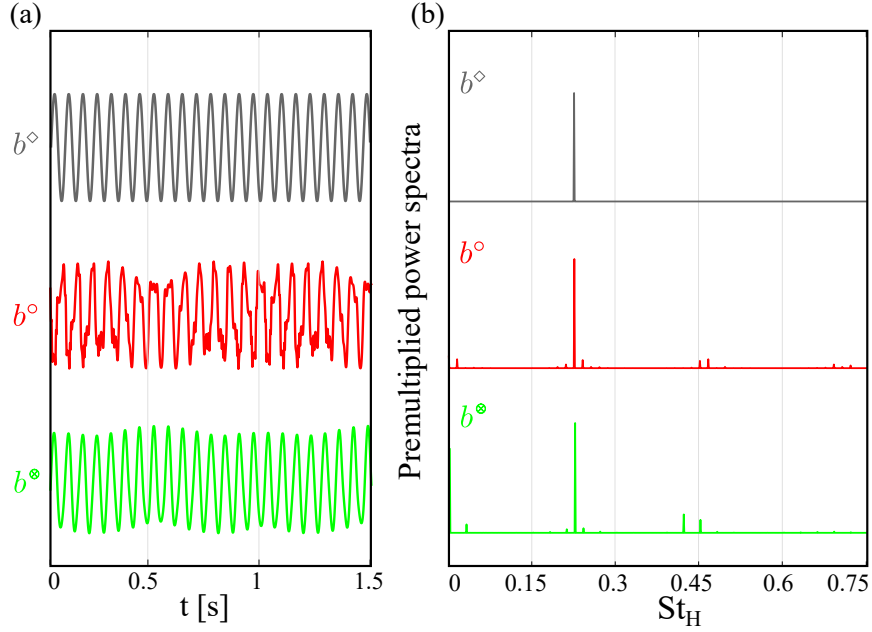


Figure 3.30 – Actuation properties for periodic forcing ( $b^{\diamond}$ ), multi-frequency forcing ( $b^{\circ}$ ), generalized feedback control ( $b^{\otimes}$ ). (a) One and a half periods of the actuation commands (b) Premultiplied power spectral densities for all cases.

The simplified version of the control law is presented in '—' green line in Figure 4.27(a). It is worth noting the number of times  $h_2$  was used to generate the signals. The same peak, at the optimal frequency, is obtained. A second one close to  $St_H \approx 0.05$  is also visible, which explains the double frequency presented in the control signal. Furthermore, a peak close to the sub-harmonic frequency is obtained. It is possible to conclude that the generalized feedback control is trying to replicate the multi-frequency forcing. However, it was able to generate a “cleaner” signal with respect to the multi-frequency one. This smoother signal has important consequences in the flow control, as it will be explained in further sections. The colour and symbol linked to the generalized feedback control will be ' $\otimes$ ' green crossed-circle symbol.

### 3.3.3 Actuation effects on the recirculation area

To study the main effects of the actuation on the flow, the FFP values extracted at the vicinity of the wall ( $y/h = 0.07$ ) are presented in Figure 3.31(a) ('—' black line: unforced flow, '—' gray line: optimal periodic forcing, '—' red line: MLC multi-frequency forcing, '—' blue line: MLC sensor feedback, '—' green line: MLC generalized feedback). This reduction at the vicinity of the step is caused by a positive velocity injection that interacts with the shear layer vortices generated at the step edge. The increase of the internal separation length and the decrease of the external separation point are clearly seen from the unforced flow ('—' black line) to the generalized feedback control ('—' green line). It is interesting to note that multi-frequency open-loop ('—' red line) out-performs the periodic forcing, but the sensor ('—' blue

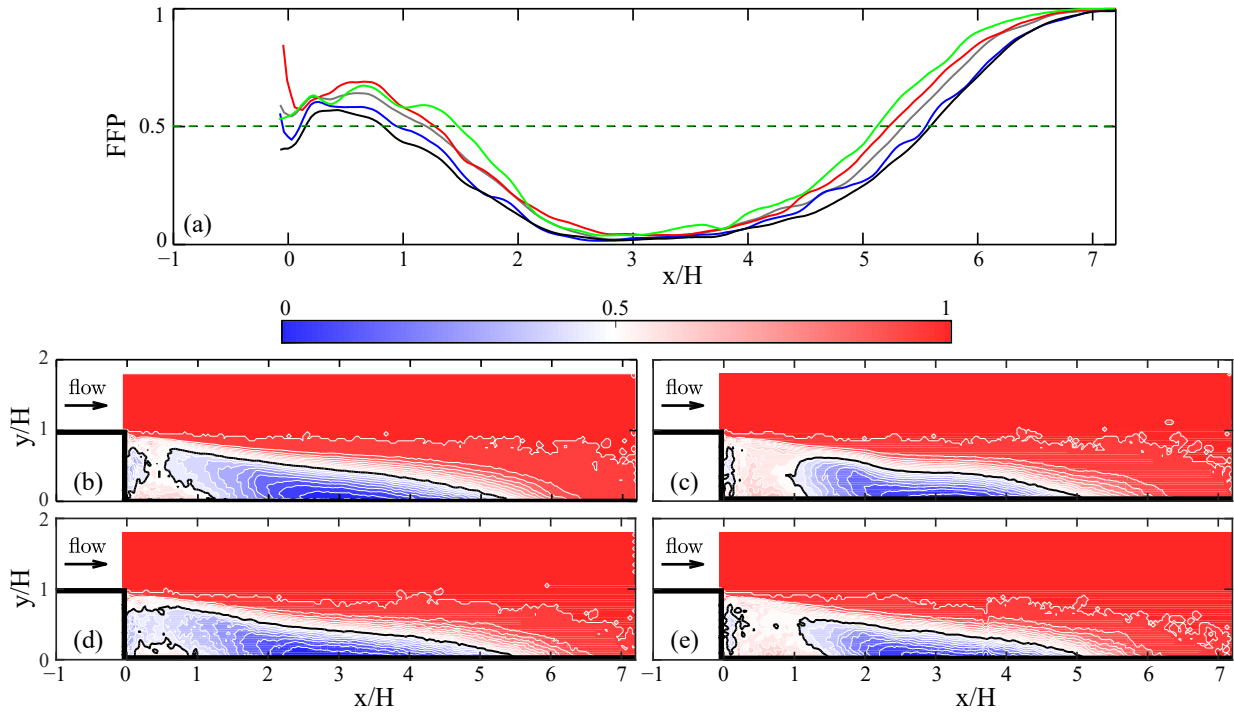


Figure 3.31 – Forward flow probability field for (a) FFP profile extracted at  $x/H=0.7$ . As a reference, the unforced flow probability profile is plotted in solid black line. Flow probability field: (b) '—' dark grey line: optimal periodic forcing, (c) '—' red line: MLC Multi-frequency, (d) '—' blue line: MLC sensor feedback, (e) '—' green line: MLC generalized feedback. Solid black line denotes the 50% value of the FFP

Control strategy	Control law	$\Delta X_r/X_r$ [%]	$\Delta L_r/L_r$ [%]	$\Delta A_r/A_r$ [%]
Periodic forcing	$b^\diamond$	38.39	-4.80	-19.04
MLC Multi-frequency forcing	$b^\circ$	63.45	-7.76	-35.45
MLC sensor feedback	$b^\times$	8.73	-1.24	-8.99
MLC generalized feedback	$b^\otimes$	70.57	-8.62	-40.74

Table 3.5 – Separation point and regions for all the cases studied.

line) control law is the least efficient. Furthermore, the forward flow probability FFP field is plotted in Figure 3.31(b) to (e). From the figures, a strong reduction of the recirculation area (blue region) is clearly seen, especially close to the step ( $x/H \leq 1$ ), compared to the unforced flow presented in Figure 3.6(b). The periodic forcing FFP field is seen in Figure 3.31(b). For the multi-frequency open-loop case (Figure 3.31(c)), a higher reduction of the external separation point ( $L_r = 5.18H$ ), compared to the optimal forcing frequency, is observed and an increase in the internal separation point  $X_r = 1.42H$  can be seen. On the contrary, for the sensor case (Figure 3.31(d)), the internal and external separation point did not change significantly; recirculation length values of  $L_r = 5.55H$  and  $X_r = 0.95H$  are obtained. As expected, the best case combines sensor feedback and open-loop forcing. The resulting generalized feedback (Figure 3.31(e)) gave a strong reduction of the external separation point up to 8.6% ( $L_r = 5.13H$ ) and an increase of 70.6% of the internal separation point  $X_r = 1.48H$ . Same results are seen for the recirculation area, where the best control law reduces this region up to 40.7%. Results show that a generalization of multi-frequency forcing and sensor feedback control law significantly reduces the turbulent recirculation zone. A summary of all the results is presented in Table 3.5.

### 3.3.4 Dynamical control mechanisms

#### Modal analysis of the optimal forcing

In order to filter the different components involved in the flow dynamics, velocity fields obtained with PIV are decomposed using the proper orthogonal decomposition technique. The goal of this decomposition is to corroborate the direct perturbation of different phenomena presented in each energetic mode. The principle of low-frequency forcing, using this actuator device, is to modify the flow with the lowest amount of energy. The objective is to perturb the phenomena presented in higher modes with small frequency modulations. High-frequency forcing will stabilize the global shear flow, modifying the most energetic modes. This decomposition results in spatial modes representative of the energetic events. Each mode represents the contribution of the total turbulent energy of the flow field. Figure 3.32 shows the cumulative energy of the first fifteen velocity modes for all the flows studied. For all the cases, the energy fraction of the first and the second POD modes were found to contain almost 20% of the total flow energy, and the first fifteen modes comprised 50% of the total turbulent energy. When the actuation is applied, the relative energy content of the first modes increased. On the contrary, lower cumulative relative energy values are obtained when no actuation or continuous blowing is used. Hereafter, only the first 5 modes will be analysed.

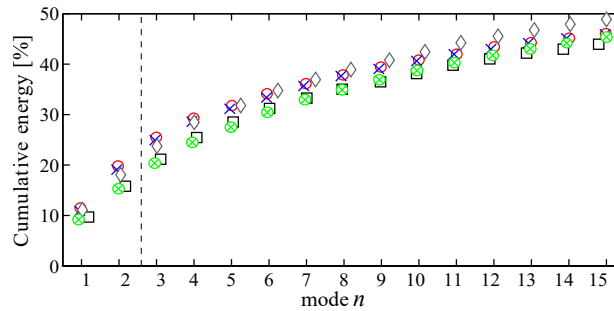


Figure 3.32 – Cumulative energy from the POD of the velocity fields for: '□' black square: Unforced flow, '◇' gray diamonds: Periodic forcing, '○' red circles: MLC Multi-frequency forcing, '×' blue crosses: MLC sensor feedback and '⊗' green crossed-circles: MLC generalized feedback

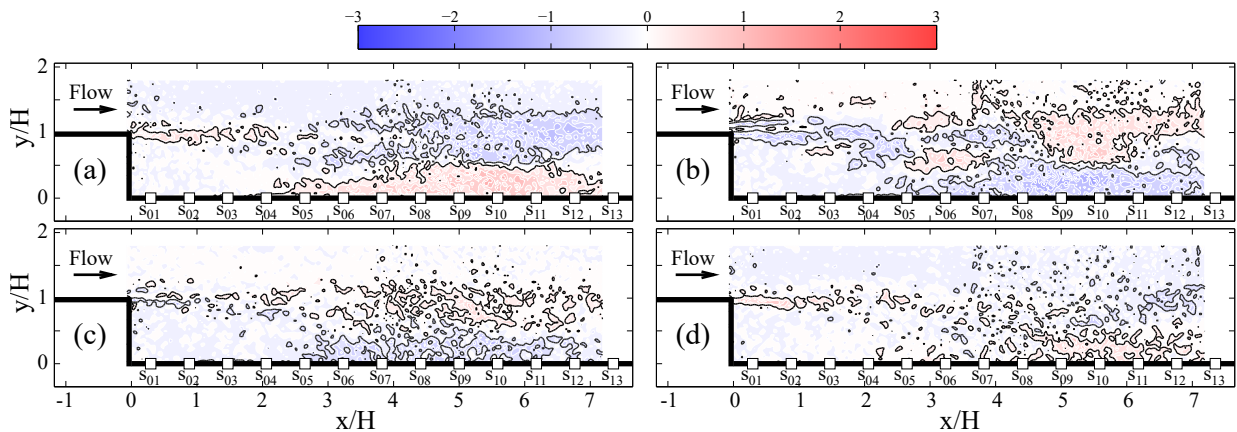


Figure 3.33 – Low-order POD velocity mode 1: (a) Periodic forcing, (b) MLC Multi-frequency forcing, (c) sensor feedback, (d) generalized feedback. Contour map shows vorticity calculated from the corresponding POD velocity basis function and normalized with the step height and free stream velocity  $U_\infty$  ( $\omega_z H / U_\infty$ ). Vorticity levels between -0.5 and 0.5 are set at zero in order to minimize noise in the contour plots enhancing the visibility of the dominant feature of the modes.

Figures 3.33 to 3.35 show the low-order POD velocity modes 1 to 5, with corresponding vorticity modes, for all the studied cases (Figure (a) Periodic forcing, Figure (b) Multi-frequency forcing, Figure (c) sensor feedback and Figure (d) generalized feedback control). The POD basis functions are non-dimensional and the vorticity calculated from the POD mode  $\omega_z$  was normalized with the step height  $H$  and free stream velocity  $U_\infty$  ( $\omega_z H / U_\infty$ ).

For all cases, the two first modes present elongated vorticity regions, a counter-clockwise (red colour)

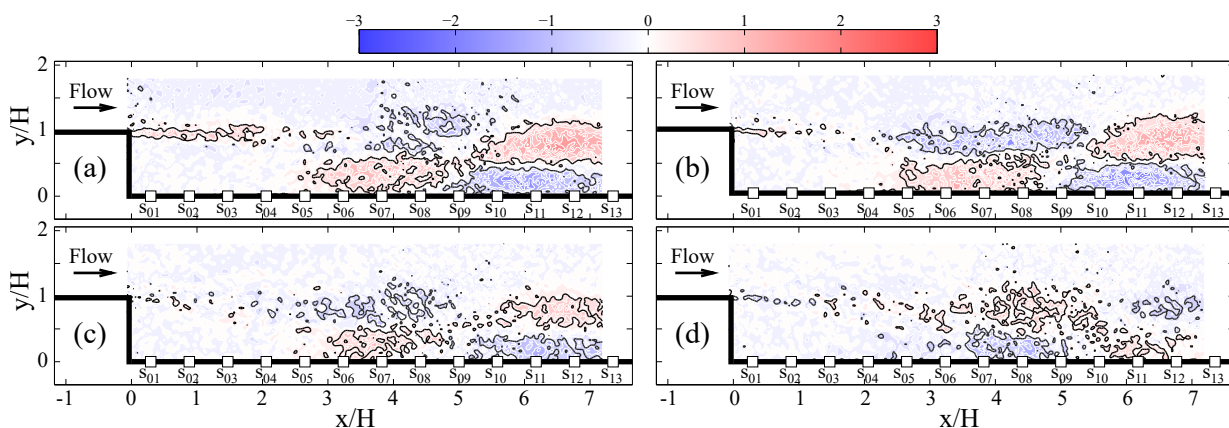


Figure 3.34 – Low-order POD velocity mode 3: (a) Periodic forcing, (b) MLC Multi-frequency forcing, (c) sensor feedback, (d) generalized feedback. Contour map shows vorticity calculated from the corresponding POD velocity basis function and normalized with the step height and free stream velocity  $U_\infty$  ( $\omega_z H/U_\infty$ ). Vorticity levels between -0.5 and 0.5 are set at zero in order to minimize noise in the contour plots enhancing the visibility of the dominant feature of the modes.

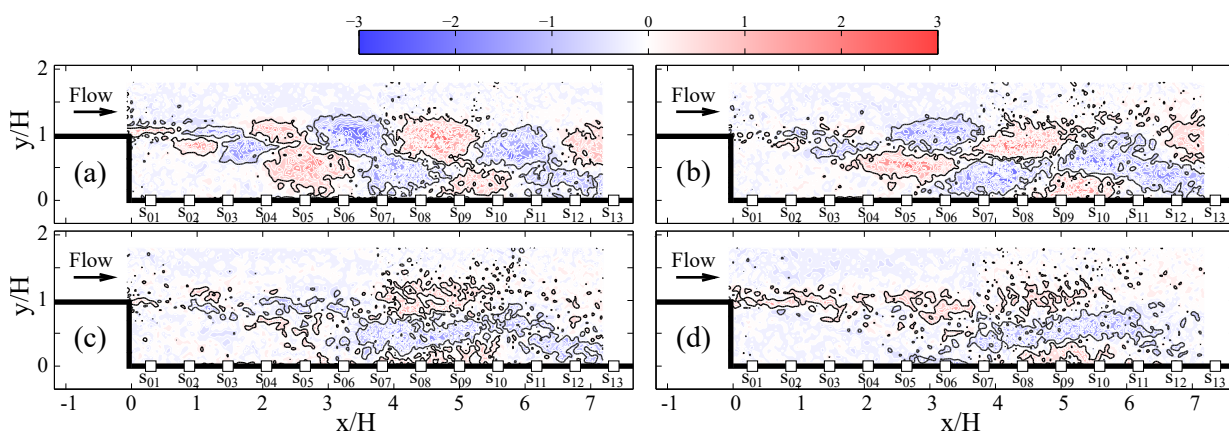


Figure 3.35 – Low-order POD velocity mode 5: (a) Periodic forcing, (b) MLC Multi-frequency forcing, (c) sensor feedback, (d) generalized feedback. Contour map shows vorticity calculated from the corresponding POD velocity basis function and normalized with the step height and free stream velocity  $U_\infty$  ( $\omega_z H/U_\infty$ ). Vorticity levels between -0.5 and 0.5 are set at zero in order to minimize noise in the contour plots enhancing the visibility of the dominant feature of the modes.

shear layer and a clockwise (blue colour) one. For the multi-frequency forcing and sensor feedback, a switch on the structures is clearly visible: clockwise up for mode 1 and down for mode 2 (not presented here). These first two modes are similar to those obtained for the unactuated case (see Figure 3.17(a) and (b)). Moreover, some smaller vortices are created when a multi-frequency forcing is applied. Generalized feedback control presents a similar behaviour to that of periodic forcing. A degradation of the vortex structures is clearly seen from (a) to (d). The shape, height, and length of the structures decrease from one actuation to the other. It is possible to assume that the structure disappearance might be due to the vortex created when noisier actuation is applied, directly perturbing the more energetic modes -linked to the flapping phenomena. For the other modes (Figures 3.34 and Figures 3.35), a round and regular shape in the streamwise direction was distinctly perceived. The actuated case shows smaller, uniformly shaped vortical structures (either positive or negative) compared to the ones of the baseline flow (Figure 3.17(c) and (d)), especially for the 5<sup>th</sup> mode. This relatively small degree of elongation was also presented in previous studies (Nguyen *et al.*, 2010; Piponniau *et al.*, 2011; Kostas *et al.*, 2002) and might be linked to vortical structure organization in space. Also, during the actuated phases, the jet leads to an opposite direction of the vortical structures, as during the unactuated phases, due to an interaction between the free stream velocity and the jet flow. Once more a degradation of the structure shape is visible from one actuation to the other. Similar results are obtained between periodic forcing and multi-frequency forcing. However, for sensor feedback and generalized feedback control, these structures start losing their rounded shape, e.g., Figures 3.35(c) and (d) present withered structures and in less amount compared to (a) and

(b). As previously commented, this variation might be due to the use of pressure probes in the actuation signal; this creates noise at the jet exit and further perturbed the flow structures.

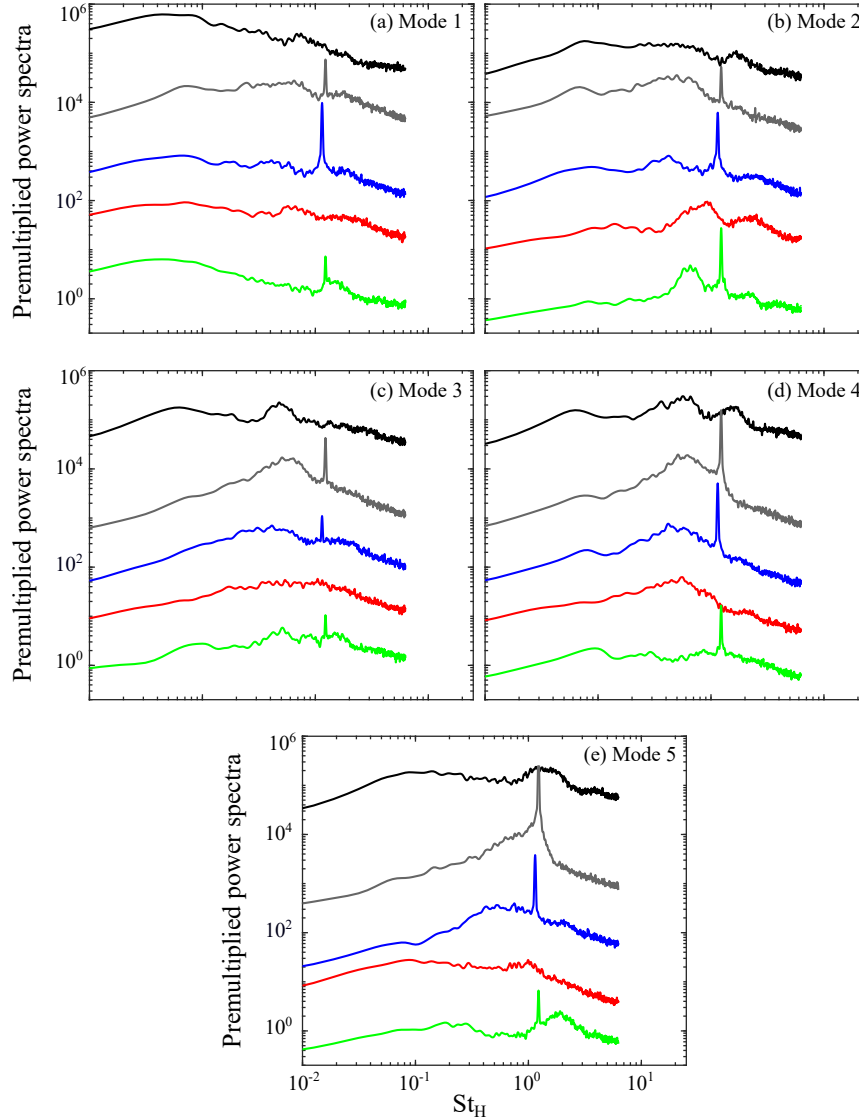


Figure 3.36 – Non-dimensional premultiplied power spectra of the estimated MQSE temporal coefficients for — black line: unforced flow, — dark grey line: optimal periodic forcing, — red line: MLC multi-frequency, — blue line: MLC sensor feedback, — green line: MLC generalized feedback: (a) mode 1, (b) mode 2, (c) mode 3, (d) mode 4, (e) mode 5

To examine the relation between the motions and wall-pressure fluctuation in the frequency domain, the MQSE techniques are used (see §2.1.2). The non-dimensional pre-multiplied power spectra of the estimated MQSE temporal coefficients for mode 1 to 5 are plotted in Figure 3.36. From the first two modes, a bump at  $St_H = 0.1$  can be seen and corresponds to the flapping frequency, more prominent in mode 2 (Figure 3.36(b)). The other modes highlight a transitioning and increasing peak associated to the shedding frequency; this peak starts at around  $St_H \approx 0.5$  increasing in frequency for a mode increase. When a harmonic actuation is applied, a peak around  $St_H \approx 1$  is clearly visible. This peak strongly modifies the shifting peak of the shedding phenomena, more predominantly seen for mode 5, where the shedding peak coincides with the actuation peak. This accentuation corroborates the importance of the last three modes, previously seen in Figures 3.34 and 3.35, in the study of actuated-flow by low frequencies. Moreover, when continuous blowing is applied ('—' blue line), a modification of both the flapping bump and the shedding peak is visible. For example, mode 2 shows a reduction of the flapping bump while for modes 3 and 5, a decrease of the shedding peak is observed. An interesting behaviour is also seen when generalized feedback control is used (combination of sensor and harmonic function inputs). The flapping bump and the shedding peak are modified, thanks to the actuation frequency, and probably linked to the use of

pressure probes and low frequency forcing in the input command. This means that the control contains important information to optimally control the flow. For periodic forcing, the peak is not reduced but just modified by the actuation frequency. For multi-frequency forcing, the peak is reduced and modified due to a combination of low- and medium- frequency actuation. When continuous blowing is applied, the shedding peak is slightly reduced. Finally, when generalized feedback control is applied, the peak is strongly modified (it almost disappears). Even though a 3-dimensional reconstruction of the flow must be done in order to fully understand the flow behaviour, a 2-dimensional reconstruction can provide some insight into the behaviour of this complex structures created and modified by different actuation mechanisms. It is also possible to conclude that the higher modes, such as the 3<sup>rd</sup>, 4<sup>th</sup> and 5<sup>th</sup>, could be retained if the interest is focused on the shedding process. The two first modes might be linked to the flapping phenomena. Results suggest that a modification in the shedding frequency can lead to a decrease of  $L_r$ , an increase of  $X_r$  and a further decrease of the recirculation area.

### Conditional approach

Finally, to deeply study the dynamical analysis, a conditional approach has to be considered on the entire period of a control signal. This method permits the identification of the key mechanism inducing the flow control. For simplicity, the conditional approach will be studied only for the optimal periodic forcing. The actuator row produces a periodic inflow and increases the roll-up of the natural Kelvin-Helmholtz oscillation leading to a noticeable reduction of the separated area. This mechanism was highlighted in Figure 3.37, showing the conditional averaging of the velocity field along a period  $T$  for the optimal forcing actuation. Square symbols represent the moment when the velocity fields, obtained from the QSE, were captured. Note that this flow reconstruction was done for all the studied cases, however, are not here presented. As stated by Berk *et al.* (2017), for low Strouhal numbers (case presented here), the roll-up of the vortices take a relatively long time and is completed at a point far downstream compared to the recirculation region. This behaviour can be clearly seen in Figure 3.37. The beginning of the actuation inflow starts in Figure 3.37(e), with an interaction of the jet velocity with the boundary layer (yellow velocity vectors close to the step edge); the vortices were clearly perturbed due to the Kelvin-Helmholtz instabilities and the shedding frequency modification. Figure 3.37(f) to (i) shows the mechanism of “forcing roll-up” induced by the periodic actuation, with a slow movement of the vortex structures ( $\times_2$ ). Finally, Figures 3.37(i) to (k) exhibit the creation of the big vortices far from the step edge ( $\times_3$ ). It is possible to see from the sequence the recurrence of the flow once the actuation was “OFF” (flow similarities between Figure 3.37(k) and (b)). This behaviour is also presented in the study of Ma *et al.* (2017) for a similar configuration.

As previously described in the literature (Berk *et al.*, 2017), frequency forcing regimes are usually discussed in terms of low- or high-frequency regimes. Generally, the low-frequency regime corresponds to shear layer amplification whereas the high-frequency regime corresponds to shear layer stabilization. The influence of the forcing frequency on the external reattachment length could be easily explain by combining insights from literature and present results (Berk *et al.*, 2017; Bhattacharjee *et al.*, 1986; Chun & Sung, 1996, 1998; Yoshioka *et al.*, 2001a,b).  $L_r$  is presented as a function of the Strouhal number in Figure 3.38 for three different cases. Based on the analysis presented by Berk *et al.* (2017), a sketch representing the flow behaviour obtained in the present work, caused by periodic perturbation, is now presented. A simplified schematic representations of vortical structures are embedded for the uncontrolled case (A), the optimal control case (B) and the highest control Strouhal case (C). The typical representation of the uncontrolled case shows the development of the shear layer and the generation of large-scale structures inducing sweep motions (from external flow toward the wall) of fluids between structures. For the case (B), corresponding to low Strouhal number actuation, the amplification of the shear layer oscillations inducing earlier large-scale structures shedding process will provoke an effect on the reattachment length. In this case, sweep motions are closer to the step edge and the deflection of the separation time-average line will

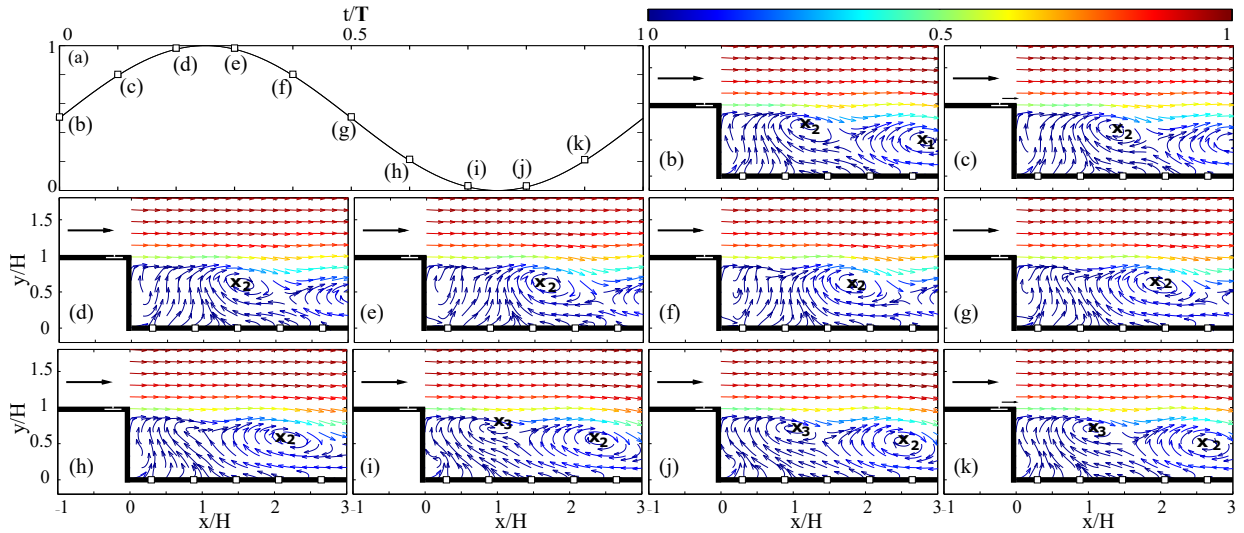


Figure 3.37 – Phase averaging of the (a) Jet velocity profile along the period  $\mathbf{T}$  for the optimal forced case. (b) to (k) temporal POD coefficient,  $a_i(t)$ , obtained from the MQSE for the 10 phases mentioned in (a). Vector lengths are normalized and equal to highlight the main flow structures. Colourbar represents the normalized velocity magnitude.

be stronger than in the uncontrolled case, see Figure 3.37. Influenced by the vortical structure growth, two type of instabilities are presented: “shear layer mode” and “wake mode” (see Hasan (1992) & Hudy *et al.* (2007)); here the former one is presented. However, if a higher frequency forcing is used, a stabilization of the shear layer is produced leading to an increase of the recirculation area (Berk *et al.*, 2017). For the last case (C), the roll-up of vortices are smaller and closer to each other preventing the generation of sweep motions. Consequently, the main effect of the high-forcing control is to stabilize the shear layer and delay the shedding of the large structures. However, The shear layer hardly responds to the actuation and there is low measure effect (Sigurdson, 1995). Furthermore, the natural shear layer also flaps upstream and downstream, so it is more difficult to prove that the “delayed shedding” near the reattachment area exits and that it differs from the natural flapping (Eaton & Johnston, 1982). Nonetheless, a hypothetical scheme of the flow behaviour, when it is perturbed at high frequency, is presented.

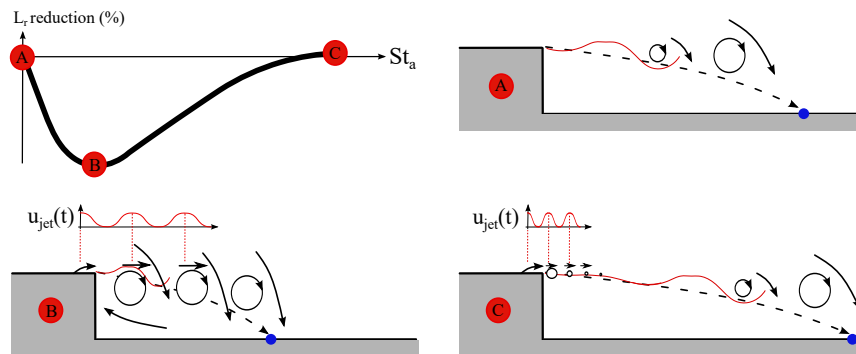


Figure 3.38 – Hypothetical scheme of reattachment length as a function of the Strouhal number, based on the Figure presented by Berk *et al.* (2017). ‘o’ blue circles denote the reattachment points. Dashed-line denotes the time-average separation line

### 3.4 Summary

Unsteady characteristics of the wall-pressure fluctuations and velocity fields in the separated/reattaching flows over a backward-facing step have been described in this chapter. Previous experimental data in a similar configuration were compared to present results, in order to clarify the flow dependency on external parameters, e.g., Reynolds number and expanding ratio (ER). Only a few experiments have been conducted at high Reynolds numbers ( $Re_H > 10^5$ ). In the former conditions, the recirculation length dependency on

the Reynolds number disappears as stated in previous experiments. However, results show that there is no constant trend after  $Re_H > 10^5$  but a decrease in the recirculation length, meaning that this reattachment point depends on other parameters. Even though discrepancies with previous authors were found, the results with close expanding ratios and Reynolds numbers showed similar values in both the pressure and the root-mean-square pressure coefficient. Therefore, it is possible to highlight that, for high Reynolds numbers, the expanding ratio dependency becomes relevant in the change of the recirculation length.

A study of the dynamical aspects of the flow is also presented. The spatial characteristics in the streamwise direction showed an intermittent structure motion throughout this axis, though the latter is stronger in the downstream direction. Pre-multiplied power spectra of the pressure fluctuations exhibit two main peaks. A reconstruction of the flow was done using POD techniques. With this procedure, the pressure fluctuation power spectra is separated in different modes. The two first modes contained a predominant peak at 0.12 corresponding to the flapping motion (low frequency of the large-scale structures). The other modes (from 3 to 5) showed a transitional and increasing peak that could be related to the shedding phenomena. For the first modes, an oscillating behaviour in the wall-pressure and MQSE estimation correlation corroborates a breathing movement of the shear layer. Alternating peaks in the correlation with the modes higher than 2 confirm the presence of the shedding phenomena; the latter modes are sensitive to the dynamics of the large-scale structures. Finally, the results obtained in the present study, from normalized rms-streamwise velocity of the last modes (3 to 5) and the decrease-increase behaviour of the convective velocity of the vortical structures, validate the “wake mode” statement presented by Hudy *et al.* (2007), where the large-scale coherent structures temporally grow in place and once they are big enough, they accelerate in the downstream direction. The knowledge of the shedding and flapping instabilities presented at high Reynolds numbers and the ability to separate them in different modes opens the door to create passive and active laws to control the flow.

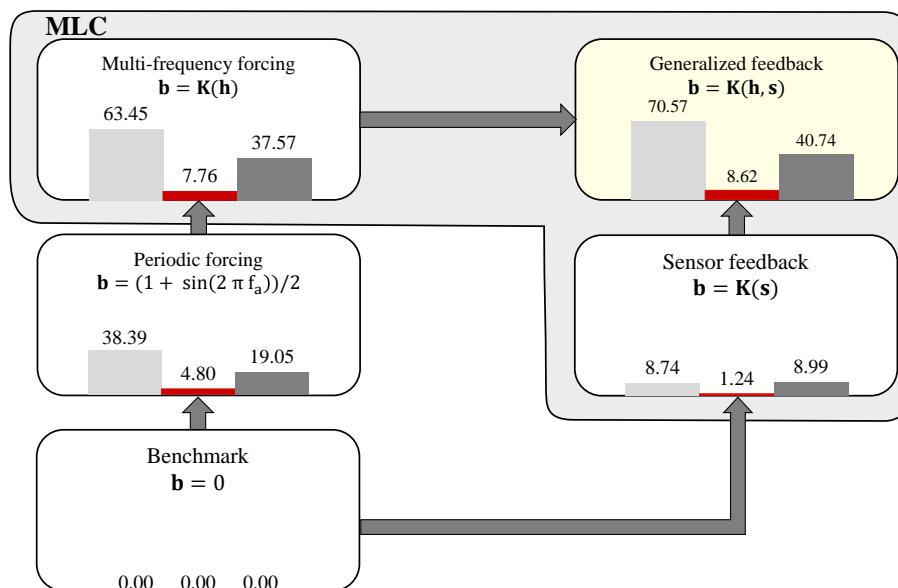


Figure 3.39 – Summary of both recirculation lengths and area; '■' dark red bars: external separation lengths  $L_r$ , '■' dark grey bars: internal separation length  $X_r$  and '■' light grey bars: separation area for all studied cases. Variations are in %

Further flow control in the separated shear layer of the backward-facing step using micro-pulsed jets is performed. These actuators are an interesting tool to achieve closed-loop control on separated flow. The ability to produce a wide range of signals, not only square- or sine- like signals of the typical devices, is a unique advantage to explore new feedback actuation mechanisms in numerous experimental applications. The control target was to modify key flow parameters, such as internal separation point, external separation point, and recirculation area, more specifically, increase the first parameter and reduce the others. Periodic forcing was able to significantly decrease the external separation point and the recirculation area and to

move up the internal separation point. Studies in this domain are conducted using Machine Learning Control (Duriez *et al.*, 2016); the results obtained present a larger reduction of the recirculation zone in a turbulent regime. Machine learning control was employed to search for new and more effective closed-loop control laws. Three MLC cases are studied: multi-frequency open-loop, sensor feedback and generalized feedback. Twenty generations with 100 individuals are needed to converge towards a control law which outperforms periodic forcing. Generalized feedback control shows to be the best control law strongly modifying all the analysed parameters. See Figure 3.39 for a summary of the results obtained in this chapter. From the power spectra wall-pressure fluctuations (at different  $x/H$  locations), actuation peaks are clearly obtained after  $St_a > 0.045$ . The  $x/H$  depth of these peaks, i.e., points where the pressure probes sensed the actuation command, are maximum close to the optimal actuation frequency, suggesting that frequencies close to this value can perturb the flow more thoroughly. Furthermore, a study of the dynamical aspects of the unactuated and actuated flows is also presented. A reconstruction of the flow was carried out using MQSE techniques. With this procedure, the pressure fluctuation power spectra is separated in different modes. The first mode contained a low-frequency predominant peak corresponding to the flapping motion. The other modes showed a transitional and increasing peak that was related to the shedding phenomena. When actuation was applied, a peak around  $St \approx 1$  was clearly visible. This peak strongly modifies the behaviour of the shedding phenomena, suggesting that this modification leads to a decrease of  $L_r$ , an increase of  $X_r$  and a further decrease of the recirculation area. In addition, a new actuation mechanism is presented. The results suggest that MLC can effectively explore and optimize new feedback actuation mechanisms and we anticipate MLC to be a game changer in turbulence control.

## Ahmed body

*Part of the following content is published in [Chovet et al. \(2018b\)](#) and [Ishar et al. \(2018b\)](#). The flow characteristics presented in a 3-dimensional configuration (square-back Ahmed body) are here analysed. The flow is manipulated by a slotted jet placed on the top trailing edge, combined with a predefined actuation angle (similar to a Coanda effect), and sensed by a drag balance. Two open-loop strategies are first presented: continuous blowing and periodic forcing. Sliding mode control (closed-loop strategy) is proposed to reduce and maintain the aerodynamic drag at a desired value. Last, to explore and optimize new feedback actuation mechanisms in this configuration, machine learning control is applied in combination with LGPC.*

**Contents**


---

4.1	Ahmed body experimental setup . . . . .	88
4.1.1	Configuration and measurement setup . . . . .	88
4.1.2	Actuation device . . . . .	88
4.1.3	Real-time system . . . . .	90
4.2	Baseline flow . . . . .	91
4.2.1	Flow statistics . . . . .	91
4.2.2	Flow field dynamics and POD analysis . . . . .	93
4.3	Open-loop investigation . . . . .	96
4.3.1	Wake modification . . . . .	97
4.3.2	Flow field dynamics and POD analysis . . . . .	101
4.4	Sliding mode control . . . . .	107
4.4.1	Experimental results of SMC application . . . . .	107
4.5	Machine learning control . . . . .	109
4.5.1	Wake modification . . . . .	113
4.5.2	Flow field dynamics and POD analysis . . . . .	115
4.6	Summary . . . . .	117

---

## 4.1 Ahmed body experimental setup

Experiments are conducted in the closed wind tunnel previously described in §2.1.1. The blunt-edged bluff body is a simplified car model, similar to a square-back Ahmed body (Ahmed *et al.*, 1984). The model has the following dimensions: height  $H=0.135\text{m}$ , width  $W=0.170\text{m}$  and length  $L=0.370\text{m}$  (Figure 4.1(a)). Its front edges are rounded with a radius  $R=0.05\text{m}$ . The model is mounted in the middle of the wind tunnel spanwise over a raised floor with a sharp leading-edge to control the boundary layer thickness. The raised floor has the following dimensions: front length  $L_{r_1} = 0.315\text{m}$ , back length  $L_{r_2} = 0.315\text{m}$ , with a total length of  $100\text{cm}$  and width  $W_r = 40\text{ cm}$  (see Figure 4.1(b) for a clear view). The back length  $L_{r_2}$  is long enough to have a complete wake development. The raised floor is  $25\text{cm}$  from the wind tunnel ground and the model is installed with a ground clearance of  $g=0.035\text{m}$  from the raised floor (Figure 4.1(c)). A support fixes the model and the raised floor to the ground and connects it to a drag balance giving a blockage ratio of  $0.57\%$ . The flow was described in a Cartesian coordinate system with  $x$ ,  $y$  and  $z$  representing streamwise, transverse (normal to ground) and spanwise directions, respectively. The origin is placed on the raised floor at the streamwise position of the rear surface. All the results presented are for a constant free-stream velocity  $U_\infty = 10\text{m/s}$ , with a corresponding Reynolds number based on the model height of  $Re_H = 9 \times 10^4$ .

### 4.1.1 Configuration and measurement setup

Three sub-miniature piezo-resistive Kulite XCQ-062 sensors are placed on the Ahmed body. These sensors are just to have a local view of the unsteady base pressure; they will not be used for flow control. The first flush-mounted Kulite transducer  $s_0$  was mounted on the front of the model at  $y = H/2$  and  $z = W/2$ . Two pressure probes were placed at the rear of the Ahmed body:  $s_1$  is located at the center plane at  $H/2$  from the bottom of the body and  $s_2$  is at a spanwise distance of the mid-span of  $z = W/3$  (Figure 4.1(d)). The sampling frequency used is  $f_s = 10\text{kHz}$  with a cut-off frequency of  $3\text{kHz}$ . The aerodynamic forces are measured using a 6-components DELTA ATI aerodynamic balance model built on the raised floor (Figures 4.1(c) and (d)). The balance has a sensing range, for the drag and lift, of  $0$  to  $165\text{N}$ , with a resolution of  $0.03\text{N}$  and a high signal-to-noise ratio. The maximum error associated with repeatability and hysteresis is found to be approximately  $0.5\%$ .

The velocity flow fields are obtained using a standard two-component TSI particle image velocimetry (PIV) system, described in §2.1.1. A multi-pass algorithm with a final interrogation window size of  $16 \times 16$  pixels<sup>2</sup> and  $50\%$  overlapping is applied. The resulting PIV domain is about  $3.7H \times 1.8H$  on the  $x$ - $y$  plane passing through the middle plane of the Ahmed body as shown in Figure 4.1(a). For every test case,  $2000$  double-frame pictures are registered to assure velocity field statistic convergence. The PIV time-uncorrelated snapshots are recorded with a repetition rate of  $7\text{Hz}$ . In order to maintain the causality between the dynamical aspect (instantaneous flow fields) and the global behaviour (drag, lift and surface-pressures time-histories) of the bluff body, the unsteady pressure measurements had to be acquired simultaneously with the PIV. To achieve synchronization, the Q-switch signal of the laser cavity B was recorded simultaneously with the pressure transducer and force signals using a 32-channel A/D converter Dewesoft data acquisition system, with a sampling frequency of  $20\text{kHz}$ . A cut-off filter at  $6\text{kHz}$  for the Q-switch and a second one at  $1\text{kHz}$  with a cut-off filter of  $300\text{Hz}$  were used. An example of the synchronization is shown in Figure 4.3.

### 4.1.2 Actuation device

The model is equipped with an actuator slit, also known as air-knife (presented in §2.2.1) at the top trailing edge, as illustrated in Figure 4.2. The pulsed blowing is driven by a FESTO-MH2 solenoid valve. The

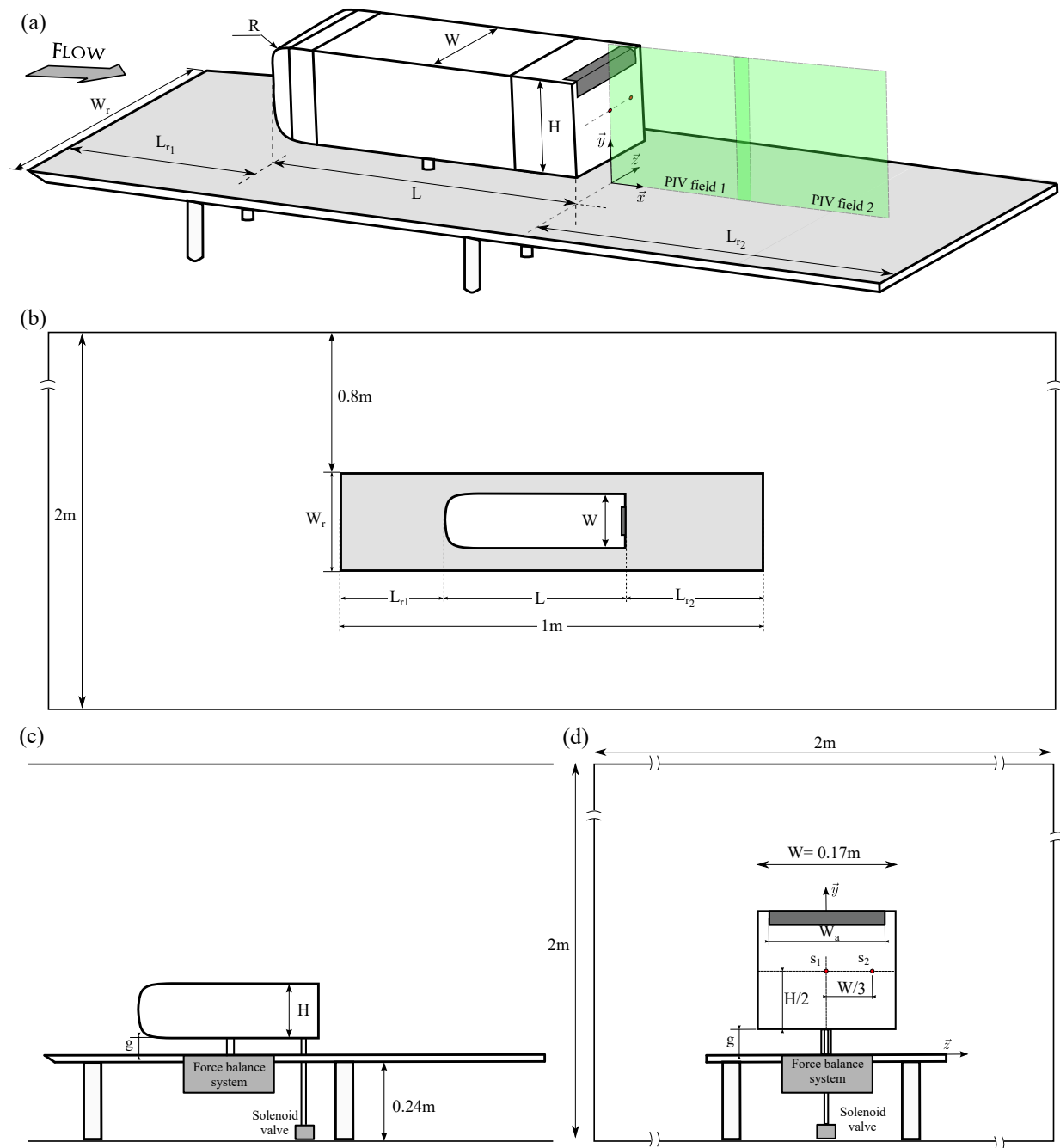


Figure 4.1 – Experimental setup of the simplified car model. (a) 3-dimensional sketch of the Ahmed body and reference system, (b) Upper view of the model and raised floor, (c) and (d) side and back view of the Ahmed body with a focus on the sensor and actuation location.

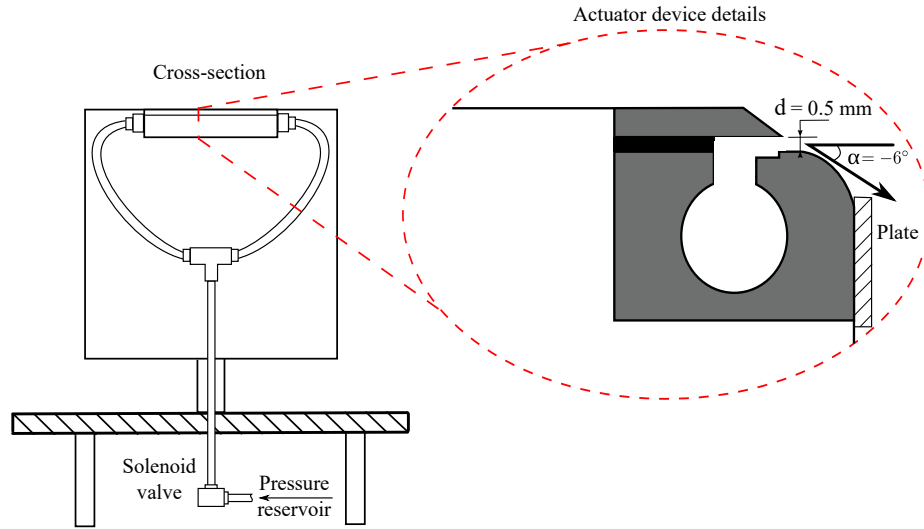


Figure 4.2 – Front view of actuation system. Cross-section view of the actuator mechanism.

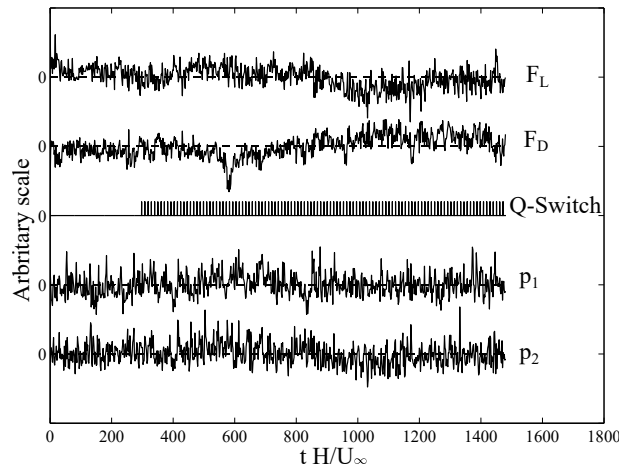


Figure 4.3 – Example of simultaneous measurement of the Q-switch signal of the laser cavity B and the unsteady pressures ( $p_1$  and  $p_2$ ) and forces ( $F_D$  and  $F_L$ ) during a PIV acquisition. + subscript denotes the  $H/U_\infty$  normalisation.

solenoid valve was placed under the raised floor as seen in Figure 4.2. A rounded surface, adjacent to the slit exit, with an additional plate, is installed to blow the jet in a predefined direction; for this case an actuation angle of  $\alpha = -6^\circ$  is used. Figure 4.2 shows a cross-section view of the surface at the exit zone. This surface resembles a boat-tail (Coanda effect) passive device for drag reduction. It is well known that the length and slant angle of the boat tail can strongly affect the drag-reduction performance (Han *et al.*, 1992; Yi, 2007). A pressure value of  $P_a = 6\text{bars}$  and a forcing frequency control DC of 50% are chosen, giving a maximum jet velocity of 32.2m/s. The mean jet velocity  $\bar{u}_{\text{jet}}$  is equal to 16.1m/s for periodic forcing, while in steady blowing configuration, the velocity  $u_{\text{jets}}$  will reach its maximum value of 32.2m/s. The jet velocity is quantified, as defined by Amitay *et al.* (2001), by the momentum coefficient:

$$C_\mu = \frac{S_{\text{jet}} \bar{u}_{\text{jet}}^2}{1/2 S_\infty U_\infty^2} = \text{DC } C_{\mu 0}, \quad (4.1)$$

where  $S_{\text{jet}}$  and  $S_\infty$  are respectively the slit and the Ahmed body cross-sectional area and  $\bar{u}_{\text{jet}}$  the mean jet velocity.  $C_{\mu 0}$  refers to the steady blowing momentum coefficient.

### 4.1.3 Real-time system

The real-time processing is achieved using an Arduino Mega board (Arduino Co., 2008). The data are measured from the sensors using the analogue inputs of the Arduino and the measurements are sent to a computer using the serial connection, which is connected to a USB port of the computer. The control

is sent to the actuators using a digital output port of the Arduino. The sampling rate is fixed at 100Hz. Higher sampling rates can be achieved by sending less text or data through the serial connection. In this case, every measured data was sent even if it was not used in the control algorithm (i.e., the drift) and the text chain sent contains a significant amount of unnecessary text in order to make it easily readable when received on the computer. The sampling rate of 100Hz was experimentally proven to be sufficient for the control algorithm developed in this work while being attainable by the Arduino.

## 4.2 Baseline flow

### 4.2.1 Flow statistics

Key aspects of the unforced flow are initially analyzed. The static properties of the “natural” flow are reviewed and the wake behaviour is first discussed. Bluff body wakes are sensitive to ground clearance (distance between the model under-surface and the ground) and 3-dimensional spanwise effects. A slight variation on the ground clearance leads to strong modifications of the wake structure, making them very sensitive to this parameter (Grandemange *et al.*, 2013b). Figure 4.4(a) presents the time-averaged cross-stream velocity with associate streamlines and the iso-line for a forward flow probability of 50%. For the present case, a classical wall-normal asymmetry is obtained. However, the main flow from the ground clearance moves toward the top edge of the body and then follows the upstream direction. This behaviour creates a large recirculation bubble located closer to the bottom edge and centred at  $x/H = 0.25$  and  $y/H = 0.4$ ; this configuration is known as an inverted asymmetric near wake. The presence of the Ahmed body support and pressure tube may also strongly perturb the bottom edge flow. These perturbations generate a small recirculation bubble on the ground wall. Evstafyeva *et al.* (2017) explained that this symmetry breaking occurs when the Reynolds number is sufficiently high to create under-body flow and thus influence the asymmetry in the wake. The flow topology resembles those found for studies with similar ground clearance (Eulalie, 2014). Furthermore, an elongated recirculation area (black solid line) is clearly visible. The recirculation length is calculated using the transitory detachment TD procedure, where the forward flow probability reaches a value of 50%. The obtained recirculation length  $L_r = 1.15H$  agrees well with previous studies (Wassen *et al.*, 2010; Lahaye *et al.*, 2014; Volpe *et al.*, 2015). The cross-stream velocity contour-plot shows the variability of the flow in the wall-normal direction. A high normal motion (red region) is clearly observed, suggesting a strong positive wall normal velocity near the recirculation area.

Figure 4.4(b) shows typical instantaneous vector velocity fields (coloured by the norm of the velocity vector) for the uncontrolled configuration. In order to highlight the unsteady flow structures, the vortex boundary identification method, introduced by Graftieaux *et al.* (2001) is used herein. Two vortical structures appear whereas the lower vortex is closer to the wall. Vortex creation at the top trailing edge is clearly seen; the presence of these coherent Kelvin-Helmholtz roll-ups in the vicinity of the upper edge have a typical length scale of  $\lambda_{KH} \approx 0.5H$ . Due to convective Kelvin-Helmholtz-type instabilities, the created roll-up vortices evolve, amplify and further dissipate downstream. The amplification of these vortices creates an interaction between the upper and lower shear layers. Finally, the instantaneous snapshot shows a flapping motion of the wake. The position and interaction of these vortices, caused by a perturbation, will enhance or diminish the drag.

The streamwise-transverse RMS-velocity ( $(u_{rms} + v_{rms})/U_\infty$ ) is plotted in Figure 4.4(c). A strong concentration of flow unsteadiness (red area) is presented all along the shear layer, close to the top edge, corroborating the creation of unsteady flow structures in this region (Figure 4.4(b)). A small positive area

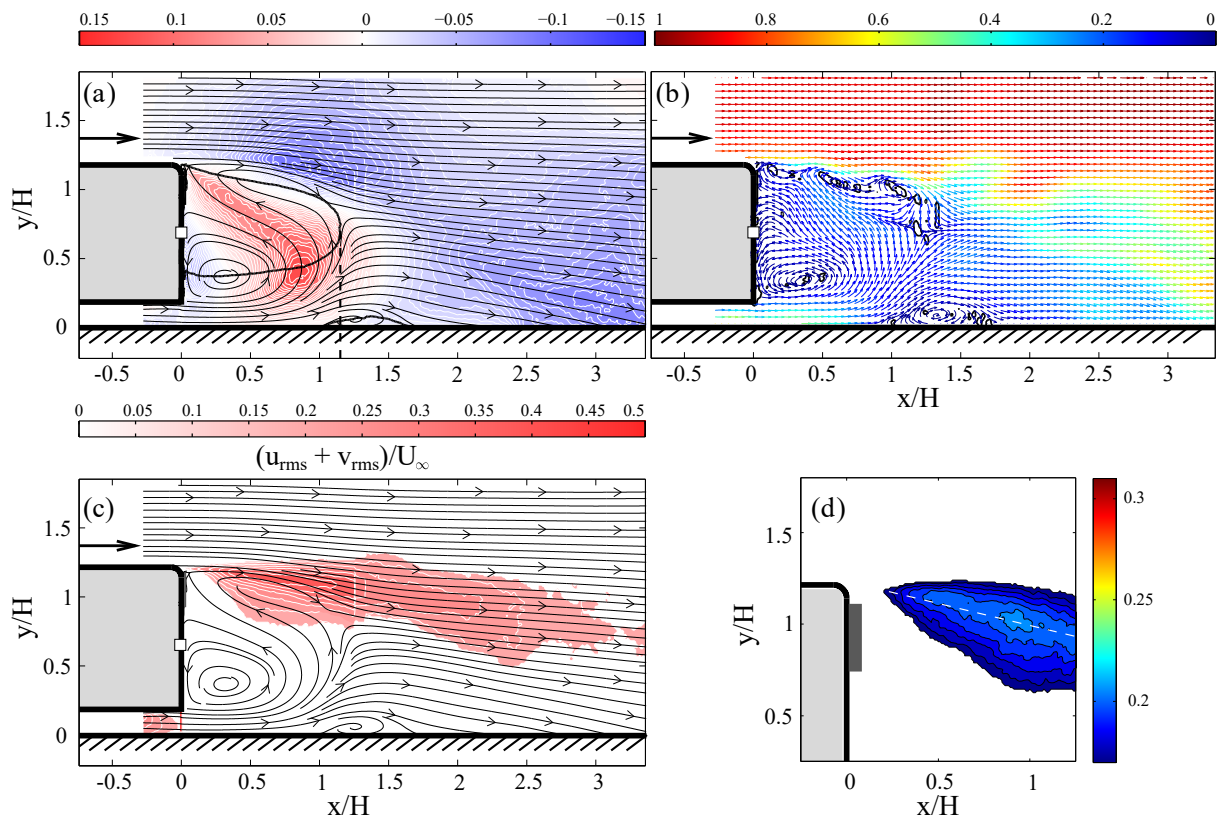


Figure 4.4 – Natural flow characteristics in the symmetry plane ( $z = 0$ ): (a) Time-averaged cross-stream velocity ( $\bar{v}^+$ ) with the associate streamlines and the iso-line of the forward flow probability of 50%. The recirculating flow length  $L_r$  is also displayed by the vertical dashed line, (b) Instantaneous flow field #265 captured by the PIV. The velocity field is indicated by dimensionless norm coloured arrows. The  $\Gamma_2$  criterion is displayed by black iso-lines revealing the unforced shear layer vortex street formation and the position of the typical main wake structures, ((c) Contour map of the streamwise-transverse RMS-velocity  $(u_{rms} + v_{rms})/U_\infty$ ) with associated streamlines, (d) Close view of the streamwise-transverse RMS-velocity.

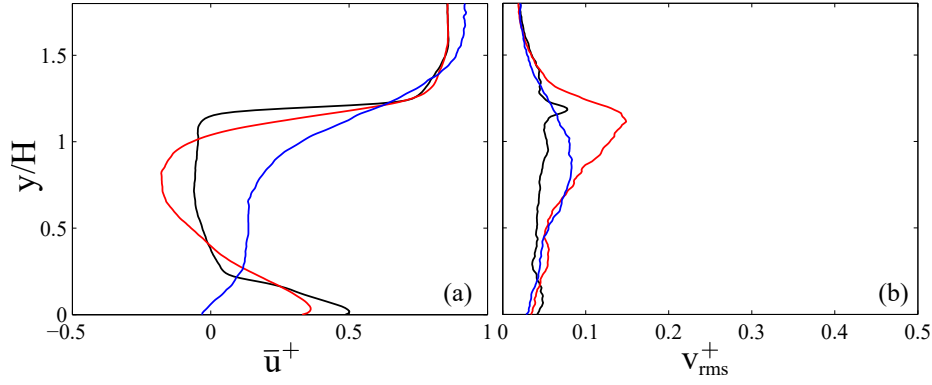


Figure 4.5 – (a) Time-averaged streamwise velocity ( $\bar{u}^+$ ), (b) Root-mean-square of the cross-stream velocity ( $v_{\text{rms}}^+$ ) profiles for various  $x/H$  positions ( $x/H =$  '—' black line: 0.2, '—' red line: 0.6, '—' blue line: 1.5).

is visible at the bottom edge, probably due to the perturbations created by the Ahmed body support and pressure tube. Also noteworthy is the influence of the RMS-velocity on the wake symmetry for which the creation of vortical eddies perturbs the wake and enlarges the bottom edge bubble. Similar results were obtained in different studies. [Barros \*et al.\* \(2016b\)](#) presented a strong streamwise-transverse velocity covariance  $\langle \bar{u}'v' \rangle$  close to the bottom edge and an asymmetric wake with the main bubble close to the top edge. [Grandemange \*et al.\* \(2013b\)](#) obtained a symmetric stress ( $\langle u'v' \rangle$ ) and a symmetric wake. A close view of the RMS-velocity is presented in Figure 4.4(d). The latter figure will be further used for comparison. The results presented in this section corroborate the strong influence of the bottom edge flow on the wake symmetry and the fact that small variations in the ground clearance may strongly influence wake behaviour.

Profiles of the time-averaged streamwise velocity ( $\bar{u}^+$ ) and root-mean-square of the cross-stream velocity ( $v_{\text{rms}}^+$ ) are presented in Figure 4.5 for various  $x/H$  positions ( $x/H =$  '—' black line:  $x/H = 0.2$ , '—' red line:  $x/H = 0.6$ , '—' blue line:  $x/H = 1.5$ ). Worth noting that the  $x/H$  positions 0.2 and 0.6 are inside the recirculation region while 1.5 is situated outside this zone.

For the time-averaged streamwise velocity  $\bar{u}^+$ , similar results are obtained for  $x/H < 1$ . The free stream velocity creates maximum positive streamwise values on the upper and lower clearance of the Ahmed body. The velocity is higher when the space between two walls is larger (upper clearance distance), while the ground clearance, space between the floor and the model, impedes the full development of the free-stream velocity. Due to the pressure difference (creation of a recirculation zone), the velocity will strongly decrease at the rear-back. The farther the velocity is registered in the streamwise direction, the lower this minimum/maximum difference will be. Outside the recirculation, more specifically at  $x/H = 1.5$ , the flow is still developing, probably caused by the development of the small recirculation area at the floor vicinity, which creates a decrease in the streamwise velocity close to the ground clearance. Concerning the cross-stream velocity  $v_{\text{rms}}^+$ , a positive peak is obtained at  $y/H \approx 1.2$ ; this peak will increase and further decrease its height and width for higher  $x/H$  values to become a bump at  $x/H = 1.5$ . Similar results were obtained by [Barros \*et al.\* \(2016b\)](#)

#### 4.2.2 Flow field dynamics and POD analysis

As previously explained, the flow structures are strongly linked to the base pressure footprints. For this reason, the normalized streamwise and normalwise pressure/velocity correlation coefficients are plotted in Figure 4.6 for both pressure probes. For the pressure probe located in the centre of the body ( $s_1$ ), Figure 4.6(a), a strong rounded negative region is clearly visible close to the sensor position. This strong negative region is related to the wide recirculation area at the lower part of the Ahmed body. A further

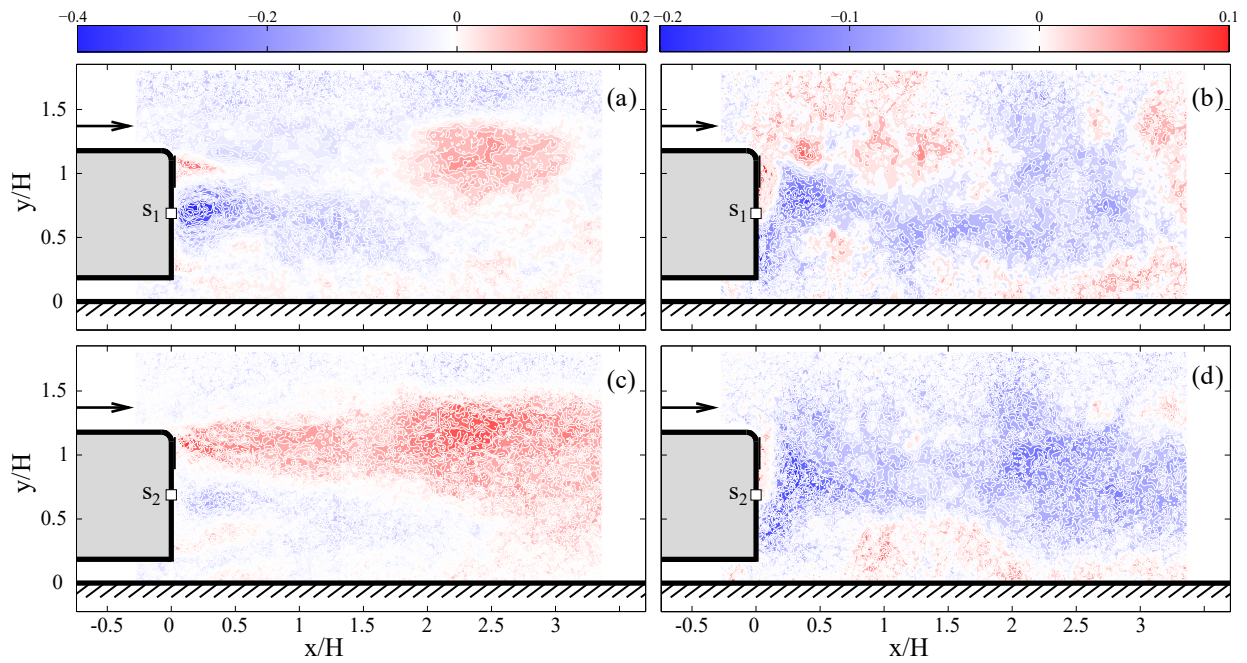


Figure 4.6 – Pressure/velocity correlation coefficient for pressure sensor  $s_1$  and  $s_2$  and  $Re_H = 9 \times 10^4$ , (a) and (c) normalized streamwise velocity/pressure  $p_1$  and  $p_2$ , respectively; (b) and (d) normalized normalwise velocity/pressure  $p_1$  and  $p_2$ , respectively.

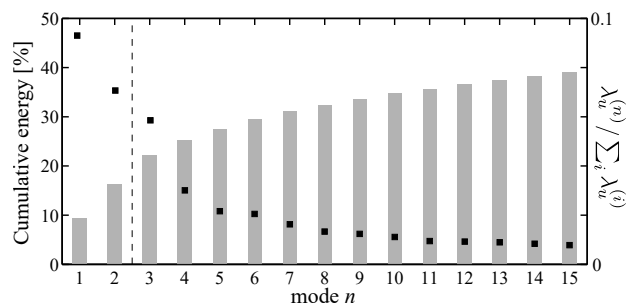


Figure 4.7 – Cumulative energy from POD decomposition of the velocity fields. '■' black square symbols denote the normalized mean square energy.

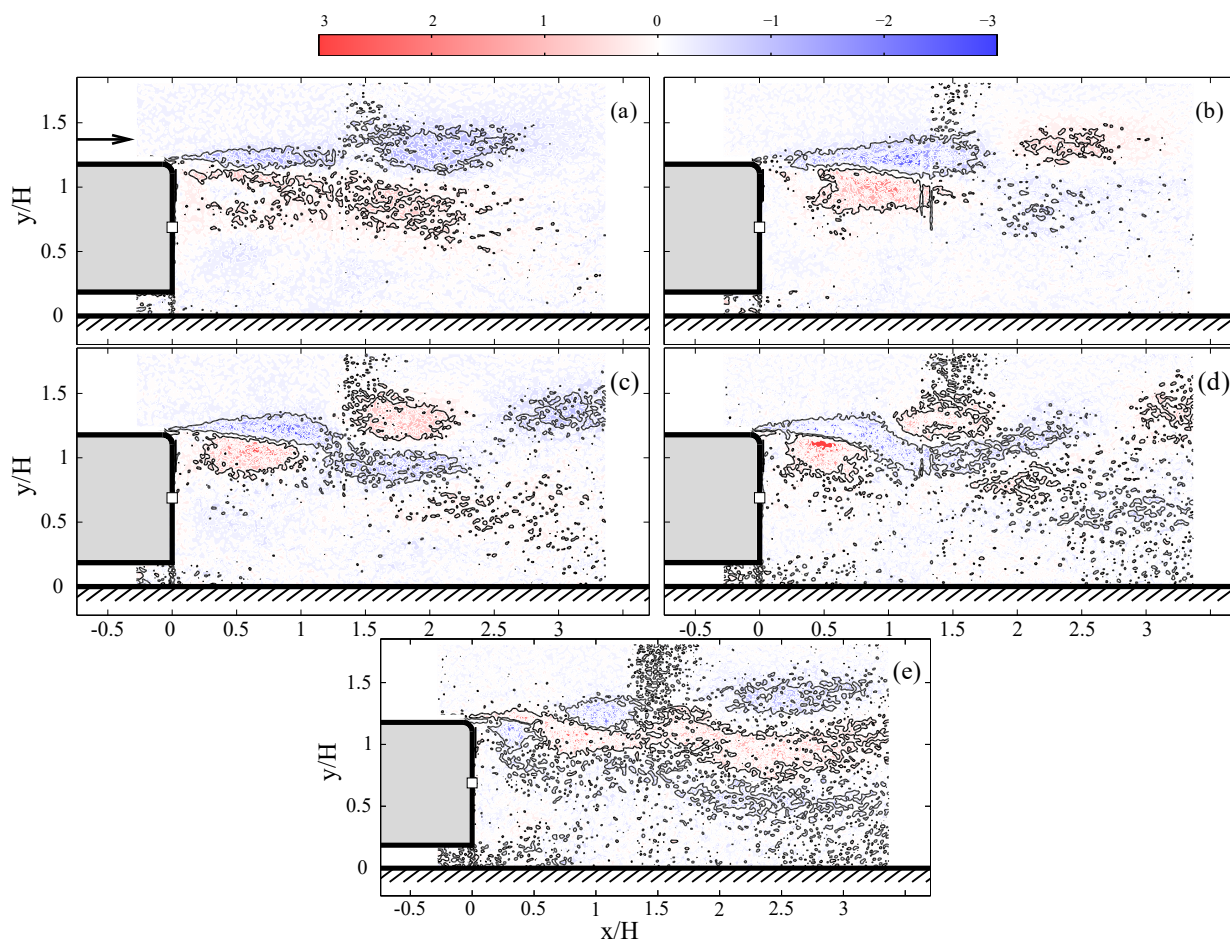


Figure 4.8 – Low-order POD velocity modes: (a) mode 1, (b) mode 2, (c) mode 3, (d) mode 4, (e) mode 5. Contour map shows the vorticity calculated from the corresponding POD velocity basis function and normalized with the step height and free-stream velocity ( $\omega_z H / U_\infty$ ).

positive zone is obtained at  $x/H \approx 2.5$ , underlining the flow structure convection. This behaviour is also seen by  $s_2$ . However, the closeness of this probe to the side edge, enhances and elongates this positive region throughout the streamwise direction, while the negative area diminishes. This strong variation is due to the flow interaction between the upper and side edges which creates counter-rotating longitudinal vortices. The normalized streamwise velocity/pressure correlation shows a similar behaviour for both probes. In this case, the correlation is half of the one obtained with the streamwise velocity. Nonetheless, a positive zone is clearly visible at the upper part of the wall (from  $y/H \approx 0.75$  to 1.25). This positive correlation is due to the flow behaviour, which moves from the ground clearance toward the top edge of the body. In this case, the sensor quantity and its correlation degree were not enough to further apply stochastic approaches in order to deeply understand the flow dynamics and describe the velocity/vorticity fluctuations.

Figure 4.7 shows the cumulative energy of the first fifteen velocity modes with the corresponding normalized mean square energy, defined as  $\lambda_u^{(n)} / \sum_i \lambda_u^{(i)}$ . Contrary to the results obtained in §3.2.2, the energy fraction of the two first modes is less than 20% of the total flow energy and the first fifteen modes comprise only 40%. Even though the cumulative energy of the 200 modes is less than 70%, some interesting information can be retained from the POD analysis. This small energy contribution (around 25%), contains potential information about flow structures. Figure 4.8 shows the low-order POD velocity modes (for  $n=1$  to 5) with corresponding vorticity modes. The POD basis functions are non-dimensional and the vorticity calculated from the POD mode  $\omega_z H / U_\infty$  is normalized with the step height  $H$  and free-stream velocity  $U_\infty$ . As also obtained in Chapter §3, the first two modes present elongated vorticity regions, a clockwise vorticity (blue region) on top of a counter-clockwise one. Higher modes show shorter and rounder shapes. However, a lot of scattering is presented for the latter ones. Nonetheless, for modes 3 and 4, the vortical structures are organized in space, corroborating previous results. If the present results are compared to

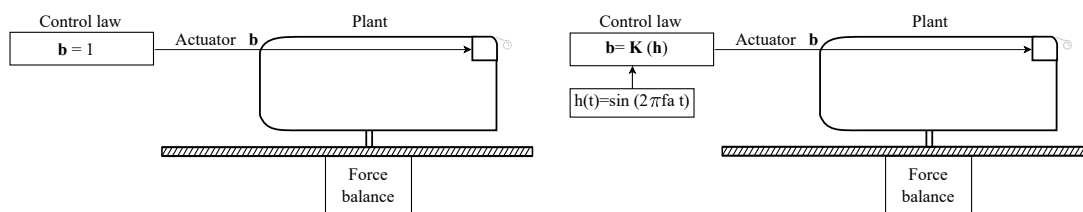


Figure 4.9 – Sketch of open-loop control. Left: continuous blowing actuation. Right: periodic forcing.

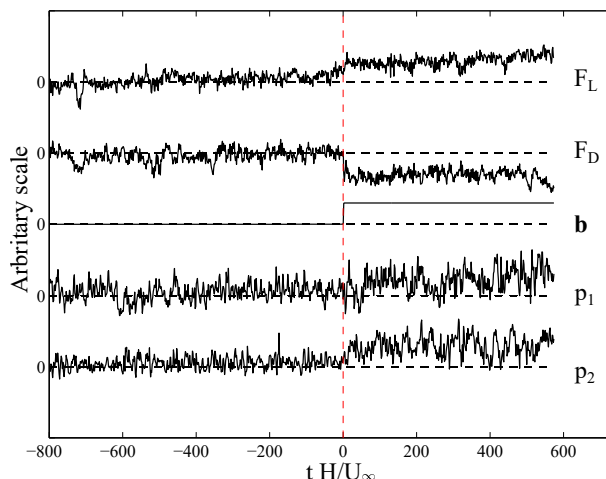


Figure 4.10 – Time-history response of the pressures and forces measurements due to a steady blowing step actuation ( $Re_H = 9 \times 10^4$ ,  $C_{\mu 0} = 1.355\%$ ).

those obtained for the backward-facing step (Chapter §3), it is possible to assume that the two first modes could be related to the flapping motion, while the other modes, which also have similar behaviour like those at the BFS case, can be retained for a study of the shedding phenomena.

### 4.3 Open-loop investigation

The response of both the baseline pressure and drag to various forcing parameters is here investigated. This work follows the conventional terminology of Control Theory in order to split different control paradigms studied. Namely, the notion open-loop control is used if control input is independent of system output (measurements), as presented in Figure 4.9, and the closed-loop control, respectively, if the input is a function of the output (see Figure 4.21). For a further understanding of the difference between open-loop and closed-loop control strategies used in the present article, a sketch of an open-loop OL plant model is displayed in Figure 4.9 and defines the input/output parameters of the physical system used for flow control. With an open-loop control law, it may be possible to achieve some desired specification without the use of measurement-based feedback control Brunton & Noack (2015). Two OL approaches are here considered: continuous and periodical blowing.

First, the ability of steady blowing to modify the rear pressure, and consequently the drag, is investigated. The actuation cost for this specific case is  $C_{\mu 0} = 1.355\%$ . Figure 4.9 shows the time-history evolution of pressure and force measurements when a steady blowing actuation is applied. The vertical red dashed line indicates the instant when the actuation is turned ON. The base pressure, as well as the aerodynamic forces, shows significant variations when the actuation is activated. While the pressures at the back ( $p_1$  and  $p_2$ ) and the lift  $F_L$  increase, the drag  $F_D$  is found to decrease. Even though a focus in drag reduction is done, a significant increase in the lift is also of particular interest; few studies take into account this parameter (Aider *et al.*, 2010) which is of great interest in the transport industry. Future analysis and control of this force will be considered for this configuration.

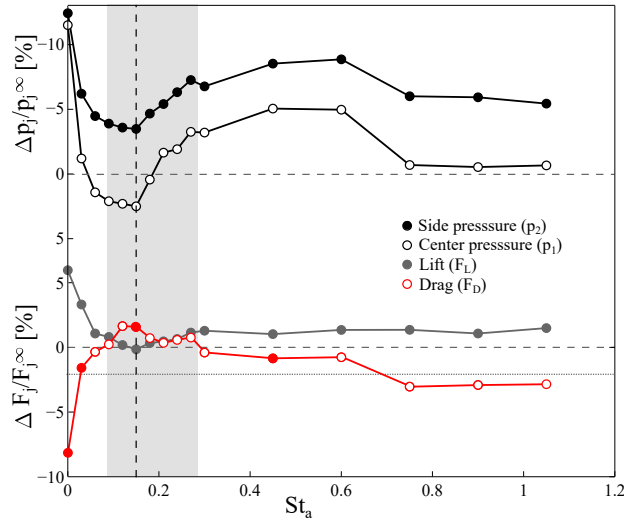


Figure 4.11 – Normalized and averaged variations of the rear pressures  $p_i$  ( $p_1$  and  $p_2$ ), and forces  $F_i$  (lift  $F_L$  and drag  $F_D$ ) compared to the natural case  $p_i^\infty$  and  $F_i^\infty$ . These parameters are plotted as functions of the actuation frequency  $St_a$  at  $C_\mu=0.00678$  for  $Re_H = 9 \times 10^4$ . The dash-line denotes the worst control case ( $St_o$ ), corresponding to the wake shedding. Note that for the steady blowing ( $St_a = 0$ ), the momentum coefficient is  $C_\mu=0.01355$  due to the duty cycle of the forcing cases. Filled red dots represent the four cases studied.

The effect of periodic blowing on the rear pressure and drag is now described. The pulsating frequency  $f_a$  is varied in the range  $[0-100]$  Hz, corresponding to a Strouhal number  $St_a$  varying in  $[0-1]$ . Figure 4.11 shows the relative variation of pressures  $p_i$  and aerodynamic forces  $F_i$  compared to the natural case  $p_i^\infty$  and  $F_i^\infty$ , against the dimensionless actuation frequency,  $St_a$ . An increase in the drag force is clearly seen for the “low-frequency” region  $St_a \in [0, 0.15]$ . An opposite behaviour is observed for the lift force ( $F_L$ ) and the base pressure ( $p_j$ ). The maximum drag value is obtained at the “worst” control case ( $St_o = 0.15$ ). Following previous studies (Eulalie, 2014; Krajnović & Davidson, 2010), this Strouhal number corresponds to the wake shedding frequency (indicated by the vertical dashed line). This tendency is inverted for the “moderate-frequency” region  $St_a \in [0.15, 0.6]$ , where the drag decreases. Again, an opposite tendency is obtained for  $F_D$ ,  $p_1$ , and  $p_2$  which agrees well with experimental and numerical investigations of the literature (Rouméas *et al.*, 2009; Wassen *et al.*, 2010). The grey area in Figure 4.11 represents a positive drag difference, while the white area represents a negative drag difference. The optimal case, from the studied cases, with a drag reduction of up to  $-8\%$ , is obtained for the steady blowing case ( $St_a = 0$ ) but at the expense of a higher  $C_\mu$  coefficient ( $1.355\%$ ), compared to that of the pulsating blowing cases ( $0.678\%$ ).

### 4.3.1 Wake modification

The effect of the open-loop forcing for different actuation frequencies on the near-wake flow is here discussed. Four different cases are considered and correspond to the red filled dots in Figure 4.11: (case I) steady blowing case with  $St_a = 0$ , (case II) “low-frequency” forcing case at  $St_a = St_o/2$  leading to a negative drag difference, (case III) “low-frequency” forcing case at  $St_a = St_o$  implying a positive drag difference and (case IV) a “moderate-frequency” forcing case at  $St_a = 3St_o$  leading to a negative drag difference.

To understand how the base pressure and drag are affected by the forcing, modifications of the topology of the flow just at the rear of the body is first examined. Streamlines of the time-averaged velocity in the measurement plane for the four forcing cases are reported in Figure 4.12(aI) to Figure 4.12(aIV). The black line shown in these figures corresponds to the iso-line of the forward flow probability of  $50\%$ . The same

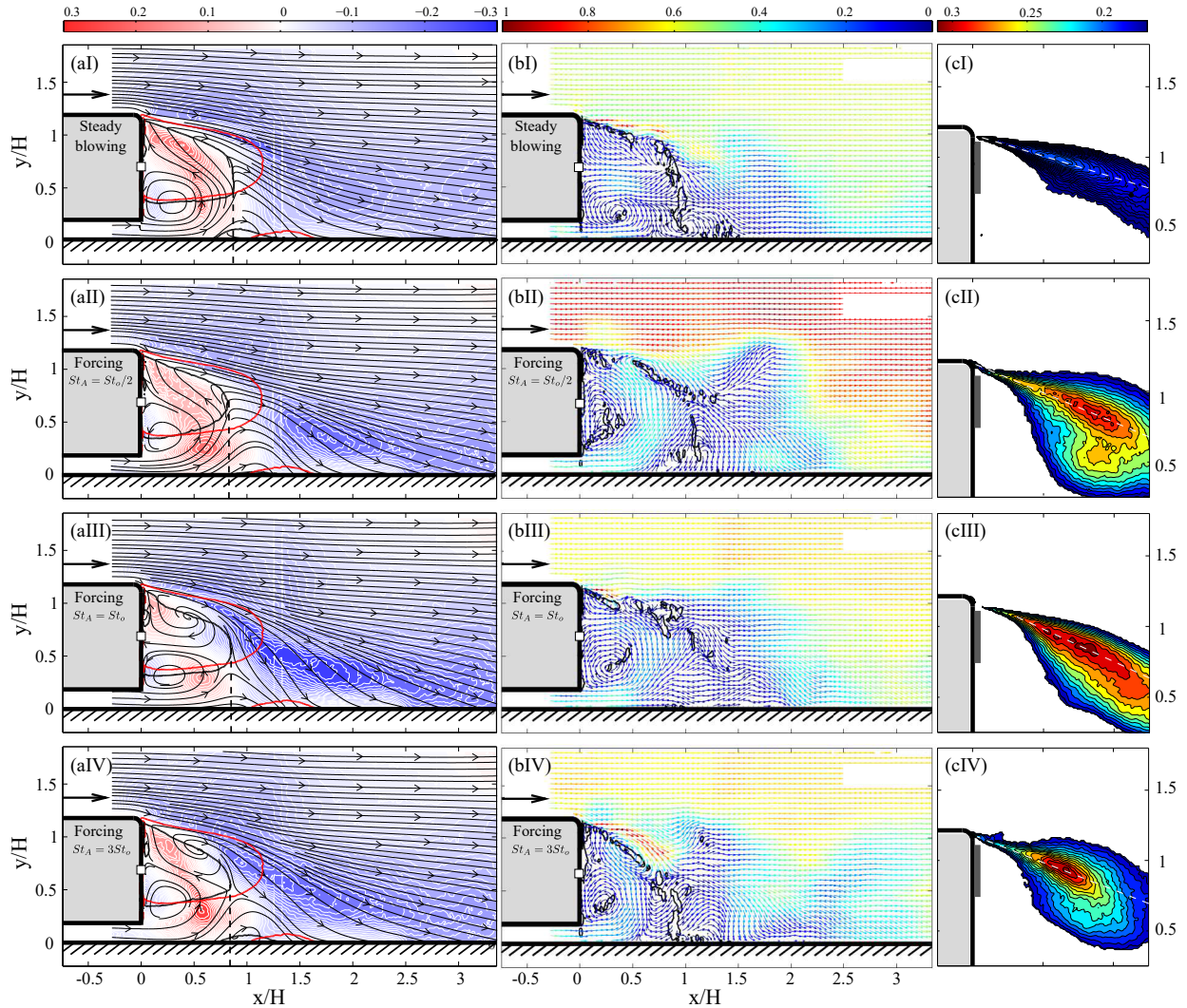


Figure 4.12 – (a) Forcing flow time-averaged cross-stream velocity ( $\bar{v}^+$ ) with the associate streamlines. The recirculating flow length  $L_r$  is displayed by the vertical dashed line. The iso-line of the forward flow probability of 50% is plotted in — for the controlled cases and in — for the natural flow reference. (b) Instantaneous flow field #265 captured by the PIV. The velocity field is indicated by dimensionless norm coloured arrows. The  $\Gamma_2$  criterion is displayed by black iso-lines revealing the unforced shear layer vortex street formation and the position of the classical main wake structures. (c) Closed view of the streamwise-transverse RMS-velocity for several, (I) Case I: Steady blowing; (II) Case II:  $St_a = St_o/2$ ; (III) Case III:  $St_a = St_o$ ; (IV) Case IV:  $St_a = 3St_o$ . For a full visualization of the wake evolution please refer to videos

information for the uncontrolled case is also reported for comparison as the red line. Finally, the colourmap represents the level of the cross-stream velocity. An inverted asymmetric near-wake is observed for cases I and II (Figure 4.12(aI) and Figure 4.12(aII), respectively). For these two cases, the height of the bubble is found to span almost half of the rear of the body while its length in the downstream direction is reduced compared to the two other forcing cases. For the steady blowing case I, the bubble is centred at the same location than that for the uncontrolled flow case (i.e.  $x/H = 0.25$  and  $y/H = 0.4$ ), while it is found closer to the bluff body wall for case II. For the other two arrangements, cases III and IV, a nearly symmetric flow with two large recirculation bubbles are observed (Figure 4.12(aIII) and Figure 4.12(aIV), respectively) with the bottom one moving counter-clockwise and the upper one clockwise. When the actuation frequency is equal, or close, to that of the wake shedding ( $St_a = St_o$ ), the bubbles are almost aligned in the x-direction with their focus at  $x/H \approx 0.25$ , as shown in Figure 4.12(aIII). In contrast, when the actuation frequency is higher than the wake shedding, the lower bubble moves closer to the wall, while the upper bubble is slightly shifted downstream, as illustrated in Figure 4.12(aIV). Finally, one of the most important variables to determine the efficiency in drag reduction is the time-averaged cross-stream velocity. For all the forcing cases leading to a negative drag difference (cases I, II and IV), a region of positive mean cross-stream velocity is clearly seen, with a maximum cross-stream velocity closer to the wall than for the uncontrolled case. This behaviour defers for the positive drag case III ( $St_a = St_o$ ), where the positive time-averaged cross-stream velocity nearly disappears.

The instantaneous velocity fields were next examined in detail. The full-time sequences of these snapshots are available online; only the main features are discussed here. Figure 4.12(bI) to Figure 4.12(bIV) show instantaneous snapshots of some of the states for the actuated cases. For the steady blowing case, Figure 4.12(bI), a direct opposition control of vortices in the near wake is applied. A continuous direct vortex perturbation in the top trailing edge shifts the convective structures closer to the body with a consequent reduction of the recirculation area. The upper and lower shear layer vortex interaction re-approaches the wall. The downward direct injection angle and the steady blowing combine together to deviate the trains of vortical structures, generated by the forcing, towards the rear face of the body as also observed by Barros *et al.* (2016b).

When periodic forcing is applied, the wake appears to be potentially modified through different processes depending on the forcing Strouhal number. When an actuation with a Strouhal number below  $St_a = 0.15$  (case I) is applied, the wake is modified through energization of the shear layer. As the Strouhal number approaches 0.1, the sensitivity of shear layers to low-frequency forcing is known to decrease, and the drag, consequently, increases due to decay in the locking effect at low actuation frequencies. Low-frequency actuation will perform similarly to the continuous blowing case, which is consistent with the results of Figure 4.12(bI), where a similar behaviour in the wake evolution as that observed for the continuous blowing case I is perceived. These similarities corroborate the resemblance of the inverted asymmetry for both continuous and low-frequency forcing. For the periodic forcing, however, the large vortical structures are found to develop over the whole height of the body, with eddies being present on a larger section of the cross-stream direction. An interesting transition in the control process occurs for forcing Strouhal numbers  $St_a \in [0.15, 0.3]$  where the forcing is found to enhance the wake symmetry by affecting the vortex-shedding mechanism. In this range of forcing Strouhal numbers, the drag force first increases until it reaches a maximum value at a forcing  $St_a$  equal to that of the wake shedding  $St_o$ , while decreasing once a symmetry in the wake is attained. Such symmetric wake is visible for case III.

In addition, the proximity between the actuated and shedding frequencies leads to an expansion of the shear layer vortices close to the edge. The combination of a transitioning wake from asymmetric to symmetric- and a shear-layer vortex expansion (unstable symmetry wake) could possibly lead to an increase in the cross-stream velocity and a decrease of the base pressure. It is noteworthy that the actuation is only applied on the upper part of the body rear face, which could possibly explain the instability of the

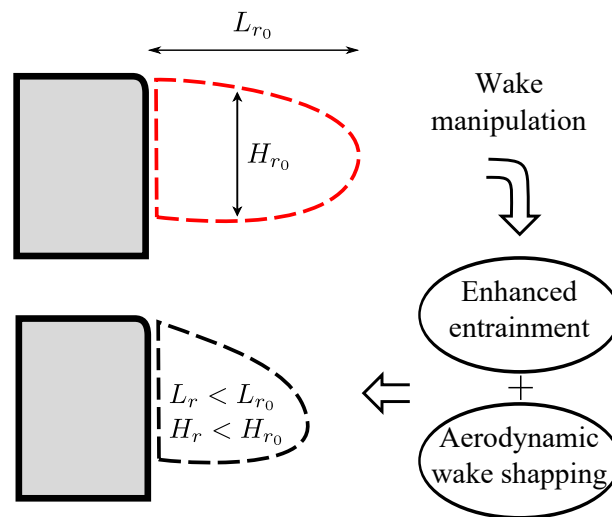


Figure 4.13 – Global effect by wake manipulation: enhanced entrainment coupled to bubble shaping. Sketch is based on the results obtained by Barros *et al.* (2016b).

symmetric wake. The results obtained here differ from some previous investigations (Pastoor *et al.*, 2008; Barros *et al.*, 2016b). Nonetheless, similar results were obtained when the Ahmed body configuration and the actuation positioning are closer to the one presented here (Eulalie, 2014).

Finally, higher forcing frequencies  $St_a > 0.3$  (case IV) are found beneficial with respect to the base pressure and drag. For such forcing case, a synchronization process between the upper and lower shear layers occurs such as is observed in Figure 4.12(bIV), accompanied by small-scale vortices that maintain the wake symmetry.

Maps of the RMS-velocity are presented for the four forcing cases in Figure 4.12(cI) to Figure 4.12(cIV). Compare to the baseline flow (Figure 4.4(d)), the line of maximum velocity is found to move downwards due to the negative actuation angle already discussed. While the pulsed forcing cases are found to enhance the maximum of velocity, a noticeable decrease is observed for the continuous blowing case. The later may be attributed to the narrow slit and large velocity of the actuation. For case III ( $St_a = St_o$ ), a thicker intense region of RMS-velocity is obtained. The unsteady vortical structures, which are intensified by the periodic shedding frequency, strongly affect the near wake. The perturbed eddies are agglomerated close to the recirculation area intensifying the unsteady flow and further decreasing the cross-stream velocity. This analysis corroborates the flow structures presented in Figure 4.12(bIII), suggesting that an increase of the perturbed vortical structures (enhance of wake shedding) at the top trailing edge might have an impact on the drag rise. Both cases II and IV present a similar velocity pattern with a rounded shape. The intensity of the area increases compared to the baseline flow, but not as strongly as for case II, ratifying the drag variation between the best and worst cases (case I and III, respectively) suggesting that to decrease the drag, the forced structures must be moved near the wake while not strongly intensified.

Barros *et al.* (2016b) described three different mechanisms for manipulating the wake: (1) a reduction of entrainment and bubble elongation, (2) a reduction of entrainment coupled to bubble shaping for high-frequency forcing and finally, (3) an enhancement of entrainment decreasing the bubble length at low-frequency forcing. With regards to the results discussed previously, we here suggest a complementary mechanism at play, illustrated in Figure 4.13. As initially mentioned, the actuation is directed downwards by combining with Coanda effect. The vortical structures generated by the pulsed actuation are, therefore, convected downwards while increasing the momentum entering into the wake. This results in a reduction of the thickness of the forced bubble as shown by Figure 4.12 and in an aerodynamic shaping of the rear flow. Nonetheless, other key parameters must be taken into account to properly understand the wake behaviour and further control it.

Figure 4.14 shows the time-averaged streamwise velocity  $\bar{u}^+$  and root-mean-square of the cross-stream velocity ( $v_{\text{rms}}^+$ ) for all the flow control cases. The  $x/H$  positions will be denoted as follows: '—' black line  $x/H = 0.2$ , '—' red line  $x/H = 0.6$ , '—' blue line  $x/H = 1.5$ . A strong peak at  $y/H \approx 1.2$  is clearly seen for both the streamwise and the rms-cross-stream velocity; the position of the peak coincides with the exit nozzle of the jet, which explains the strong variation in both  $x$  and  $y$ -directions.

For the time-averaged streamwise velocity ( $\bar{u}^+$ ), similar results, without taking into account the jet perturbation, compared to the unforced flow are obtained for  $x/H < 1$ . The free stream velocity creates maximum positive streamwise values on the upper and lower clearances of the Ahmed body. Once again, the velocity is higher when the space between two walls is larger (upper edge).

However, interesting differences are seen for the  $v_{\text{rms}}^+$ . Recalling Figure 4.5(b), a positive pick was obtained at  $y/H \approx 1.2$ ; this peak increased and further decreased its height and width for farther  $x/H$  values, to become a bump at  $x/H = 1.5$ . Due to the actuation mechanism, the peak created will strongly vary. When continuous blowing is applied, Figure 4.14(bI), the  $v_{\text{rms}}^+$  peak will decrease and move down in the  $y/H$ , corroborating the negative angle jet flow. At  $x/H = 1.5$ , the velocity will have similar behaviour as the one obtained for the baseline flow. Even though the initial peaks are not as deep as when periodic forcing is applied, Figure 4.14(bII), Figure 4.14(bIII), and Figure 4.14(bIV), its consequences will go further in the streamwise direction; e.g., the bump obtained at  $x/H = 1.5$  will have higher  $v_{\text{rms}}^+$  values and will spread wider in the normalwise direction. Moreover, the peak is strongly linked to the type of periodic forcing that is applied. For a  $St_a = St_o/2$  (Figure 4.14(bII)), the peak increases its width size and moves lower in the  $y/H$  direction, compared to continuous blowing. At  $x/H = 1.5$ , the maximum  $v_{\text{rms}}^+$  value is located at  $y/H \approx 0.5$  and it goes up to  $v_{\text{rms}}^+ = 0.25$ . Similar results are obtained for  $St_a = 3St_o$ , Figure 4.14(bIV). For this case, the peak is less prominent but wider. A different behaviour is seen for  $St_a = St_o$ . When an analysis is done close to the recirculation zone, a wider bump is visible, '—' blue line in Figure 4.14(bIII). The maximum  $v_{\text{rms}}^+$  value is presented from the bottom trailing edge of the Ahmed body spreading up to the upper edge. The maximum root-mean-square of the cross-stream velocity is equal to case II. Taking into account these considerations, the cross-stream velocity might have an impact on the drag forces. The worst case,  $St_a = St_o$ , has a higher value of  $v_{\text{rms}}^+$  and it is dispersed along almost all of the Ahmed body height  $x = H$ . For case IV, the bump is less prominent but still wide. On the contrary, for  $St_a = St_o/2$  the bump has a high  $v_{\text{rms}}^+$  maximum but it does not cover the whole Ahmed body height. Two main conclusions can be proposed. The first one is the strong influence of the cross-stream velocity on the drag modification, corroborating the results presented in Figure 4.12. The second one is linked to the optimal jet position and angle in order to strongly perturb the mean flow. As an example, the best case, continuous blowing, presents strong variations in the shear layer region, energetically modifying the recirculation bubble, without further perturbation of the mean wake flow.

### 4.3.2 Flow field dynamics and POD analysis

Figures 4.15 and 4.16 show the normalized streamwise and normalwise pressure/velocity correlation for the sensor probes  $s_1$  and  $s_2$ , respectively. For simplification purposes, only the results of cases I and II will be presented. Case III shows similar behaviour, for the stream- and normalwise correlation for both pressure probes, to those obtained for case II. Case IV does not show significant velocity/pressure correlations to propose an accurate conclusion. When analysing the streamwise velocity pressure  $s_1$  correlation (Figure 4.15(a)), a similar negative region is obtained close to the pressure probe. This region is less rounded and wider when continuous blowing is applied (Figure 4.15(aI)). Also, when this strategy is used, a positive elongated thin region over a negative one is observed close to the top trailing edge. This positive correlation is due to a continuous actuation of the control mechanism. Once again, strong variations are obtained when periodic forcing is applied. For case II, a secondary positive region appears

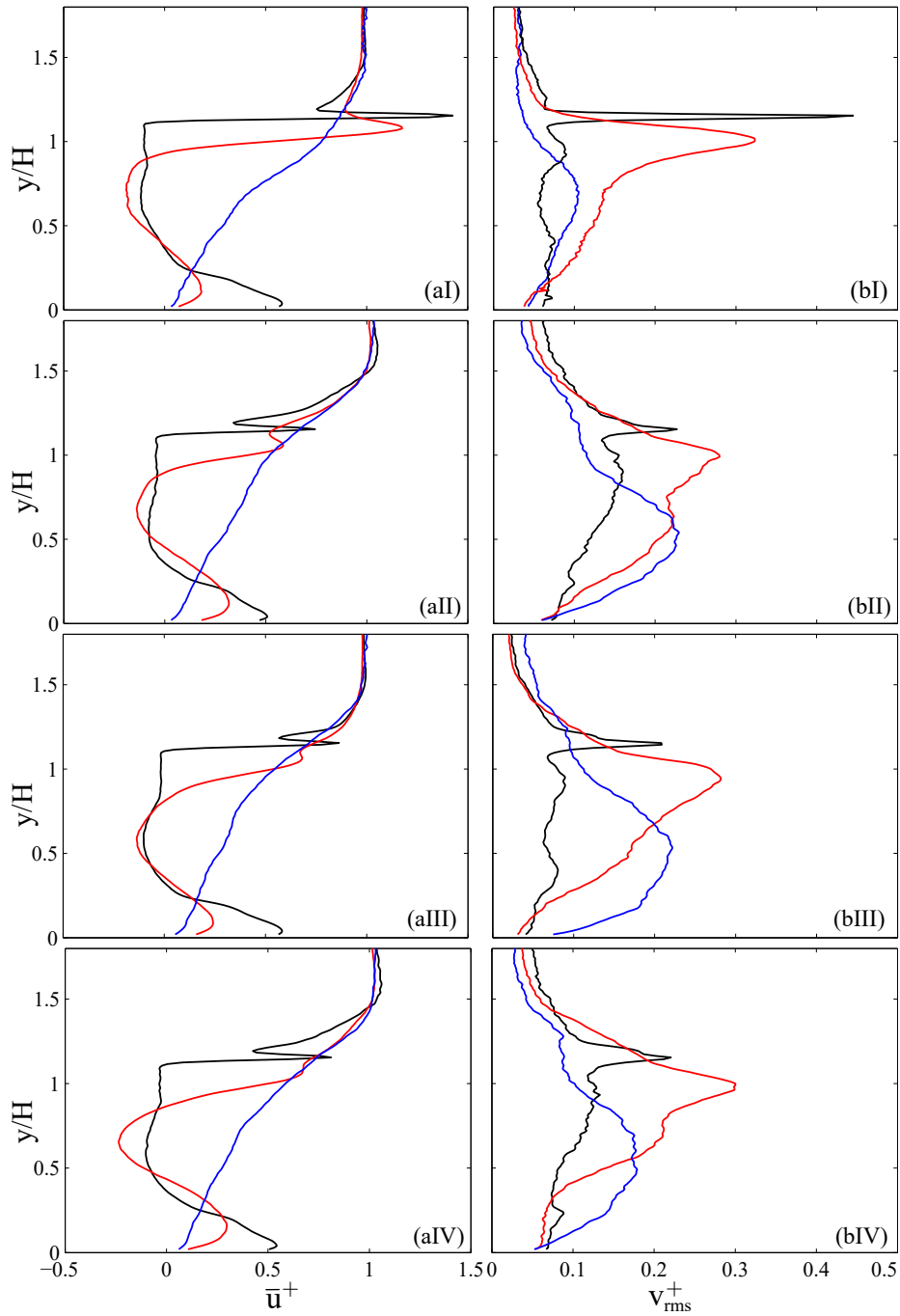


Figure 4.14 – (a) Time-averaged streamwise velocity ( $\bar{u}^+$ ) and (b) Root-mean-square of the cross-stream velocity ( $v_{\text{rms}}^+$ ) profiles for various  $x/H$  positions ('—' black line:  $x/H = 0.2$ , '—' red line:  $x/H = 0.6$ , '—' blue line:  $x/H = 1.5$ ). (I) Case I: Steady blowing, (II) Case II:  $St_a = St_o/2$ , (III) Case III:  $St_a = St_o$ , (IV) Case IV:  $St_a = 3St_o$

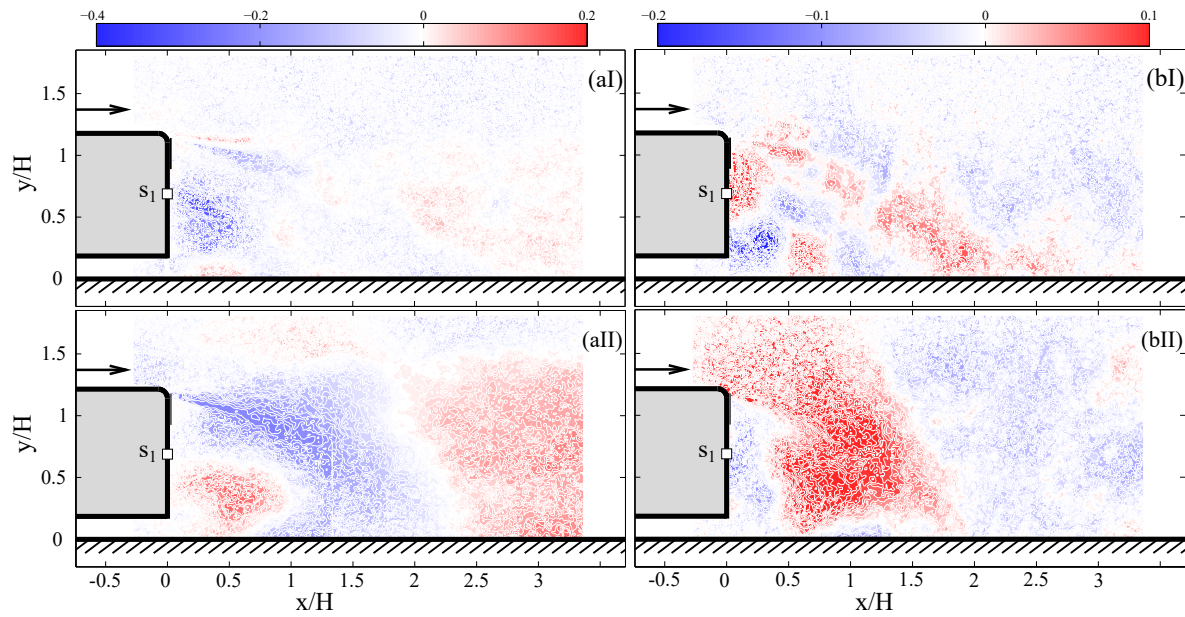


Figure 4.15 – Pressure/velocity correlation coefficient for pressure sensor  $s_1$  and  $Re_H = 9 \times 10^4$ , (a) Normalized streamwise velocity/pressure and (b) Normalized normalwise velocity/pressure. (I) Case I: Steady blowing; (II) Case II:  $St_a = St_o/2$ .

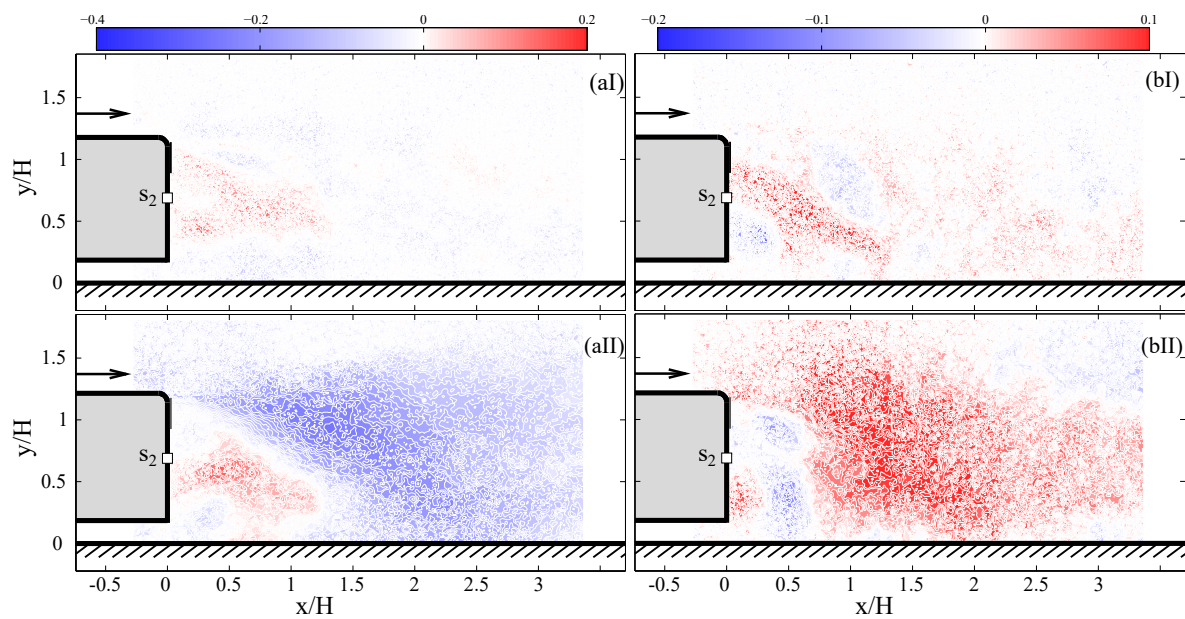


Figure 4.16 – Pressure/velocity correlation coefficient for pressure sensor  $s_2$  and  $Re_H = 9 \times 10^4$ , (a) Normalized streamwise velocity/pressure and (b) Normalized normalwise velocity/pressure. (I) Case I: Steady blowing; (II) Case II:  $St_a = St_o/2$ .

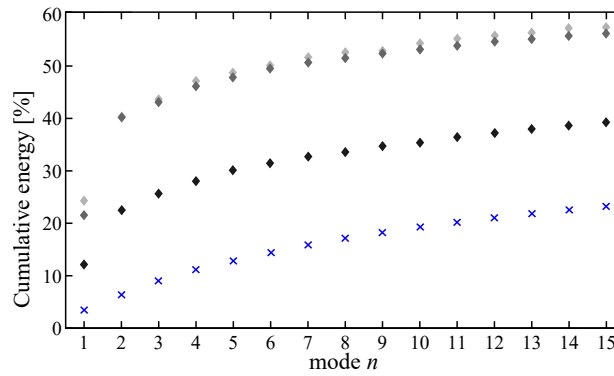


Figure 4.17 – Cumulative energy from POD decomposition of the velocity fields. 'x' blue cross: case I, '◊' light gray diamond: case II, '◊' gray diamond: case III, '◊' dark gray diamond: case IV.

under the negative one, moving the latter close to the trailing edge. When periodic forcing is applied, a positive region appears closer to the bottom edge. This enlargement of a positive region might have strong consequence in the flow analysis. The symmetry between the negative and positive correlations, obtained for case II, could be a consequence of the symmetric wake presented in the mean-flow results, which leaves a strong imprint in the pressure sensor  $s_1$ . As previously stated, interesting results are obtained for the cross-stream velocity. Figure 4.6(b) shows a positive zone at the upper part of the back wall. This zone grows when continuous blowing is applied, covering more than half of the body height. This increase is strongly connected to the flow movement inside the recirculation, which might further decrease the drag. For periodic forcing, a negative correlation is obtained close to the wall with a greater neighbouring positive one.

Similar results are presented when studying the velocity/pressure correlation with the pressure probe  $s_2$  (Figure 4.16). For both the streamwise and cross-stream velocities, the pressure print is similar when periodic forcing is applied. However, for continuous blowing, a small dissimilarity is seen for the cross-stream velocity correlation with pressure probe  $s_2$  (Figure 4.16(bI)). A positive elongated zone is surrounding the back of the Ahmed body; the elongated vortical structures (red area) nearly disappears when continuous blowing is applied. This behaviour might be linked to the strong influence of steady blowing in the 3-dimensional wake. The pressure/velocity correlation might give an insight of the flow structure movement and how it is perceived by the pressure sensors. The pressure/velocity correlations can be strongly perturbed by the actuation mechanism, which is really close to the pressure sensor and might leave some unwanted noise. Also, the negative angle of the jet velocity might have an impact on the pressure signal. However, a general analysis of this correlations can elucidate some indicators of the flow behaviour when actuation is applied and the optimal location of the sensors to detect them.

Figure 4.17 shows the cumulative energy of the first fifteen velocity modes for the four cases studied. The total energy will depend on the actuation mechanism. A strong decrease of the total energy is clearly seen from the lowest frequency to the highest one, being continuous blowing the case with the least cumulative energy. The two first modes of cases II and III ('◊' light gray diamond and '◊' gray diamond, respectively) comprise 40% of the total energy. In contrast, for case IV, only 20% is obtained, and even less for continuous blowing (around 10%). The first fifteen modes for the lowest frequencies reach almost 60% of the total energy, close to the 200 modes of the unforced case. For the other cases, the cumulative energy values of the first fifteen modes are less than 40% and 30% for cases III and I, accordingly. Nonetheless, an overview of the flow behaviour for each mode can be analysed taking into account the first 200 modes.

Figures 4.18 to 4.20 show the low-order POD velocity modes (for  $n=1$  to 5) with corresponding vorticity modes. For mode 1 (Figure 4.18(a)), cases II, III and IV (periodic frequencies) present elongated vortical structures; the size and width of these structures are significantly lower compared to those obtained for the unforced case (Figure 4.8(a)). However, cases II and III present a shift on the vortical structures, with

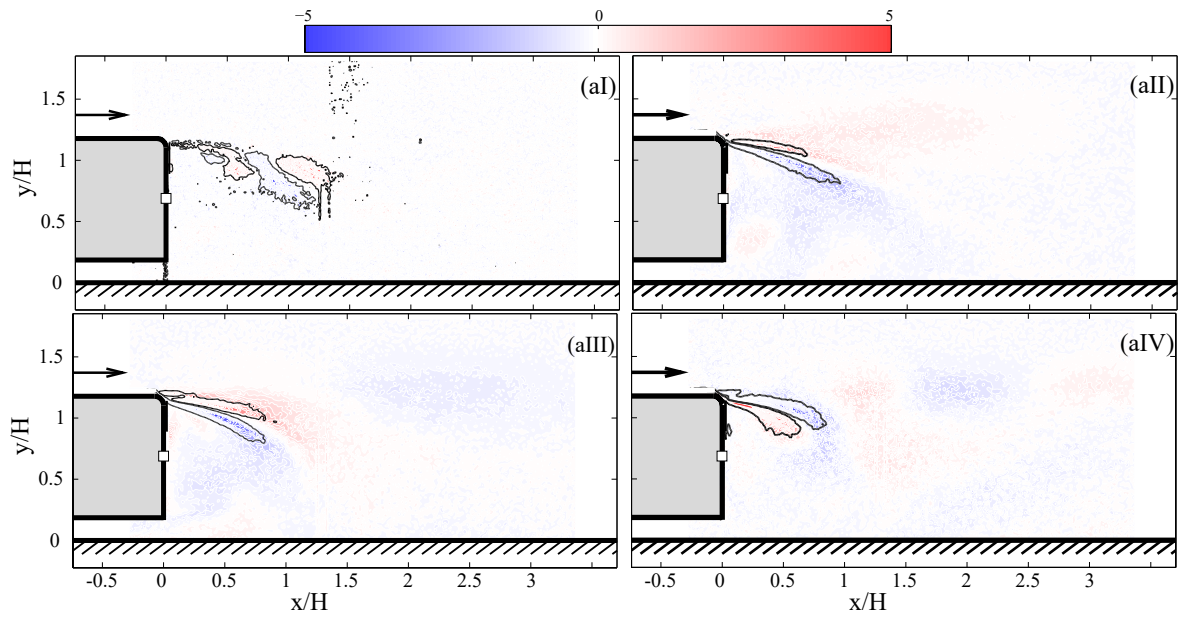


Figure 4.18 – (a) Low-order POD velocity mode 1. (I) Case I: Steady blowing, (II) Case II:  $St_a = St_o/2$ , (III) Case III:  $St_a = St_o$ , (IV) Case IV:  $St_a = 3St_o$ .

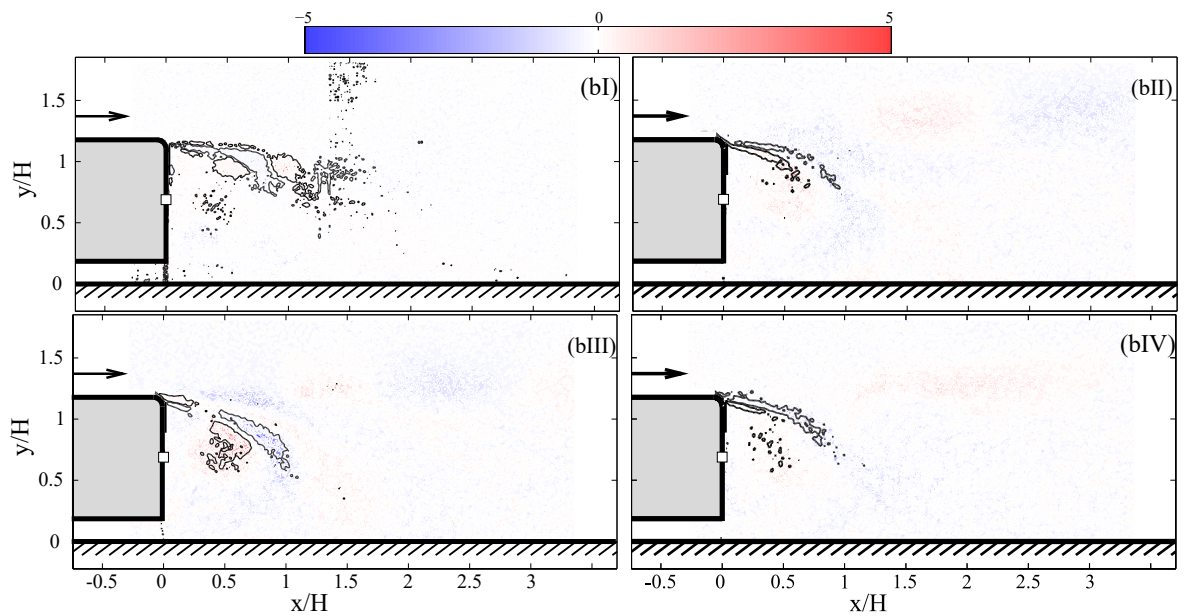


Figure 4.19 – (b) Low-order POD velocity mode 3. (I) Case I: Steady blowing, (II) Case II:  $St_a = St_o/2$ , (III) Case III:  $St_a = St_o$ , (IV) Case IV:  $St_a = 3St_o$ .

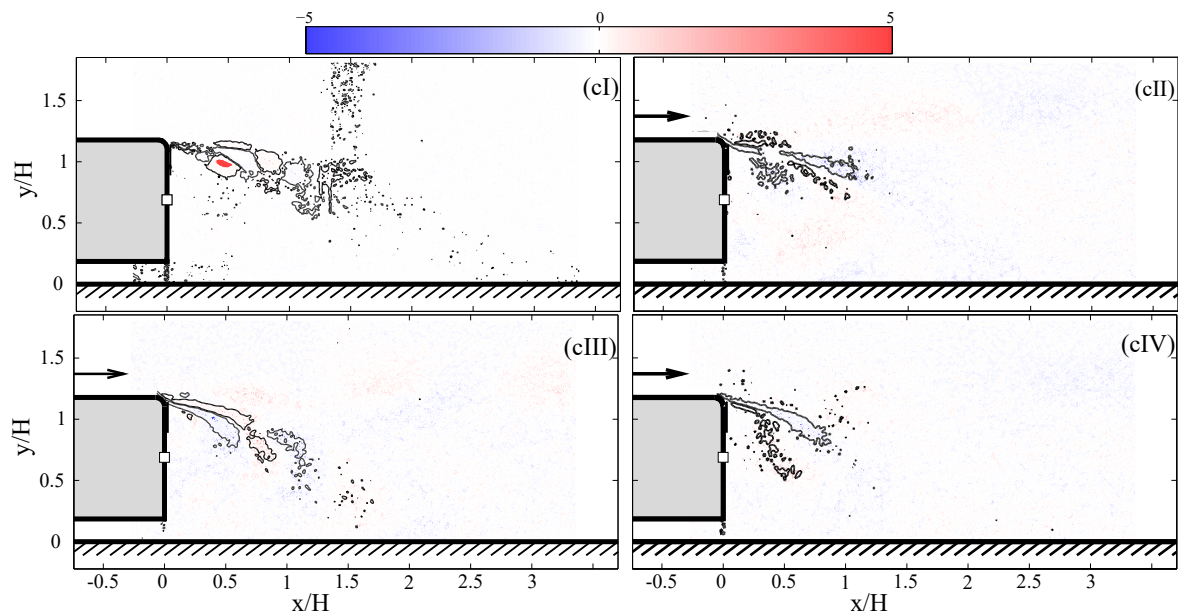


Figure 4.20 – (c) Low-order POD velocity mode 5, (I) Case I: Steady blowing, (II) Case II:  $St_a = St_o/2$ , (III) Case III:  $St_a = St_o$ ; (IV) Case IV:  $St_a = 3St_o$ .

the counter-clockwise over the clockwise one. A completely different behaviour is seen for the continuous blowing, where smaller vortical structures are generated from the shear layer. Taking the considerations stated in Chapter §3 and the results from the unforced flow, the flapping motion (presented in the two first modes) is strongly perturbed by the continuous and periodic forcing, more forcefully for the steady case. When analysing the second mode, not presented herein, the highest frequency presents a similar behaviour to that of the continuous mode, where smaller and rounder structures are seen close to the top shear layer.

If a focus on the other modes is executed, the continuous blowing is always perturbing the flow with organized small structures closer to the edge. The vortical structure sizes and closeness between each other decrease from one mode to another (See Figure 4.19 and Figure 4.194.20). This constant perturbation of the formed eddies of the flapping and shedding instabilities might have a strong influence on the wake behaviour and further decrease of the drag force. The creation of smaller and more continuous structures near the wake will shift the convective structures closer to the body, corroborating the results obtained in Figures 4.12(I). The structures perceived by the continuous blowing are not the same as those obtained by the periodic forcing. Contrary to case I, the other cases present once again elongated positive-negative structures close to the top trailing edge. For cases II and IV, these structures are visible for all the modes, while for case III, the structures are curved closer to the wall and create other vortical elongated structures inside the recirculation zone. If the vortical structure placements are compared, case I, II and IV are farther away from the wall, while case III creates structures closer to the Ahmed body. From this analysis, it is possible to remark that if a reduction of the drag is required, the vortical structures must be developed close to the shear layer region and not inside the wake and that the creation of smaller and rounder structures near the shear layer might have a strong impact on drag reduction. Once again, the cumulative energy and the pressure/velocity correlation are not sufficiently high to be carried out further analysis; the results presented in this section can give an insight on the flow behaviour and how both the flapping motion and the shedding phenomena can be modified using specific actuation mechanisms in order to decrease the aerodynamic drag forces. The goal of this section is to deliver some initial knowledge of flow behaviour when continuous blowing or periodic forcing is applied at the top trailing edge of a car model.

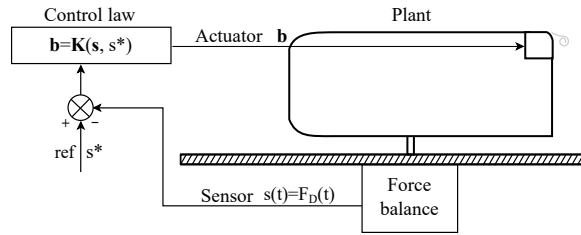


Figure 4.21 – Sketch of closed-loop control. The loop performs the real-time closed-loop control. The plant feeds back the sensor output  $s$  to the controller  $\mathbf{K}$  with regards to a tracking reference  $s^*$ . The controller computes the actuation command,  $\mathbf{b}$  based on  $s$  and  $s^*$  and sends it back to the plant.

## 4.4 Sliding mode control

An overview of the closed-loop process implemented here is illustrated in Figure 4.21. A desired tracking reference point  $s^*$  is initially set by the user. The plant feeds back the sensor output ( $s(t) = F_D(t)$ ) in real-time to the controller  $\mathbf{K}$ . An actuation command  $\mathbf{b}$  is computed based on  $s$  and  $s^*$  and it is finally fed back to the plant. The main goal is to track, reach and maintain the set-point, regardless of the flow perturbations presented upstream.

### 4.4.1 Experimental results of SMC application

The goal of this investigation is to reduce the drag to a desired value (set-point) and maintain it regardless of incoming flow perturbations or against measurement noises and model inaccuracies. A maximum actuation switch frequency,  $f_{sw}$  is fixed at 100 Hz. To evaluate the cost of the control, the following instantaneous momentum coefficient is defined,

$$C_{\mu}^*(t) = C_{\mu 0} DC^*(t) = C_{\mu 0} \frac{1}{T_f} \int_{t-T_f}^t b(\tau) d\tau, \quad (4.2)$$

where  $DC^*(t)$  defines the blowing fraction at time  $t$  averaged over a duration  $T_f$ . The Reynolds number is kept constant at  $Re_H = 9.10^4$  while the time window is  $T_f = 60/f_{sw} = 0.3s$ . Based on the open-loop results discussed in the previous section, the set-point  $s^* = -2.5\%$  is considered as the tracked value.

Figure 4.22 shows a summary of the results obtained with SMC. Figure 4.22(a) shows the time response of the drag (top line) for the forcing command  $b(t)$  when the closed-loop controller is activated (bottom line). The calculated instantaneous duty cycle  $DC^*$  is also reported in this figure (middle line). Snapshots at four distinct instants of these time histories are reported from Figure 4.22(b) to Figure 4.22(e). Three distinct control phases are noticeable in Figure 4.22(a). When the actuation is activated ( $tH/U_{\infty} = 0$ ), the controller enters a phase known as "reaching phase" the object of which is to approach rapidly the targeted set-point and during which the drag force is found to rapidly decrease. In the present case, this phase corresponds to a steady blowing forcing as seen in Figure 4.22(a), where the  $DC^*$  is found equal to unity. The duration of this phase can be chosen by the user and was, in the present work, stopped at  $tH/U_{\infty} = 200$ . A transition phase ( $200 < tH/U_{\infty} < 280$ ) is then observed during which the controller seeks the adequate ON-OFF combination to rapidly reach the targeted set-point. Finally, the last phase ( $tH/U_{\infty} > 280$ ) corresponds to the so-called "sliding phase", where the controller attempts to maintain the drag at the tracked value  $s^*$  despite any disturbances on the plant.

The different stages reached by the near-wake flow can be examined thanks to the instantaneous snapshots of Figure 4.22(b) to Figure 4.22(e). During the unactuated phase ( $tH/U_{\infty} < 0$ ), Figure 4.22(b), a train of vortices at the top trailing edge is clearly visible, where the shear layer roll-ups evolve and convect downstream. The shear layer interacts with the near wake and creates an inverted asymmetric topology, as already discussed in §4.2. During the reaching phase, Figure 4.22(c), since the actuation corresponds to a steady blowing forcing, the near-wake flow resembles that described for the open-loop case I with the

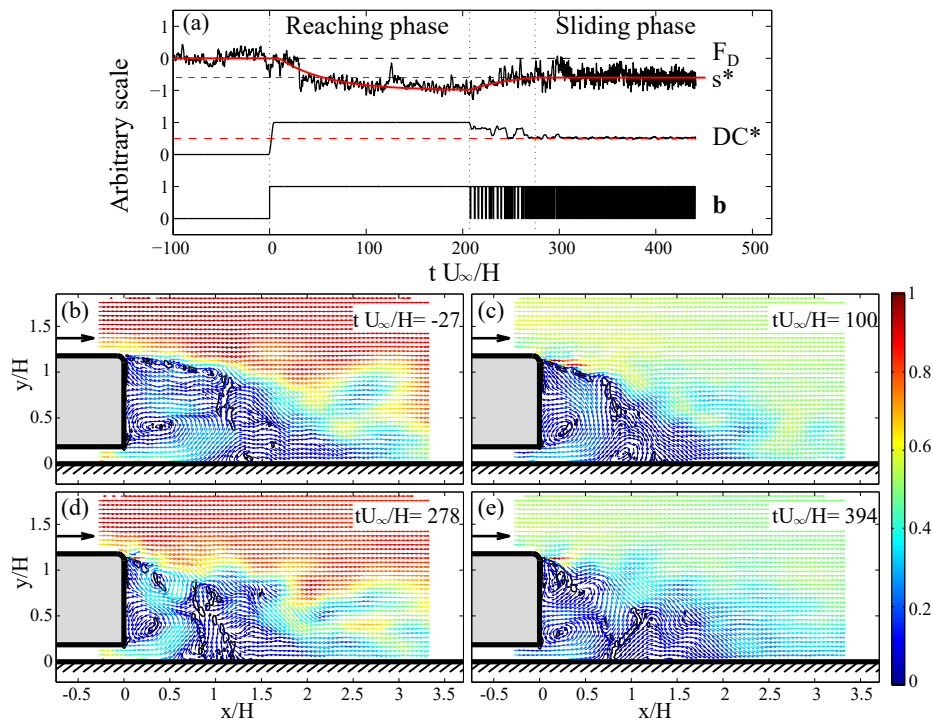


Figure 4.22 – Sliding mode control set-point tracking results: upper plot shows the time history response of the drag force  $F_D$ , control law **b** and the blowing fraction  $DC^*$ . Instantaneous flow field captured by the PIV for several forced configurations time histories are plotted for: Unforced flow  $tH/U_\infty = -27$ , reaching phase  $tH/U_\infty = 100$ , transition  $tH/U_\infty = 278$ , sliding phase  $tH/U_\infty = 394$

presence of an asymmetric wake behaviour, a shift of the convective structures closer to the recirculation and a development of large vortical structures evolving near the ground. During the transition phase, Figure 4.22(d), a transition in the near-wake shape is noticeable. The flow is evolving from an asymmetric configuration (energization of the shear layer) to a symmetric one (strengthening of the wake symmetry by forcing the vortex shedding), as it was also obtained for the open-loop case III. This transition of the sliding mode mechanisms - and further wake variation- triggers a periodic forcing modification that will increase the drag force, as seen in Figure 4.22(a). Finally, once the actuation is in the sliding phase, a synchronization of both shear layers is clearly observed (Figure 4.22(e)) similar to that identified in the open-loop case IV. The implemented controller is, therefore, found to be satisfactory in terms of set-point tracking with, in particular, a negligible steady-state error.

To corroborate the robustness and efficiency of this control approach, a second experiment was conducted to show disturbance rejection of the controller. Figure 4.23 shows two different up-stream flow perturbations  $p_0$  with corresponding drag force  $F_D$  and generated control law **b**. It is possible to observe how the control law is adapted to maintain the drag force at the desired  $s^*$  value. The controller, unaware of the up-stream disturbances, reacts immediately and drives the system to the set-point. The control limitation will come with the actuator capacity. If the drag strongly increases, the control command will apply continuous blowing. In contrast, if the drag is reduced, the control will stop and wait for an increase of  $F_D$  up to the desired value. The set-point determination and actuator's limitation are of great importance to obtain an optimal and robust control approach. From these results, it is possible to conclude that the implemented controller shows a satisfactory performance in disturbance rejection. The superiority of feedback control in contrast to open-loop control is emphasized. In real-world applications, flow control has to subsist with varying oncoming velocities, high turbulence levels, and other perturbations. Hence, the benefits of the sliding mode control can be fully exploited. In future work, a SIMO model will be pursued to improve wake stabilization. Also, the control performance will be graded by energy consumption. Finally, to target an industrial application for closed-loop flow control, we would like to use this approach in a more realistic car model, taking into account the 3-dimensional wake instabilities presented in a bluff-body turbulent flow.

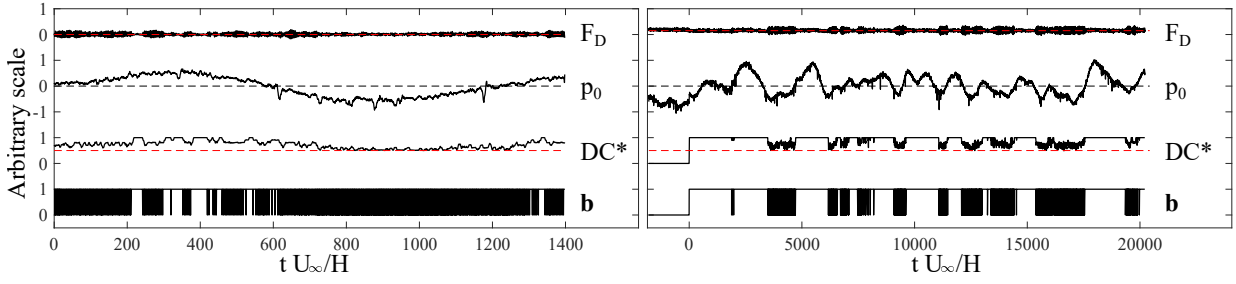


Figure 4.23 – Disturbance rejection results. Figures show the time history response of the control law  $\mathbf{b}$  and the blowing fraction  $DC^*$  for: Left: a sinusoidal up-stream perturbation  $p_0$ , Right: randomly generated up-stream perturbation.

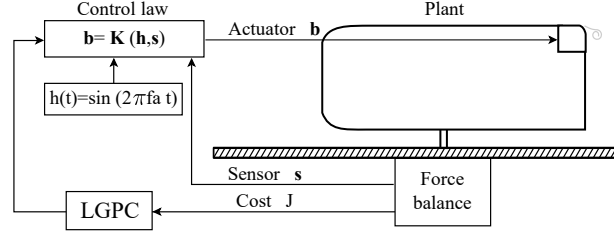


Figure 4.24 – Schematic of LGPC architecture for the experiment.

## 4.5 Machine learning control

Even though the optimal control mechanism is continuous blowing, machine learning control is performed to explore interesting control strategies able to optimize the control objective without using high energy consumption. The same actuator used for the periodic forcing and sliding mode control will be used to apply the control laws. For this case, the objective will be to find an optimal control law which optimizes drag reduction. Linear-based genetic programming (LGPC, Li (2017)) representation will be employed. The learning process is divided into two parts. The first one contained 100 individuals and 7 generations with an evaluation time of 15s. The second one included 50 control law candidates and 8 generations. The latter will be explained hereafter. A total amount of 15 generations was set, which was the minimum to converge towards the optimal individual. The MLC approach is once again represented in Figure 4.24. For this approach, the sensor input will be the drag force obtained through the balance. The LGPC parameters assigned for this experience are presented in Table 4.1. Similar parameters as the one set in §3.3.2 are used for this experiment. The tournament selection size is  $N_t = 5$  and the elementary operations are  $+$ ,  $-$ ,  $\times$ ,  $\div$ ,  $\sin$ ,  $\cos$ ,  $\tanh$ . Moreover, a new input parameter is used when LGPC is applied. A finite amount of constant is selected as input and is equal to  $N_c = 2$ . Even though these are not real input conditions, they will be treated as so, for comparison purposes.

As already stated, the main goal is to reduce the aerodynamic drag force  $F_D$  using the following cost function

$$J = \frac{\langle F_D \rangle - \langle F_D^\infty \rangle}{\langle F_D^\infty \rangle} + \gamma \langle b \rangle, \quad (4.3)$$

where  $F_D^\infty$  is the unforced drag. The evaluation time was set to  $T_e = 10s$  to reduce total learning time. The penalization parameter was set to  $\gamma = 0.5$  in order to penalize the high amount of energy consumed by the actuation mechanism. A further penalization was applied when the control law was steady blowing or no actuation at all. When this condition was presented,  $\gamma$  was automatically set to 1. With this limitation, the control laws were less prompt to be steady blowing or unforced flow.

The same approach as in §3.3.2 is considered. Multi-frequency forcing is extracted from the results obtained in periodic forcing. The control law combination was set to  $b^\circ = \mathbf{H}(\sin(\mathbf{h}))$ , where  $\mathbf{H}$  represents a Heaviside function in which the values over 0.5 are equal to 1, while the values under 0.5 are equal to 0, and  $\mathbf{h}$  is a harmonic function defined as  $h(t) = u_{jet}(1 + \sin(2\pi f_a t))/2$ . Five different frequencies are chosen

Parameters	Value
Genetic programming approach	Linear
Population size	$M = 50$
Tournament size	$N_t = 5$
Elitism	$N_e = 1$
Replication	$P_r = 10\%$
Crossover	$P_c = 60\%$
Mutation	$P_m = 30\%$
Operations	$+, -, \times, \div, \sin, \cos, \tanh$
Number of constants	$N_c = 2$
Constant range	$[0,1]$

Table 4.1 – LGPC parameters.

Controller input	$h_1$	$h_2$	$h_3$	$h_4$	$h_5$
$f_a$ [Hz]	1	5	10	30	70
$St_a$	0.0135	0.0675	0.135	0.405	0.945

Table 4.2 – Harmonic functions  $h(t) = \sin(2\pi f_a t)$  used as inputs of LGPC.

and presented in Table 4.2. The ability of MLC to find the accurate harmonic function to control the flow will be tested when a wide range of frequencies are formulated as input conditions. The sensor feedback is expressed as  $\mathbf{b}^\times = \mathbf{H}(\mathbf{K}(\mathbf{s}))$  and will use  $F_D(t)$  as sensor input  $\mathbf{s}$ . Finally, the generalized feedback law will use both the multi-frequency forcing and the sensor input  $\mathbf{b}^\otimes = \mathbf{H}(\mathbf{K}(\mathbf{h}, \mathbf{s}))$ . As previously commented, two constants will also be used to generate the control laws and will be taken as input conditions for all cases  $\mathbf{b} = \mathbf{H}(\mathbf{K}(\mathbf{h}, \mathbf{s}, \mathbf{c}))$ .

The evolution of the cost values  $J$  for each individual through the generation is presented in Figure 4.25 for the three cases. The multi-frequency forcing and the generalized feedback control (Figure 4.25(a) and Figure 4.25(c), respectively) present similar behaviours. A “step” variation is seen for both cases; the first individuals have similar cost values and then a sudden increase is seen around  $i=15$  reaching a second level of similar  $J$  values. The behaviour is repeated for higher individual values. This is due to a binary command ON/OFF, where a Heaviside function is applied, generating the same actuation  $\mathbf{b}$  for different control laws. The “step behaviour” is more prominent for the sensor feedback control (Figure 4.25(b)), probably caused by the limited amount of input signals to create the control laws. The amount of cost values closer to the optimal one increases for higher generations. The optimal values are obtained rapidly, which corroborates the use of 8 generations to arrive to an optimal control law.

Once more, the percentage  $\mathbf{P}_s$  of having an input parameter in the individual is calculated in order to determine the proper inputs to generate an optimal control law. Figure 4.26 presents this percentage for the three cases studied; note that all the input parameters,  $\mathbf{h}$ ,  $\mathbf{s}$  and  $\mathbf{c}$ , are taken into account. For the multi-frequency forcing, the five harmonic functions and the constant values are taken into consideration. Initially,  $h_4$  had the highest percentage which is linked to a frequency of 30 Hz. However, the frequency percentage values balanced through the generation, giving similar values for the last generation. For sensor feedback, no important change is seen between the drag force and the constants, probably due to the limited amount of sensors used to create the control laws. This limitation will bring further consequences in the control law creation. Interesting results are obtained when all the input parameters are taken into account (Figure 4.26(c)). For the second generation, the highest percentages are given to the second harmonic function (10 Hz), the drag force and the first constant. The lowest percentages are given to the other

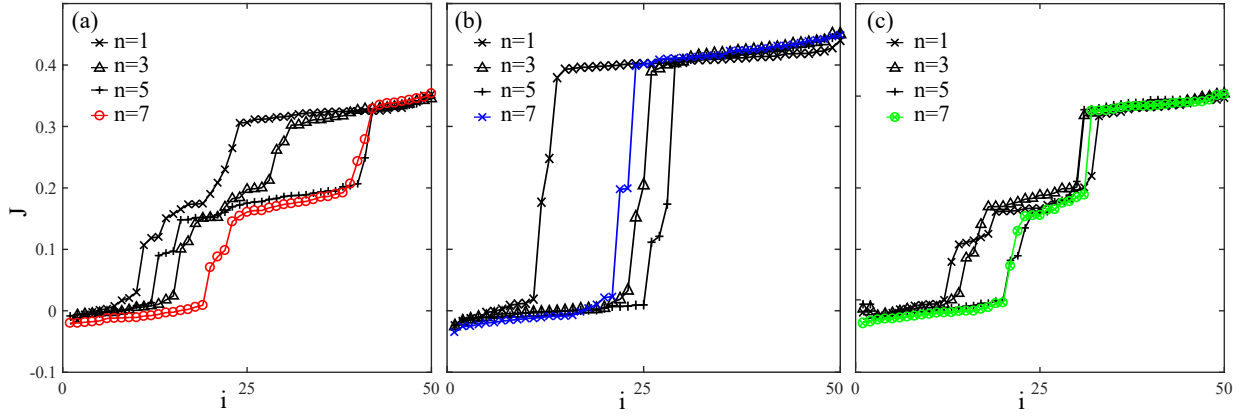


Figure 4.25 – Evolution of the cost function  $J$  versus the individuals  $i$  for generations  $n=1,3,5,7$ . (a) 'o' red circle symbol: multi-frequency forcing, (b) 'x' blue cross symbol: sensor feedback, (c) '⊗' green circled-cross symbol: generalized feedback control.

harmonic functions and constants. Even though the drag was strongly used in the first generations, its importance strongly decreases, which means that no optimal control laws are obtained when this sensor is taken as an input. A change in the harmonic function use is visible throughout the generations. The highest frequency (70 Hz) seems to be of great importance in the creation of the control laws, while the others lose their use for each generation. The frequency less used is the fourth one (30 Hz).

After the learning process is over, the control functions of the three cases are acquired. The multi-frequency forcing uses only the second and the fifth harmonic functions, associated to the frequencies  $f_a = 5$  and  $f_a = 70$ , and denoted as

$$b^\circ = 2 \times (h_5 + \cos(h_2)) - (-1.35 - h_2) - (-1.35 - h_2) \times \cos(h_5 + \cos(h_2)) + 1.35 + h_2).$$

Two interesting facts are obtained from this equation. The first one is that the frequencies used to generate the control law are those that decrease the drag force, white area in Figure 4.11. The second one is the repetition of the same block of combinations  $h_5 + \cos(h_2)$  and  $-1.35 - h_2$ ; this is probably due to the linear genetic approach which has a list of instructions. If the instruction generates a positive control, there are more chances that it will be used, in the elitism or replication and cross-over and/or mutation, in the tournament phase. To clearly view the obtained control law, please refer to '—' red line in Figure 4.27. When applying a power spectral analysis to the control law obtained, two strong peaks are clearly visible at  $St_H \approx 0.85$  and  $0.95$ , which are close to  $St_a = 0.945$ . A smaller peak is obtained near  $St_a = 0.0675$ . This lower Strouhal value creates an ON/OFF behaviour which contains a combination of continuous blowing (ON state) and a periodic forcing (OFF state). Hereafter, multi-frequency forcing will be denoted as ' $b^\circ$ '. The sensor-feedback creates a continuous blowing of  $b^\times = 1$ . This control law was already studied in section §4.3 and will not be further analysed. The complete control law did not contain the drag force as an input parameter. A less complex control law is obtained for the generalized feedback case and contains three different harmonic functions ( $St_a = 0.0135, 0.405$  and  $0.945$ ). Furthermore, the drag force is not used, which means that MLC created a second multi-frequency forcing control law,

$$b^\otimes = \sin(h_4/h_1) - (h_5 + (h_1 \times h_4)).$$

The simplified version can also be found in '—' green line in Figure 4.27. For this case, the same strong peak is obtained at  $St_a = 0.945$ . However, no low-frequency peaks are presented. Conversely, three peaks arise at Strouhal values between  $0.3 < St_H < 0.6$ . Even though these peaks still might decrease the drag, they are also close to a zone where the drag increases compared to the unforced flow, see Figure 4.11. The combination of these peaks might bring negative results to drag control. In this case, the control law obtained shows more of an aleatory ON/OFF signal with a repetition rate. Shorter control laws are obtained when the LGPC approach is used, compared to the control laws obtained for TGP in §3.3.2. This might facilitate the processing of the control laws to find different individuals in the same generation. The

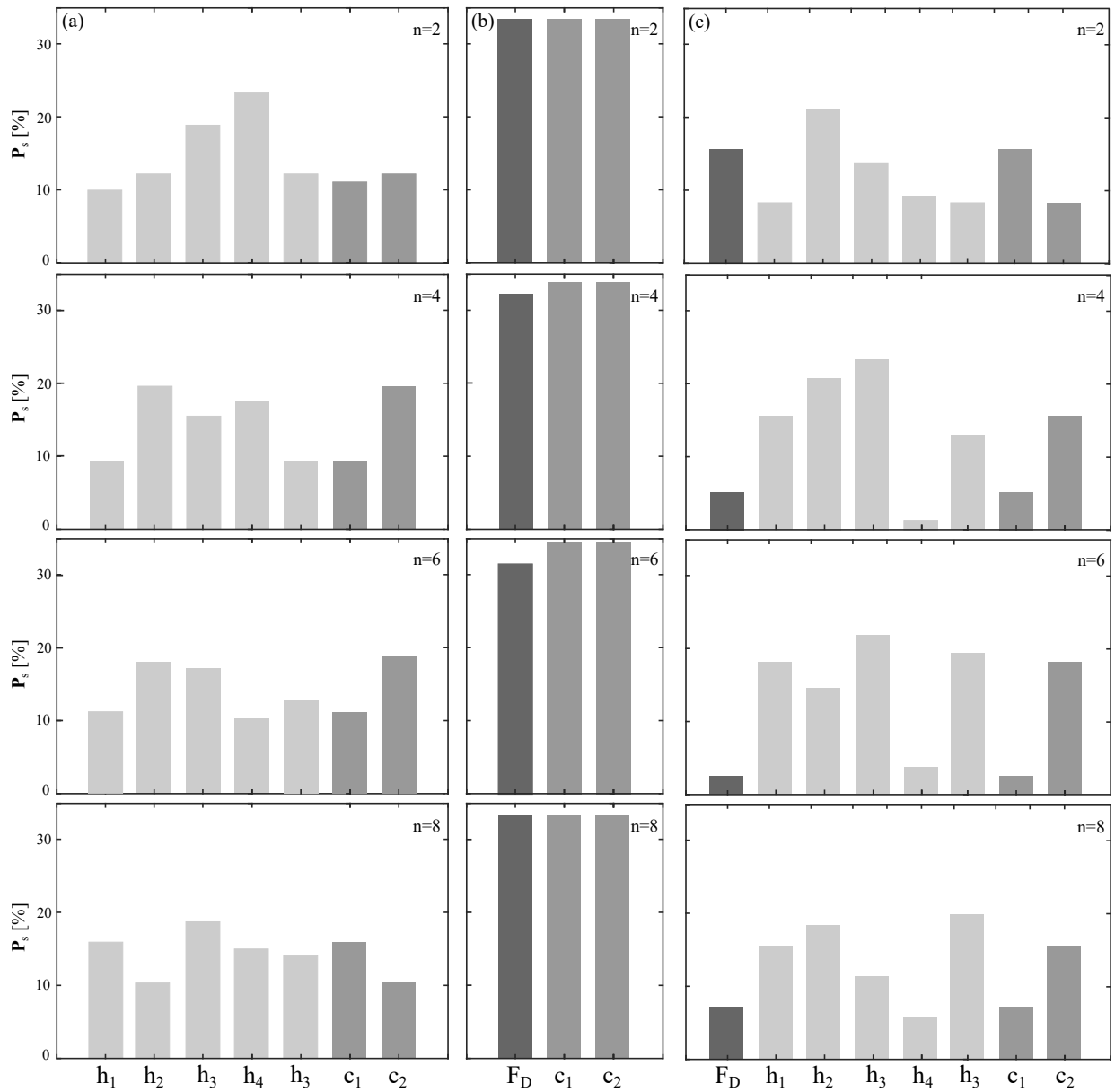


Figure 4.26 – Percentage  $P_s$  of sensors  $h_i$  in the control law. (a) Multi-frequency forcing, (b) Sensor feedback, (c) Generalized feedback control.

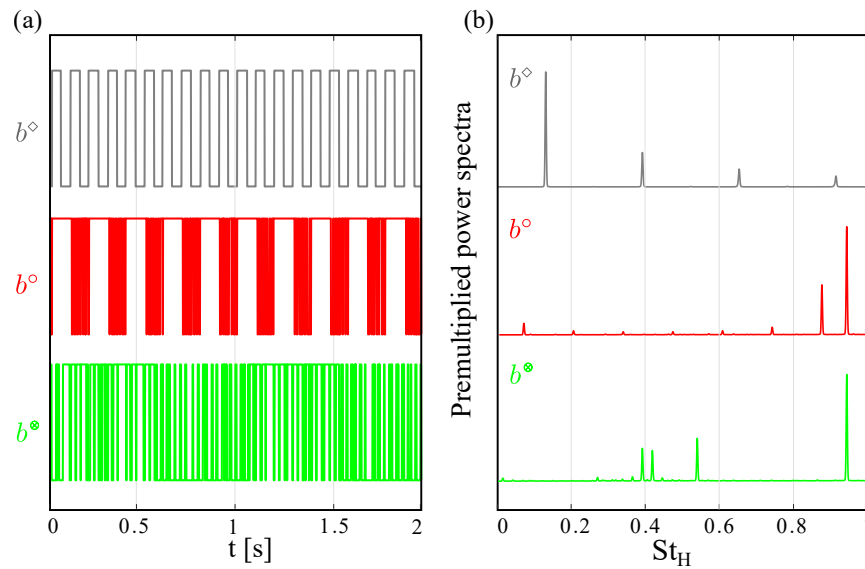


Figure 4.27 – Actuation properties for periodic forcing  $b^\circ$ , multi-frequency forcing  $b^\circ$ , generalized feedback control  $b^\circ$ . (a) One and a half periods of the actuation commands (b) Premultiplied power spectral densities for all cases.

generalized feedback case will be presented as ' $b^\circ$ ' hereafter.

#### 4.5.1 Wake modification

The effects of MLC in the modification of the flow topology are now discussed. Two cases will be studied: (case V) multi-frequency forcing, which obtained a drag reduction of around 3 %, while (case VI) generalized feedback control presented a lower reduction of around 2 %. Even though these values are not as high as expected, they might be significant compared to the 8% obtained for the optimal case. The notation for each MLC case follows the open-loop study. A first analysis of the rear wake is done. Figure 4.28(aV) and Figure 4.28(aVI) present the time-averaged cross-stream velocity with corresponding flow field streamlines. Solid black lines denote a forward flow probability of 50%, while the red one is for the uncontrolled case used for comparison. For both cases, the height and length of the recirculation bubble is strongly reduced compared to that of the unforced flow. The recirculation point is shorter than the one obtained for the baseline case. A nearly symmetric flow topology is clearly seen, similar to the one obtained for cases II and III (Figure 4.12(aII) and Figure 4.12(aIII)). The lower recirculation bubble is centred closer to the bluff body wall. This near to wall bubble is also present for frequencies higher than the shedding  $St_a > St_o$ , which agrees well with the frequencies presented in the control laws. When analysing the cross-stream velocity, a high positive region (red zone) is visible for the multi-frequency case (Figure 4.28(aV)), similar to the one obtained for case I. This positive area decreases for the generalized feedback case which is in between cases II and III. The results corroborate the strong relation between the cross-stream velocity and the drag force. The instantaneous velocity fields are also examined in details in Figure 4.12(bV) and Figure 4.12(bVI). A high periodical forcing at the top trailing edge, direct wake perturbation, shifts the convective structures closer to the wall, which explains the height and length reduction of the recirculation area. Also, as a consequence of high-frequency forcing, which creates small-scale vortices, a wake symmetry is obtained (similar to case III and IV). However, due to a combination of low and high frequencies, the wake is modified with both an energization of the shear layer and wake symmetry, which might not be beneficial to drag reduction. From the results, it is possible to highlight that high-frequency forcing -shear layer stabilization- causes a drag reduction. For this specific case, a combination of both low- and high-frequency forcing, as suggested by the control laws obtained, does not bring any further improvement. Finally, maps of the RMS-velocity are presented for the two MLC cases in Figures 4.12(cV) and Figures 4.12(cVI). As already discussed, the negative actuation angle moves the maximum velocity downwards. Furthermore,

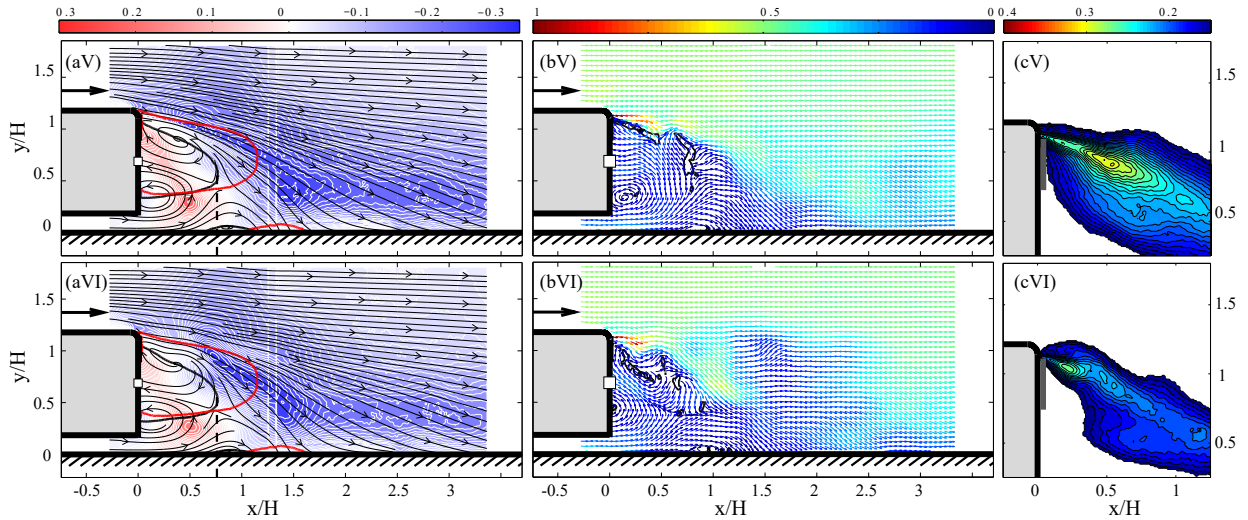


Figure 4.28 – (a) Forcing flow time-averaged cross-stream velocity ( $\bar{v}^+$ ) with the associate streamlines. The recirculating flow length  $L_r$  is displayed by the vertical dashed line. The iso-line of the forward flow probability of 50 % is plotted in black for the controlled cases and in red for the natural flow reference. (b) Instantaneous flow field #265 captured by the PIV. The velocity field is indicated by dimensionless norm coloured arrows. The  $\Gamma_2$  criterion is displayed by black iso-lines revealing the unforced shear layer vortex street formation and the position of the classical main wake structures. (c) Closed view of the streamwise-transverse RMS-velocity for several, (V) Case V: Multi-frequency forcing; (VI) Case VI: generalized feedback control.

periodic forcing increases maximum velocity. For case V, a thicker region of RMS-velocity is obtained, compared to all other cases. The unsteady vortical structures are intensified and affect the near wake. Case VI presents maximum RMS-values at the jet exit, which means a cluster of structures at the shear layer. This variation close to the shear layer strongly affects the near wake structures and might be the cause of an attenuation of the ability of high periodic forcing to decrease the drag. This also corroborates an increase of the perturbed vortical structures (enhancement of wake shedding) at the top trailing edge and might have an impact on the drag rise. The position of the forced structures is key to improve flow control. A further study of these eddy structures, created by actuation, and near wake interaction might give some important tools to better control turbulent flows.

An analysis of the streamwise ( $\bar{u}^+$ ) and cross-streamwise ( $v_{\text{rms}}^+$ ) velocity behaviour is shown in Figure 4.29. Three  $x/H$  positions will be studied and are denoted as follows: '—' black line  $x/H = 0.2$ , '—' red line  $x/H = 0.6$ , '—' blue line  $x/H = 1.5$ . A strong peak is once again seen at  $y/H \approx 1.2$  for cases V and VI. The peaks reach maximum velocity values of  $\bar{u}^+ \approx 1.5$  for ('—' black line  $x/H = 0.2$ ), similar to the one obtained for continuous blowing. In addition, the velocity variation before the peak (at higher  $y/H$  values) is less prominent than that of the other periodic cases, e.g., the velocity at  $y/H \approx 1.25$  is around  $\bar{u}^+ = 1$ , while for the periodic cases, the velocity at the same  $y/H$  position is  $\bar{u}^+ = 0.5$ . No other strong variation are obtained for the  $\bar{u}^+$  velocity compared to the results presented for the open-loop cases. It is worth noting that the velocity behaviour might strongly vary in the same  $x$ -direction due to the movement of the reticulation length closer to the vertical wall when machine learning control is applied. Similar results to periodic forcing cases III and IV are visible, for the bump at  $x/H = 1.5$  ('—' blue lines in Figure 4.29(b)), where the protuberance has higher  $v_{\text{rms}}^+$  values and is spread wider in the normalwise direction. The width of the bump, for both cases, is bigger than the ones previously observed, and the position of the maximum  $v_{\text{rms}}^+$  value is located at  $y/H < 0.5$  and spreads close to the upper edge, similar to case III. Finally, case VI presents a double peak inside the recirculation area, '—' black line, which intensifies at  $x/H = 0.6$  ('—' red line). The reduction of the recirculation length might be the cause of a non-detectable peak at this specific  $x/H$  point for previous cases. The results corroborate the importance of the cross-stream velocity in the drag modification, and the position and direction of the actuation perturbation in order to improve the desired objective.

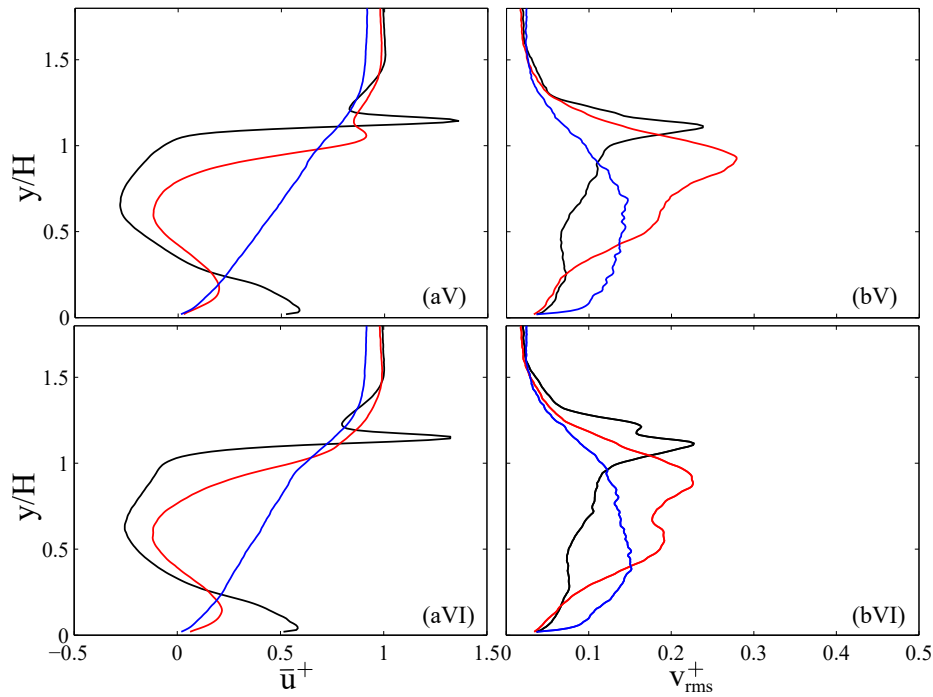


Figure 4.29 – (a) Time-averaged streamwise velocity ( $\bar{u}^+$ ) and (b) root-mean-square of the cross-stream velocity ( $v_{\text{rms}}^+$ ) profiles for various  $x/H$  positions ('—' black line:  $x/H = 0.2$ , '—' red line:  $x/H = 0.6$ , '—' blue line:  $x/H = 1.5$ ). (V) Case V: Multi-frequency forcing; (VI) Case VI: generalized feedback control.

#### 4.5.2 Flow field dynamics and POD analysis

The pressure/velocity correlation between the normalized streamwise and normalwise velocities and the sensor probes  $s_1$  and  $s_2$  is presented in Figure 4.30 and Figure 4.31, respectively. For the pressure/velocity correlation for  $s_1$ , a positive region is obtained at the top trailing edge spreading in the stream- and normalwise direction. Under this positive zone, a small rounded negative one is obtained close to the bottom trailing edge from the body wall to an  $x/H$  distance of 1. The positive zone covers more area for case VI than for case V. (Figure 4.30(a)). The behaviour is linked to the wake symmetry presented for these cases. This same pattern is obtained for the correlation between the normalwise velocity and sensor probe  $s_1$  and for the streamwise velocity and sensor probe  $s_2$ , Figure 4.30(b) and Figure 4.31(a). For the latter, the correlation is lower than for those obtained with  $s_1$ . A similar correlation is also seen for case III in (Figure 4.30(bIII)). Figure 4.31(b) shows a completely different behaviour. Small positive areas are presented close to the body and expand and spread in the free stream-direction. These circular small regions are presented all over the rear wall of the Ahmed body. As previously explained, it is worth noting that when actuation is applied, the correlation might be strongly affected by the mechanism's movements and impact in the pressure signal, which might create some undesired experimental errors. The correlation for these cases is lower for  $s_2$  than for  $s_1$ .

Finally, a proper orthogonal decomposition analysis is presented. Figure 4.32 shows the cumulative energy of the first fifteen velocity modes for the two MLC cases. Both results ('o' red circle symbols: multi-frequency forcing, 'x' green crossed-circle symbols: generalized feedback control) show a total cumulative energy of 40% for the first fifteen modes, close to the ones obtained for the unforced case and in between cases III and IV ('d' gray diamond and 'd' dark gray diamond in Figure 4.17). However, as previously explained, some interesting information can be obtained from the first five modes. For this reason, Figure 4.33 presents the low-order POD velocity modes (for  $n=1$  to 5) with corresponding vorticity modes, for cases V and VI. The first three modes (Figure 4.33(a) and Figure 4.33(b)) present short elongated vortical structures at the top trailing edge. The clockwise vortical structure is over the counter-clockwise one. These structures are even smaller than those obtained for periodic forcing (Figures 4.18). After mode 3, a third vortical structure is formed under the two first ones. These eddies will perturb the upper ones diminishing their

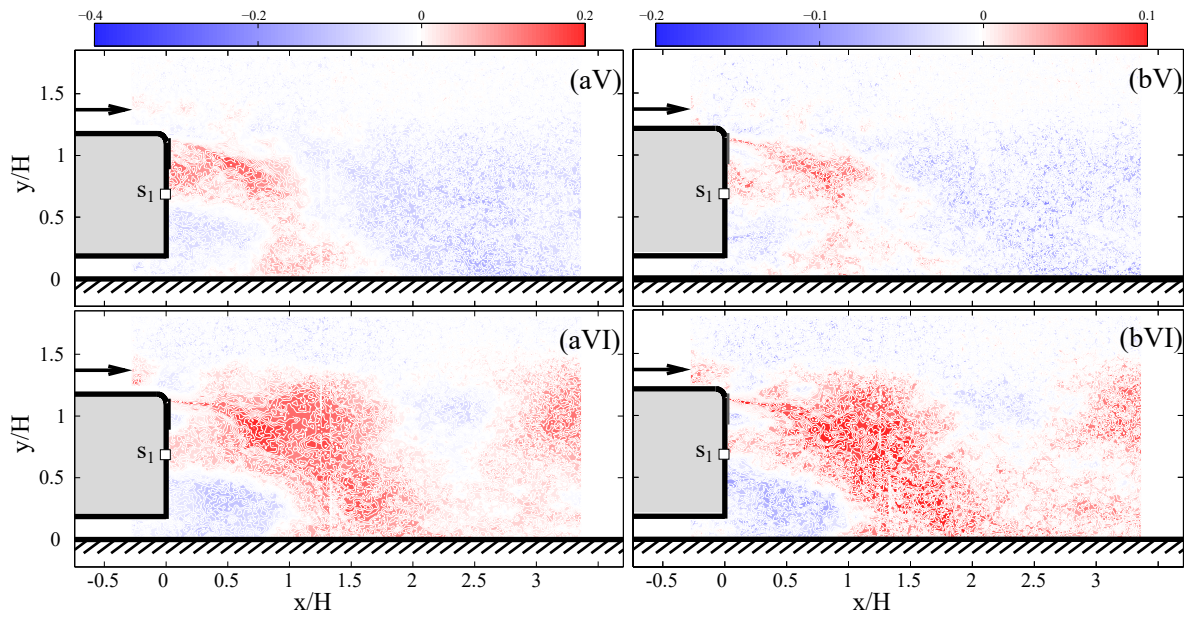


Figure 4.30 – Pressure/velocity correlation coefficient for pressure sensor  $s_1$  and  $Re_H = 9 \times 10^4$ , (a) normalized streamwise velocity/pressure and (b) normalized normalwise velocity/pressure. (V) Case V: Multi-frequency forcing; (VI) Case VI: generalized feedback control.

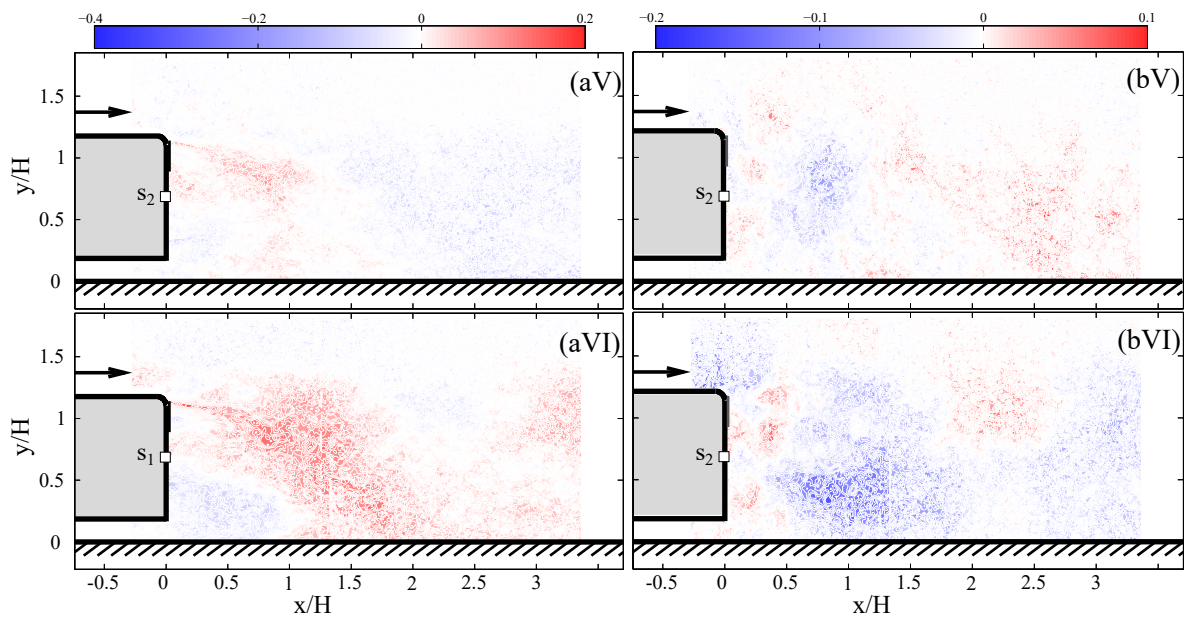


Figure 4.31 – Pressure/velocity correlation coefficient for pressure sensor  $s_1$  and  $Re_H = 9 \times 10^4$ , (a) normalized streamwise velocity/pressure and (b) normalized normalwise velocity/pressure. (V) Case V: Multi-frequency forcing; (VI) Case VI: generalized feedback control.

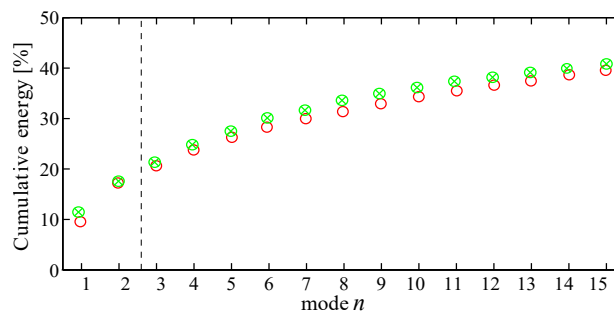


Figure 4.32 – Cumulative energy from POD decomposition of the velocity fields. 'o' red circle: multi-frequency forcing, '⊗' green crossed-circles: generalized feedback control.

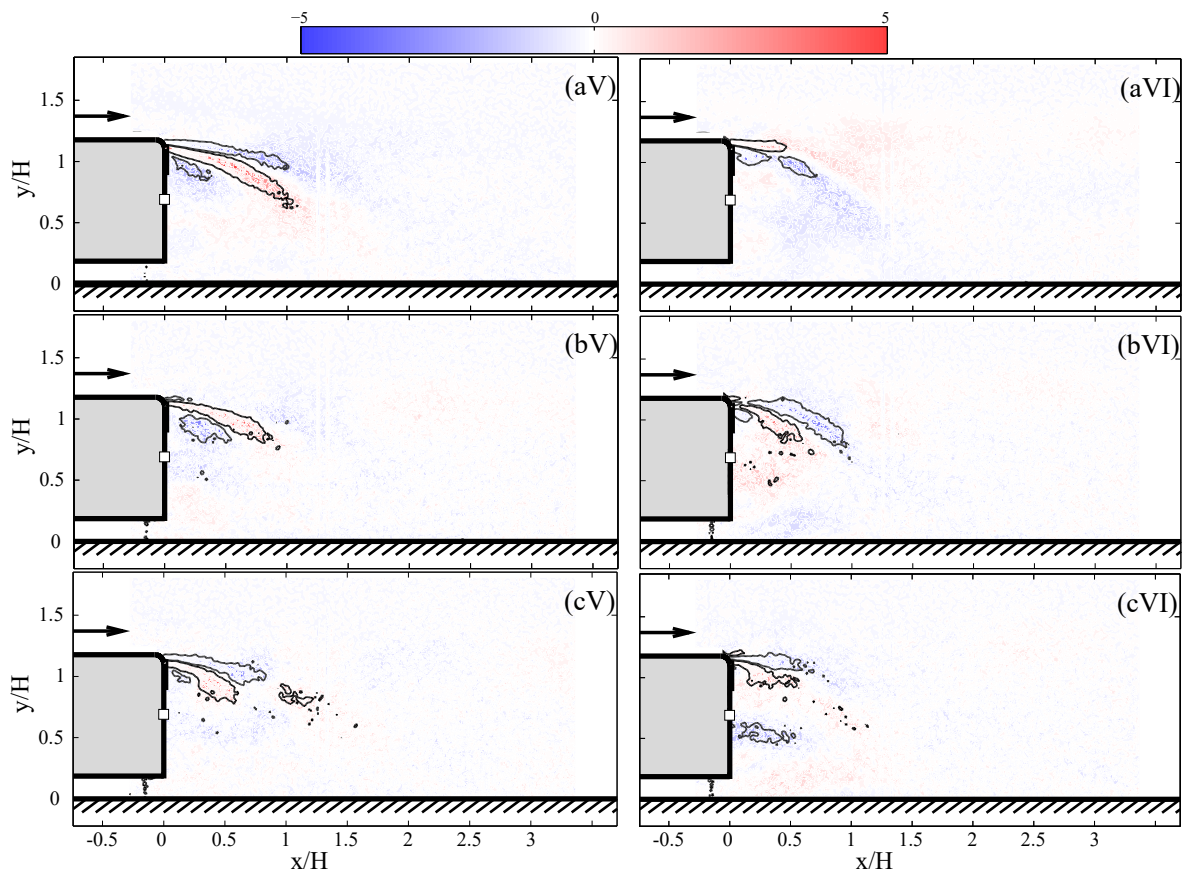


Figure 4.33 – Low-order POD velocity (a) mode 1, (b) mode 3 and (c) mode 5, (V) Case V: Multi-frequency forcing, (VI) Case VI: generalized feedback control.

size and shifting their rotation. Mode 5 shows the same behaviour as mode 4, not shown here. For case VI, the structures are even smaller in size. For this case, a third structure already appears in the second mode. For the 3<sup>rd</sup> mode the vortical structures increase in size and width. For the 5<sup>th</sup> mode, the small structures reappear at the edge of the Ahmed body and scatter near the rear wake. These small structures located close to the top trailing edge corroborate the perturbation of small vortical eddies near the shear layer due to MLC actuation, as previously mentioned in Figure 4.28. It is worth mentioning that these small structures have different shapes from those obtained for continuous blowing, which are more rounded and symmetrical.

## 4.6 Summary

Open- and closed-loop strategies are examined targeting the drag reduction of a turbulent flow around a square-back Ahmed body. Complementary velocity fields, acquired from particle image velocimetry, are presented. A further reconstruction of the flow is done using proper orthogonal decomposition to elucidate the main flow structures presented in this complex flow. The baseline flow is first investigated in order to understand the dynamical aspects of the unforced flow. A typical inverted wall-normal asymmetry was obtained. POD results corroborate the existence of the shedding and flapping instabilities presented at high Reynolds numbers, and the ability to separate them in different modes. It was not possible to conduct further analysis due to the lack of pressure measurements at the back of the Ahmed body.

The impact of steady blowing and periodic forcing as open-loop control strategies in the wake are further studied. The actuation is performed with pulsed jets at the top trailing edge combined with an angle, similar to a Coanda effect. The addition of the Coanda effect to the actuator system reinforces the flow deviation close to the model. The flow is monitored in time with pressure, lift and drag sensors. The best control

law is steady blowing ( $St_a = 0$ ), with a drag reduction of up to  $-8\%$ . When periodic forcing is applied, an increase in the drag force is clearly seen for the “low-frequency” regime  $St_a \in [0, 0.15]$ . A decrease in the drag is obtained after  $St_a = 0.15$ . A shortening of both the recirculation length and height is caused by a direct perturbation (due to the angle effect) of the pulsed jet vortical eddies. For a “low-frequency” regime, the near-wake instabilities are strongly dependent on the Strouhal number. A transition in the flow wake will decrease the cross-stream velocity and increase the drag force. Conversely, for “high-frequency” regimes ( $St_a > 0.15$ ), the actuation creates small vortices close to the edge, roll-up evolution, which keeps the wake symmetric and reduces the drag. Further dynamical studies showed a strong perturbation of the flapping mode by small vortical structures, especially for the continuous blowing. These results might improve researchers understanding of how bluff body drag varies with low- and high-wake forcing, which is crucial to find novel control strategies and implementations (Brunton & Noack, 2015).

Two other flow control strategies will be applied to the same configuration and are previously described in §2.3.1 and §2.3.2: sliding mode control and machine learning control. SMC is a closed-loop robust approach to reduce and maintain the drag at a certain value. The first experimental result, in a turbulent flow using sliding mode control, is presented. The main goal is to minimize the drag to a set-point  $s^*$  and stabilize it regardless of external conditions. The control approach is based on an initial black-box model identification presented by Feingessicht *et al.* (2017). The set of data obtained from open-loop control were used for the model design. In principle, the control idea can be a compilation of open-loop control strategies. However, the actuation frequency has to be selected carefully in real-time depending on the external parameters up- and down-stream of the flow, otherwise actuation energy is wasted. The robustness and easy implementation in an experimental setup make this approach convenient for industrial applications. From the results, it is possible to conclude that the implemented controller shows a satisfactory performance in disturbance rejection. In real-world applications, flow control has to subsist with varying oncoming velocities, high turbulence levels, and other perturbations. Hence, the benefits of sliding mode control can be fully exploited.

Once more, three different machine learning control cases are also applied: multi-frequency forcing, sensor feedback control, and generalized feedback control. The goal of machine learning control is to explore and find new feedback mechanisms to optimize drag reduction. Eight generations of 50 individuals were used to obtain a satisfactory control law. The actuator limitation to ON/OFF was a challenge for machine learning control to find the optimal law. A penalization in continuous blowing actuation was applied to the control algorithm, due to high energy consumption and in order to explore other control strategies. Even though no individuals better than those for continuous blowing are obtained, the control laws presented by MLC are interesting approaches to study flow perturbation by complex input signals. While multi-frequency forcing and generalized feedback control generated two different multi-frequency signals, the sensor feedback approach found continuous blowing as optimal control. The multi-frequency forcing, given by MLC, presented two main harmonic functions, a low-frequency around  $St_a = 0.07$  and a higher one at  $St_a = 0.95$ . A further analysis in the wake is done when MLC control is applied. Results are similar to those obtained by periodic forcing. The use of MLC also gives the possibility to have a great data set of different control approaches, in order to do post-processing analysis. MLC gives important information regarding sensor placement and the repetitiveness of the input parameters in the creation of control laws. The results of MLC are key to improve flow control actuation.

Figure 4.34 presents a summary of all the control strategies used in order to modify the drag of a complex configuration. The results presented in this graphic are approximate values of the difference between uncontrolled and actuated cases. Open-loop actuation was used in order to have an initial idea of flow control using continuous blowing or periodic forcing. Sliding mode control is applied as a robust approach, in order to reduce and maintain the drag at a desired value, while machine learning control was developed to explore other control laws that could potentially optimize drag decrease. All the approaches

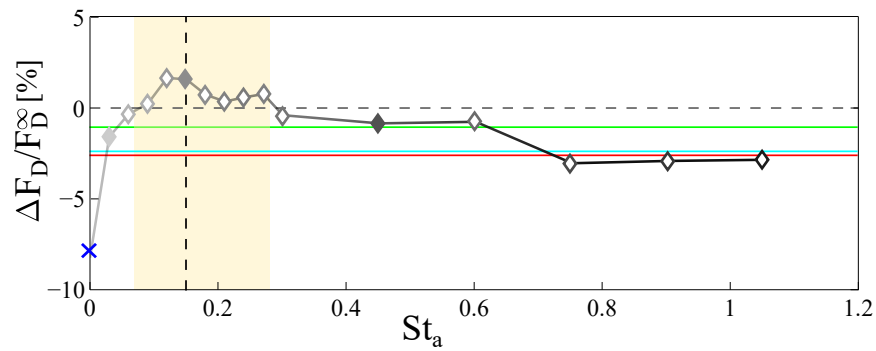


Figure 4.34 – Summary of the control strategies presented in this chapter regarding approximate modification of the drag force  $F_D$ . -◇- Periodic forcing actuation, × Continuous blowing, — Sliding mode control, — Multi-frequency forcing, — generalized feedback control.

presented here have their advantages and drawbacks. There is no perfect control strategy to optimize a specific parameter and keep it regardless of external perturbations. For this case, if the optimal actuation frequency (continuous blowing) is kept, the energy consumed will overpass the one saved by the actuation. For this reason, a balance between optimization and robustness must be achieved. The energy consumed by the actuator must be also considered in the search for an optimal control strategy. The knowledge and application of each approach might give an insight into how to improve each law or how to combine them to attain the desired objective. A hybrid between MLC and SMC may provide adaptive control exploiting the best non-linear actuation mechanisms. It is highly important to highlight these topics if a focus in more industrial applications is desired.



# Industrial application-Real vehicle results

*Some of the following content is published in [Chovet et al. \(2018c\)](#). In this last short chapter, the first real vehicle results, performed in a race track, will be presented. The first actuator device idea and sensor mechanism are also addressed here.*

## Contents

---

5.1	Experimental configuration . . . . .	121
5.2	Force estimation . . . . .	123
5.3	First results . . . . .	124

---

The results presented in this thesis gave an insight into the necessary elements to successfully control a turbulent flow. The analysis of the sensors, actuators, physical systems, and control strategies gave important information to choose the right parameters to control a real vehicle.

## 5.1 Experimental configuration

The instrumented vehicle used for experiment purposes is a Renault Twingo II C44 GT owned by LAMIH laboratory. The dimensions of the car are as follows: height  $H$  of 1.47 m (from the top part of the car to the floor), width  $W=1.39$  m and length  $L=3.69$  m (see Figure 5.1(a) and Figure 5.1(b)). To launch the software system two people are necessary inside the vehicle. For this reason, two different ground clearances are obtained. The first one closer to the front wheel  $g_1=38.6$  cm while the second measured at the back wheel is equal to  $g_2=51$  cm. These ground clearances might change depending on the weight inside the car, nonetheless, they were measured for each experience performed. The results presented are for car velocities from 45 km/h to 130 km/h, which correspond to Reynolds numbers, based on the car height

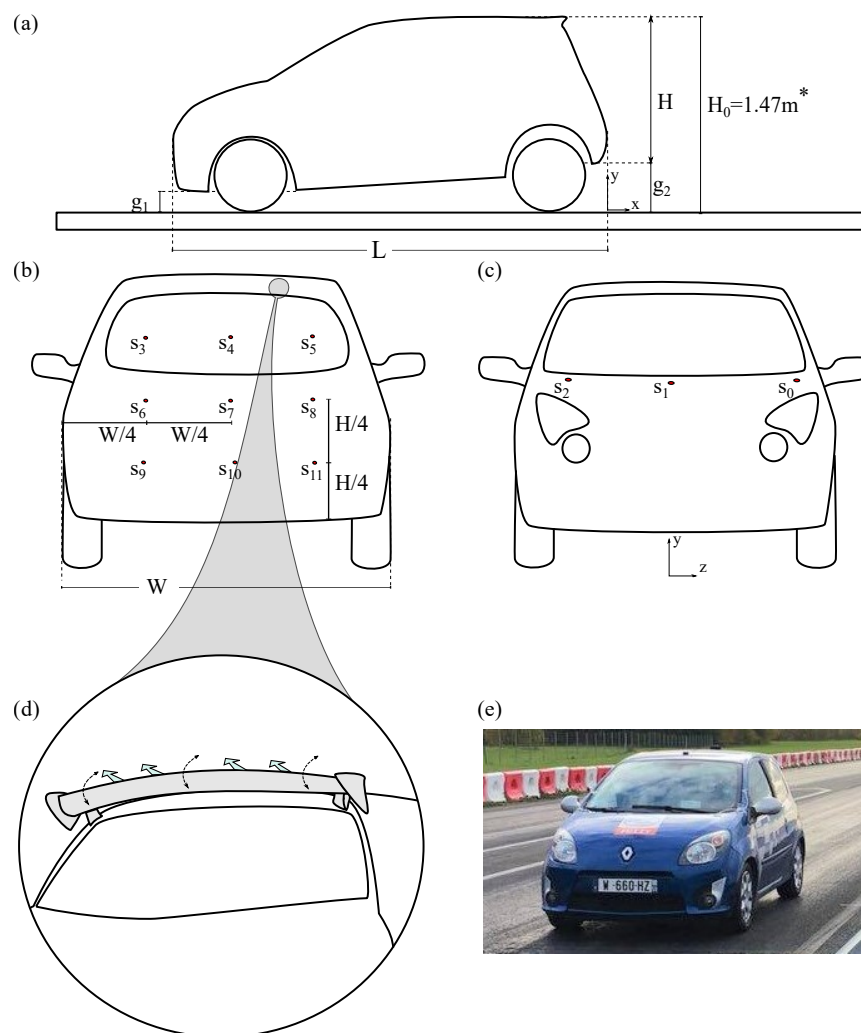


Figure 5.1 – Sketch of the vehicle Twingo GT. (a) Rear view, (b) Front view, (c) Actuation mechanism, (d) Real vehicle image, (e) Side view.

$H \approx 0.96$ , of  $Re_H = 6 \times 10^6 - 19 \times 10^6$ . The results will be described in a Cartesian coordinate system  $x$ ,  $y$ , and  $z$  representing the stream-, transverse- (normal to ground) and span-wise directions, respectively (see Figure 5.1(a) and Figure 5.1(c)). Experiments will take place in a 2km race track located at Clastres (North of France). The track is travelled in both directions, direction I (dI): departure to arrival and direction II (dII): arrival to departure.

The car is equipped with a GPS which is able to measure the longitude and latitude coordinates ( $x$  and  $z$  directions, respectively). The slope of the road is retrieved from GPS measurements. GPS data is projected in a local plane (Lambert Projection 93), and the  $x - z$  data is then projected on a local coordinate system aligned with the track and centred at the end of the runway. To reduce estimation errors, it is imperative to avoid small lateral variations. In the local coordinate system at the track, an  $x$ -coordinate equal to 1 corresponds to a situation close to the starting point and 0 will be close to the starting point. The  $z$ -coordinate measures the lateral deviation from the reference axis. The data returned by the GPS does not fit very well in the  $y$ -coordinate. Normally, GPS is generally configured to have good  $x$ - $z$  positioning accuracy at the expense of  $y$ -accuracy. Furthermore, the car is also equipped with two acquisition systems: DEWESoft and dSpace. Since two measurement devices are used, the data must be re-calibrated. For this, a binary signal is sent from dSpace to DEWESoft. The registration is then carried out by synchronizing the first rising edge. Figure 5.2(a) presents an example of the synchronization procedure. The objective of a properly synchronized data selection is to find a portion of the record for which the vehicle is in a steady

state: the average of the physical values becomes significant. To find this portion, criterion  $C$  is calculated:

$$C = (v > v_{\min}) \& (|\frac{dv(t)}{dt}| < a_{\max}) \& (|\frac{dV_y}{dt}| < v_{y_{\min}}) \& (bc == 1),$$

where  $v$  is the vehicle velocity,  $a$  is the acceleration, and  $bc$  is the break contact. An example of a record is shown in Figure 5.2(b); the first plot illustrates the criterion. This criterion is valid over several periods; the portion retained is the greater validity period of the criterion.

Twelve sub-miniature piezo-resistive Kulite XCQ-0.62 sensors are placed at the front and the back of the car. Three of them are placed at the front close to the windshield; the first one is located at the center plane  $w/2$  from the side of the body while the other two are at distance  $w/8$  from the car side edge (one on each side). On the rear, 9 pressure sensors were also set. The distance between each sensor is  $y = h/4$  and  $x = w/4$  starting at the same  $x - y$  distance, for a clear view of the sensor positions please refer to Figure 5.1(b) and Figure 5.1(c). Finally, an innovative actuation mechanism will be placed at the top trailing edge of the vehicle (see Figure 5.1(d)). A movable spoiler (commercially available) will be equipped with slotted jets in order to vary key actuation parameters such as angle, pressure (jet velocity), DC (Duty cycle) and frequency.

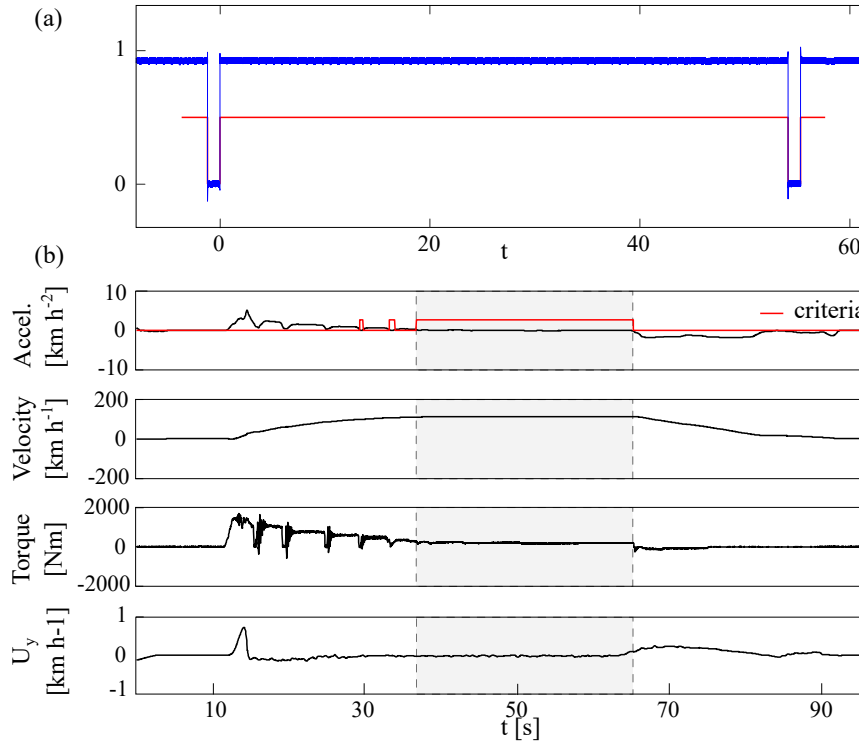


Figure 5.2 – Sketch of the vehicle Twingo GT. (a) Synchronization of Dspace and Dewesoft measurements, (b) Example of acquire measurements.

## 5.2 Force estimation

In order to estimate the drag force, two mechanisms will be here presented. The first one is with an interpretation of the Onorato relation (Onorato *et al.*, 1984) presented in §1.3.2. 80% of the total drag force is related to the pressure forces. From this statement, the integral balance of momentum is simplified as:

$$F_D = \iint_{S_w} (Pt^\infty - Pt^{S_w}) d\sigma, \quad (5.1)$$

where  $S_w$  denotes the surface of the wake downstream the vehicle,  $Pt^\infty$  and  $Pt^{S_w}$  are the upstream pressure and the pressure in the wake  $S_w$ . With this equation, the drag coefficient  $C_x$  can be calculated from Eq.(1.1) in §1.3.2. Taking into account the twelve pressure probes placed in the car, and an equal area for all the

sensors, one could approximate a drag coefficient value from Eq.(5.1):

$$C_D \approx \frac{\sum_{n=1}^3 (Pt_n^\infty) - \sum_{n=1}^9 (Pt_n^{S_w})}{1/2\rho U_\infty^2} \quad (5.2)$$

The second one is through an estimation of the external forces presented in the car. Once a portion of the data is selected, it is now possible to estimate the forces outside the vehicle. The dynamics of the vehicle is expressed in the form of an energy balance equation:

$$M \frac{dv(t)}{dt} = F_{\text{mot}}(t) \pm mg \sin(\vartheta(d(t))) - F_{\text{ext}}(t). \quad (5.3)$$

The longitudinal acceleration  $\frac{dv(t)}{dt}$  is obtained through the central inertial unit, while the slope  $\vartheta$  was previously measured using the average slope measurement as a function of the distance  $d(t)$  travelled. The  $\pm$  sign in equation.5.4 is related to the fact that the track is travelled in both directions. In the direction I, the vehicle undergoes a upwind and a slight rise. In direction II the vehicle undergoes a downwind and a slight descent. The estimation of the external force  $F_{\text{ext}}(t)$  is trivial via Eq.(5.4). An example is shown in Figure 5.3. Two tests are shown; results present relatively similar external force values. It is possible to note that the variation of torque is compensated by the slight oscillations of the acceleration giving a relatively constant external force. Additionally, the external force is decomposed as follows:

$$F_{\text{ext}}(t) = C_{rr}mg \cos(\pm\vartheta) + 1/2\rho Af C_d (v(t) \pm v_{\text{wind}})^2, \quad (5.4)$$

with  $v_{\text{wind}}$  the unknown wind velocity assumed constant. For simplification,  $\alpha_1 = C_{rr}mg \cos(\pm\vartheta)$  and  $\alpha_2 = 1/2\rho Af C_d$  giving the equation:

$$F_{\text{ext}}(t) = \alpha_1 + \alpha_2 (v(t) \pm v_{\text{wind}})^2. \quad (5.5)$$

In Eq.(5.6) the term  $\cos(\pm\vartheta)$  is assumed constant because the co-sinus function is even, so the sign of the slope will not influence the results. Each test is thus reduced to a pair  $(\bar{v}(i), \bar{F}_{\text{ext}}(i))$ . Then the parameters are estimated by minimizing a quadratic model error:

$$J = \sum_{i.e.dI} (\bar{F}_{\text{ext}}(i) - \alpha_1 - \alpha_2(\bar{v}(i) - v_{\text{wind}})^2)^2 + \sum_{i.e.dII} (\bar{F}_{\text{ext}}(i) - \alpha_1 - \alpha_2(\bar{v}(i) + v_{\text{wind}})^2)^2. \quad (5.6)$$

The minimization of  $J$ , starting from a realistic solution, relates to an optimization problem and leads to solve a linear problem for  $\alpha_1$  and  $\alpha_2$  which can be solved in a straightforward manner. The introduction of wind speed complicates the calculation of the solution and a Trust-Region Quasi Newton algorithm is necessary.

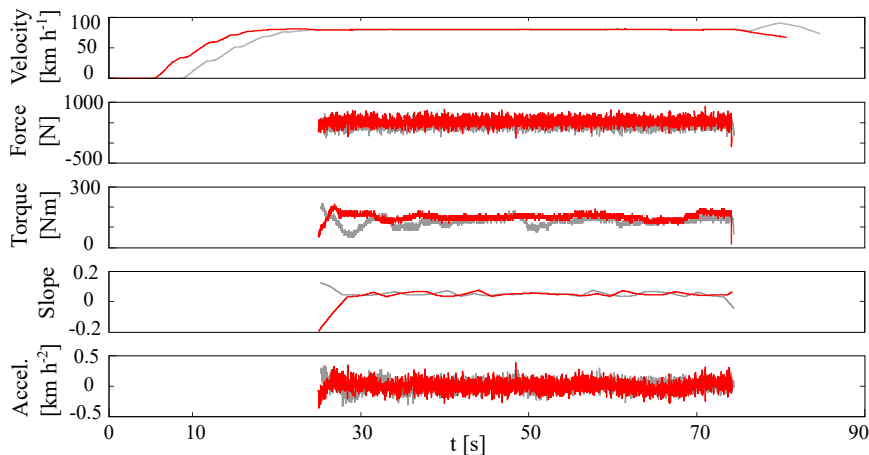


Figure 5.3 – Example of an external force estimation.

### 5.3 First results

Figure 5.4 shows the drag coefficient for a velocity range of  $U_\infty \in [45 \text{ km/h} - 130 \text{ km/h}]$  calculated from the two estimation approaches (red symbols: results using estimation approach, black symbols: results using

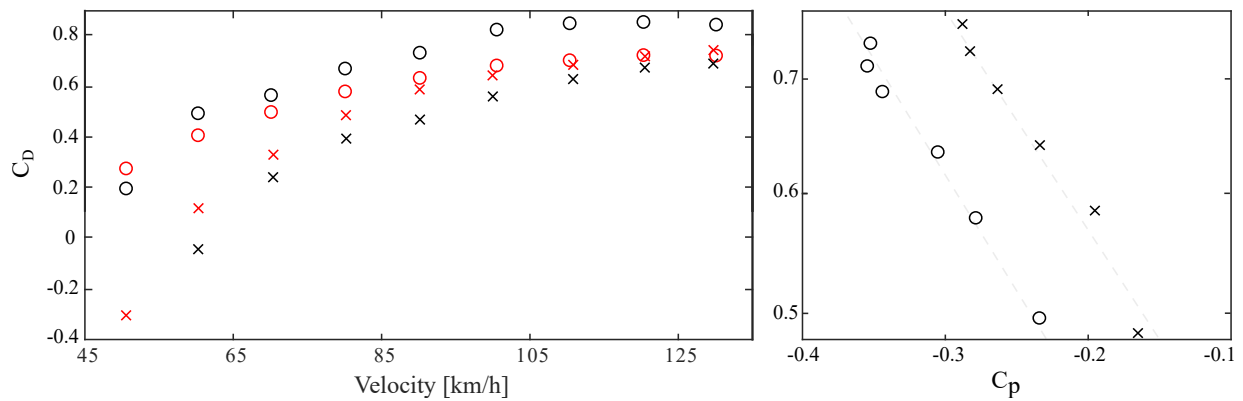


Figure 5.4 – (a)  $C_x$  obtained for different velocities using the two approaches. '—' red symbols: results using estimation approach,  $C_x$  obtained for different velocities using the two approaches. '—' black symbols: results using Onorato's drag approximation. 'o' circles represent the "Direction I" trajectory while 'x' crosses are related to the "Direction II" trajectory. (b) Relation between  $C_x$  and  $C_p$ .

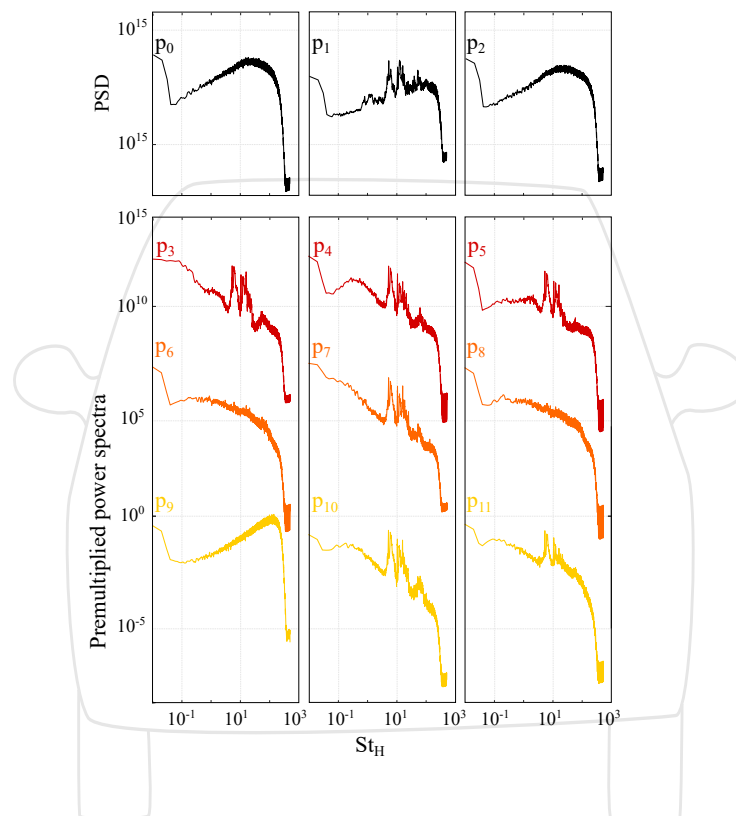


Figure 5.5 – Power spectral analysis of the pressure probes located at the rear wall.

Onorato's drag approximation). The figure contains both direction results. A positive curved of the  $C_x$  is presented for an increase in the velocity. Similar results are obtained for both approaches, which means there is an agreement in the drag force estimation. Ideally, a further simulation in the same conditions might give some accuracy of the estimated results presented here. A small gap is seen from the results in direction I (departure to arrival, denoted by 'o' circles) and direction II (arrival to departure, denoted by 'x' crosses). This is caused by wind effects that clearly induced some variations in the results (depending in which direction the track is run). The ratio between the  $C_p$ , obtained from the pressure sensor, and the  $C_x$ , estimated from the energy balance, is presented in Figure 5.4(b). A linear ratio is obtained for both directions. It is possible to conclude that both methodologies could be applied as sensor inputs to estimate the drag of a real vehicle, and further control this value using different control approaches. It is worth noting that external parameters, such as wind speed, probably vary and therefore, errors are introduced in the measurements. One solution to this problem would be to perform decelerations from high to low velocities. An initial acceleration is done until a velocity of 130 km/h is reached, then the vehicle is allowed

to decelerate under the sole force of aerodynamics (the other forces assumed to be constant). So in 2-3 tests, it should be possible to remove information on the overall operation of the vehicle. Furthermore, some of the control strategies presented in this work (e.g., sliding mode control) could take this perturbation in the model design and the robustness of the approach might be able to keep the drag at a certain value, regardless of these flow perturbations. Moreover, some interesting result could be obtained for low velocities ( $U_\infty < 45$  km/h), especially an analysis of the  $C_x$  variation for different car angles.

Finally, some power spectral analysis are presented for the pressure sensors installed in the front and rear part. Figure 5.5 shows the power spectral densities of the 12 pressure probes, obtained at a velocity of 100 km/h. Pressure probe  $P_9$  stooped working while the experiment was carried out. All the back pressure probes (except the side-center ones,  $p_6$  and  $p_8$ ) and the front-center ones present two strong peaks at frequencies around  $f \approx 5$  Hz and 11 Hz. The top probes ('—' dark red lines) show a clear bump at  $f \approx 1$  Hz (around a  $St_H$  of 0.003); this attenuated peak is strong in the center probe. Similar results were obtained by Grandemange (2013), who suggests that this peak corresponds to a global phenomenon. Another bump is also visible, more prominently in the central probes, at a frequency of 50 Hz.

This short chapter explains the main vehicle characteristics, equipment, and actuator used to control the drag. The vehicle is already equipped with apparatus able to acquire measurements such as pressure, position, etc. Furthermore, a movable spoiler with jets will be added in order to control the rear wake. To achieve closed-loop control, two approaches are proposed in order to estimate the drag. The first one is an approximation of Onorato's equation while the second one is an estimation of the drag force through external forces equation. Similar drag coefficients  $C_x$  were obtained for both propositions. The initial results introduce the possibility to directly estimate the drag of a car. This first test proposes a potential solution to reduce the drag force, and consequently the gas emission, employing easy to use actuation mechanisms and control approaches.

# Conclusions and perspectives

## General synthesis

The flow around a vehicle is inherently three-dimensional and presents highly complex characteristics. The effects of these flows on the vehicle's aerodynamic performance are related to fuel consumption and greenhouse gas emission. Drag reduction is strongly linked to the total power expenses. The manipulation and/or control of the wake flow provides a great potential to achieve drag reduction. This approach is, therefore, a great challenge for transport industry which may be undertaken as a multidisciplinary field.

A first literature review lists, in a non-exhaustive way, the research that has been done on drag reduction for vehicles. An analysis of the wake dynamics in a simplified car model and a backward-facing step are presented. Furthermore, two types of control approaches emerge. On one hand, passive solutions are recognized as effective tools to reduce the drag using deflectors, porous devices or vortex generators. On the other hand, active control solutions have been the subject of recent studies and are generally related to flow control by fluidic actuators. A combination of passive and active devices might further decrease the drag force. A precise understanding of the mechanisms is necessary to apply effective control approaches.

The work presented is entirely experimental. The main mechanisms, devices, and numerical methods used in the experiments are summarized in the first chapter. The analysis and comparison of the micro-blowers and air-knives are also performed. Murata micro-blowers energized the boundary layer to directly perturb the vortex structures formed in the shear layer region. The air-knife studied has a rounded surface, adjacent to the slit exit, which could be considered as an active boat tail (Coanda effect) for drag reduction. The goal is to find the optimal actuator that balances price, power, efficiency and energy consumption, all of this in a small device. A brief explanation of the most complex flow control strategies, sliding mode control (SMC) and machine learning control (MLC), is done. SMC is a robust closed-loop algorithm to track, reach and maintain a predefined set-point; this approach has on-line adaptivity in changing conditions. Machine learning control is a model-free approach to control non-linear systems. It was used with genetic programming to learn an effective control law that is judged and optimized with respect to a problem-specific cost/objective function. The advantages and drawbacks of each control approach are also presented. Using the information provided in this chapter, the results obtained are divided into two parts.

The first part is devoted to characterize and control a 2-dimensional configuration (backward-facing step BFS). The main goal is to reduce the reattachment point and mitigate the unstable dynamics (previously analysed) with an effective control. To characterize the flow, particle image velocimetry, PIV, is used in order to generate the flow fields. A further analysis was done using the proper orthogonal decomposition POD approach. With the data obtained from the analysis, enough information is acquired to apply different control strategies. The flow is manipulated by a row of 20 micro-blowers and sensed by 25 pressure sensors. An initial open-loop control (periodic forcing PF) approach is used, and a reduction of the recirculation length, up to 4.8%, is obtained for this case. In an international collaboration, a new closed-loop approach is attempted. Machine learning control, MLC, is implemented to exploit its performance benefits to find a cost-effective control law. The study demonstrates the efficiency of MLC to reduce the recirculation zone in a turbulent flow regime. Once the best control cases were found, the same dynamical analysis (PIV + POD) was done to the actuated cases (PF and MLC). The results obtained in the first experiment led to the publication of 3 articles in well-known journals and the participation in numerous congress papers, e.g., CFM, ASME, FSSIC, IFAC, MLC, GDR2016.

The results of the first part also guided the work to a 3-dimensional configuration. For a better approach of the results to an industrial project, a car model (square-back Ahmed body) is chosen. For this case, the main goal is to reduce the aerodynamic drag force of the bluff body in a turbulent regime. As previously done, a first analysis of the flow was accomplished using PIV and POD techniques. It is worth noting that the majority of the results obtained are for a 2-dimensional space, and some important information might be lost for this type of test conditions. The flow was manipulated by a slit (air-knife) placed on the top trailing edge and sensed by a force balance, which was able to measure drag, lift and drift forces. The open-loop approach is enlarged, in this case, steady blowing and periodic forcing control laws are applied. The best control scenario is found to be continuous blowing. The closed-loop case is also expanded. MLC is used to explore new possible control law combinations in a more industrial way; the goal for using machine learning control is to find control laws different from the trivial continuous blowing. Another approach is also employed. Sliding Mode Control (SMC) is used as a robust mechanism to steer and maintain the drag to a predefined set-point. The same post-processing used for BFS is employed for the actuated results of the Ahmed body. The second experiment also brought important publications and conference participations (GDR2017, VEHICULAR2018, DEWESOFT MEASUREMENT CONFERENCE).

## Conclusions

To this date, a large number of investigations have been devoted to understanding and controlling turbulent flows around vehicles (Grandemange, 2013; Choi *et al.*, 2014; Aider *et al.*, 2009). Ideally, measurements should be made in a real car, however, this type of geometry is highly complex. For this reason, a simplified car model (Ahmed body) is commonly chosen. Once more, extensive literature can be found for this type of configuration. Barros (2015); Li (2017) & Eulalie (2014), to name a few, vigorously characterize and control this type of flow topology. Furthermore, to analyse the simplest flow structures presented in this complex flows, a 2-dimensional configuration, backward-facing step, has also been investigated. This simplified separated/reattaching flow, has been thoroughly studied in past years (Chun & Sung, 1998; Sujar, 2014; Berk *et al.*, 2017). Moreover, multiple approaches have been investigated to control this turbulent flow. Passive and active devices are being developed to achieve drag reduction in real cars, while several algorithms were created and exploited to successfully control these flows (Joseph, 2012; Aider *et al.*, 2010; Brunton & Noack, 2015; Feingesicht, 2017). However, no experimental study has been able to compile and pre-evaluate all the knowledge presented until now in order to research the drag reduction in complex configurations. For this reason, the aim of this work is to experimentally pre-evaluate flow control parameters to reduce the drag on a real vehicle. In this context, the study is focused in characterizing and controlling the flow downstream

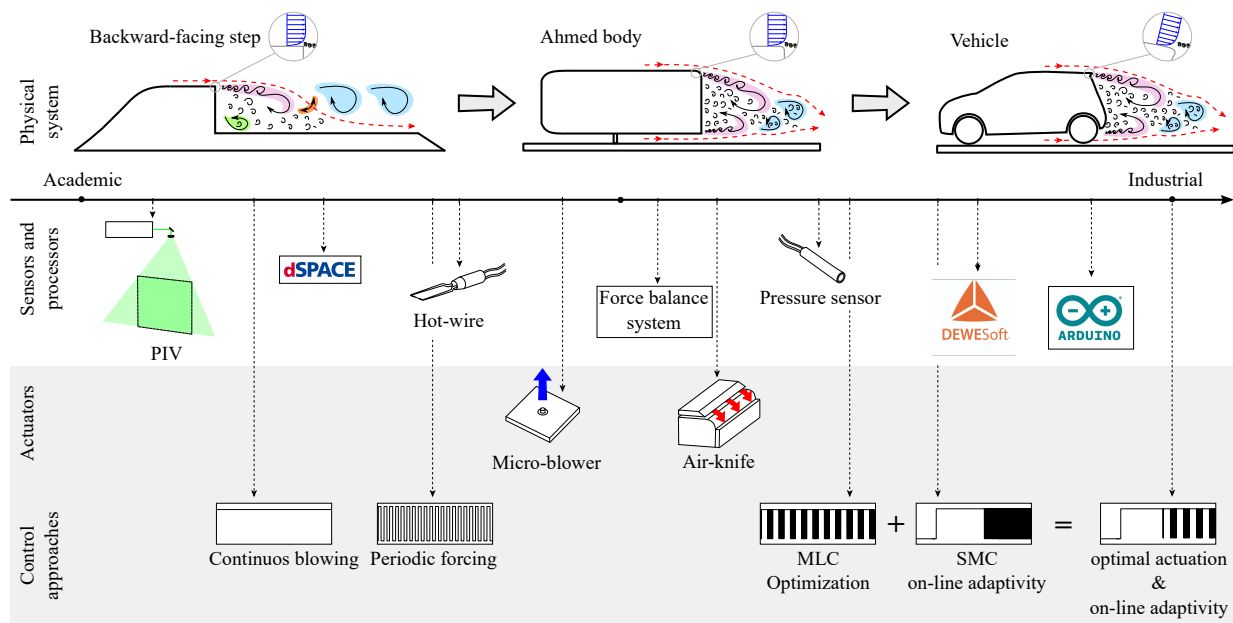


Figure 5.6 – Summary of topics presented in the thesis work.

of 3-dimensional and 2-dimensional configurations. Taking into consideration all the subjects undertaken in this thesis, it is possible to summarize the work done in a spectrum from an academic approach to an industrial one, shown in Figure 5.6.

The flow characteristics from a BFS (academic configuration) unlocked interesting dynamics also present in a more industrial application: the square-back Ahmed body, and consequently with similar flow characteristics to those found in a square-back vehicle. Even though complex physics are seen in a more industrial application, the analysis of the simplified configurations give an overview of the wake physics in separated/reattaching flows. The type and position of both the sensors and actuators are critical parameters to successfully control turbulent flows. For sensors and processors, the main characteristics, such as size, weight, cost, ease of placement and most importantly, effectiveness, are considered to rank them. Concerning the sensors, the study presents different sensor mechanisms to characterize and control the wake. The main sensors used are hot-wires, force balance, and pressure sensors. Hot-wires are highly accurate and they are able to precisely measure a local parameter. However, they are delicate. Force balance is interesting for 3-dimensional configuration, due to its ability to calculate force and torque in three different axes. Nonetheless, it is used in industrial applications is almost non-existent. Although the pressure sensors are quite expensive, it is possible to use them in a real vehicle, as seen in Chapter §5. For the processors, dSPACE is able to accurately measure sensor signals with high acquisition frequencies, ideal for turbulent flows; however, it is bigger, more expensive and difficult to use. DEWESoft, hardware and software, is an accurate data acquisition system able to obtain any type of signal regardless of the environmental conditions. Its compact design enables its use in industrial applications, nevertheless, it lacks a full interface to simultaneously do data acquisition and control. Furthermore, Arduino boards proved to be sufficiently efficient to acquire the sensor data and control the actuator with enough accuracy. One key point is to classify the actuators used for all the experimental tests. Two different devices are analysed and compared: micro-blowers and air-knives. Micro-blowers fulfil almost all the requirements of an optimal actuator; these actuators are ideal for boundary layer energization. However, the jet momentum is not high enough to control the turbulent flow of a car at high velocities. On the contrary, air-knives are more expensive, heavier and harder to mount but, nonetheless, their ability to strongly perturb the flow could be of great interest in vehicle flow control. Their rounded surfaces could be considered as an active Coanda effect for drag reduction. Finally, the control approaches are classified depending on their efficiency, energy consumption and evaluation time. Different open-loop and closed-loop control approaches are presented in order to find the optimal control law, such as continuous blowing, periodic forcing, machine learning control,

and sliding mode. All open-loop approaches are less efficient and not suitable for industrial applications. In contrast, MLC and SMC show great potential to control turbulent flows. The main constraint presented for the first one is evaluation time, which might be a limitation for industrial applications. For the second, it is its energy waste due to the continuous blowing phase. The implementation of different control strategies can lead to revolutionary solutions in flow control. A hybrid between MLC and SMC may provide adaptive control, exploiting the best non-linear actuation mechanisms.

The results presented in this thesis show great promises to control the flow of a real vehicle. Through this work, strong internal, regional and international collaborations were created. Concerning the internal ones, the "DÉSIRE" project was developed in the same framework as the thesis, enabling communications between the Mechanical and Automatic departments in LAMIH. The knowledge exchange created interesting ideas for an industrial flow control application, which are being solved in a co-directed thesis (directed by Prof. Keirsbulck and Prof. Delprat) and started in September 2017 executed by Baptiste Plumjeau. For regional partners, the use of SMC permitted a collaboration with INRIA Lille, where innovative approaches, of both the configuration and control strategy, are now being implemented. Finally, but not less important, two main international collaborations were activated. The first one with Prof. Karjnović in Chalmers University (Sweden), with whom simulated and experimental data was exchanged. Results corroboration could improve simulation and experiment parametrization. The second one with the MLC community (USA, Canada, Argentina, France, China, Germany, etc.), where a large network of students and professors exchange closed-loop control strategies in different complex flow configurations. This collaboration fostered the "Second Machine Control workshop (wMLC-2)" held in Valenciennes. The international automatic and mechanic community gathered to discuss the studies being done and future flow control improvements. This work is a pre-evaluation of the main topics presented in flow control. The goal of this research was to introduce the experimental limitation from an academic to an industrial point of view. Now that most of the points have been presented, new experimental and simulated tests can be undertaken; already some of them are the perspectives presented hereafter.

## Perspectives

Taking into consideration the global results presented in this thesis work, some topics can be thoroughly studied and improved. As the work was mainly focused on flow control, a deeper understanding of the flow dynamics must be pursued. The flow over a vehicle is highly complex and variable through time. Flow simulations, estimations, and linearisations are important to find solutions in order to understand the characteristics presented, and moreover, to successfully control key parameters linked to drag reduction. Modal and stochastic analysis tools could elucidate important information that might be hidden in plain sight.

Flow control is a wide-reaching field. Many topics have been extensively analysed. However, there is still place for development. Here, we will address the improvements closely related to the present work.

As previously stated, the work was mainly devoted to drag control; nonetheless, there are other key parameters that must be considered, such as drift and lift. For this, a new thesis work has already started to pursue better and more accurate results in both the Ahmed body configuration and the real vehicle. The thesis entitled "Aerodynamic flow control of an Ahmed body" and conducted by Baptiste Plumjeau (director Prof. Keirsbulck, and co-director Prof. Delprat) will undertake and improve the topics that were not deeply studied in the present work. This thesis will deal with other flow characteristics presented in an Ahmed body and a real vehicle.

Concerning the actuator devices, the flow interaction between the actuation jet and the boundary layer should be studied. As seen in the present work, this interaction is of great importance in the creation

of turbulent vortices at the rear edge. An understanding of the flow perturbation in this section could help improve the actuation mechanism and position. In this context, the thesis work of Celestin Ott (see Appendix §A) is devoted to analyse and characterize this problematic.

Likewise, the actuators should be able to control other types of configurations. The micro-blowers were successfully used in another configuration in collaboration with Chalmers University (see Appendix §A). Furthermore, these actuators are currently mounted in the LAMIH Ahmed body to control the bi-stability presented in this type of configuration. The actuators are mounted on the rear-edges of the Ahmed body. The objective is to use the approaches here presented to control this instability in real time. Regarding the air-knife, similar actuation devices will be installed in a real vehicle (as already presented in Appendix §5) to control the drag.

Finally, this project mainly worked with SISO and MISO models. Nevertheless, as already explained, there are many parameters that should be taken into consideration, for example, vehicle velocity, upstream conditions, wind gust, drift, shift, energy consumption, etc. Herewith, if the goal is to reduce fuel consumption, the control approaches should be enhanced. The present research must be extended to more complex conditions. For sliding mode control, SIMO and MIMO model will be pursued to improve wake stabilization. An extension of the sliding mode control methodology to multi-input bi-linear systems with delays is already being developed. Some theoretical results on control design and robustness analysis have already been obtained. This control approach will be applied to both configurations. Also, the control performance will be graded by energy consumption.

More complex conditions, such as velocity variation and wind gust, will be extended in Machine Learning Control. A robust control with LGPC will be pursued by adding sensors upstream (additional sensors) or extending the cost function to different operating conditions. Furthermore, the creation of performance estimators will help to decrease the learning process. Kaiser *et al.* (2017) proposed an estimator to calculate the cost function of untested individuals, based on the information obtained from previous tests. The accelerating improvements of machine learning control with LGPC will play an important role in future flow control approaches. One of these MLC application and cluster analysis will be presented in Appendix §B.

The propositions presented in this document may be used as a reference to guide the work of flow control towards drag reduction. The ideas proposed here are a consequence of all the work done for simplified configurations. Their use in an industrial application or as an “experimental showcase” is of great promise for future works.



# Bibliography

- ACTION MOTO MAGAZINE. 2007 "Petits arrangements avec le vent" No.144, pp. 104-107.
- ADAMS, E.W. & JOHNSTON, J.P. 1988 Effects of the separating shear layer on the reattachment flow structure Part 1: Pressure and turbulence quantities. *Exp. Fluids* **6**, 400-408.
- ADAMS, E.W. & JOHNSTON, J.P. 1988 Effects of the separating shear layer on the reattachment flow structure Part 2: Reattachment length and wall shear stress. *Exp. Fluids* **6**, 493-499.
- ADRIAN, R. 1991 Particle-imaging techniques for experimental fluid mechanics. *Ann. Rev. Fluid Mech.* **23**, 261-304.
- AHMED, S. R., RAMM, G. & FALTIN, G. 1984 Some salient features of the time averaged ground vehicle wake. *Society of Automotive Engineers, SAE Inc* **840300**.
- AHMED, S. R., GAWTHORPE, R.G. & MACKRODT, P.A. 1985 Aerodynamics of road and rail vehicles. *Veh. Syst. Dyn.* **14**, 319-392.
- AIDER, J.-L., LASSERRE, J.-J., BEAUDOIN, J.-F., HERBERT, V., & WESFREID, J.-E. 2009 "Contrôle d'écoulement en Aérodynamique automobile". In *19th CFM Congress*, pp. 1-6.
- AIDER, J. -L, BEAUDOIN, J. -F & WESFREID, J.E. 2009 Drag and lift reduction of a 3D bluff-body using active vortex generators. *Exp. Fluids* **49**, 771-89.
- AMITAY, M., SMITH, D.R., KIBENS, V., PAREKH, D. & GLEZER, A. 2001 Aerodynamic Flow Control over an Unconventional Airfoil Using Synthetic Jet Actuators. *AIAA journal* **39**(3), 361-370.
- ARDUINO CO. 2008 All Rights Reserved. [www.arduino.cc](http://www.arduino.cc).
- ARIYUR, K.B. & KRSTIC, M. 2004 Slope seeking: a generalization of extremum seeking. *Int. J. Adap. control and signal Proc.* **18**, 1-22.
- ARMALY, B.F., DURST, F., PEREIRA, J.C. & SCHÖNUNG, B. 1983 Experimental and theoretical investigation of a backward-facing step flow. *J. Fluid Mech.* **127**, 473-496.
- ARTANA, G., SOSA, R., MOREAU, E. & TOUCHARD, G. 2003 Control of the near-wake flow around a circular cylinder with electro-hydrodynamic actuator. *Exp. Fluids* **35**(6), 580-588.
- AUBRUN, S., McNALLY, J., ALVI, F. & KOURTA, A. 2011 Separation flow control on a generic ground vehicle using steady microjet arrays. *Exp. Fluids* **51**(5), 1177-11878.
- BAARS, W.J. & TINNEY, C.E. 2014 Proper orthogonal decomposition-based spectral higher-order stochastic estimation. *Phys. of Fluids* **26**, 055112.
- BAGHERI, S., BRANDT, L. & HENNINGSON, D.S. 2009 Input-output analysis, model reduction and control of the flat-plate boundary layer. *J. Fluid Mech.* **620**, 263-298.

- BAKER, C. 2010a The flow around high-speed trains, *J. Wind. Eng. Ind. Aerodyn.* **98**, 277-98.
- BARBEE, J.G. & ELLZEY, J.L. 1989 The effect of aspect ratio on the flow over a rearward facing step. *Exp. Fluids* **7**, 447-452.
- BARROS, D. 2015 Wake and Drag Manipulation of a Bluff Body Using Fluidic Forcing. PhD. thesis, École Nationale Supérieure de Mécanique et d'Aérotechnique, Poitiers, France.
- BARROS, D., BORÉE, J., NOACK, B.R. & SPOHN, A. 2016a Resonances in the forced turbulent wake past a 3D blunt body. *Phys. Fluids* **28**(6), 065104.
- BARROS, D., BORÉE, J., NOACK, B.R., SPOHN, A. & RUIZ, T. 2016b Bluff body drag manipulation using pulsed jets and Coanda effect. *J. Fluid Mech.* **805**, 422-459.
- BARROS, D., BORÉE, J., O., CADOT., A., SPOHN & NOACK, B. R. 2017 Forcing symmetry exchanges and flow reversals in turbulent wakes. *J. Fluid Mech.* **829**.
- BAYRAKTAR, I., LANDMAN, D. & BAYSAL, O. 2001 Experimental and computational investigation of Ahmed body for ground vehicle aerodynamics. *Tech. Rep.*. SAE Technical Paper.
- BEARMAN, P.W. 1965 Investigation of the flow behind a two-dimensional model with a blunt trailing edge and fitted with splitter plates. *J. Fluid Mech.* **21**(2), 241-255.
- BEAUDOIN, J.-F., CADOT, O., AIDER, J.-L. & WESFREID, J. E. 2004 Three-dimensional stationary flow over a backward-facing step. *European J. of Mech. - B/Fluids* **23**, 147-155.
- BEAUDOIN, J.-F., CADOT, O., AIDER, J.-L. & WESFREID, J. E. 2006 Bluff-body drag reduction by extremum-seeking control step. *F. Fluids and Struct.*, 973-978.
- BEAUDOIN J.-F., AND AIDER J.-L. 2008 Drag and lift reduction of a 3D bluff body using flaps. *Exp. Fluids***44**(4), 491-501.
- BECKER, R., GARWON, M., GUTKNECHT, C., BARWOLFF, G. & KING, R. 2015 Robust control of separated shear flows in simulation and experiment. *J. Process Control* **15**(6), 691-700.
- BELSON, B., SEMERARO, O., ROWLEY, C. & HENNGINSON, D.S. 2013 Feedback control of instabilities in the two-dimensional blasius boundary layer: The role of sensors and actuators. *Phys. Fluids*, **25**.
- BERA, J.C., MICHARD, M., GROSJEAN, N. & COMTE-BELLOT, G. 2001 Flow analysis in two-dimensional pulsed jet by particle image velocimetry *Exp. Fluids*, 519-532.
- BERGER, E., SCHOLZ, D. & SCHUMM, M. 1990 Coherent vortex structures in the wake of a sphere and a circular disk at rest and under forced vibrations. *J. Fluids Struct.* **4**(3), 231-257.
- BERK, T., MEDJNOUN, T. & GANAPATHISUBRAMANI, B. 2017 Entrainment effects in periodic forcing of the flow over a backward-facing step. *Phys. Rev. Fluids* **2**, 074605.
- BHATTACHARJEE, S., SCHEELKE, B. & TROUTT, T.R. 1986 Modification of vortex interactions in a reattaching separated flow. *AIAA journal* **24**, 623-629.
- BMW 2001 BMW Gina Light Visionary Concept - Design. [www.bmw.tv](http://www.bmw.tv).
- BONS, J.P., RIVIR, R.B. & SONDERGAARD, R. 2002 The fluid dynamics of LPT blade separation control using pulsed jets. *J. Turbomach.* **124**,77-85.
- BRADLEY, R. 2015 Technology roadmap for the 21st century truck program. *Tech. Rep.* 21CT-001, US Dep. Energy, Washington, DC.
- BRADSHAW, P. & WONG, F.Y.F. 1972 The reattachment and relaxation of a turbulent shear layer. *J. Fluid Mech.* **52**(1), 113-135.
- BRAMEIER, M. & BANZHAF, W. 2007 Linear Genetic Programming. *Springer Science & Business Media*.
- BRUNEAU, C.H., CREUSÉ, E., DEPEYRAS, D., GILLIÉRON, P. & MORTAZAVI, I. 2010 Coupling active and passive techniques to control the flow past the square back Ahmed body. *Comp. and fluids* **39**(10), 1875-1892.

- BRUNEAU, C.H., CREUSÉ, E., DEPEYRAS, D., GILLIÉRON, P. & MORTAZAVI, I. 2011 Active procedures to control the flow past the Ahmed body with a 25° rear window *Int. J. Aero.* **1**(3/4), 299-317.
- BRUNTON, S. L. & NOACK, B. R. 2015 Closed-loop turbulence control: Progress and challenges. *Appl. Mech. Rev.* **67**(5), 050801:01-48.
- BRUNN, A., WASSEN, E., SPERBER, D., NITSCHKE, W. & THIELE, F. 2007 Active Drag Control for a Generic Car Model. In *King R. (eds) Active Flow Control. Notes on Numerical Fluid Mechanics and Multidisciplinary Design (NNFM) 95*. Springer, Berlin, Heidelberg.
- CASTRO, P. & CASTRO, A. 1987 The structure of a turbulent shear layer bounding a separation region. *J. Fluid Mech.* **179**, 439.
- CATTAFESTA, L., GARG, S., CHOUDHARI, M. & LI, F. 1997 Active control of flow-induced cavity resonance. In *28th AIAA Fluid Dyn. Conference*, 97-1804, Colorado, USA.
- CATTAFESTA, L., GARG, S. & SHUKLA, D. 2001 Development of piezoelectric actuators for active flow control. *AIAA journal* **39**, 1562–1568.
- CATTAFESTA, L. & SHELPACK, M. 2011 Actuators for active flow control. *Ann. Rev. Fluid Mech.* **43**, 247-272.
- CHALIGNÉ, S., CASTELAIN, T., MICHARD, M. & JUV'É, D. 2013 Unsteady measurements in a separated and reattaching flow. *Comptes Rendus Mécanique* **341**(3), 289-297.
- CHERRY, N.J., HILLIER, R. & LATOUR, M.E. 1984 Active control of the flow behind a two-dimensional bluff body in ground proximity. *J. Fluid Mech.* **144**, 13-46.
- CHOI, H., JEON, W.P. & KIM, J. 2008 Control of flow over a bluff body. *Ann. Rev. Fluid Mech.* **40**, 113-139.
- CHOI, H., LEE, J. & PARK, H. 2014 Aerodynamics of heavy vehicles. *Ann. Rev. Fluid Mech.* **46**, 441-468.
- CHOVET, C., LIPPERT, M., KEIRSBULCK, L., & FOUCAUT, J.-M. 2016 Dynamic characterization of piezoelectric micro-blowers for separation flow control. *Sensors and Actuators A: Physical* **249**,122-130.
- CHOVET, C., LIPPERT, M., KEIRSBULCK, L., & FOUCAUT, J.-M. 2017a Dynamical aspects of a backward-facing step flow at large Reynolds numbers. *Exp. Fluids* **58**, 162.
- CHOVET, C., KEIRSBULCK, L., NOACK, B. R., LIPPERT, M. & FOUCAUT, J.-M. 2017b Machine learning control for experimental shear flows targeting the reduction of a recirculation bubble. In *20th World Congress IFAC*, pp. 1-4, Toulouse, France.
- CHOVET, C., LIPPERT, M., KEIRSBULCK, L. & FOUCAUT, J.-M. 2018a Unsteady behaviour of a backward-facing step in forced flow. *Flow Turb. Comb.* (in revision).
- CHOVET, C., FEINGESICHT, M., PLUMEJEAU1, B., LIPPERT, M., KEIRSBULCK, L., KERHERVÉ, F., ABASSI, W., POLYAKOV, A., RICHARD, J.-P. & FOUCAUT, J.-M. 2018b Sliding mode control applied to a square-back Ahmed body. *Under consideration for European J. of Mech. - B/Fluids*
- CHOVET, C., FEINGESICHT, M., PLUMEJEAU1, B., DELPRAT, S., L., KERHERVÉ, W., POLYAKOV, A., LIPPERT, M., KEIRSBULCK, RICHARD, J.-P. & FOUCAUT, J.-M. 2018c Reducing Car Consumption by Means of a Closed-loop Drag Control. In *7th International Conference on Advances in Vehicular Systems, Tech. and Appl.*, Venice, Italy.
- CHUN, K.B. & SUNG, H.J. 1996 Control of turbulent separated flow over a backward-facing step by local forcing. *Exp in Fluids* **21**, 417-426
- CHUN, K.B. & SUNG, H.J. 1998 Visualization of a locally-forced separated flow over a backward-facing step *Exp in Fluids* **25**, 133-142.
- CHUN, S., LEE, I. & SUNG, H.J. 1999 Effect of a spanwise-varying local forcing on turbulent separated flow over a backward-facing step *Exp in Fluids* **26**, 437-440.
- COANDA, H. 1934 Procédé et dispositif pour faire devier une veine fluide penetrant autre fluids. *French Pat.*,788, 140.

- COMPTON, D.A. & JOHNSTON, J.P. 1992 Streamwise vortex production by pitched and skewed jets in a turbulent boundary layer. *AIAA journal* **30**, 640–47.
- CORKE, T., POST, M. & ORLOV, D. 2007 SDBD plasma enhanced aerodynamics: concepts, optimization and applications. *Prog. Aerosp. Sci.* **43**, 193–217.
- CORNEJO MACEDA, G. Y. 2017 Machine learning control applied to wake stabilization. Master's thesis, LIMSI and ENSAM, Paris, France.
- CUVIER, C. 2012 Active control of a separated turbulent boundary layer in adverse pressure gradient. PhD. thesis, École central de Lille, France.
- DE BREDERODE, V. & BRADSHAW, P. 1972 Three-dimensional flow in nominally two-dimensional separation bubbles. I. Flow behind a rearward-facing step. *Imp. College Aero Rep.* **72-19**.
- DE BREDERODE, V. & BRADSHAW, P. 1978 Influence of the side walls on the turbulent centerplane boundary-layer in a squareduct. *Trans. ASME I: J. Fluids Eng.* **100**, 91-96.
- DEEM, E., CATTAFESTA, L., ZHANG, H., ROWLEY, C., HEMATI, M., CADIEUX, F., & MITTAL, R. 2017 Identifying Dynamic Modes of Separated Flow Subject to ZNMF-based Control from Surface Pressure Measurements. In *47th AIAA Fluid Dynamics Conference*, pp. 1-19. Denver, Colorado.
- DETEMPLE-LAAKE, E., & ECKELMANN, H. 1989 Phenomenology of Kármán vortex streets in oscillatory flow. *Exp. Fluids* **7**, 217-227.
- DEWESoft Co. 2000 All Rights Reserved. [www.dewesoft.com](http://www.dewesoft.com).
- DI CICCIA, G.M., SPAZZINI, P.G., IUSO, G., MALVANO, R., POLLEDRO, P. & ONORATO, M. 2003 PIV investigation on a controlled backward facing step flow. *Proceedings of PSFVIP-4*, Chamonix, France.
- DRAZIN, P. G. & REID, W. H. 2004 Hydrodynamic stability. *Cambridge university press*.
- DRIVER, D.M. & SEEGMILLER, H.L. 1985 Features of a reattaching shear layer in divergent channel flow. *AIAA journal* **23**(2), 163-171.
- DRIVER, D.M., SEEGMILLER, H.L. & MARVIN, J.G. 1987 Time-Dependent Behaviour of a Reattaching Shear Layer. *AIAA journal* **25**, 914-919.
- DSPACE CO. 2002 All Rights Reserved. [www.dspace.com](http://www.dspace.com).
- DUELL, E.G. & GEORGE, A.R. 1993 Measurements in the unsteady near wakes of ground vehicle bodies. *Tech. Rep.*. SAE Technical Paper.
- DUELL, E.G. 1994 Experimental Investigation of Unsteady Near Wakes of Ground Vehicle Bodies. PhD. thesis, Cornell University, USA.
- DUELL, E.G. & GEORGE, A.R. 1999 Experimental study of a ground vehicle body unsteady near wake. *Tech. Rep.*. SAE Technical Paper.
- DURIEZ, T., PAREZANOVIC, V., LAURENTIE, J.-C., FOURMENT, C., DELVILLE, J., BONNET, J.-P., CORDIER, L., NOACK, B. R., SEGOND, M., ABEL, M. W., GAUTIER, N., AIDER, J.-L., RAIBAUDO, C., CUVIER, C., STANISLAS, M., & BRUNTON, S. L. 2014 Closed-loop control of experimental shear flows using machine learning. In *7th AIAA Flow Control Conference*, Atlanta, USA.
- DURIEZ, T., BRUNTON, S. & NOACK, B. R. 2016 *Machine Learning Control – Taming Nonlinear Dynamics and Turbulence. Fluid Mechanics and Its Applications* 116. Springer-Verlag.
- DURST, F. & TROPEA, C. 1981 Turbulent backward-facing step flows in two-dimensional ducts and channels. *Proceedings of turbulent shear flow 3 symposium Davis*
- EATON, J.K. & JOHNSTON, J.P. 1982 Low Frequency Unsteadiness of a Reattaching Turbulent Shear Layer. In *Bradbury L.J.S., Durst F., Launder B.E., Schmidt F.W., Whitelaw J.H. (eds) Turbulent Shear Flows 3*, pp. 162-170. Springer, Berlin, Heidelberg.
- ENGLAR, R. J. 2004 Pneumatic heavy vehicle aerodynamic drag reduction, safety enhancement, and performance improvement. In *the Aerodynamics of Heavy Vehicles: Trucks, Buses, and Trains*, pp. 277-302, Springer.

- EULALIE, Y. 2014 Aerodynamic analysis and drag reduction around an Ahmed bluff body. PhD. thesis, Bordeaux University, Bordeaux, France.
- EVARD, A., CADOT, O., HERBERT, V., RICOT, D., VIGNERON, R. & DÉLERY, J. 2016 Fluid force and symmetry breaking modes of a 3D bluff body with a base cavity. *J. Fluids and Struct.* **61**, 99-114.
- EVSTAFYEVA, O., MORGANS, A. S. & DALLA LONGA, L. 2016b Simulation and feedback control of the Ahmed body flow exhibiting symmetry breaking behaviour *J. Fluid Mech.* **817**, R2.
- FADLA, F., GRAZIANI, A., KERHERVE, F., MATHIS, R., LIPPERT, M., UYSTEPRUYST, D. & KEIRSBULCK, L. 2016 Electrochemical Measurements for Real-Time Stochastic Reconstruction of Large-Scale Dynamics of a Separated Flow. *J. of Fluids Eng.* **138**(12), 121204.
- FAGO, B., LINDNER, H. & MAHREHOLTZ, O. 1991 The effect of ground simulation on the flow around vehicles in wind tunnel testing. *J. Wind Eng. Ind. Aerodyn.* **38**, 47-57.
- FAN, D., WU, Z., ZHOU, Y., LI, R. & NOACK, B. R. 2017 Optimization of jet mixing using machine learning control. *J. Fluid Mech. Rapids* (in revision).
- FARABEE, M. & CASARELLA, M.J. 1986 Measurements of fluctuating wall pressure for separated/reattached boundary layer flows. *ASME J. Vib., Acoust., Stress, Reliab. Des.* **108**, 301.
- FEINGESICHT M., RAIBAUDO, C., POLYAKOV A., KERHERVÉ F. & RICHARD J. -P. 2016 A bilinear input-output model with state-dependent delay for separated flow control. In *European Control Conference* Aalborg, Denmark.
- FEINGESICHT, M., POLYAKOV, A., KERHERVÉ, F. & RICHARD J. -P. 2017 SISO model-based control of separated flows: Sliding mode and optimal control approaches. *Int. J. Robust and Nonlinear Control* **27**(18), 5008-5027.
- FEINGESICHT, M. 2017 “Contrôle non linéaire actif d’écoulements turbulents décollés : Théorie et expérimentations”. PhD. thesis, Inria/CRISTAL, France.
- FLATT, J. 1961 The History of Boundary Layer Control Research in the United States of America. In *Boundary Layer and Flow Control*, G.V. Lachemann, ed., Pergamon Press, pp. 122-143, New York, USA.
- FURUICHI, N. & KUMADA, M. 2003 An experimental study of a spanwise structure around a reattachment region of a two-dimensional backward-facing step. *Exp. Fluids***32**, 179-187.
- FURUICHI, N., HACHIGA, T. & KUMADA, M. 2004 An experimental investigation of a large scale structure of a two-dimensional backward-facing step by using advanced multi-point LDV. *Exp. Fluids***36**, 274-281.
- GALLAS, Q., LAMOUREUX, M., MONNIER, J.-C., GILLIOT, A., VERBEKE, C. & DELVA, J. 2016 Flow Control and Analysis on Simplified Ship Helideck. In *34th AIAA Applied Aerodynamics Conference*, 2016-3262, Washington, D.C., USA.
- GAD-EL-HAK, M. 1996 Modern developments in flow control *App. Mech. Rev.* **49**, 365-379.
- GARWON, M., DARMADI, L.H., URZYNICOK, F. BÄRWOLFF, G. & KING, R. 2003 daptive control of separated flows. In *European Control Conference*, Cambridge, UK.
- GAO, N., LI, Y. Q., BAI, H. L. & WU, C. J. 2016 Effects of synthetic jets on a D-shaped cylinder wake at a subcritical Reynolds number. *Flow Turb. Comb.* **97**(3), 729-742.
- GAUTIER, N. & AIDER, J. -L 2013 Control of the flow behind a backwards facing step with visual feedback. *Proc. R. Soc. Lond A* **469**,2160.
- GAUTIER, N. & AIDER, J. -L 2014a Frequency lock closed-loop control of a separated flow using visual feedback. *J. Fluid Mech.* **759**, 181-196.
- GAUTIER, N., AIDER, J. -L., DURIEZ, T., NOACK, B. R., SEGOND, M. & ABEL, M. W. 2015 Closed-loop separation control using machine learning. *J. Fluid Mech.* **770**, 424-441.
- GAUTIER, N. 2014 Flow control using optical sensors PhD. thesis, PMMH, France.
- GERRARD, J. H 1966 The mechanics of the formation region of vortices behind bluff bodies. *J. Fluid Mech.* **25**(2), 401-413.

- GILHOMME, B.R. 2002 Unsteady and time-averaged near-wake flow over the rear of Sedan automobiles. Ph.D. *thesis*, Monash University, Australia.
- GILLIÉRON P. 2000 “Analyse, modélisation et typologie des écoulements de culot dans l’automobile” *36eme colloque d’aérodynamique appliquée*.
- GLEZER, A. & AMITAY, M. 2002 Synthetic Jets. *Ann. Rev. Fluid Mech.* **34**, 503-529.
- GLEZER, A., AMITAY, M. & HONOHAN, A. M. 2005 Aspects of low-and high-frequency actuation for aerodynamic flow control. *AIAA journal* **43**(7), 1501-1511.
- GODARD, G. & STANISLAS, M. 2006a Control of a decelerating boundary layer. part 3: Optimization of round jets vortex generators. *Aero. Sc. and Tech.* **10**(6), 455-464.
- GRAFTIEAUX L., MICHARD M. & GROSJEAN N. 2001 Combining PIV, POD and vortex identification algorithms for the study of unsteady turbulent swirling flows. *Measurement science and technology* **12**, 1422-1429.
- GRANDEMANGE, M. 2013 Analysis and Control of Three-dimensional Turbulent Wakes: from Axisymmetric Bodies to Road Vehicles Ph.D. thesis, ENSTA ParisTech, Paris, France.
- GRANDEMANGE, M., GOHLKE, M. & CADOT, O. 2013a Bi-stability in the turbulent wake past parallelepiped bodies with various aspect ratios and wall effects. *Phys. Fluids* **25**(9), 095103.
- GRANDEMANGE, M., GOHLKE, M. & CADOT, O. 2013b Turbulent wake past a three-dimensional blunt body. Part 1. *J. Fluid Mech.* **722**, 51-84.
- GRUND, T. & NITSCHKE, W. 2010 Active Flow Control on a S10 Glider Configuration. In *Active flow control II*, pp. 31-43, Springer.
- GUEZENNEC, Y.G. 1989 Stochastic estimation of coherent structures in turbulent boundary-layers. *Phys. Fluids* **1**(6), 1054-1060.
- GUILMINEAU, E., DENG, G. & WACKERS, J. 2011 Numerical simulation with a DES approach for automotive flows. *J. Fluid Struct.* **27**, 807-16.
- HALL, S.D., BEHNIA, M., FLETCHER, C.A.J. & MORRISON, G.L. 2003 Investigation of the secondary corner vortex in a benchmark turbulent backward-facing step using crosscorrelation particle imaging velocimetry. *Exp. Fluids* **35**, 139-151.
- HAN, T. 1989 Computational Analysis of Three-Dimensional Turbulent Flow Around a Bluff Body in Ground Proximity. *AIAA journal*, 1213-1219.
- HAN, T., HAMMOND, D. C. & SAGI, C. J. 1992 Optimization of bluff body for minimum drag in ground proximity. *AIAA journal* **30**(4), 882-889.
- HAN, T., SUMANTRAN, V., HARRIS, C., KUZMANOV, T., HUEBLER, M., & ZAK, T. 1996 Flow-field simulations of three simplified vehicle shapes and comparisons with experimental measurements. *Tech. Pap.* **30960678**, SAE Int., Warrendale, PA.
- HASAN, M.A.Z. 1992 The flow over a backward-facing step under controlled perturbation : laminar separation. *J. Fluid Mech.* **238**, 73-96.
- HEENAN, A.F. & MORRISON, J.F. 1998 Passive control of pressure fluctuations generated by separated flow. *AIAA journal* **36**, 1014-1022.
- HENNING, L. & KING, R. 2007 Robust multivariable closed-loop control of a turbulent backward-facing step flow. *J. Aircraft* **44**.
- HO, C.M. & HUERRE, P. 1984 Perturbed Free Shear Layers *Ann. Rev. Fluid Mech.* **16**(1), 365-422.
- HOERNER, S.F. 1965 Fluid-dynamic drag. *Hoerner fluid dynamics*, Brick Town, NJ.
- HOLMAN, R., UTTURKAR, Y., MITTAL, R., SMITH, B. L., & CATTAFESTA, L. 2005 Formation Criterion for Synthetic Jets. *AIAA journal* **43**(10), 2110-2116.
- HUCHO, W. -H. & SOVRAN G. 1993 Aerodynamics of road vehicles. *Ann. Rev. Fluid Mech.* **25**, 485-537.
- HUCHO, W. -H., e.d. 1998 *Aerodynamics of road vehicles*. Society of Automotive Engineers.

- HUERRE, P. & MONKETWITZ, P. A. 1990 Local and global instabilities in spatially developing flows. *Ann. Rev. Fluid Mech.* **22**, 473-537.
- HUERRE, P. & ROSSI, M. 1998 Hydrodynamic instabilities in open flow. In *Cambridge university press.*, 81-294.
- HUDY, L.M., NAGUIB, A. & HUMPHREYS, W.M. 2007 Stochastic estimation of a separated-flow field using wall-pressure-array measurements. *Phys. Fluids* **19**, 024103.
- HYUN, K.T. & CHUN, C.H. 2003 The wake flow control behind a circular cylinder using ion wind. *Exp. Fluids* **35**(6), 541-552.
- ISHAR, R., KAISER, E., MORZYNSKI, M., FERNEX, D., SEMAAN, R., ALBERS, M., MEYSONNAT, P. S., SCHRÖDER, W. & NOACK, B.R. 2018a Metric for attractor overlap *J. Fluid Mech.* (in revision).
- ISHAR, R., CHOVET, C., NOACK, B.R, LIPPERT, M., LI, R., KEIRSBULCK, L. & KAISER, E. 2018b Metric for attractor overlap applied to a turbulent flow *Under construction for Exp. Fluids*
- ISOMOTO, K. & HONAMI, S. 1989 The effect of inlet turbulence intensity on the reattachment process over a backward-facing step. *J. Fluid Eng.***111**(1), 87-92.
- JACQUIN L. & TABELING P., e.d. 2006 “Turbulences et Tourbillons”. *Cours de l’école Polytechnique.*
- JERRY, A. 1977 The Shannon Sampling Theorem-Its Various Extensions and Applications : A Tutorial Review. *Proceedings of the IEEE.* **65**(11),1565-1596.
- JEON, W.P. & BLACKWELDER, R.F. 2000 erturbations in the wall region using flushmounted piezoceramic actuators. *Exp. Fluids* **28**, 485-496.
- JOSEPH, P. 2012 Application of flow control by pulsed jets on a bluff body. PhD. thesis, Pierre and Marie Curie University, Paris, France.
- JOSEPH, P., AMANDOLESE, X., EDOUARD, C. & AIDER, J.-L. 2013 Flow control using MEMS pulsed micro-jets on the Ahmed body. *Exp. Fluids* **54**(1), 1-12.
- JOSLIN, R.D. & MILLER, D.N. 2009 Fundamentals and Applications of Modern Flow Control. *Prog. Aeronaut. Astronaut.* **231**.
- KAISER, E., LI, R. & NOACK, B. R. 2017 On the control landscape topology. In *20th World Congress IFAC*, pp. 1-5, Toulouse, France.
- KEAN, R. & ADRIAN, R. 1992 Theory of cross-correlation analysis of PIV images. *Applied Scientific Research* **49**, 191-215.
- KERSTENS, W., PLEIFFER, J., WILLIAMS, D. KING, R. & COLONIUS, T. 2011 Closed-loop control of lift for longitudinal gust suppression at low reynolds numbers. *AIAA journal* **49**(8).
- KHALIGHI, B., ZHANG, S., KOROMILAS, C., BALKANYI, S. R., BERNAL, L. P., IACCARINO, G. & MOIN, P. 2001 Experimental and computational study of unsteady wake flow behind a bluff body with a drag reduction device. *Tech. Rep.*, SAE Technical Paper.
- KHALIGHI, B., CHEN, K. H. & IACCARINO, G. 2012 Unsteady aerodynamic flow investigation around a simplified square-back road vehicle with drag reduction devices. *J. Fluids Engeg.*,**134**(6), 061101.
- KHAN, Z.U. 1999 On the dominant vortex created by a pitched and skewed jet in a cross-flow. PhD. thesis, Stanford university, Stanford, USA.
- KHAN, Z.U. & JOHNSTON, J.P. 1985 On vortex generating jets. *Int. J. Heat and Fluid Flow* **21**(5), 506-511.
- KIYA, M. & SASAKI, K. 1985 Structure of large-scale vortices and unsteady reverse flow in the reattaching zone of a turbulent separation bubble. *J. Fluid Mech.* **154**, 463-491.
- KOIKE, M., NAGAYOSHI, T., & HAMAMOTO, N. 2004 Research on aerodynamic drag reduction by vortex generators *Mitsubishi Motors Tech. Rev.* **16**, 11-16.
- KOSTAS, J., SORIA, J. & CHONG, M.S. 2002 Particle image velocimetry measurements of a backward-facing step flow. *Exp. Fluids* **33**, 838-853.

- KOSTAS, J., FOUCAUT, J.-M. & STANISLAS, M. 2007 The Flow Structure Produced by Pulsed-jet Vortex Generators in a Turbulent Boundary Layer in an Adverse Pressure Gradient. *Flow. Turb. Comb.* **78**, 331-363.
- KOSTAS, J., FOUCAUT, J.-M. & STANISLAS, M. 2007 The effects of pulse frequency and duty cycle on the skin friction downstream of pulsed-jet vortex generators in an adverse pressure gradient turbulent boundary layer. *Sci. and Tech.* **13**, 36-48.
- KOURTA A., & GILLIÉRON P. 2009 Impact of the Automotive Aerodynamic Control on the Economic Issues. *J. App. Fluid Mech.* **2**(2), 69-75.
- KOZA, J. R. 1992 Genetic Programming: On the Programming of Computers by Means of Natural Selection. *MIT Press*. **1**, Cambridge.
- KOZA, J. R., BENNETT, F. H. III AND STIFFELMAN & O.(1999) Genetic Programming as a Darwinian Invention Machine. *Poli R., Nordin P., Langdon W.B., Fogarty T.C. (eds) Lecture Notes in Computer Science.* **1598**, pp. 484-493. Springer, Berlin, Heidelberg.
- KRAJNOVIĆ, S. & DAVIDSON, L. 2003 Numerical Study of the Flow Around a Bus-Shaped Body. *J. Fluids Eng.* **125**(3), 500-509.
- KRAJNOVIĆ, S. & DAVIDSON, L. 2005a Flow around a simplified car, Part 1: Large Eddy Simulation. *J. Fluids Eng.* **127**(5), 907-918.
- KRAJNOVIĆ, S. & DAVIDSON, L. 2005b Flow around a simplified car, Part 2: Understanding the flow. *J. Fluids Eng.* **127**(5), 919-928.
- KRAJNOVIĆ, S. & DAVIDSON, L. 2005c Influence of floor motions in wind tunnels on the aerodynamics of road vehicles. *J. Wind Eng. Ind. Aerody.* **93**, 677-698.
- KRAJNOVIĆ, S. & FERNANDES, J. 2010 Numerical Simulation of the flow around a simplified vehicle model with active flow control. *Int. J. of Heat and Fluid Flow* **32**(1), 192-200.
- KRAL, L.D 2000 Active flow control technology *ASME Technical Brief*.
- KRENTEL, D., MUMINOVIC, R., BRUNN, A., NITSCHKE, W. & KING, R. 2010 Application of active flow control on generic 3D car models. In *Active flow control II*, pp. 223-239. Springer.
- KUNHARDT, E. 2000 Generation of large-volume, atmospheric-pressure, nonequilibrium plasmas *IEEE Trans. Plasma Sci.* **28**, 189-200.
- LAHAYE, A., LEROY, A. & KOURTA, A. 2014 Aerodynamic characterisation of a square back bluff body flow. *Int. J. Aerod.***4**(1-2), 43-60.
- LAI, S.J.C., YUE, J. & PLATZER, M.F. 2002 Control of a backward-facing step flow using a flapping foil. *Exp. Fluids* **32**, 44-54.
- LASAGNA, D., ORAZI, M., LUSO, G.(2013) Multi-time delay, linear stochastic estimation of a cavity shear layer velocity from wall-pressure measurements. *Phy. of Fluids* **25**, 017101.
- LECLERC, C. 2008 Simplified car geometry drag reduction by synthetic jet active control. PhD. thesis, INP Toulouse, Toulouse, France.
- LEE, I. & SUNG, H. 2001a Characteristics of wall pressure fluctuations in separated flows over a backward-facing step: Part I. Time-mean statistics and cross-spectral analysis. *Exp. Fluids* **30**, 262-272.
- LEE, I. & SUNG, H. 2001b Characteristics of wall pressure fluctuations in separated flows over a backward-facing step: Part II. Unsteady wavelet analysis. *Exp. Fluids* **30**, 273-281.
- LEE, I. & SUNG, H. 2002 Multiple-arrayed pressure measurement for investigation of the unsteady flow structure of a reattaching shear layer. *J. Fluid Mech.* **463**, 377-402.
- LEE, I. & CHOI, H. 2009 Large eddy simulation of flow over a three-dimensional model vehicle. In *Proc. 6th Int. Symp. Turbul. Shear Flow Phenom.* **1**, pp. 735-739, Seoul, Korea.
- LEHUGEUR, B. & GILLIÉRON, P. 2006 Active control of vortex breakdown phenomenon in the wake of a simplified car geometry. In *FEDSM No.98349*, Miami, Florida.

- LEVALLOIS, E. & GILLIÉRON P 2005 “Réduction de traînée en aérodynamique automobile par contrôle passif des écoulements – analyse par PIV”. *FLUVISU 11*, pp. 7-9, EC Lyon.
- LI, R., NOACK, B. R., CORDIER, L., BORÉE, J. & HARAMBAT, F. 2017a Drag reduction of a car model by linear genetic programming control. *Exp. Fluids* **58**(103), 1-20.
- LI, R. 2017 Aerodynamic drag reduction of a square-back car model using linear genetic programming and physics-based control. PhD. thesis, Pprime, Poitiers, France.
- LI, Y. & NAGUIB, A.M. 2005 High-Frequency Oscillating-Hot-Wire Sensor for Near-Wall Diagnostics in Separated Flows. *AIAA journal* **25**(3), 520-529.
- LI, Z., GAO, N. & BAI, H. 2015 Effect of the periodic perturbations on the wall pressure downstream of a backward facing step. In *Int. Conference on Fluid Mechanics* **25**.
- LI, Z., BAI, H. & GAO, N. 2015 Response of turbulent fluctuations to the periodic perturbations in a flow over a backward-facing step. *Theoretical and Applied Mech. Letters* **5**(5), 191-195.
- LIENHART, H., STOOT, C. & BECKER, S., 2002 Flow and turbulence structures in the wake of a simplified car model(Ahmed model). In *Wagner S., Rist U., Heinemann H.J., Hilbig R. (eds) New Results in Numerical and Experimental Fluid Mechanics III. Notes on Numerical Fluid Mechanics (NNFM)***77**, pp. 323-330. Springer, Berlin, Heidelberg.
- LIENHART, H. & BECKER, S. 2003 Flow and turbulence structure in the wake of a simplified car model. *Tech. Rep.*, SAE Technical Paper.
- LIEPMANN, H.W. & NOSENCHUCK, D.M. 1982 Active control of laminar-turbulent transition. *J. Fluid Mech.* **118**, 201-204.
- LITTLEWOOD, R.P. & PASSMORE, M.A. 2003 Aerodynamic drag reduction of a simplified squareback vehicle using steady blowing. *Exp. Fluids* **53**(2), 519-529.
- LUCHTENBURG, D.M. 2010 Low-dimensional modelling and control of separated shear flows. PhD. thesis, Berlin Institute of Technology, Berlin, Germany.
- LUMLEY, J.L. 1967 The structure of inhomogeneous turbulent flows. *Atmospheric Turbulence and Radio Wave Propagation*, pp. 166-178, Nauka, Moscow, 166–178.
- MA, X., KARNIADAKIS, G., PARK, H. & GHARIB, M. 2003 DPIV-driven flow simulation: a new computational paradigm *Proc. R. Soc. Series A.* **459**, 547-65.
- MA, X., GEISLER, R. & SCHRÖDER, A. 2017 Experimental Investigation of Separated Shear Flow under Subharmonic Perturbations over a Backward-Facing Step. *Flow Turbu. Comb.*, **99**(1), 71-99.
- MAHESH, K. 2013 The Interaction of Jets with Crossflow. *Ann. Rev. Fluid Mech.* **45**, 379-407.
- MCCALLEN, R. C., SALARI, K., ORTEGA, J. M., DECHANT, L. J., HASSAN, B., ROY, C. J., POINTER, W. D., BROWAND, F., HAMMACHE, M., HSU, T.-Y., LEONARD, A., RUBEL, M., CHATELAIN, P., ENGLAR, R., ROSS, J., SATRAN, D., HEINECK, J. T., WALKER, S., YASTE, D. & STORMS, B. 2004 DOE’s Effort to Reduce Truck Aerodynamic Drag - Joint Experiments and Computations Lead to Smart Design. *AIAA paper*, 2014-2249.
- MCCORMICK, D.C. 2000 Boundary Layer Separation Control with direct Synthetic jets. In *25th AIAA Fluid. Dyn. Conference*, pp. 1-11, Colorado, USA.
- MCMANUS, K. R., JOSHI, P. B., LEGNER, H. H., & DAVIS, S. J. 1994 Active control of aerodynamic stall using pulsed jet actuators. *AIAA paper* **94**, 2218.
- MCMANUS, K. R. 1996 Separation control in incompressible and compressible flows using pulsed jets. In *27th AIAA Fluid Dyn. Conference*, New Orleans, USA.
- MILANOVIC, I.V. & ZAMAN, K.B.M.Q. 2005 Synthetic jets in cross-flow. *AIAA journal* **43**(5), 929-940.
- MINELLI, G., HARTONO, A., CHERNORAY, V., HJELM, L., & KRAJNOVIĆ, S. 2017 Aerodynamic Flow Control for a Generic Truck Cabin Using Synthetic Jets. *J. Wind Eng. Ind. Aerodyn.* **168**, 81-90.
- MINELLI, G. 2017 Active Flow Control for Reducing Drag on Trucks: from Concept to Full Scale Testing PhD. thesis, Chalmers University of Technology, Sweden.

- MINGUEZ, M., PASQUETTI, R. & SERRE E. 2008 High-order large-eddy simulation of flow over the Ahmed body car model. *Phys. Fluids* **20**, 095101.
- MODI, V. 1997 Moving Surface Boundary-Layer Control: a Review *J. Fluids and Struct.* **11**(6), 627-663.
- MOREAU, E. 2007 Airflow control by non-thermal plasma actuators. *J. Phys. D Appl. Phys.* **40**, 605–636.
- MURRAY, E. & UKEILEY, L.S. 2003 Estimation of the flow field from surface pressure measurements in an open cavity. *AIAA journal* **41**, 969.
- MURRAY, E. & UKEILEY, L.S. 2007 Modified quadratic stochastic estimation of resonating subsonic cavity flow. *J. Turbulence* **8**, 53.
- MURATA MANUFACTURING CO. 1944 All Rights Reserved. [www.murata.com](http://www.murata.com).
- NAGUIB A.M., WARK C.E. & JUCKENHOFEL O. 2001 Stochastic estimation and flow sources associated with surface pressure events in a turbulent boundary layer. *Phys. Fluids* **13**(9), 2611.
- NADGE, P.M. & GOVARDHAN, R.N. 2014 High Reynolds number flow over a backward-facing step: structure of the mean separation bubble. *Exp. Fluids* **55**, 1657.
- NAYERI, C.N., HAFF, J., GREENBLATT, D., LOEFDAHL, L. & PASCHEREIT, C.O. 2009 Drag reduction on a generic tractor-trailer using active ow control in combination with solid flaps. In *Browand F., McCallen R., Ross J. (eds) The Aerodynamics of Heavy Vehicles II: Trucks, Buses, and Trains. Lecture Notes in Applied and Computational Mechanics* **41**, pp. 179-191. Springer, Berlin, Heidelberg.
- NGUYEN, T.D., CRAIGWELLS, J., MOKHASI, P. & REMPFER, D. 2010 Proper orthogonal decomposition-based estimations of the flow field from particle image velocimetry wall-gradient measurements in the backward-facing step flow. *Meas. Sci. and Tech.* **21**, 115406.
- ONORATO, M., COSTELLI, A. F. & GARONNE A. 1984 Drag measurement through wake analysis. In *SAE, SP-569, International congress and Exposition*, pp. 85-93, Detroit, USA.
- ÖSTH, J. & KRAJNOVIĆ, S. 2012 The flow around a simplified tractor-trailer model studied by large eddy simulation. *J. Wind Eng. Ind. Aerodyn.* **102**, 36–47.
- ÖTÜGEN, M.V. 2014 Expansion ratio effects on the separated shear layer and reattachment downstream of a backward-facing step. *Exp. Fluids* **10**, 273-281.
- OXLADE, A.R., MORRISON, J.F., QUBAIN, A. & RIGAS, G. 2015 High-frequency forcing of a turbulent axisymmetric wake. *J. Fluid Mech.* **770**, 305-318.
- PARK, H., LEE, D., JEON, W.-P., HAHN, S., KIM, J., KIM, J., CHOI, J. & CHOI, H. 2006 Drag reduction in flow over a two-dimensional bluff body with a blunt trailing edge using a new passive device. *J. Fluid Mech.* **563**, 389-414.
- PARK, H., CHO, J.-H., LEE, J., LEE, D. -H. & KIM, K. -H 2013 Aerodynamic drag reduction of Ahmed model using synthetic jet array. *Tech. Rep.*. SAE Technical Paper.
- PAREZANOVIĆ, V., CORDIER, L., SPOHN, A., DURIEZ, T., NOACK, B. R., BONNET, J.-P., SEGOND, M., ABEL, M. & BRUNTON, S. L. 2016 Frequency selection by feedback control in a turbulent shear flow. *J. Fluid Mech.* **797**, 247-283.
- PAREZANOVIĆ, V., LAURENTIE, J. C., FOURMENT, C., DELVILLE, J., BONNET, J. P., SPOHN, A., DURIEZ, T., CORDIER, L., NOACK, B. R. & ABEL, M. 2015 Mixing layer manipulation experiment: From open-loop forcing to closed-loop machine learning control. *Flow. Turb. Comb.* **94**(1), 155-173.
- PASTOOR, M., HENNING, L., NOACK, B. R., KING, R. & TADMOR, G. 2008 Feedback shear layer control for bluff body drag reduction. *J. Fluid Mech.* **608**, 161-196.
- PATNAIK, B.S.V. & WEI, G.W. 2002 Controlling wake turbulence. *Phys. Rev. Letter* **88**.
- PICARD, C. & DELVILLE, J. 2000 Pressure velocity coupling in a subsonic round jet *Int. J. Heat Fluid Flow* **21**, 359-364.
- PIER B.; HUERRE P. 2001 Nonlinear synchronization in open flows. *J. of Fluids and Struct.* **15**(3-4), 471-480.

- PINIER, J.T., AUSSEUR, J.M., GLAUSER, M.N. & HIGUCHI, H. 2007 Proportional Closed-Loop Feedback Control of Flow Separation. *AIAA journal* **45**, 181-190.
- PIPONNAU, S., COLLIN, E., DUPONT, P., DEBIEVE & J.-F. 2011 Simultaneous wall pressure-PIV measurements in a shock wake/turbulent boundary layer interaction. In *7th International Symp. on Turbul. and Shear Flow Phenomena*.
- , PELLERIN, S., PODVIN, B. & PASTUR, L. 2016 Characterization of the Near-Wake of an Ahmed Body Profile. *World Academy of Science, Engineering and Technology International Journal of Aerospace and Mechanical Engineering* **10**(5), 919-924.
- PODVIN, B., NGUIMATSIA, S., FOUCAUT, J.-M., CUVIER, C. & FRAIGNEAU, Y. 2018 On combining linear stochastic estimation and proper orthogonal decomposition for flow reconstruction. *Exp. Fluids* **59**:58.
- POLYAKOV A. 2012 Minimization of disturbances effects in time delay predictor-based sliding mode control systems. *J. of the Franklin Institute* **39**(4), 1380-1396.
- RQBUBAIN, A. 2009 Active control of a turbulent bluff body wake PhD. thesis, Imperial College London, London, England.
- RAIBAUDO, C., ZHONG, P., MARTINUZZI, R.J. & NOACK, B.R. 2017 Closed-loop control of a triangular bluff body using rotating cylinders. In *20th World Congress IFAC*, pp. 1-6, Toulouse, France.
- RAGHUNATHAN, R. S., KIM, H. D. & SETOGUCHI, T. 2002 Aerodynamics of high-speed railway train. *Prog. Aerosp. Sci.* **38**, 469-514.
- RAMAN, G. & CAIN, A.B. 2002 Innovative actuators for active flow and noise control. *Proc. Inst. Mech. Eng. G. J. Aerosp. Eng.* **216**, 303-324.
- RICHARD, J.P., GOUAISBAUT, F. & PERRUQUETTI, W. 2001 Sliding mode control in the presence of delay. *Kybernetika* **37**(3), 277-294.
- ROSHKO, A. On the wake and drag of bluff bodies. *J. Aeron. Sciences* **22**(2), 124-132.
- ROSSITTO, G. Influence of after body rounding on the aerodynamics of a fastback vehicle. PhD. thesis, École Nationale Supérieure de Mécanique et d'Aérotechnique, Poitiers, France.
- ROUMÉAS, M., GILLIÉRON, P. & KOURTA, A. 2009 Drag reduction by flow separation control on a car after body. *Int. J. Num. Mech. Fluids* **60**(11), 1222-1240.
- ROUSSOPOULOS, K. 1993 Feedback control of vortex shedding at low Reynolds numbers. *J. FLUID MECH.* **248**, 267-296.
- ROWLEY, C.W., WILLIAMS, D.R., COLONIUS, T., MURRAY, R.M. & MACMYNOWSKI, D.G. 2006 Linear models for control of cavity flow oscillations. *J. FLUID MECH.* **547**, 317-330.
- RUDERICH, R. & FERNHOLZ, H.H. 1986 An experimental investigation of a turbulent shear flow with separation, reverse flow, and reattachment. *J. FLUID MECH.* **163**, 283-322.
- SAMIMY, M., DEBIASI, M., CARABALLO, E., SERRANI, YUAN, X., LITTLE, J. & MYATT, J.H. 2007 Feedback control of subsonic cavity flows using reduced-order models. *J. FLUID MECH.* **579**, 315-346.
- SHAQARIN, T. 2011 Closed-loop active control to reattach a thick turbulent boundary layer. PhD. thesis, University of Lille 1, Lille, France.
- SIGURDSON, L.W. 1995 The structure and control of a turbulent reattaching flow. *J. FLUID MECH.* **298**, 139-165.
- SIROVICH, L. 2007 Turbulence and the dynamics of coherent structures part i : Coherent structures. *Quart. Appl. Math.* **45**(3), 561-571.
- SCHMIDT, H.J., WOSZIDLO, R., NAYERI, C. N. & PASCHEREIT, C. O. 2015 Drag reduction on a rectangular bluff body with base flaps and fluidic oscillators. *Exp. Fluids* **56**(7), 1-16.
- SEIFERT, A., BACHAR, T., WYGNANSKI, I., KOSS, D. & SHEPSHELOVICH, M. 1999 Oscillatory Blowing, A Tool to Delay Boundary Layer Separation. *AIAA journal* **31**(11).

- SEIFERT, A., ARWATZ, G. & PALEI, V. 2007 Heavy Trucks Base-Drag Reduction Using Active Flow Control. In *Tel Aviv, Heavy Vehicle-Aerodynamics II Conference*, Lake Tahoe, USA.
- SELBY, G. V., LIN, J. C., & HOWARD, F. G. 1992 Control of low-speed turbulent separated flow using jet vortex generators. *Exp. Fluids* **12**, 394-400.
- SIMPSON, R.L. 1996 Aspects of turbulent boundary-layer separation. *Prog. Aerospace Sci.* **32**, 457-521.
- SMITH, B.L. & GLEZER, A. 1998 The formation and evolution of synthetic jets. *Phys. Fluids* **10**, 2281-2297.
- SONTAG, E.D. 2005 Input to state stability: Basic concepts and results. *Nistri P., Stefani G. (eds) Nonlinear and Optimal Control Theory. Lecture Notes in Mathematics* **1932**, pp. 163-220. Springer, Berlin, Heidelberg.
- SOUSANIS, J. 2011 World vehicle population tops 1 billion units. <http://wardsauto.com/news-analysis/world-vehicle-population-tops-1-billion-units/>, [accessed: 15-August-2011].
- SPAZZINI, P.G., IUSO, G., ONORATO, M., ZURLO, N. & DI CICCA G.M. 2001 Unsteady behavior of back-facing step flow. *Exp. Fluids* **30**, 551-561.
- SPEHLING, D. & GORDON, D. 2008 Two billion cars: transforming a culture. *TR news* 259.
- SUJAR, P. 2014 Active control of the turbulent flow downstream of a backward facing step with dielectric barrier discharge plasma actuators PhD. thesis, Pprime, Poitiers, France.
- TANNER, M. 1972 A method of reducing the base drag of wings with blunt trailing edges. *Aeronaut. Q* **23**, 15-23.
- TAYLOR, J.A. & GLAUSER, M.N.(2004) Towards Practical Flow Sensing and Control via POD and LSE Based Low-Dimensional Tools. *J. Fluid Eng.* **126**.
- TESAR, V., HUNG, C. & ZIMMERMAN, W. 2006 o-moving-part hybrid-synthetic jet actuator. *Sensors and Actuators A: Physical* **125**, 159-169.
- TESAR, V. & KORDIK, J. 2012 Transition in synthetic jets. *Sensors and Actuators A: Physical* **187**, 105-117.
- THOMAS, F., CORKE, T., IQBAL, M., KOZLOV, A. & SCHATZMAN, D. 2009 Optimization of dielectric barrier discharge plasma actuators for active aerodynamic flow control. *AIAA journal* **47**(9).
- TILMANN, C., LANGAN, K., BETTERTON, J. & WILSON, M. 2003 Characterization of pulsed vortex generator jets for active flow control. In *RTO AVT Symposium on "Active Control Technology" for Enhanced Performance Operational Capabilities of Military Aircraft, Land Vehicles and Sea Vehicles*, Germany.
- TILMANN, C., LANGAN, K., BETTERTON, J. & WILSON, M. 2003 Characterization of pulsed generator jets for active flow control. *AFRL-VA-WP-TP-2003-336*, 503-529.
- TINNEY, C.E., UKEILEY, L.S., GLAUSER, M.N. 2008 Low-dimensional characteristics of a transonic jet. Part 2. Estimate and far-field prediction. *J. FLUID MECH.* **615**, 53-92.
- THACKER, A., AUBRUN, S., LEROY, A. & DEVINANT, P. 2010 Unsteady analyses of the flow separation on the rear window of a simplified ground vehicle model. In *28TH AIAA APPL. AERODYN. CONFERENCE*, Chicago, AIAA-4569.
- TROUTT, T.R., SCHEELKE, B. & NORMAN, T.R. 1984 Organized structures in a reattaching separated flow field *J. FLUID MECH.* **143**, 413-427.
- UTKIN, V. 1991 Sliding Modes in Control Optimization. *CCES Springer-Verlag*, Berlin.
- VERZICCO, R., FATICA, M., IACCARINO, G., MOIN, P. & KHALIGHI, B. 2002 Large eddy simulation of a road vehicle with drag-reduction devices. *AIAA journal* **40**, 2447-55.
- VOLPE, R., DEVINANT, P. & KOURTA, A. 2015 Experimental characterization of the unsteady natural wake of the full-scale square back Ahmed body: flow bi-stability and spectral analysis. *Exp. Fluids* **56**(5), 1-22.

- VUKASINOVIC, B., RUSAK, Z. & GLEZER, A. 2010 Dissipative small-scale actuation of a turbulent shear layer. *J. Fluid Mech.* **656**, 51-81.
- WASSEN, E., EICHINGER, S. & THIELE, F. 2010 Simulation of active drag reduction for a square-back vehicle. In *Active flow control II*, pp. 241-255. Springer.
- WESTPHAL, R.V. & JOHNSTON, J.P. 1984 Effect of initial conditions on turbulent reattachment downstream of a backward-facing step. *AIAA journal* **22**, 1727-1732.
- WENGLE, H., HUPPERTZ, A., BÄRWOLFF, G. AND JANKE, G. 2001 The manipulated transitional backward-facing step flow: an experimental and direct numerical simulation. investigation. *European J. of Mech. - B/Fluids* **20**, 25-46.
- WILLIAMS, D., CORNELIUS, D. & ROWLEY, C.W. 2007 Supersonic cavity response to open-loop forcing. In *King R. (eds) Active Flow Control. Notes on Numerical Fluid Mechanics and Multidisciplinary Design (NNFM)* **95**, pp. 230-243. Springer, Berlin, Heidelberg.
- WU, Z., FAN, D., ZHOU, Y., LI, R. & NOACK, B.R. 2018 Jet mixing enhancement using machine learning control. *Exp. Fluids* (in revision).
- YI, W. 2007 Drag reduction of a three-dimensional car model using passive control device. PhD. thesis, Seoul Natl. University, Seoul, South Korea.
- YOSHIOKA, S., OBI, S. & MASUDA, S. 2001a Turbulence statistics of periodically perturbed separated flow over a backward-facing step. *Int. J. Num. Meth. Fluids* **22**, 393-401.
- YOSHIOKA, S., OBI, S. & MASUDA, S. 2001b Organized vortex motion in periodically perturbed turbulent separated flow over a backward-facing step. *Int. J. Num. Meth. Fluids* **22**, 301-307.
- ZHANG, M., CHENG, L. & ZHOU, Y. 2004 Closed-loop-controlled vortex shedding and vibration of a flexibly supported square cylinder under different schemes. *Phys. Fluids* **16**(5), 1439-1448.
- ZÜHLKE, O. 2007 Investigation of aerodynamic devices to reduce aerodynamic drag of a generic tractor trailer. Diploma thesis, ISTA (HFI), TU Berlin, Berlin, Germany.



## Additional investigated configurations

Some parallel projects are described in this appendix. Advances in actuation mechanisms, control strategies, sensor placement, data post-processing and physical systems are here presented.

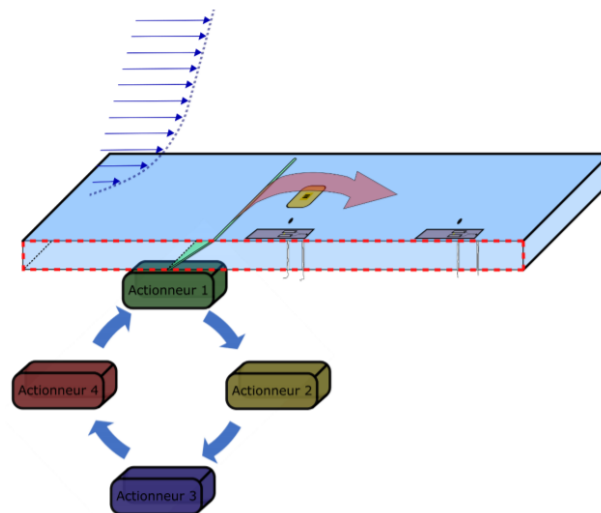


Figure A.1 – Actuators characterization with a single actuation area.

Through the thesis project of Celestin Ott (Directed by Quentin Gallas and Laurent Keirsbulck), a new perspective is being held between the ONERA and the LAMIH laboratory. The main objective of the thesis is to highlight the dynamic mechanisms involved in the interaction between a jet (non-continuous, generated in different ways) and the flow to be controlled, in order to extract a general metric of the effectiveness of a control solution as a function of the control objective. The studied flow will be of two types: an established turbulent boundary layer plane without pressure gradient, and a 3-dimensional flow case. The thesis will be based on the metrological expertise developed within the Lille ELV unit, as well as on the experiments of the LAMIH laboratory at Valenciennes on advanced post-treatment methods (modal and stochastic methods). Some of the main topics being dealt with in this thesis are as follows:

definition of 2 geometric configurations (plane plate and 3-dimensional flow), a definition of 4 types of fluidic actuators (continuous, pulsed, synthetic, and sweeping), development of wind tunnel testing programs for a 2-dimensional campaign at ONERA Lille, and semi-industrial 3-dimensional campaign using the wind tunnel of LAMIH. The experiments will rely on a metrological protocol allowing highly spatio-temporal measurements to be resolved: velocity measurements (PIV resolved in time, hot wire), pressure, and friction. Finally, an analysis of the physics involved: PIV card processing and in-depth analysis (POD, DMD, etc.), temporal and spectral analysis of coherent structures, inter-correlation between measured quantities, etc. Some interesting results were already presented at the GDR “Contrôle Des Décollements” congress.



Figure A.2 – Simplified truck model with a movable cylinder equipped with 20 micro-blowers. Figures obtained from [Minelli \(2017\)](#)

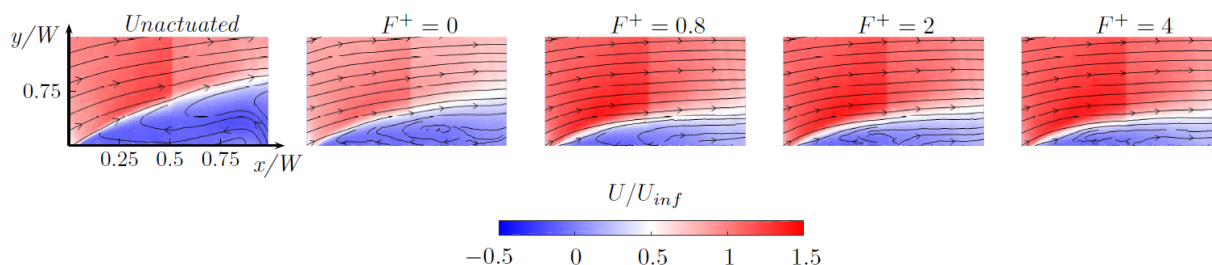


Figure A.3 – Simplified truck model with a movable cylinder equipped with 20 micro-blowers. Results obtained from [Minelli \(2017\)](#)

Another application of the micro-blowers, presented in §2.2.2, was in collaboration with Chalmers University (Dr. Minelli and Pr. Krajnović). A simplified truck cabin was equipped with 20 micro-blowers attached to a movable cylinder, see Figure A.2. The goal was to reduce the recirculation bubble downstream of a forward-facing step. The experiments took place in the LAMIH wind tunnel. PIV measurements, previously described in §2.1.1, were carried out at  $Re_H = 1.25 \times 10^5$ , based on the box height  $H$ . Figure A.3 presents some preliminary results for different actuation signals, previously introduced by [Minelli \(2017\)](#). The micro-blowers strongly affects the main recirculation bubble. An initial continuous blowing actuation is applied ( $F^+ = St_a = 0$ ). A reduction of the bubble length is clearly visible. However, periodic forcing improves bubble reduction. Three periodic forcing frequencies were tested,  $F^+ = St_a = 0.8, 2$  and  $4$ . From results, the optimal frequency was at  $F^+ = St_a = 0.8$  with the strongest thickness reduction. These first results underline the effectiveness of these actuators to control the flow and introduce promising results for higher Reynolds numbers.

# Metric for attractor overlap (MAO)

## B.1 Metric for attractor overlap

A general metric of attractor overlap MAO is implemented for six different control laws applied to a square-back Ahmed body. The operating conditions comprise unforced flow, continuous blowing, low-frequency forcing, and three different multi-frequency forcing. MAO compares and classifies these flows in agreement with physical intuition. The configuration used is the same as the one presented in §4.1. In this section, the main results obtained using MAO are presented; for a thorough explanation of the quantification of attractor overlap please refer to [Ishar \*et al.\* \(2018a\)](#). Here, the experimental comparison Ahmed body attractors is performed following the proposed methodology by [Ishar \*et al.\* \(2018a\)](#); *all the experiment results are presented in [Ishar \*et al.\* \(2018b\)](#)*. Three steps are conducted in order to obtain the proposed metric. First, all states are clustered into discrete centroid-based bins. Second, the probability distribution of each operating condition is determined. Third, the difference of these probability distributions is assessed with the Jensen-Shannon entropy.

A summary of all the control strategies studied is presented in Table 3.4. Phase I represents the

Phase	time	Actuation	Control law	$\bar{F}_D$ (%)	$C_\mu$ (%)
I	$t \leq 50$	Unforced reference	$\mathbf{b}_0 = 0$	0	
II	$t \in (50, 100]$	LGPC sensor-based feedback	$\mathbf{b}_c = 1$	-8	1.355
III	$t \in (100, 150]$	Periodic forcing	$\mathbf{b}_p = \mathbf{H}(h_3)$	+2	0.678
IV	$t \in (150, 200]$	LGPC multi-frequency forcing $m=1$	$\mathbf{b}_1^h = \mathbf{H}(\mathbf{K}_1(h_2, h_5))$	-3	0.678
V	$t \in (200, 250]$	LGPC multi-frequency forcing $m=20$	$\mathbf{b}_2^h = \mathbf{H}(\mathbf{K}_2(h_1, h_3))$	-1	0.678
V	$t \in (250, 300]$	LGPC non-autonomous $m=1$	$\mathbf{b}_n = \mathbf{H}(\mathbf{K}_3(h_1, h_4))$	-2	0.678

Table B.1 – with  $\mathbf{K}_1 = h^* + h^* \times \cos(h^*)$ ,  $h^* = h_5 + \cos(h_2) + 1.35 + h_2$ ,  $\mathbf{K}_2 = h_1 + h_3 + \sin(h_3) \times \sin(\cos(h_3) - 8.35)$  and  $\mathbf{K}_3 = \sin(h_4^2/h_1) - h_5 + h_1 \times h_4$

uncontrolled case used as a benchmark. Phase II is the continuous blowing obtained by LGPC sensor-based feedback, this control law accomplished a drag reduction of approximately 8% making this approach the “optimal case” control strategy. In contrast, phase III represents the periodic forcing  $St_a = St_o$ , with  $St_o$  the wake shedding frequency, acquired from previous studies and will be considered as the “pessimal case” with a drag increase of around 2%. This frequency was added in order to have the maximum and the minimum values for drag modifications. Phase IV and V are two different LGPC multi-frequency forcing. The first one  $b_h^1$  is linked to the best control. When a power spectral analysis is applied to the control law obtained, not presented here, two strong peaks are seen at  $St_H \approx 0.85$  and  $0.95$ , which are close to  $St_A = 0.945$ . A smaller peak is obtained at a closer value of  $St_A = 0.0675$ . This lower Strouhal value creates an ON/OFF behaviour which contains a combination of continuous blowing (ON state) and a periodic forcing (OFF state).  $b_h^2$  was a randomly chosen individual in the last generation, which happens to be individual number  $m = 20$ . This control law contains four dominant peaks between Strouhal values  $0.3 < St_H < 0.6$  and one at  $St_H = St_o$ . Finally, Phase VI is the control law  $b_n$  obtained for the non-autonomous case, with a drag reduction of -1%. For this case, the same strong peak is obtained at  $St_A = 0.945$ . However, no low-frequency peaks are presented. Conversely, similar peaks, to the one obtained for  $b_h^2$  arise at Strouhal values between  $0.3 < St_H < 0.6$ .

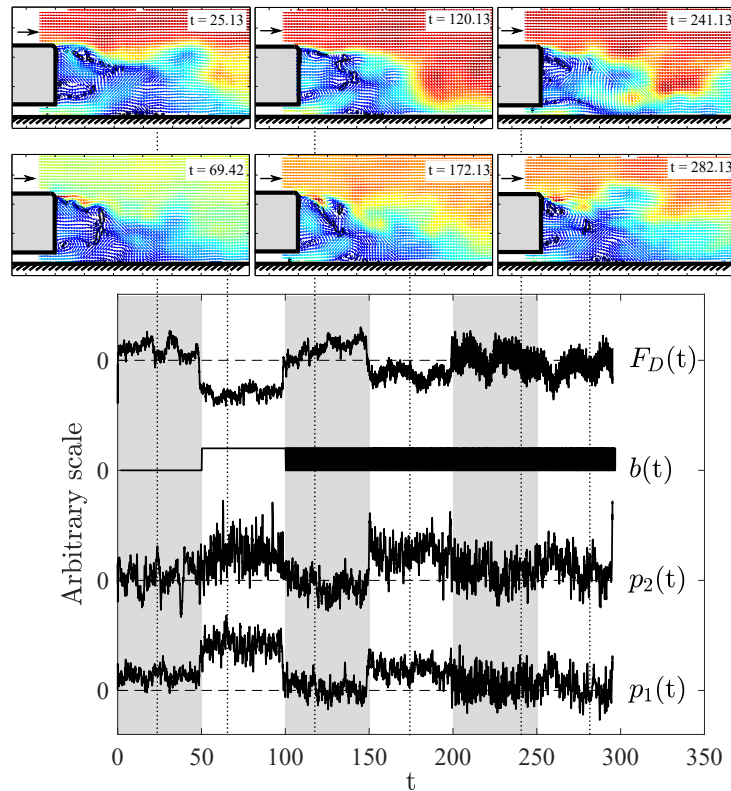


Figure B.1 – Ahmed body experience. Bottom: Time series of the actuation command with corresponding drag force and pressure measurements. Actuation command is delimited by gray and white areas. Top: Instantaneous flow field captured by the PIV for each phase.

The Ahmed body experience for MAO is resumed in Figure B.1. The time response of the drag  $F_D(t)$  for the total command  $b(t)$  when the phases are activated one after another is presented. The pressure sensors at the rear of the Ahmed body  $p_1$  and  $p_2$  are plotted. Snapshots at six distinct instants of these time histories are reported in Figure B.1 and correspond to each phase studied, note that each phase is applied for a time  $t = 50s$ . First, a typical instantaneous vector velocity field (coloured by the norm of the velocity vector) is presented at  $t = 25.13s$  for the uncontrolled configuration. Two vortical structures appear, the lower vortex is closer to the wall. Vortex creation at the top trailing edge is clearly seen, the presence of these coherent Kelvin-Helmholtz structures is present in the vicinity of the upper edge and roll-up vortices evolve, amplify and further dissipate downstream. The amplification of these vortices creates an interaction between the upper and lower shear layers. The second phase is represented at the

instant  $t = 69.42$  corresponds to a steady blowing. A direct and continuous opposition control of vortices in the near wake is applied, shifting the convective structures closer to the body. The upper and lower shear layer vortex interaction re-approaches the wall. The downward direct injection angle and the steady blowing combine together to deviate the trains of vortical structures, generated by the forcing, towards the rear face of the body. Similar behaviour can be also seen in phases IV and VI ( $t = 172.13$  and  $t = 282.13$ ). Periodic forcing (Phase III) is visible at  $t = 120.13$ ; the proximity between the actuated and shedding frequencies leads to an expansion of the shear layer vortices close to the edge. The presence of a symmetric-wake and a shear layer vortex expansion leads to a decrease of the base pressure. Finally, Phase V is seen at  $t = 241.13$  and presents characteristics from phase III and phases IV and VI. The shear layer interaction between the vortex structures formed at the upper and lower trailing edges is closer to those present for phase III; nonetheless, its interaction presents similar characteristics to those of periodic forcing. To better understand Figure B.1, the highest snapshots represent the highest values of drag, and correspond to the odd phases (I, III and V), while the lower snapshots are those with the lowest drag values, for even phases (II, IV and VI).

### B.1.1 Clustering

The clustering against the snapshot is plotted in Figure B.2 for the whole experience. This is done by  $\bar{k}^{++}$  taking 50 clusters, 2000 initial conditions and 20000 iterations. The plot shows to which cluster each snapshot corresponds.

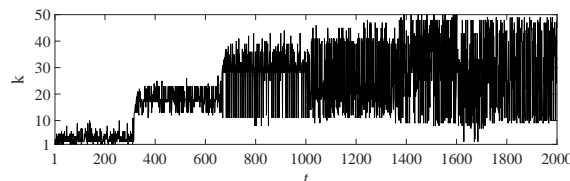


Figure B.2 – Cluster affiliation in terms of time. By construction, new cluster indices are a monotonously increasing function of time

### B.1.2 Frequency analysis

From the results obtained in Figure B.2, each snapshot from each phase  $l$  will be attributed to a particular cluster  $k$ . Hence, each element of the matrix represents the probability of a phase  $l$  to lie in the cluster  $k$ . This is equal to the number of snapshots of phase  $l$  lying in cluster  $k$  divided by the total number of snapshots in phase  $l$ . For example, most of the snapshots presented in phase  $l = 1$  are contained in the first clusters  $k < 10$ , while the second phase (continuous blowing) is comprised in the clusters  $12 < k < 25$  and the third (periodic forcing) is between  $25 < k < 40$ . The rest of the snapshots in the last phases are scattered in clusters  $k > 10$ . It is worth noting that phase IV comprises the same clusters as phase II, plus others of higher values, which corroborates the presence of a continuous state obtained for this phase (MLC multi-frequency forcing). This graphic gives a first hint of the resemblance between the control algorithms obtained using open-loop actuation and machine learning control.

### B.1.3 Metric of attractor overlap

The metric of attractor overlap is based on the centroid geometric configuration characterized by the distance between all centroids. The attractor similarity is calculated as the average distance of the centroids

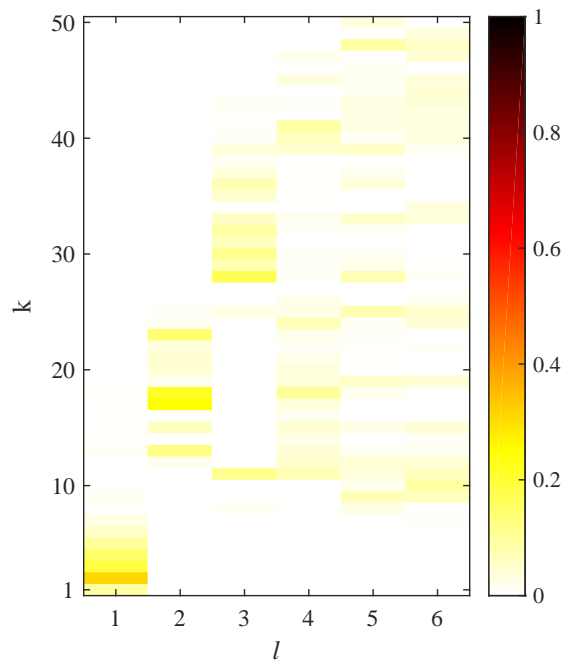


Figure B.3 – Population probabilities of the clusters for the six phases. The abscissa denotes the phase  $l$  and the ordinate the cluster index  $k$ . Each box represents a non-vanishing probability. The yellow to red tones indicate the population probability or relative frequency  $P_k^l$

of attractors and quantified by the *Kullback-Leiber divergence* also called *relative entropy*,

$$D_{\text{geom}}(\vec{P} \parallel \vec{Q}) = \sum_{k=1}^K P_k \ln \left[ \frac{P_k}{Q_k} \right]$$

where  $\vec{Q} = [Q_1, \dots, Q_k]$  is a reference probability distributions and  $\vec{P} = [P_1, \dots, P_k]$  a new measured one. The visualization of the  $D_{\text{geom}}(\vec{P} \parallel \vec{Q})$  equation is presented in Figure B.4(Left); note that this is just a visualization of  $D_{\text{geom}}$ . Broadly, the more the distance between the attractors, the farther they are geometrically. Phase I is far away from the other ones (with  $D_{\text{geom}}$  values over 8), while phases V and VI are quite similar, with distances almost equal to 0. Once more, phases II and IV present similar attributes.

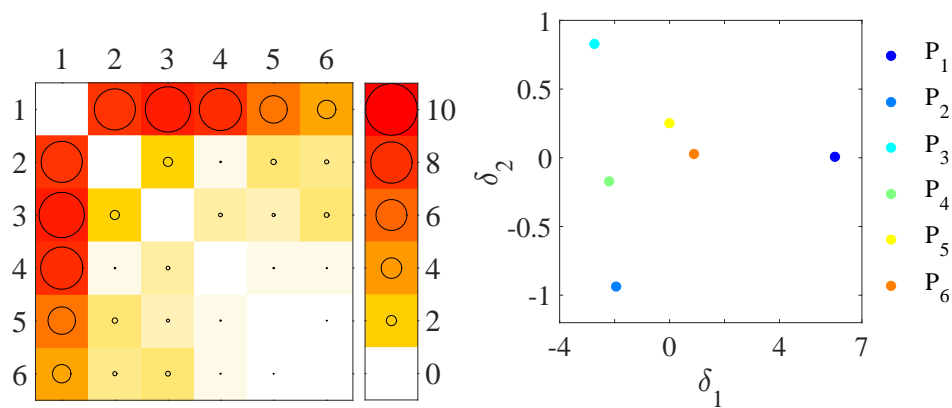


Figure B.4 – Left: Metric of attractor overlap for the six control laws. The value of  $D_{\text{geom}}(P \parallel Q)$  is shown in the  $l$ th row and  $n$ th column as a color code from white to red and by the size of the circle (see the caption on the right). Right: Attractor proximity map based on the geometric MAO. The points  $P_1 \dots P_6$  correspond to the six control laws.

The proximity map for the attractors based on MAO is depicted in Figure B.4(Right). Here, the feature coordinate  $\delta_1$  corresponds to the cross-stream rms-velocity penetration while  $\delta_2$  correlates with the drag.

# Notations

In this appendix all the main notation used are listed. The notation was attempted to be as consistent as possible throughout the book.

## Acronyms

<b>AC</b>	Alternating current
AR	Aspect ratio of the flow configuration
BFS	Backward-facing step
CL	Closed-loop
DC	Duty cycle
<b>DC</b>	Direct current
ER	Expanding ratio of the flow configuration
FFP	Forward flow probability
GP	Genetic programming
LSE	Linear stochastic estimation
MAO	Metric of attractor overlap
MLC	Machine learning control
OL	Open-loop
PID	Proportional integral derivative
PIV	Particle image velocimetry

PF	Periodic forcing
POD	Proper orthogonal decomposition
QSE	Quadratic stochastic estimation
SMC	Sliding mode control
VR	Velocity ratio

## Latin letters

$a_n$	$n^{\text{th}}$ POD temporal coefficient [s]
$A_r$	Recirculation area [ $\text{m}^2$ ]
$A_{ij}, B_{ijk}$	Stochastic estimation coefficients
<b>b</b>	Control law
$C_p$	Mean pressure coefficient
$C_{p_{\text{rms}}}$	Rms Pressure coefficient
$C_\mu$	Momentum coefficient
$C_x = C_D$	Drag coefficient [N]
$C_y$	Drift coefficient [N]
$C_z = C_L$	Lift coefficient [N]
$d$	Hole diameter of the actuator [m]
$E(f)$	PSD of the wall pressure fluctuation
$f$	Frequency [Hz]
$f_a$	Actuation frequency [Hz]
$f_s$	Sampling frequency [Hz]
$F_x = F_D$	Drag force [N]
$F_y$	Drift force [N]
$F_z = F_L$	Lift force [N]
$g$	Ground clearance [m]
$H$	Model height [m]
<b>H</b>	Heavy side function
<b>h</b>	Harmonic function
$H_r$	Recirculation bubble height [m]
$H_0$	Experimental facility height [m]
$i$	MLC individual
$J$	Cost function
$L$	Model length [m]
$L_r$	External reattachment length [m]
$l_{\text{jet}}$	Distance between to actuator holes [m]
$m$	MLC total number of individuals

$n$	MLC generation number
$n$	Mode number
$P$	Mean static pressure [Pa]
$p$	Fluctuating pressure [Pa]
$P_s$	MLC percentage of having an input in the control function
$q$	Flow rate [ $\text{m}^3 \text{s}^{-1}$ ]
$Re_H$	Reynolds number based on the model height
$Re_\delta$	Reynolds number based on $\delta$
$Re_\vartheta$	Reynolds number based on $\vartheta$
$s$	Sensor
$S_{\text{jet}}$	Cross-section of the actuator device [ $\text{m}^2$ ]
$S_\infty$	Reference surface of the model [ $\text{m}^2$ ]
$St_a$	Actuation Strouhal number based on H
$St_\vartheta$	Actuation Strouhal number based on $\vartheta$ and H
$St_H$	Strouhal number based on H
$St$	Strouhal number based on $L_{r0}$
$t$	Time [s]
$t_s$	Settling time [s]
$t_d$	Delay time [s]
$U_c$	Convection velocity [ $\text{m s}^{-1}$ ]
$U$	Mean streamwise velocity [ $\text{m s}^{-1}$ ]
$u_i$	$i^{\text{th}}$ component of the fluctuating velocity [ $\text{m s}^{-1}$ ]
$u_{\text{jet}}$	Jet velocity [ $\text{m s}^{-1}$ ]
$\bar{u}_{\text{jet}}$	Mean jet velocity [ $\text{m s}^{-1}$ ]
$u_{\text{jetmax}}$	Maximum jet velocity [ $\text{m s}^{-1}$ ]
$u_{\text{jets}}$	Jet velocity for continuous blowing [ $\text{m s}^{-1}$ ]
$\bar{u}$	Mean velocity [ $\text{m s}^{-1}$ ]
$u_{\text{rms}}$	Root-mean-square of the streamwise velocity
$U_w$	Mean streamwise velocity close to the wall [ $\text{m s}^{-1}$ ]
$\bar{u}^+$	Normalized mean streamwise velocity by $U_\infty$
$U^+$	Normalized mean jet velocity by $u_{\text{jetmax}}$
$\bar{u}$	Fluctuating velocity vector [ $\text{m s}^{-1}$ ]
$U_\infty$	Free-stream velocity [ $\text{m s}^{-1}$ ]
$V_{\text{jet}}$	Jet velocity amplitude [ $\text{m s}^{-1}$ ]
$V_e$	Actuation power supply [Volts]
$v_{\text{rms}}^+$	Normalized root-mean-square of the normalwise velocity by $U_\infty$
$X_r$	Internal separation length [m]
$x, y, z$	Spatial coordinates [m]

$\bar{x}$	Position vector [m]
$\Delta\bar{x}$	Space interval
$w_z$	Spanwise fluctuation vorticity [ $s^{-1}$ ]
W	Model width [m]

## Greek letters

$\alpha$	Slanted angle [ $^\circ$ ]
$\beta$	Sliding mode constant
$\delta$	Incoming boundary layer thickness [m]
$\varepsilon$	POD estimation error
$\gamma$	MLC penalization
$\Phi^{(n)}$	$n^{\text{th}}$ Spatial POD eigenfunction [m]
$\varkappa$	Sliding mode perturbation magnitude
$\lambda^{(n)}$	$n^{\text{th}}$ POD eigenvalue
$\Lambda$	Shear layer vorticity thickness [m]
$\Omega^+$	Ensemble-averaged vorticity [ $m^{-2}$ ]
$\Omega_z$	Spanwise fluctuating vorticity [ $m s^{-2}$ ]
$\sigma$	Sliding mode variable
$\vartheta$	Momentum thickness [m]
$\tau$	Correlation wall-pressure time delay [s]
T	Input delay [s]
$\xi$	Stream-wise separation interval [m]
$\zeta$	Sliding mode constant

## Linear Algebra

$\langle . \rangle$	Time-average operator
$\tilde{\cdot}$	Stochastic estimation
$\langle .   . \rangle$	Conditional-average operator
$\  \cdot \ _{L_2}$	Classical euclidean norm



## MANIPULATION DE LA TURBULENCE EN UTILISANT LE CONTRÔLE PAR MODE GLISSANT ET LE CONTRÔLE PAR APPRENTISSAGE: DE L'ÉCOULEMENT SUR UNE MARCHE DESCENDANTE À UNE VOITURE RÉEL.

Ce travail vise à faire une pré-évaluation des paramètres de contrôle en vue de réduire la traînée sur véhicule réel. Deux mécanismes d'actionnement différents (Murata micro-blower et couteau d'air) ont été caractérisés et comparés en vue de déterminer leurs qualités ainsi que leurs limites. Les micro-blowers ont pour but d'exciter la couche limite en vue de perturber directement les structures tourbillonnaires formées dans la couche de cisaillement. Le couteau d'air étudié, à surface arrondie, pourrait être considéré comme un dispositif actif de réduction de la traînée à effet Coanda équivalent au dispositif passif de type boat-tail. Différentes stratégies de contrôle en boucles ouverte et fermée sont examinées, telles que le soufflage continu, le forçage périodique, le contrôle du mode glissant (SMC) et le contrôle par apprentissage (MLC). La SMC est un algorithme robuste en boucle fermée permettant de suivre, d'atteindre et de maintenir une consigne prédéfinie; cette approche présente l'intérêt d'avoir une capacité d'adaptation prenant en compte les perturbations extérieures inconnues. Le contrôle par apprentissage est un contrôle sans modèle qui permet de définir des lois de contrôle efficaces qualifiées et optimisées via une fonction coût/objectif spécifique au problème donné. Une solution hybride entre MLC et SMC peut également fournir un contrôle adaptatif exploitant les mécanismes d'actionnement non linéaires les plus adaptés au problème. L'ensemble de ces techniques de contrôle ont été testées sur diverses applications expérimentales allant d'une simple configuration académique de marche descendante jusqu'à des géométries représentant une structure d'écoulement représentatives de véhicules réels. Pour la configuration de marche descendante, l'objectif était de réduire expérimentalement la zone de recirculation via une rangée de micro-jets et de l'estimer par des capteurs de pression. Les contrôles d'écoulement ont été réalisés par forçage périodique ainsi que par MLC. On démontre dans ce cas que la MLC peut surpasser le contrôle par forçage périodique. Pour la configuration sur corps épais (corps d'Ahmed), l'objectif était de réduire et/ou de maintenir la traînée aérodynamique via un couteau d'air placé sur la partie supérieure du hayon arrière et évalué par le biais d'une balance aérodynamique. Le soufflage continu et le forçage périodique ont été utilisés dans ce cas comme stratégies de contrôle en boucle ouverte permettant ainsi de faire une comparaison avec les algorithmes SMC et MLC. La pré-évaluation des paramètres de contrôle a permis d'obtenir des informations importantes en vue d'une réduction de la traînée sur un véhicule réel. Dans ce cadre, les premiers essais de caractérisation sur véhicules réels ont été réalisés sur piste et un dispositif d'actionnement ainsi qu'un protocole expérimental sont également présentés en perspective à ce travail.

**Mots clés:** écoulement turbulent, contrôle de flux actif, micro-blower, couteau d'air, contrôle du mode coulissant, contrôle par apprentissage

## TURBULENT FLOW MANIPULATION USING SLIDING MODE AND MACHINE LEARNING CONTROL: FROM THE FLOW OVER A BACKWARD-FACING STEP TO A REAL-WORLD CAR.

The present work aims to pre-evaluate flow control parameters to reduce the drag in a real vehicle. Two different actuation mechanisms (Murata's micro-blower, and air-knives) are characterized and compared to define their advantages and limitations. Murata micro-blowers energized the boundary layer to directly perturb the vortex structures formed in the shear layer region. The air-knife has a rounded surface, adjacent to the slit exit, that could be considered as an active boat-tail (Coanda effect) for drag reduction. Different open-loop and closed-loop control strategies are examined, such as continuous blowing, periodic forcing, sliding mode control (SMC) and machine learning control (MLC). SMC is a robust closed-loop algorithm to track, reach and maintain a predefined set-point; this approach has on-line adaptivity in changing conditions. Machine learning control is a model-free control that learns an effective control law that is judged and optimized with respect to a problem-specific cost/objective function. A hybrid between MLC and SMC may provide adaptive control exploiting the best non-linear actuation mechanisms. Finally, all these parameters are brought together and tested in real experimental applications representative of the mean wake and shear-layer structures related to control of real cars. For the backward-facing step, the goal is to experimentally reduce the recirculation zone. The flow is manipulated by a row of micro-blowers and sensed by pressure sensors. Initial measurements were carried out varying the periodic forcing. MLC is used to improve performance optimizing a control law with respect to a cost function. MLC is shown to outperform periodic forcing. For the Ahmed body, the goal is to reduce the aerodynamic drag of the square-back Ahmed body. The flow is manipulated by an air-knife placed on the top trailing edge and sensed by a force balance. Continuous blowing and periodic forcing are used as open-loop strategies. SMC and MLC algorithms are applied and compared to the open-loop cases. The pre-evaluation of the flow control parameters yielded important information to reduce the drag of a car. The first real vehicle experiments were performed on a race track. The first actuator device concept and sensor mechanism are presented.

**Keywords:** Turbulent flow, active flow control, micro-blower, air-knife, sliding mode control, machine learning control